Fuel Retention in Plasma Facing Materials of the JET ITER-like wall



Carmen Makepeace
Wolfson College
University of Oxford

A thesis submitted for the degree of
Doctor of Philosophy

Hilary 2021

This thesis is dedicated to my sister, Bronte, without whom I would not have completed it. Thank you for all the support you have given me.

Thank you to my Dad, who diligently read through and helped correct many typos. It is a gift I truly appreciate.

Thank you to my Mum for encouraging me through a severe head injury to finish and be proud of my work. Our 6am stretching sessions throughout lockdown 3.0 helped me recover so much quicker.

Thank you also to my friends who I've shared my Fusion CDT with. Alex and John have been fantastic and ceaseless co-conspirators always up for a drink and a chat.

Finally, thank you to the corner office for an endless supply of coffee, cake, and hugs.

Acknowledgements

I would like to thank both of my supervisors: Dr Anna Widdowson at CCFE, and Prof Sergio Lozano-Perez at the University of Oxford; for their support and patience during the four years of my DPhil.

I would also like to thank the work and collaboration undertaken between myself and Dr Cedric Pardanaud during my 3 month placement in Marseille, which led to the first novel result of my thesis: BeOD bonding found with Raman at the melted dump plate site.

I would like to thank EUROFusion colleagues, without whom I would not have been able to compare my results quite so well to laboratory specimens presented in the literature review. In particular I thank Dr Antti Hakola, without whom I would not have received the materials.

I would like to thank Dr Andree De Backer at CCFE for her help and support with the TMAP7 software and procedure, alongside our collaboration on the TMAP 7 results of the eroded and deposited JET beryllium regions.

Finally, I would like to thank the help and collaboration I have received from Xinlei Liu, a fellow DPhil student at the University of Oxford, and his supervisor Dr Rebecca Nicholls, whom have kindly provided the Density Functional Theory modelling in support of the EELS data and analysis of JET Beryllium undertaken during this thesis. This contribution has provided much in terms of argument and rational.

Abstract

This thesis, presents results from the Joint European Torus (JET), beryllium ITER-like wall. Isotopic hydrogen retention is investigated at three microstructurally unique sites: erosion zones, co-deposition zones, and melted material, found across the reactor at the inner and outer wall limiters and dump plate tiles. The techniques applied to these novel in-service materials were: Scanning Electron Microscopy with Energy Dispersive X-Ray (SEM-EDX), Raman Spectroscopy; Focused Ion Beam (FIB) 3D milling; Scanning Transmission Electron Microscopy (STEM) with Electron Energy Loss Spectroscopy (EELS) and Energy Dispersive X-Ray (EDX); Atom Probe Tomography and Thermal Desorption Spectroscopy (TDS).

Clustering of deuterium (D) with beryllium deuteride (BeD_2) was found at the outer eroded material, whilst not at the inner. BeD_2 was present at the core of D clusters up to 8 at%. Co-deposition at the outer limiter tile was governed by beryllium oxide (BeO), whilst at the inner it was governed by Be with D. EUROFusion samples produced from High Power Impulse Magnetron Sputtering (HiPIMS) returned similar EELS results to JET samples; presenting a reasonable model. Melted material produced highly oxidised zones devoid of metallic impurities from marker layers in spatially optimum sites, surrounded by grains produced via high temperature material mixing. Several types of beryllium deuteroxide (BeOD) with varying stoichiometries were presented

Retention is lowest at the inner wall eroded zone, increasing at the outer wall eroded zone, and increasing further between inner to outer wall co-deposits. Melted material, remains an outlier. Overall total retention, in melted materials was similar to outer wall co-deposit, however composed of over 77% H. Material mixing was suggested the cause due to beryllium/nickel alloying seen in melted materials.

Contents

1 Introduction **1**

2 Literature **6**

2.1 JET and the preparation for a Be ITER-like wall prior to the first campaign. 6

2.2 The Joint European Torus and the 2011-2012 first ITER-like wall campaign parameters 10

2.3 An introduction to fuel retention preceding the ITER-like wall at JET 11

2.4 The JET-ILW1 fuel retention findings: TDS and IBA, material erosion, migration and co-deposition 13

2.5 Thermal desorption and microstructural results of laboratory implanted beryllium 19

2.5.1 A summary of the general trends of laboratory produced and implanted tokamak-like beryllium materials 19

2.5.2 Hydrogenic implantation into crystalline beryllium 20

2.5.3 Thermal desorption and microstructural analysis of deposited laboratory beryllium materials 27

2.5.3.1 Thermal desorption of Be-D layers 28

2.5.3.2 The effect of other impurities in co-deposited layers: O, C, W, N 29

2.6 TMAP, applied to hydrogenic trapping in beryllium 31

2.7 Beryllium binary phase diagrams 34

2.7.1 EELS of beryllium materials 35

2.7.2 Atom probe tomography of beryllium materials 37

2.7.3 Literature summary 37

3 Experimental Methods **38**
3.1 Sample preparation 38
3.2 Microscopy 40
3.2.1 Scanning Electron Microscope and Energy Dispersive X-Ray . 40
3.2.2 Focused Ion Beam and sequential milling 41
3.2.2.1 The FIB process: "trenching" for serial milling studies 41
3.2.2.2 Serial Milling studies 44
3.2.2.3 The FIB process: "undercutting" for lift-out production 46
3.2.2.4 The FIB process: "Lifting out" the sample 48
3.2.2.5 The FIB process: Attaching the lift-out to an omniprobe grid 48
3.2.2.6 The FIB process: smoothing the lift-out sides for Raman analysis 49
3.2.2.7 The FIB process: smoothing the lift-out sides for TEM analysis 50
3.2.3 Raman Microscopy 52
3.2.4 Transmission Electron Microscopy and Electron Energy Loss Spectroscopy 53
3.2.5 Atom Probe Microscopy 56
3.2.6 Thermal Desorption Spectroscopy 60

4 Microstructural analysis of eroded JET materials **63**
4.1 An introduction to eroded materials in JET 63
4.2 Scanning Electron Microscopy of eroded JET surfaces 64
4.2.1 Energy Dispersive X-Ray and 3D milling of eroded cross sections in JET produced via Focused Ion Beam (FIB) milling . . 66
4.3 Transmission Electron Microscopy of eroded materials with application of Electron Energy Loss Spectroscopy (EELS) 69
4.3.1 STEM with EELS and EDX of non-exposed beryllium 71
4.3.2 STEM with EELS and EDX of the JET Inner wall eroded beryllium sample 73
4.3.3 STEM with EELS and EDX of the JET Outer wall eroded beryllium sample 77
4.4 Atom Probe tomography findings from eroded materials in JET . . . 80
4.5 Integrated TDS data comparing relative H isotopes present at the Inner and Outer wall eroded regions 87

4.6 A results summary from eroded JET inner and outer wall samples; and a NE-Be sample . . . 88

5 Microstructural analysis of deposited JET materials 90

5.1 An overview of the chapter's analysis of deposited JET materials . . . 90

5.2 Scanning Electron Microscopy (SEM) of deposited surfaces and subsurfaces in JET . . . 91

5.2.1 The Inner wall deposit . . . 91

5.2.2 The outer wall deposit: SEM imaging . . . 92

5.3 Energy Dispersive X-Ray of deposited cross sections in JET produced via Focused Ion Beam (FIB) milling . . . 94

5.3.1 The inner wall deposit: EDX . . . 94

5.3.2 The outer wall deposit: EDX . . . 96

5.4 Transmission Electron Microscopy of deposited materials with application of Electron Energy Loss Spectrosocpy (EELS) . . . 97

5.4.1 The inner wall deposit: STEM with EELS and EDX . . . 98

5.4.2 The outer wall deposit: STEM with EELS and EDX . . . 103

5.4.2.1 The outer wall deposit; left poloidal edge . . . 103

5.4.2.2 The outer wall deposit, sample centre . . . 105

5.4.2.3 The outer wall deposit; right poloidal edge . . . 107

5.4.3 EELS of EUROFusion samples produced via HiPIMS . . . 109

5.5 Atom Probe tomography of JET deposits . . . 112

5.6 Integrated TDS of relative H isotopes present between IW and OW JET deposits . . . 114

5.7 Summary JET IW and OW deposits . . . 115

6 Microstructural analysis of melted JET materials 118

6.1 An introduction to melted materials in JET . . . 118

6.2 SEM of the surface morphology and microstructures present . . . 119

6.3 The melted ridge microstructure . . . 120

6.3.1 Subsurface SEM and 3D milling studies . . . 120

6.3.2 Surface: Raman Spectroscopy & Confocal microscopy . . . 121

6.3.3 SEM-EDX of melt region lift-outs . . . 126

6.3.4 Scanning Transmission Electron Microscopy of the melted lift-out with EELS and EDS . . . 128

6.3.4.1 STEM and EDS . . . 128

6.3.4.2 STEM and EELS . . . 130

6.4 The second microstructure at the surface: 136
6.4.1 Subsurface SEM-EDX of lift-outs of the second microstructure 136
6.4.2 Scanning Transmission Electron Microscopy of the second microstructure 137
6.4.2.1 STEM-EDX, lift-out surface into depth: 138
6.4.2.2 Scanning Transmission Electron Microscopy with EELS, of the second microstructure found at the dump plate tile 141
6.4.3 Integrated TDS data showing relative H isotopes present at dump plate in JET 145
6.4.4 Summary and discussion of the results seen at the Dump plate castellation in JET 146

7 Conclusions 148

A Supplementary work on eroded regions: TEM brightfield, and EELS fitting examples, 154
A.1 Supplementary table of precipitate image analysis of eroded regions . 154
A.2 Supplementary Brightfield TEM images of eroded regions 154
A.3 Supplementary examples of EELS hyperspy curve fitting accuracy for integrated stoichiometric calculations 156

B Further supplementary work on melted materials: Expanded Image analysis, further examples of STEM-EDX and STEM-EELS 157
B.1 Thresholding melted regions 157
B.2 Further STEM-EDX examples 159
B.3 Further STEM-EELS examples 160

C Supplementary Wall temperature information, and Thermal Desorption Spectroscopy graphs and analysis for future work 161
C.1 Supplementary JET thermocouple data, showing the inaccuracies of wall measurement and high uncertainties 161
C.2 Supplementary Thermal Desorption Spectroscopy graphs: eroded materials 162
C.3 Supplementary Thermal Desorption Spectroscopy graphs: deposited materials 164

C.4 Supplementary Thermal Desorption Spectroscopy graphs: melted materials 166
C.5 Initial results in collaboration with modellers, using TMAP7 to model release from eroded and deposited materials 166

D Supplementary Raman results on beryllium lift-outs from the JET ILW1 **167**

Bibliography **170**

List of Figures

1.1 Overview of the ITER-like wall final design in and around the JET torus; showing beryllium limiters of S65-H, inner wall cladding inserts of Inconel and Be coatings and neutral beam injection shine path protections; alongside the bulk W divertor and W-coated carbon-fibre-composites [1] 4
1.2 A poloidal cross section of the JET ILW showing the positions of tiles removed. For the purposes of this study the tiles analysed were the '2XR10' inner poloidal limiter tile; the '4D14' outer poloidal limiter tile and the '2B2C' dump plate tile at the top of the vessel. 4
1.3 An overview of top: the inner poloidal limiter tile with central eroded, and wing deposited castellations marked, from which experimentation occurred; and bottom: the outer poloidal limiter with sample positions also marked. 5
1.4 Overview of the JET 2010-2012 Dump plate tile and extracted castellation, on which further analysis occurred. 5

2.1 An exploded view of the beryllium tile assembly, showing the 5 slices; to reduce eddy current loads and thermal expansion stresses, and the castellated surfaces to reduce thermal loads [2] 7
2.2 A graph from [3], top (a) and (b), Secondary Ion Mass Spectroscopy before and after thermal testing of marker layer coatings; and bottom (c) cross section SEM SE image and EDS of the coatings post cyclic test. 9
2.3 Overview of gas balance measurements for deuterium [4] at JET. Red and yellow bars refer to gas balance measurements for ILW1, at shorter and longer integrated times. Black bars, show measurements from JET's carbon wall. Measurements are by Low (L-mode), and High power (H mode) operational modes. 11

2.4 A comparison of past and present plasma facing materials and their saturation behaviour on deuterium loading [5] 12
2.5 The photographic survey of the Inner wall Guard limiter (one of the mid-plane tiles, this thesis analyses (f)), showing melting trails due to plasma bombardment [6]. 14
2.6 An overview of the outer poloidal limiter mid-plane tile (where 2 castellations analysed in this thesis originate). Top: optical photograph of the beryllium tile; bottom: IBA analysis showing the relative concetrations of Deuterium and Ni across the toroidal positions from left wing to right wing [7]. 14
2.7 A comparison of TDS data for the outer poloidal limiter mid-plane for the second ITER-like wall campaign [8]. 15
2.8 SEM SE image showing the inner wall limiter midplane erosion region; the morphology has been linked to light ion plasma exposure [9]. . . . 16
2.9 SEM SE image showing the inner wall limiter midplane at the outer wing edge; the morpghology is described as “cabbage-like” and linked to molten materials arriving at the tile [9]. 16
2.10 Tritium depth profile of beryllium samples from the inner wall limiter (IWGL) erosion zone, the outer poloidal limiter (WPL) deposition zone, and the upper dump plate tile (away from the melt ridge) [9]. . 17
2.11 Ion Beam Analysis showing the Ni, Cr, and Fe impurities present at the inner midplane poloidal limiter from the 3rd ITER-like wall campaign (the same position as the inner poloidal limiter tile from ILW1 analysed in this thesis) [10]. 18
2.12 A cross section of deposit on tile 6 at the outer divertor (just beyond the strike point location) [11]. 18
2.13 NRA yield of Deuterium release on 2K/s thermal ramps between samples implanted to high depth with D at 60keV, or implanted with D at 60keV with additional implantation at 15keV of He, or a final sample implanted with D at 60keV with additional H implantation to 10keV [12]. 21

2.14 Deuterium bubble formation from implantation of beryllium at 700K with 10keV D ions to a fluence of $4x10^{21}Dm^{-2}$. (a) TEM image showing the bubbles present in the structure; (b) a schematic showing the proposed composition of the bubble formation in a cross section of the beryllium (1) BeO layer at the surface; (2) small prismatic D_2 bubbles; (3) larger oblate D_2 cavities; (4) grain boundaries and (5) grain boundary oxides [13]. 22
2.15 TEM images (bright field) showing bubble formation and coarsening between (a) 3keV 200K, and (b) 10keV 500K, D ion implantations undertaken by Chernikov [14]. (b) Dense prismatic bubbles are seen along the hcp c-axis; larger oblate bubbles are also seen at these conditions. 23
2.16 An overview surface image of the S65 grade Be subjected to (left to right) high temperature exposure, low temperature exposure and no plasma exposure [15] 24
2.17 Thermal desorption spectra showing D_2 signal when heated at $1Ks^{-1}$ (the JET TDS ramp rate) after a fluence of 3keV D_3^+ ions at 2 x $10^{17}cm^{-2}$ at room temperature [16]. 25
2.18 Thermal desorption spectra showing D_2 signal changes between release states; when heated at $1Ks^{-1}$ (same conditions as JET samples) on increasing fluence of 3keV D_3^+ ions at room temperature [16]. 25
2.19 Thermal desorption spectra showing D_2 signal changes between release states; when heated at $1Ks^{-1}$ (same conditions as JET samples) at two implantation temperatures of 320K and 530K for 3keV D_3^+ ions [16]. 25
2.20 The results from TVA co-deposits implanted with high energy deuterium ions with the amount of retain fraction shown against the implantation temperature, of different mixed materials [17]. For comparison the author has also shown literature values [12, 18, 19, 20]. . . . 29
2.21 (a) thermal desorption of room temperature compounds of Be, Be_12W, Be_2C samples; (b) thermal desorption of room temperature mixed layer deposits of Be, with W at 10%, 60%; (c) thermal desorption of room temperature mixed layer deposits of Be with C 8% and 50%, (d) thermal desorption for beryllium layer implanted at room temperature, versus 423K, and 573K [21]. 30
2.22 Table displaying the variation in experimentally measured and reported diffusivity and solubility data for beryllium by Abramov [22]. 32

2.23 Diffusion coefficients calculated by multilayer permeability approach between an ultra purity beryllium grade (1) and a further less pure comparison at two different thickness (2) and (3); in comparison to previous reported literature values [22]. 32
2.24 The variation of reported diffusivity across the literature in Be and BeO respectively. Dotted lines refer to measured hydrogenic species diffusivities in BeO; whilst solid lines refer to hydrogenic diffusivities in Be [23]. 32
2.25 The application of a free parameter of the D diffusivity in BeO to create a good fit to under and overlayer co-deposits superposition in the applied TMAP7 model is shown [23]. 33
2.26 The beryllium-copper alloying system [24]. 35
2.27 The beryllium-nickel alloying system [24]. 35
2.28 The low loss region via REELS of a beryllium MaTeck sample (99.8%) implanted by D ions without oxygenation. A comparison between experiment and modelling for two angular geometries. 36
2.29 STEM with EELS in standard geometry with a Gatan GIF detector, of samples under neutron, T and He implantation at the Petten high flux reactor in the Netherlands under the HIDOBE II program. (a): STEM HAADF image of the region, (b): Low Loss EELS spectra of a linescan across the HAADF feature [25]. 36
2.30 Trailing APT time of flight Da peaks for beryllium with no dpa damage and 0.4dpa from neutron bombardment and He production [26]. . . . 37

3.1 A schematic cross section of the starting tile microstructure, from top to bottom showing the bulk crystalline beryllium, the nickel TVA 3μm interlayer and the beryllium 8μm TVA surface layer. 39
3.2 A schematic of the trenching process for serial milling studies. The image displays the SEM surface area from a bird's eye vantage point. The navy blue boxes surrounding the region of interest (on which platinum is deposited) represent the rough cut trenched regions to 15μm depths; note the white spacing left around the region of interest during this step. This was to reduce any chance of beam drift interacting with the region of interest at high current. The inset red boxed regions represent the finer mill of the trenching process to abut the region of interest. This is done at 22nA for greater accuracy and milling precision. 42

3.3 A SEM secondary Electron (SE) image of the cross section of the sample's surface. From top to bottom the regions seen are: white - the platinum protective layer; mid grey scale - the beryllium surface abutting the protective platinum layer. The bottom of the image corresponds to approximately 8-10μm depths into the beryllium surface. The beryllium region is smooth and uniform, with white precipitates (oxides) present primarily at the grain boundaries. This is an example of the surface finish needed for a serial milling study. 43
3.4 A schematic showing the optimum design and position of a fiducial to the top left corner of the region of interest, as perceived from a bird's eye vantage of the sample's surface. 44
3.5 A schematic showing the lift-out surface from a bird's eye vantage. A further rough cut (navy blue boxing) and fine cut (red boxing) at 65nA and 22nA ion beam currents is undertaken (relative to the figure above the region of interest), completing the trenching process. 46
3.6 A schematic showing the relative view present in the FIB beam (relative to the surface at 52 degrees). The surface is displayed in sky blue, whilst the trenched royal blue regions would appear shaded in the 'real' image due to the material removed in these areas. The region of interest would be displayed as suggested with the platinum (white) facing outwards at the surface and the depth profile of the beryllium lift-out retreating into the page slightly. The undercut region is outlined by rough cut in navy and then on attachment of the lift-out to the micromanipulator needle, the 'bridge' remaining, attaching the sample to the surface would be removed at smaller currents as indicated by the red boxed regions. 47
3.7 An SEM SE image of the omni-probe grid at position A with the lift-out attached in the 'v' position for added structural stability. The face of the lift-out seen is the depth profile of the lift-out from top to bottom relative to the top of the image. 49

3.8 An SEM SE image of a lift-out from the dump plate (melted) material. (a): showing the redeposited surface after undercutting where the wedge profile remains. (b): From top to bottom; the platinum protective surface region (white/light grey); the darker grey beryllium sample whose global surface abuts the platinum layer, going into depth; surrounded by a platinum and beryllium (high contrast/white saturated region) - a sputtered window to give added strength to the thinned region. The smooth uniform sides are appropriate for Raman or EDX analysis, showing microstructural features. 50
3.9 An SEM SE image of an inner wall eroded region lift-out prepared for EELS and transparent at 5kV in the SEM beam. The platinum signal at the top of both windows is almost completely gone. The milled window on the right of the lift-out is more transparent than the left (from contrast). A hole can be seen in both lift-outs at the base. . . 52
3.10 A schematic showing the STEM mode with EELS and the orientation of EELS and EDX detectors 54

4.1 Left: Navcam image (optical) from the FIB: showing a schematic of the sampling locations for the inner eroded wall castellation. Right: Navcam image (optical) from the FIB: showing a schematic of the sampling locations for the outer eroded wall castellation. (The abbreviation 'APT' stands for Atom Probe Tomography samples.) 64
4.2 Overview surface Scanning Electron Microscope (SEM) secondary electron images of a NE-Be sample: (a) central location at low magnification; (b-c) central and corner location at high magnification. 65
4.3 Overview Scanning Electron Microscope (SEM) Secondary Electron (SE) images of the surface of the inner eroded limiter castellation at increasing magnification. 65
4.4 Overview Scanning Electron Microscope (SEM) Secondary Electron (SE) images of the surface of the outer eroded limiter castellation at increasing magnification. 65
4.5 (a) & (b): The first and $60th$ slice, SEM secondary electron images of the NE-Be produced from FIB 3D milling at the centre of the castellation. (c): The thresholded 60th slice produced via FIJI, showing particles decorating grain boundaries. 66

4.6 (a) & (b): The first and $60th$ slice, SEM secondary electron images of the inner wall eroded sample, produced from FIB 3D milling at the centre of the castellation. (c): The thresholded 60th slice produced via FIJI, showing particles decorating grain boundaries. 66
4.7 (a) & (b): The first and $60th$ slice, SEM secondary electron images of the outer wall eroded sample, produced from FIB 3D milling at the centre of the castellation. (c): The thresholded 60th slice produced via FIJI, showing particles decorating grain boundaries. 66
4.8 A logarithmic frequency distribution. Particle areas have been binned into size distributions. The results compare the inner and outer eroded sample with the NE-Be sample. 67
4.9 Scanning Electron Microscope, Secondary Electron image of the inner wall eroded depth profile, and corresponding Energy Dispersive X-Ray map of the Oxygen K-series. 68
4.10 Scanning Electron Microscope, Secondary Electron Image of the outer wall eroded depth profile and corresponding Energy Dispersive X-Ray map of the Oxygen K-series. 68
4.11 (a): High Angle Annular Dark Field (HAADF) STEM images montaged, showing Z contrast of the NE-Be sample. (b): The corresponding FIB image prior to electron transparency. 70
4.12 The inner wall eroded TEM lamella. (a): Lower magnification Bright Field STEM overview image. (b): STEM High Angle Annular Dark Field (HAADF) images montaged at higher magnification showing the Z contrast. 70
4.13 The outer wall eroded TEM lamella; (a) FIB lift-out prior to electron transparency (white square from SEM C contamination, subsequently removed), (b) STEM HAADF Z contrast image. (c) Higher magnification HAADF of the EELS area, (d) Annular Dark Field STEM image of EELS area, showing diffraction contrast. 70
4.14 Figure displaying the as-received beryllium material; (a): STEM HAADF image overview of regions of interest. (b): STEM HAADF EELS linescan. (c): Atomic % beryllium and oxygen along the linescan via curve fitting. 71

4.15 (a): Following EELS results, two integrated areas were analysed by EDX along the linescan, those with higher oxygen levels - concern the red region, those with lower oxygen levels, the blue region. (b): The EDX spectra of the two regions. 72
4.16 Extracted EELS curves of the same integrated areas displayed in figure 4.15(a). (a): The Be core loss for the red and blue regions. (b): The O core loss for the red and blue regions. 72
4.17 Left: STEM HAADF image of the as-received beryllium material, with sampled positions marked along a linescan. Right: Normalised low loss spectra of marked positions, with addition of DFT modelled EELS data (dotted lines). 73
4.18 The inner wall eroded region. (a): STEM Annular ADF1 overview image, with regions of interest. (b): Be EELS at% map at region 3. (c): O EELS at% map at region 3. 74
4.19 The inner wall eroded region. (a): STEM Annular ADF1 overview image with regions of interest. (b): Be EELS at% map at region 4. (c): O EELS at% map at region 4. 74
4.20 The inner wall eroded region. (a): STEM Annular ADF1 overview image with regions of interest. (b): Be EELS at% map at region 5. (c): O EELS at% map at region 5, furthest into depth. 74
4.21 Figure displaying region 3 of the inner wall; (a) STEM HAADF image at the surface, and (b) Background subtracted normalised Be core loss point spectra, compared against the DFT modelled spectra. 75
4.22 Figure displaying region 3 of the inner wall. (a): STEM HAADF image at the surface. (b): Background subtracted normalised O core loss point spectra, compared against the DFT modelled spectra. . . . 76
4.23 Figure displaying the corresponding low loss spectra relating to figures 4.21 & 4.22. Low loss point spectra are compared against the DFT modelled Be-O-H structures. 76
4.24 The outer wall eroded region. (a): STEM HAADF image of the region of interest. (b): STEM higher magnification HAADF image. (c): STEM ADF image showing diffraction contrast at the grain boundary. 77
4.25 The outer wall eroded region. (a) STEM HAADF EELS area scan. (b): Be EELS atomic % map. (c): O EELS atomic % map. 77

4.26 The outer wall eroded region. (a): STEM HAADF EELS area scan region. (b): EDS overview of the 3 equivalent count integrated regions: red - the large oxide, green - the small oxide, and blue - the matrix region. (c) the Oxygen EDS peak of the 3 regions. 78
4.27 Figure displaying normalized Be core loss spectra of the three averaged regions discussed in figure 4.26(a), compared to DFT EELS models of Be-O-H systems. 78
4.28 Figure displaying normalized O core loss spectra of the three averaged regions discussed in figure 4.26, compared to DFT EELS models of Be-O-H systems. 79
4.29 Figure displaying normalized low loss spectra of the three averaged regions discussed in figure 4.26, compared to DFT EELS models of Be-O-H systems. 79
4.30 The outer wall eroded region. (a): STEM HAADF EELS area scan with extracted points. (b): low loss spectra and DFT model comparison. 80
4.31 Comparison of decomposed ion ranges in atomic % across JET erosion regions 81
4.32 Comparison of decomposed ion ranges in atomic % across JET erosion regions: showing H isoptopic changes between samples 82
4.33 A three-dimensional reconstruction of the first atom probe measurement of the outer wall erosion zone 83
4.34 A three-dimensional reconstruction of the second successful atom probe measurement of the outer wall erosion zone 83
4.35 A three-dimensional reconstruction of the third successful atom probe measurement of the outer wall erosion zone 83
4.36 A three-dimensional reconstruction of the first successful atom probe measurement of the inner wall erosion zone 84
4.37 A three-dimensional reconstruction of the second successful atom probe measurement of the inner wall erosion zone 84
4.38 The BeD (11Da) isosurface of sample 140.17 extracted from sample 140.17's APT reconstruction; showing the ionic percentage concentration gradient of BeD (11Da) and D (2Da) into the surface 85
4.39 Left: A comparison of extracted Atom Probe BeD (11Da) isosurfaces of samples 140.17, 140.22, and 140.26, into the surface. Right: A comparison of D concentrations in the BeD isosurfaces of samples 140.17, 140.22, and 140.26. 86

4.40 Comparison of hydrogen isotopic release for the inner and outer wall eroded materials as a function of elapsed time. Left: inner eroded sample results. Right: outer eroded sample results. 87
4.41 A comparison of APT and TDS data considering atomic % of hydrogen isotopes from the two techniques. 88

5.1 A Navigational optical image. Left: the inner wall deposited castellation. Right: the outer wall deposited castellation. The notation 'LO' stands for lift-out produced via FIB milling. 'APT' stands for atom probe microscopy. The navigational image shows the locations and techniques applied on sampling. 91
5.2 SEM SE images of the IW-deposit showing: surface morphology perpendicular to the sample surface at LHS (a), centre (b) and RHS (c) poloidal positions. 92
5.3 SEM SE images. (a-b): LHS IW-deposit sub surface with no deposit present. (c-d): RHS IW-deposit sub surface with $\sim 5\mu$m of plasma deposit additional to the starting structure: TVA Be, TVA Ni, and S65-H Be. 92
5.4 A figure displaying (b-j): optical positions along the toroidal direction (LHS-RHS poloidal edges) of the OW-deposit indicated by the green cross. (a-i) Respective SEM SE images of those positions. 93
5.5 (a-b): Figure showing the surface and depth profile at the LHS poloidal edge, position 5. (c-d): A RHS intermediate surface and subsurface, position 2. (e-f): The RHS poloidal edge, position 1. 93
5.6 Background subtracted SEM SE EDX images: low magnification overview SEM-SE image; high magnification SEM-SE image of EDX scan area, Nickel K line elemental map, Tungsten M line elemental map, and Oxygen K line elemental map. 94
5.7 SEM SE image (a) showing the top of 'marker layer' Be with oxidised surfaces; (b) SEM SE at higher magnification of sub surface deposit layer with two apparent microstructural features white contrast precipitates, and a dark contrast matrix; (c) Background subtracted EDX spectra of the two extracted areal regions: spectra 4 (light contrast) rich in nickel, iron and oxygen; spectra 7, beryllium matrix with small nickel contributions. 95

5.8 SEM SE images from (a-d) at increasing magnification; showing a right poloidal edge liftout after the higher magnification 3D milling study. Images (c) and (d) show the intense variability of feature densities at the 500nm scale from two regions less than 3 μm apart. 96
5.9 SEM-EDX maps of the lift-out from figure 5.8, showing the horizontal 'sedimentary-like' deposit structure with rich alternating layers of nickel oxide, nitrogen associated with Cu, and fewer layers of aluminium, iron and tungsten associated elements. 97
5.10 A High Angle Annular Dark Field (HAADF) STEM image of the deposited inner wall at the right poloidal edge, where deposition is most frequently seen. Those regions indicated are further explored via EELS and EDS. 98
5.11 A HAADF STEM image and associated EDS spectra at low magnification of region 1 defined in figure 5.10, showing low resolution changes in deposit composition. All images are background subtracted 99
5.12 Higher resolution EDS spectra and HAADF STEM image of Region 2 outlined in Figure 5.10, showing the deposit compositional changes and both a surface oxide as well as the second deposit layer beneath. All images are background subtracted. 99
5.13 Linescan of Region 3 at the inner wall deposit. (a): STEM HAADF image with atomic contrast, with integrated regions marked. (b): extracted EDS at.% bar chart. (c): EELS low loss extracted spectra. (d): EELS Be core loss extracted spectra. 100
5.14 (a): HAADF STEM image of the inner wall Region 3 deposit, right poloidal edge at higher magnification. (b): EDX linescan results, as a bar chart with distances along the scan numbered. (c) Low loss EELS of extracted numbered regions. (d): Be core loss EELS of numbered regions. 101
5.15 (a): HAADF STEM image left of the inner wall region 3 deposit at higher magnification, investigating the sponge-like matrix. (b): EDX extracted linescan at.%. (c): EELS low loss extracted spectra. (d): EELS Be core loss extracted spectra. (e): EDX extracted spectra. . . 101

5.16 (a): HAADF STEM image of the inner wall at region 1, deposited right poloidal edge of the castellation at higher magnification investigating a linescan intersecting sedimentary-like deposit at the surface; and the second deposit structure into depth. (b) EDX ectracted at.%. (c): EELS low loss and (d): Be core loss are presented alongside EDX extracted spectra (e). 102
5.17 Overview of the outer wall left hand poloidal edge deposit. (a): STEM HAADF image, (b): SEM SE image of the original surface morphology. (c): SEM SE lift-out image, prior to thinning. The region of interest in (a) where EELS and EDX occurred, is indicated by the red box in (c). 103
5.18 STEM HAADF images (a and c), and ADF images (b and d) showing atomic weight contrast in the former and diffraction contrast in the latter. These images are from the outer wall left hand poloidal edge deposit. The STEM-EELS region of interest scanned, is indicated by the red box in (a). 104
5.19 (a): STEM HAADF image at low magnification of the outer wall left hand poloidal edge deposit. (b-e): EDS maps of: Be (K), O (K), N (K), and C (K). (f): Nitrogen EDX map, with extracted EDX positions marked in red numbered 1-10 from top to bottom. (g): EDX atomic % compositions of extracted points. 105
5.20 (a): Overview of central poloidal OW-deposit surface morphology. (b): FIB lift-out thinning process showing four microstructures: surface bubbles, sedimentary layers, pores, and TVA Be. (c): STEM ADF diffraction contrast image. (d): STEM HAADF atomic contrast image. 105
5.21 (a): STEM EDS map of the region, integrated normalised pixel areas from which spectra were extracted for EDS and EELS are indicated. (b): Graph showing, left axis: EDX at.% composition measured in situ, right axis: EELS curve fit at.% Be and O. 106
5.22 (a): STEM EDS map of the region probed. (b): EELS Be core loss extracted spectra. (c): EELS O core loss extracted spectra. Points 3 and 5 have greater oxidation. 106

5.23 (a): SEM SE image, showing the right poloidal OW-deposit lift-out. (b): SEM SE surface morphology image at the region of interest. (c): STEM HAADF image of the remaining lift-out post fracture in transit. (d): The remaining surface bubble morphology of the lift-out after transport. Two EDX integrated spectra of the bubble surface and fractured bottom surface respectively. 108
5.24 A comparison of EDX elemental impurity at%, between inner and outer wall deposits. 2 deposit structures appear at the inner wall; some variation in heavier elements at the base of OW-deposits could classify a second OW-deposit structure. 108
5.25 An EELS Be core loss comparison of averaged normalised spectra of: JET IW and OW sedimentary deposits; EUROFusion BeO, BeOD, and BeD samples (via the HiPIMS method [27]); and DFT modelled spectra. Those spectra showing closest affinity are plotted at the same y-height. 109
5.26 An EELS O core loss comparison of averaged normalised spectra of: JET IW and OW sedimentary deposits; EUROFusion BeO, BeOD, and BeD samples (via the HiPIMS method [27]); and DFT modelled spectra. 110
5.27 An EELS low loss comparison of averaged normalised spectra of: JET IW and OW sedimentary deposits; EUROFusion BeO, BeOD, and BeD samples (via the HiPIMS method [27]); and DFT modelled spectra. Those modelled spectra showing closest affinity are plotted at the same y-height. 111
5.28 A three-dimensional reconstruction of the first atom probe measurement of the inner wall limiter deposition zone 112
5.29 A three-dimensional reconstruction of the first atom probe measurement of the outer wall limiter deposition zone 112
5.30 Comparison of atomic % composition of all ions decomposed between outer and inner wall deposited zones and a NE-Be JET sample. . . . 113
5.31 A comparison of all decomposed H isotopes present in outer and inner wall deposition zones alongside a NE-Be JET sample. 113
5.32 Comparison of hydrogen isotopic release for the inner and outer wall deposited materials as a function of elapsed time. Left: Inner wall deposited castellation results. Right: outer wall deposition castellation results. 114

5.33 A comparison of APT and TDS data considering atomic % of hydrogen isotopes from the two techniques. 115

6.1 A SEM SE image of the dump plate castellation; providing an overview image of the whole surface area. 119
6.2 Three SEM images. (a): SE image of the left poloidal melted mound and to the right, the secondary microstructure. (b): the same position via a backscattered electron image. Lighter regions refer to heavier elements. (c): BSE image of the sample's surface at the centre. White regions are valleys. Dark spots occur from de-lamination. 120
6.3 A (FIB) optical image, via the navigational camera; overlaid with sampling locations and their typical microstructural SEM SE images. . . 120
6.4 Top (a-c): three SEM SE images of the melted mound at the top poloidal LHS sample edge. (a): Overview of a Raman region which identified BeOD bonding. (b): The final slice of the 3D milling study. (c): A 3D milling slice of the exposed face with high contrast precipitates in a low contrast Be matrix. (d-f) Three identical examples of at the sample's left poloidal base. (d): region of interest, (e): 3D milling study, (f): representative slice. 121
6.5 Two SEM SE images showing the area of the Raman mapped surface region at increasing magnification from (a-b) 122
6.6 (a): SEM SE image showing the Raman mapped surface region. (b): The corresponding Raman optical image with the mapped region marked in red. 122
6.7 (a) Graphed prospective spectral bands: Be stretching mode at $\sim$450cm^{-1}, the Be phonon densities of states (PDOS), correlate to defect number densities; BeD_2 spectra [28], BeC_2 and amorphous carbon B&G bands [29]; BeOD and BeO positional spectral bands [30]. (b): A typical JET spectrum from the melt region. Increasing background is due to carbon contamination. Areal maps (c-e): show areas where spectral regions have high associated intensity of BeO and BeOD bonding. (f): A schematic marking those surface areas with highest intensities of relative component bands, Be up-shifted, Be, BeO, C, and two suggested types of BeOD. 123

6.8 Three extracted Raman spectra from an additional map of the same region, with expanded spectral range showing: a highly resonant band correlated to the BeOD and smaller bands at 1040, 1110, 1240, and 1460 cm^{-1}. Changing relative intensities of the bands: 2840, 2880, 2910 cm^{-2}, alongside 1040, 1110, 1240, and 1460 cm^{-1}; suggests presence of multiple BeOD stoichiometries. 124
6.9 Two montaged Raman optical images. (a): The total length of the melted region, areas where BeOD was present are marked in green. Regions in red had no BeOD bonding present. (b): The region with greatest BeOD density at higher magnification. BeOD appears sensitive to the plasma direction, relative to the mound. 125
6.10 (a): Confocal microscopy heat map results of the area (figure 6.9). Fast Fourier Transforms (FFT) were applied to separate large waveforms, of macroscopic gradients, from changes in local roughness. (b): FFT results of the mound's local waveform and height. The mound is $\sim 10\mu$m higher than the remaining sample surface. Other extracted waveforms from their line profiles are also presented. The central maxima shifts spatially, from sample top to bottom. 125
6.11 Figure (a-b) the second microstructure's localised waveform, right of figure 6.10's melt pool; and FFT extracted profile. Figures (c-d) FFT areal roughness map and, respective midplane profile. 126
6.12 Three pairs of figures showing the relative beryllium and oxygen EDS maps (left to right): 15keV, 10keV, and 5keV, with signals corresponding to interaction volumes of approximately 2μm, 400nm and 250nm respectively. 127
6.13 Higher magnification SE image. (a): The lift-out. (b): Higher magnification of the lift-out beneath the oxide region. (c): EDS spectra of higher contrast white precipitates rich in Ni, Al, C, and O. 127
6.14 (a): STEM HAADF overview of a central slice of the melted BeO Raman region, showing the subsurface BeO seen with low magnification EDS, marked in red. The EDS region indicated by 'EDX map1' is displayed in (b): W (L) map, (c): C (K) map, (d): O (K) map, and (e): Ni (K) map. 128

6.15 A comparison of EDS composition between the two regions seen in the overview; that of the surface oxide and the subsurface matrix region. (a): STEM HAADF image of the regions. (b): EDS spectral compositions of the respective areas. 129
6.16 Point scans extracted from the oxide region in (a): the STEM HAADF image. (b): The extracted stacked bar chart of the points' EDS compositions. 129
6.17 (a): Area EDS scans of bright precipitates present in the STEM HAADF image (the same area was investigated with EELS). (b) The corresponding EDS compositions. 130
6.18 The melted lift-out region. (a): EELS Be at.% map. (b): EELS O at.% map. Regions marked in red are presented in (c): graphing EELS Be and O stochiometries (line) against EDS impurities (bars). Cu (M) (green) was also calculated in the EELS stoichiometries, because of a pre-edge region indicative of a transition element impurity. 131
6.19 EELS Be core loss spectra of points displayed in figure 6.18, the JET positions are plotted normalised to 2.5 times, DFT modelled EELS spectra of different structures containing Be, O and H are graphed iteratively. Only the fine structural shape is accurate 132
6.20 EELS O core loss spectra of points displayed in figure 6.18, the JET positions are plotted normalised to 2.5 times, DFT modelled EELS spectra of different structures containing Be, O and H are graphed iteratively. Only the fine structural shape is accurate 132
6.21 EELS low loss spectra of points displayed in figure 6.18, the JET positions are plotted normalised to 2.5 times, DFT modelled EELS spectra of different structures containing Be, O and H are graphed iteratively. Both shape and onset energies are accurate. 133
6.22 Raman lift-out region after second thinning ruling out thickness effects. (a): STEM HAADF image at low magnification, with integrated areas marked in red from A1(oxide)-A4 (into depth). (b): Be and O at.% via curve fitting. (c): EDX of the 4 regions. 134
6.23 EELS Be core loss for regions 1-4 of figure 6.22, with DFT modelled spectra superimposed. The modelled spectra are accurate in shape but less in position. Some energy adjustment has been utilised +/- 1-2eV to show, where overlay could occur. 134

6.24 EELS O core loss for region 1 (figure 6.22), vs DFT modelled spectra. Modelled spectra are accurate in shape but less in position. Some energy adjustment has been utilised +/- 1-2eV to show, where overlay could occur. 135
6.25 EELS low loss for regions 1-4 (figure 6.22), vs DFT modelled spectra. Modelled spectra are accurate in shape and position. 135
6.26 SEM SE images (a) from a central region, of the second microstructure of the dump plate; and (b) the lift-out region of interest, perpendicular to the surface. (c): Be K EDS map into depth. (d): O K EDS map into depth. (e): Ni K EDS map into depth. (f): Pt M EDS map into depth. (g): C K EDS map into depth. (h): Cu L EDS map into depth. 137
6.27 (a): SEM SE image of the lift-out region of interest from the sample's centre (second microstructure). (b): SEM SE lift-out during thinning. A schematic of 4 potential microstructures is shown. The lift-out spans $\sim$25μm into depth. (c): SEM SE image at 3kV highlighting regions of electron transparency, implying differing atomic weight. 137
6.28 STEM ADF image (a): displaying diffraction contrast of the first two surface microstructures of the lift-out. STEM HAADF (b): displaying atomic weight contrast. Lighter regions represent higher Z elements. . 138
6.29 (a): HAADF image of the surface microstructure with (b): EDX line scan results presented as a bar chart. 138
6.30 (a): HAADF image of the first 600nm of the surface microstructure of figure 6.29 with EDX line scan results presented in (b): the bar chart. 139
6.31 (a): HAADF image of the transition between microstructures 1-2, in figure 6.27(b), with EDX line scan results presented in (b): the bar chart. 139
6.32 (a): HAADF image of the 2nd microstructure in figure 6.27(b), with EDX line scan results presented in (b): the bar chart. 140
6.33 (a): HAADF image of the 3rd and 4th microstructures in figure 6.27(b), with EDX point scan results presented in (b): the bar chart. 140
6.34 (a): STEM ADF overview image of the two surface lift-out regions where EELS mapping took place. (b): STEM HAADF image of the first EELS region. (c): STEM HAADF image of second EELS region. 141
6.35 (a): STEM HAADF EELS map region 1, with standard count areas 1-4. (b): spectra were fitted and at% extracted. 141

6.36 Carbon and Beryllium core loss EELS spectra 1-4, with modelled DFT results overlaid. 142
6.37 Oxygen and Nickel core loss EELS spectra 1-4, with modelled results overlaid. 142
6.38 Low loss EELS spectra 1-4, with modelled DFT results overlaid. . . . 142
6.39 (a) STEM HAADF EELS map region 2, with standard count areas 1-13, (b) spectra were fitted and at.% extracted. 143
6.40 Carbon and Beryllium core loss EELS spectra 1-13, with modelled DFT results overlaid. 144
6.41 Oxygen and Nickel core loss EELS spectra 1-13, with modelled DFT results overlaid. 144
6.42 Low loss EELS spectra 1-13, with modelled DFT results overlaid. . . 144
6.43 (a): Optical image of the JET dump plate tile. The sample marked in red, underwent microstructural analysis. The sample marked in blue underwent TDS analysis. (b): TDS desorption data from sample 92 (blue) against time (s) 145
6.44 A final comparison of hydrogenic retention in the JET samples found across the reactor to conclude the dump plate tile. Integrated area counts are calibrated via a calibrated leak of H_2, HD, and D_2. Calibration for DT and T_2, use the D_2 factors. 146

A.1 Extracted statistics comparing thresholded precipitates of the inner wall and outer wall eroded regions, against the unexposed as received JET beryllium 154
A.2 Figure displaying the supersaturated region at the surface of the eroded inner wall, indicated from the TDS desorption spectra and EELS BeD_2 inference. 155
A.3 Figure displaying the bubble coarsening at the surface of the eroded outer wall, indicated from the APT clustering data, TDS desorption spectra, and EELS BeD_2 inference. 155
A.4 Figure displaying an example of EELS Be spectral fitting for quantification in hyperspy. The data set is the second presented of a point in the second microsctructure seen in the dump plate found in figure 6.36. 156
A.5 Figure displaying an example of EELS O spectral fitting for quantification in hyperspy. The data set is the second presented of a point in the second microsctructure seen in the dump plate found in figure 6.36. 156

B.1 Figure shows every tenth slice of the 3D milling study (1). Image (a) shows the extracted SEM SE images of each 10th slice iteration. Image (b) the result of thresholding the SE images. Image (c) shows the results of particle analysis, with the particles marked. 157
B.2 Figure shows every tenth slice of the 3D milling study (2). Image (a) shows the extracted SEM SE images of each 10th slice iteration. Image (b) the result of thresholding the SE images. Image (c) shows the results of particle analysis, with the particles marked. 158
B.3 a) A STEM HAADF image of the EELS area scan and b) the average EDS composition with errors of the total area shown. 159
B.4 a) A STEM HAADF image of the sub oxide matrix region, on and off precipitates showing their EDS composition with errors shown. 159
B.5 A higher magnification STEM HAADF area of the surface oxide and their extracted spectra of the beryllium core loss (b) and the oxygen core loss (c). 160
B.6 A higher magnification STEM HAADF area of the surface oxide and extracted EELS low loss spectra. 160

C.1 A comparison of thermocouple temperature measurements between the outer and inner wall limiter with increasing integrated plasma time of the first ITER-like wall campaign 161
C.2 Figure displaying the Inner wall Eroded TDS data: a) Nitrogen, Oxygen, CO_2 release; (b) Mass 2 -H_2 release, Mass 3-HD release, Mass 4 -D_2 release, Mass 5 -DT release, Mass 6 -T_2 release, and M18 -H_2O release. 162
C.3 Figure displaying the Outer wall Eroded TDS data: a) Nitrogen, Oxygen, CO_2 release; (b) Mass 2 -H_2 release, Mass 3-HD release, Mass 4 -D_2 release, Mass 5 -DT release, Mass 6 -T_2 release, and M18 -H_2O release. 162
C.4 Figure displaying the inner (left) and outer (right) TDS spectra of the mass 3 and 4 peaks corresponding to HD and D_2 peaks respectively. From the literature these peaks are thought the response of a supersaturation of the H isotope at the surface, which is greater in the D_2 for the outer wall. 163

C.5 Figure displaying the Inner wall deposited TDS data: a) Nitrogen, Oxygen, CO_2 release; (b) Mass 2 -H_2 release, Mass 3-HD release, Mass 4 -D_2 release, Mass 5 -DT release, Mass 6 -T_2 release, and M18 -H_2O release. 164
C.6 Figure displaying the Outer wall deposited TDS data: a) Nitrogen, Oxygen, CO_2 release; (b) Mass 2 -H_2 release, Mass 3-HD release, Mass 4 -D_2 release, Mass 5 -DT release, Mass 6 -T_2 release, and M18 -H_2O release. 164
C.7 Figure displaying the melted dump plate TDS data: Mass 2 -H_2 release, Mass 3-HD release, Mass 4 -D_2 release, Mass 5 -DT release, Mass 6 -T_2 release, and M18 -H_2O release. 166
C.8 Figure displaying the modelled release, utilising a recombination limited surface: left the eroded central limiter region and right the outer wing deposit. 166

D.1 Figure of the Inner Wall deposit, displaying: left: maps corresponding to the, right: spectra presented with increased resolution provided of the Raman spectra in the bottom graph, showing hydride formation. 167
D.2 Figure of the Outer Wall deposit, displaying: left: maps corresponding to the, right: spectra presented with increased resolution provided of the Raman spectra in the bottom graph, showing hydride formation. 168
D.3 Figure of the Inner Wall erosion zone, displaying: left: maps corresponding to the, right: spectra presented with increased resolution provided of the Raman spectra in the bottom graph, showing hydride formation. 168
D.4 Figure of the Outer Wall erosion zone, displaying: left: maps corresponding to the, right: spectra presented with increased resolution provided of the Raman spectra in the bottom graph, showing hydride formation. 169

Chapter 1

Introduction

This thesis analyses the ways in which hydrogen isotopes are retained in the beryllium wall materials of a fusion reactor.

Fusion energy is a key component of the future energy generation landscape. Climate change, resulting from fossil fuel emissions cannot be ignored. The need for carbon free energy production is pivotal [31, 32, 33, 34]. Many green energy production technologies exist, however the high energy density of fusion could provide a large percentage of base-load need alone. Fusion energy's goal within the next 30-50 years, is to provide proof of net energy generation, alongside semi-continuous operation. Critically, the venture must be commercially viable.

Fusion's energy production goals alone, are proving challenging even without further design constraints limiting nuclear activation of reactor materials during operation [35, 36]. The world's current largest, and most successful fusion reactor, is situated in Oxfordshire, UK. The Joint European Torus (JET) produced world leading records in energy production, wall material choice, and plasma operational experience [37]. JET produced 0.95 +/- 0.17 of total input power, as output power in 1997.

The International Thermonuclear Experimental Reactor (ITER) is currently being built in southern France. This novel reactor will be the largest next generation fusion device. Whilst JET has a major radius of 3m and a plasma volume of 100m^3, ITER will have a major radius of 6.2m and a plasma volume of approximately 840m^3. Current understanding has driven this scaled approach [38]. ITER seeks to be the first fusion reactor to provide a net energy output factor greater than 1. The goal for ITER stands at producing 10 times the energy out than that needed to start and maintain the fusion reaction. The act of increasing reactor size and therefore plasma volume is thought to elongate the confinement time, the length of time that a helium

ion (one by-product) takes to leave the core, whilst imparting its kinetic energy to the plasma, thereby aiding plasma temperature.

Fusion is a process which occurs naturally in the sun [39]. Protons overcome coulomb repulsion via extreme temperatures and pressure, fusing together to form helium and by-products in many reaction pathways. This pathway is highly inefficient and results in the prolonged lifetime of stars. On Earth, in order to make this reaction more commercially viable, isotopes of hydrogen: tritium (T) and deuterium (D), are utilised. This combination increases the reaction cross section (the probability of collision) enabling a faster and more successful process. The fusion reaction undertaken at JET, in 1997, was:

$$D + T = He + n$$

Helium is produced with 3.5MeV energy, whilst neutrons have 14.1 MeV of energy. The incredibly high energy of the neutrons are rarely contained in the plasma. Helium retention within the plasma therefore, for elongated periods of time (the confinement time), is the key to plasma temperature maintenance, and continued fusion. Increased confinement times will support semi-continuous pulse (up to 600s) operation, alongside output energy fractions greater than one. These issues of plasma retention, confinement, and power-handling are ongoing areas of study in plasma physics. This thesis however, investigates the interplay between JET's beryllium wall and isotopic hydrogen ions.

Several key requirements govern material choice in a tokamak's (fusion reactor) wall cladding. The overall material choice requirement enables power handling to be maximised for fusion power production. The primary objective concerns mitigating radiative loss. Hot plasma in contact with the wall in the outer flux surface, provides a particle stream towards the wall, resulting in physical sputtering and deposition reactions. A sputtered wall ion resulting from incoming plasma ion bombardment, can be absorbed back into the plasma volume. The plasma volume is predominantly isotopic hydrogen. The heavier wall ion therefore provides a convenient conduit for radiative loss, either by cross field or in field transport to the divertor (base of the reactor). Radiative losses must be reduced to all feasible lengths to ensure that the plasma maintains the fusion reaction and its temperature. The primary constraint on wall material choice is therefore its atomic weight.

JET has undergone many wall material configurations, in chronological order: a carbon wall; a carbon wall with beryllium limiters; and finally a beryllium limited plasma with tungsten and tungsten coated-carbon fibre divertor. JET's current wall

configuration, beryllium cladding in the first wall (upper chamber) and a tungsten divertor (base of the torus) was chosen in 2010 as a test bed to prepare and support the ITER choice [40, 41, 42, 43].

Both beryllium and carbon are suitable light element wall materials with good thermal properties. ITER chose beryllium preferentially for many reasons. Beryllium does not sublimate. Whilst beryllium has a lower operating temperature, carbon sublimation results in rapid erosion rates. Erosion of this level was considered too high for prolonged operation - a principal goal. Plasma purity also impacts radiative loss. Beryllium is celebrated for its 'good oxygen gettering', which improves plasma performance by plasma oxidation at the wall. However this advantage is offset by a reduction in thermal shock resistance [44]. There are many complex property interplays within wall material choice.

Beryllium has significantly reduced chemical sputtering; whilst tritiated hydrocarbons are produced from a carbon wall, under the same plasma conditions. Tritium (one of the two fusion reactant isotopes), is hazardous to human health. The French nuclear authority has imposed a 700g limit for total retained tritium in ITER, across the whole machine [45]. The larger ITER wall area $\sim$700m^2, would produce significant quantities of tritiated hydrocarbon dust under a carbon wall, thereby ruling out the option. The significance of the ITER beryllium wall choice was confirmed by JET in 2011. On operation, a 10 fold reduction in total hydrogen retained, occurred in the first application of the JET ITER-like beryllium wall [46, 47].

In 2010 JET chose to update its wall materials to the beryllium first wall and tungsten divertor ITER choice, to provide knowledge and support to future ITER operations [40, 41, 42, 43].

Whilst beryllium was on paper the optimum first wall choice, there are still areas in hydrogen retention properties where crucial understanding is missing from the literature. Understanding the effect of hydrogen retention on the material properties including: erosion, deposit layer formation, melt behaviour formation, and efficient hydrogen removal in line with regulatory tritium limits; remains an area of ongoing research. ITER's goals are to achieve a Q value of 10, a pulse length up to 600s, and an early proof of concept. These goals will enable the first commercial fusion device, DEMO to be built by 2050.

The aim of this thesis was to understand: how hydrogen is retained in the beryllium wall, whether chemically or spatially, and under different wall conditions; and finally how this hydrogen can most effectively be removed. This thesis prepared castellations (chequer board cut tiles to reduce thermal and mechanical stresses [2,

48, 1, 49]) of the first wall beryllium limiter tiles from the inner limiter, outer limiter, and dump plate; and analysed them with a variety of techniques. Figure 1.1 provides an overview of the final 2011 ITER-like wall design at JET.

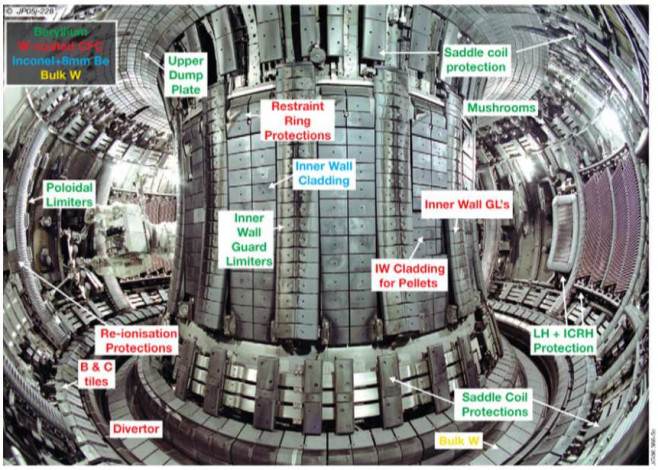


Figure 1.1: Overview of the ITER-like wall final design in and around the JET torus; showing beryllium limiters of S65-H, inner wall cladding inserts of Inconel and Be coatings and neutral beam injection shine path protections; alongside the bulk W divertor and W-coated carbon-fibre-composites [1]

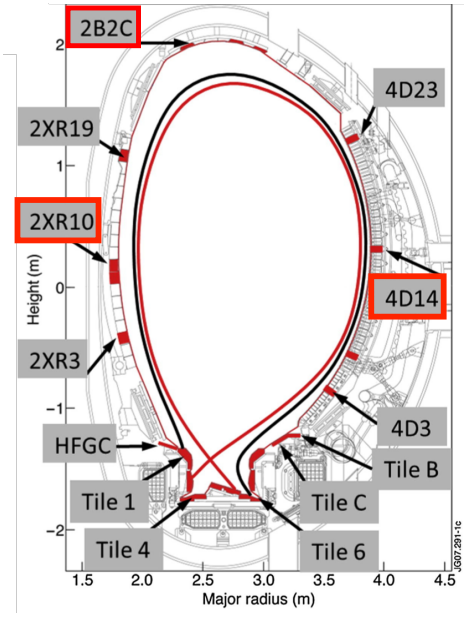


Figure 1.2: A poloidal cross section of the JET ILW showing the positions of tiles removed. For the purposes of this study the tiles analysed were the '2XR10' inner poloidal limiter tile; the '4D14' outer poloidal limiter tile and the '2B2C' dump plate tile at the top of the vessel.

The poloidal cross section of the torus is presented in figure 1.2. Tiles 2XR10 and 4D14, the inner and outer limiter, respectively are shown in figure 1.3. The castellations prepared are marked in red. Within both inner and outer limiter tiles, a central castellation, designated an erosion area, and a wing castellation designated a deposition area were prepared for comparison.

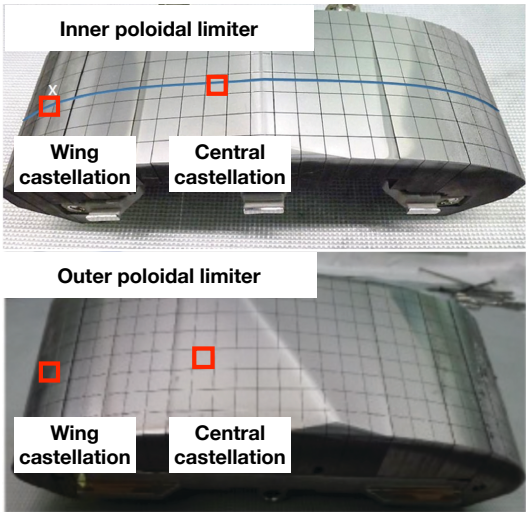


Figure 1.3: An overview of top: the inner poloidal limiter tile with central eroded, and wing deposited castellations marked, from which experimentation occurred; and bottom: the outer poloidal limiter with sample positions also marked.

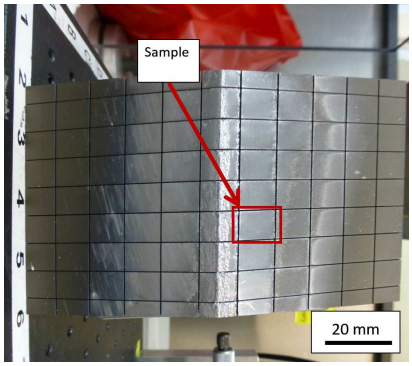


Figure 1.4: Overview of the JET 2010-2012 Dump plate tile and extracted castellation, on which further analysis occurred.

Finally a castellation taken from the dump plate tile 2B2C, marked in figure 1.4, was prepared to study the effects of melt behaviour on hydrogen retention.

Chapter 2

Literature

This thesis analyses microstructures prevalent in JET's beryllium ITER-Like Wall (ILW) from the first ILW campaign (2011-2012). A review of the material testing and beryllium grade choices alongside engineering design of the first ILW tiles is given. A review of the first ILW campaign is given, focusing on the campaign parameters, plasma conditions and spectroscopic observations of the wall. The current knowledge from post mortem investigation of the tiles is presented. A discussion of experimental set-ups in universities and laboratories, mimicking tokamak relevant materials is provided. This discussion is subdivided into direct H isotopic implantation of beryllium materials and compared to deposited beryllium materials. Both microstructural findings and thermal desorption studies are discussed. A small discussion is presented surrounding the current knowledge accumulated via Density Functional Theory, providing a first principles approach of hydrogen traps expected in beryllium materials. The Tritium Migration Analysis Program (TMAP 7) is presented as the primary route, by which researchers analyse thermal desorption results on the macroscopic scale. A smaller section covers phase diagram associated to binary systems of beryllium, relevant to the material mixing seen in subsequent chapters, alongside a review of specialist techniques applied to JET materials in this thesis; Atom Probe Tomography (APT) and Electron Energy Loss Spectroscopy (EELS).

2.1 JET and the preparation for a Be ITER-like wall prior to the first campaign.

JET transferred to an all metal first wall with beryllium cladding in the main chamber [43] and a combination of tungsten and/or carbon fibre coated tungsten, in the

divertor. These changes enabled a long term program to aid ITER knowledge of operational parametric space.

The beryllium grade chosen was S65-H, an impact ground beryllium powder with very low levels of metallic impurities and BeO [50, 44, 51]. Early off-gas results from the first ILW campaign at JET showed a factor of 10 reduction in fuel retention [46, 47].

The proposed effect of radiation damage in both ITER and DEMO, on beryllium materials is embrittlement. Neutron defect production, swelling from helium (resulting from the fusion reaction) [44] and high temperatures, will all contribute [44]. Beryllium's 'good oxygen gettering' improves plasma performance whilst further reducing thermal shock resistance [44]. Thermal shock is particularly important for plasma conditions classified as Edge Localised Modes (ELMS) (described subsequently), which are predicted with higher rates in ITER. These aspects of wall material properties are not directly concerned with hydrogen retention, however they present the complicated material property and functional durability challenge concerning optimal material design and choice, able to sustain continuous operations long term.

In JET, the geometric design of the limiters, was optimised into groves (castellations) and tile sections to minimise thermal shock [1, 2, 48, 49, 52] and large temperature spikes. A schematic enabling reduction of thermal and magnetic stresses on the tiles is given in figure 2.1.

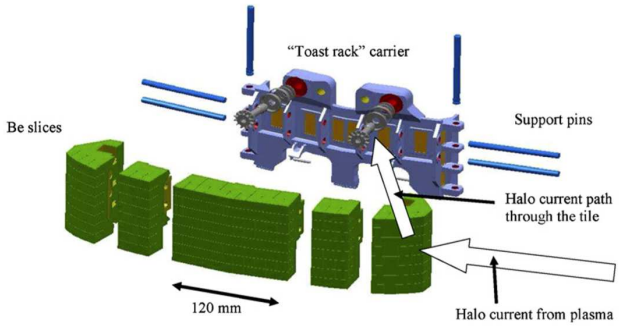


Figure 2.1: An exploded view of the beryllium tile assembly, showing the 5 slices; to reduce eddy current loads and thermal expansion stresses, and the castellated surfaces to reduce thermal loads [2]

This reduction utilised finite element modelling of wall materials exposed under 10MW 10s scenarios [2, 44, 48]. Initial results predicted that plasma orientation

on localised exposed faces could produce temperatures up to 1843K, above beryllium's melting point. This lead to design of castellated surfaces 12 x 12 mm [2] down to 16mm depths [53]. These surfaces reduce low cycle fatigue and ductility loss. However, despite operational needs to remain below beryllium's melting point, operational evidence suggests localised hotspots still occur from glancing plasma incidence at exposed toroidal faces [2, 49].

Operational evidence shows root tile temperatures increase throughout a day of pulses [53]. ELMs require further wall maintenance consideration. ELM energy is transferred to components sat furthest into the plasma scrape off layer (the outer edge of the plasma): beryllium main chamber limiters, and dump plates tiles; under very small time periods [1, 54]. 5-30% of total plasma power is estimated off loaded to the wall [1, 54].

The beryllium limiters were prepared via electro-machining at $3.03 cm^3 h^{-1}$ [55], and processed by chemical etching [44], with 1%HF-25%HNO_3 solution, to remove residual Cu and Zn [55]. Approximately 11μm of surface beryllium was removed by the etching process [55].

Erosion, deposition and material migration, remain a large area of research. 'Marker layer' tiles were produced at JET to enable erosion and deposition measurement. At the end of every campaign both marker layer and non marker tiles are removed for post mortem analysis.

Marker layers are constructed of a nickel interlayer of 2-3μm atop the bulk beryllium tile, and covered at the surface by a further 8-10μm of beryllium deposit [44]. Nickel has a similar thermal expansion coefficient to beryllium, and only forms a beryllium−nickel intermetalic above 1273K [44]. Marker layers were produced via Thermionic Vacuum Arc (TVA). The process assumed formation of high density layers [56]. X-Ray diffraction results of the beryllium films grown were crystalline. Auger electron spectroscopy (AES) produced a final stoichiometry: O 6.33at%, C 4.7 at%, and Be 88.97 at%. These values have comparatively high impurity levels versus the Brush Wellman (now Materion Inc) S65 H bulk, chosen for its exceptionally low impurity levels [57]: Be 99.2 at%; BeO 0.9 at%; C 0.09at%; Al 0.05at%; Mg & Cr 0.01at%; Ni, Cu, Ti, Zr, 0.025at%; Zn, Mn, Ag, Co, Pb, Ca, Mo 0.005at%; Si 0.045at%; and U 0.015at%. All other impurities are a maximum of 0.04 at% [58, 59]. Both metallic and non metallic impurities in beryllium, detrimentally affect strength and ductility via grain boundary pinning reducing the primary basal slip system [60]. Grain size also has a large impact. A summary of all the processing techniques of common beryllium grades culminating in the choice of the S65-C grade for ITER can be found

here [59], including surface finish and impurities from powder processes. Less pure marker layers are potentially weaker and more brittle.

The marker layers were tested prior to installation in JET, via electron beams up to 1-6MWm^{-2} for 10s, alongside cyclic loading at 3.5MWm^{-2} for 50 cycles [3, 44]. No damage or chemical change to the layers occurred. The marker layer operational limits proposed were 1MWm^{-2} [44]. Inclusion of hydrogen flux reduced marker layer resilience. Layers produced under PISCES-B plasmas with hydrogen ion bombardment (90eV, 7.0x10^{17}Dcm^{-2}s^{-1}, 0.1MWcm^{-2}, above 490°C [61]) broke and exposed the Ni layer. The Ni/Be diffusion rate was 4.5 x 10^{-13}cm^{-2}s^{-1} at 625° [61]. Ni intermixed down to 1μm of the surface deposit (originally the marker layer) and a further 2μm into the beryllium substrate. The final Ni layer composition was 25 at% Be, 45 at% Ni, and 30 at% C [61].

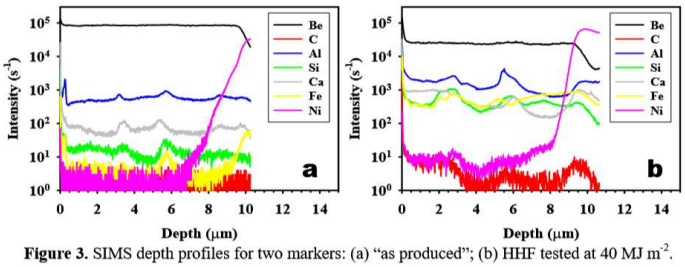


Figure 3. SIMS depth profiles for two markers: (a) "as produced"; (b) HHF tested at 40 MJ m^{-2}.

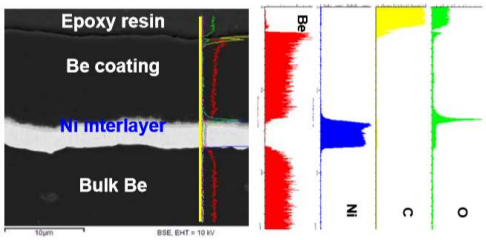


Figure 4. Metallographic cross-section of a marker coupon after cyclic test (50 pulses) at 3.5 MW m^{-2}.

Figure 2.2: A graph from [3], top (a) and (b), Secondary Ion Mass Spectroscopy before and after thermal testing of marker layer coatings; and bottom (c) cross section SEM SE image and EDS of the coatings post cyclic test.

Figure 2.2(c) shows the only cross sectional data of these layers. Oxidation occurs at interfaces. The SEM BSE image resolution shows non porous layers.

Further past beryllium experience at JET can be found here [52]. Historically mechanical failure did not occur from either localised surface melting or large scale beryllium belt limiter melting. Micro-cracking, the result of re-solidification, was linked to transients, ELMs or high angular plasma loading [52]. The uncertainty of the power loadings onto tiles is noted [52]. Melting of the Mark I castellated beryllium

divertor tiles, on extreme heat loads of 14MWm $^{-2}$, produced cracking both vertically and laterally which disrupted heat flow and conduction.

This section presented the design considerations that lead to: beryllium limiter tile castellation [55], power handling, marker layer production, and operating wall temperature uncertainty, prior to and during ITER-like wall operation.

2.2 The Joint European Torus and the 2011-2012 first ITER-like wall campaign parameters

The program of the first ITER-like wall campaign (2011-2012) commenced by studying wall material migration and mixing under Ohmic plasmas. The second phase utilised limiter-dominated plasmas (L-modes). The third phase concerned H-mode (high power) plasmas. The fourth phase concerned H modes and ELM mitigation techniques. The fifth and sixth phases concerned hybrid operational modes and higher power, investigating machine operational space. The campaign finished with standardized plasmas investigating long term retention [62] in H-mode.

Erosion and migration of beryllium at the first wall remains an area of considerable concern and interest for effective understanding of a metal machine under ITER relevant plasma scenarios [1, 44, 62]. In terms of beryllium hydrogenic retention it is assumed in the literature that the final phase of operation had the greatest impact on the resulting hydrogen trap behaviour and microstructure.

Prior to installation wall preparation to remove unwanted carbon occurred via vacuum, wall baking at 325°C, and glow discharge cleaning in a deuterium plasma for 100h at 200°C [63, 55].

Carbon traces (measured via spectroscopy) were a factor of 20 reduced on start up. Oxygen plasma impurities were an order of magnitude lower [63]. Beryllium performance 'even tolerated an air leak into the vessel' [63], without plasma degradation. Power handling performance increased, with large consequences to the beryllium materials. Disruptions occurred more regularly on ILW dump plate tiles, rationalised from reduced impurity content and greater plasma power [4, 55, 63].

The typical percentage of the ILW radiative fraction was under 50% of the total energy, the remaining fraction transferring directly to wall tiles. Electron energies were recorded at 1keV. Current quench times for the beryllium wall remained higher, enabling vertical displacement events and melting of dump plates [63]. Melting also occurred on non-midplane limiter tiles during emergency shut down, as a result of wall

management system failure [55]. High temperatures occurred at exposed edges [55] alongside evidence of beryllium vaporisation.

Massive gas injection of Ar, 10% and D_2 90% decreased beryllium temperatures below 400°C [63, 4]. Nitrogen injection increased radiative power and plasma confinement [4], whilst increasing tile temperatures [4]. Contaminants of Ar and N are therefore likely in post-mortem materials.

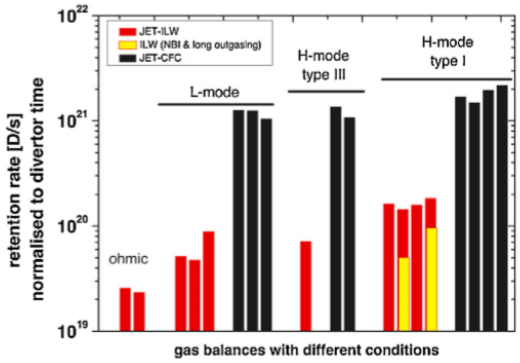


Figure 2.3: Overview of gas balance measurements for deuterium [4] at JET. Red and yellow bars refer to gas balance measurements for ILW1, at shorter and longer integrated times. Black bars, show measurements from JET's carbon wall. Measurements are by Low (L-mode), and High power (H mode) operational modes.

Fuel retention (figure 2.3), was an order of magnitude lower for all plasma operational modes [4]. Greater dynamic release during limited plasmas is suggested the result of D implantation above saturation. These low energy trap populations desorb quickly during post pulse high wall temperatures.

Ohmic plasmas were used to measure beryllium migration onto the divertor surfaces. At low densities, sputtering was linked to self-beryllium ion sputtering [4].

Further impurity measurements [63] over 1300 JET ILW pulses, showed 65% of particles were W, 24% Ni, and 8% Fe. Ion Cyclotron Resonance Heating plasmas were linked to higher tungsten impurities [4, 63].

2.3 An introduction to fuel retention preceding the ITER-like wall at JET

The topic of fuel retention is now introduced. This section provides an overview of the ideas circulated on fuel retention prior to employment of the JET ILW. The necessity of tritium inventory limits due to wall retention was first realised when 36g

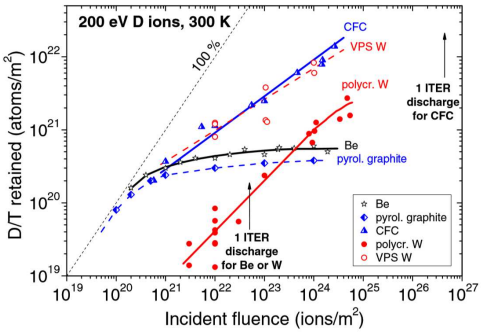


Figure 2.4: A comparison of past and present plasma facing materials and their saturation behaviour on deuterium loading [5]

of tritium was injected during the JET-C DT campaign and approximately 35% was retained [5].

Many reports assess retention in tokamak devices as dominated by co-deposition via erosion, material migration, and re-deposition [5]. The main wall is considered a source of co-deposited material; the inner divertor an area of highest deposit; and the outer divertor, under net erosion [5]. ITER is predicted to follow a similar pattern of Be-erosion from the main chamber, and co-deposition of Be and D at the inner divertor [5].

The knowledge and processes of retention prior to the JET-ILW are summarised here [5]. High Z materials (W) are governed by implantation. Co-deposition is considered the primary process of low Z materials (Be and C). Implantation of Be by hydrogenic species was reported up to 30 at% in the ion implantation range, followed by saturation [5] due to low H isotopic diffusivity.

Further loading above saturation released hydrogen isotopes back into the vacuum. CFC recorded porosity, provided a new understanding of saturation behaviour. Retention increased as a square root of the applied fluence [5]. Diffusion into the bulk was aided by newly created porous channels. CFC fibre pores were found decorated with D-rich amorphous layers [5]. Figure 2.4, presents saturation behaviours of plasma facing materials [5].

Co-deposition (governing Be and C) is broken into three processes [5]: commencing with bulk material erosion. Physical Be sputtering is understood at ion bombardment energies greater than 1keV; but less at the lower energies of the JET Scrape Off Layer (SOL) [64]. Sputtered ions in JET deposit to energetically favourable locations (line of sight). Re-erosion of plasma deposited layers [5] then occurs, with a factor of 2 rate increase [5]. The final step incorporates hydrogen isotopes into deposited layers.

Low H concentrations have been linked to lower ion impact energies. Ion energy is thought to dominate over oxygen content [5]. Lower uncertainties of ion energies is therefore desirable.

Limiter plasma loading scenarios in JET, gave consistent loading and therefore sub-saturation results [65]. Dynamic loading, -desorption of hydrogenic species (retained in the wall) on pulse cessation, was consistent with low retention memory for 8 operational months [65].

Unfortunately, yet commonly, 'trap' behaviour was discussed without microscopic evidence [65]. Dynamic retention was presented the result of temporary trap site filling, across all materials; followed by room temperature desorption [65]. Bulk materials are suggested governed by implantation, diffusion, and surface recombination; whilst codeposits release via in-service plasma sputtering.

Total dynamic retention during ILW-1 was estimated to be 10^{16}Dcm^{-2}; corresponding to 0.2-2 D/Be [65]. Ion impact energy modelling, suggested a D-ion maximum interaction depths of 3-8nm into bulk beryllium. A recombination coefficient of 1-2x10^{23}m^{-2} [65] was estimated.

These conclusions are limited by uncertainties and global machine measurements, which do not account for local effects. It is highly unlikely that microscopic behaviour can be implied across such length scales.

2.4 The JET-ILW1 fuel retention findings: TDS and IBA, material erosion, migration and co-deposition

Results produced from Thermal Desorption Spectroscopy (TDS) and Ion Beam Analysis (IBA) of ILW1 Be materials removed after the ILW campaign are presented. Hydrogen retention results are presented alongside material composition observations.

Materials are removed from JET with utmost care. Figure 1.2 presented the post mortem poloidal cross section of tiles removed [66]. Tiles are removed remotely from the vessel, extracted from the backing Inconel holders, separated into the 5 constituent tile sections, and processed at the National Institute for Laser, Plasma and Radiation Physics in Romania; to prepare TDS relevant samples [67]. Temperatures during cutting are maintained below 55°C; with no lubricant. Wherever possible D and T surface desorption and isotopic exchange is mitigated [67].

Photographic surveys (ILW1 shut down) confirmed the frequency of localised melting (figure 2.5). Arc tracks present in positions (a) and (h) [6] matched tile profiling,

confirming a dominant erosion pattern at tile centres [68]. Melt directions are consistent to j x B Lorentz forces present in the plasma [6]. Considerable melting was seen at dump plate tiles [68].

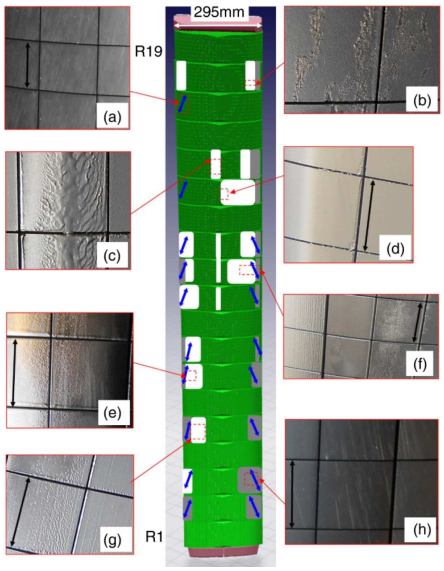


Figure 2.5: The photographic survey of the Inner wall Guard limiter (one of the mid-plane tiles, this thesis analyses (f)), showing melting trails due to plasma bombardment [6].

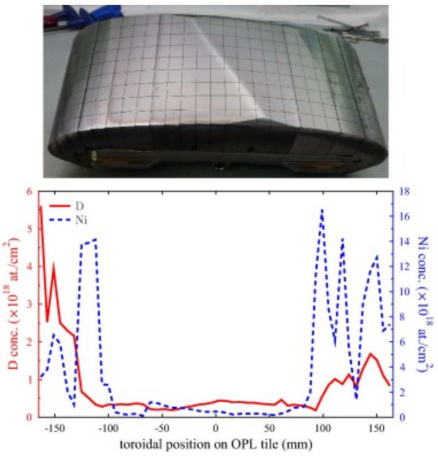


Figure 2.6: An overview of the outer poloidal limiter mid-plane tile (where 2 castellations analysed in this thesis originate). Top: optical photograph of the beryllium tile; bottom: IBA analysis showing the relative concetrations of Deuterium and Ni across the toroidal positions from left wing to right wing [7].

IBA showed erosion present at the mid-plane outer poloidal limiter tile centre, via reduced Be and Ni surface layers (figure 2.6) [7, 11, 66, 69]. Evidence of total marker

layer erosion was reported [66]. A net minimum of 10μm was estimated removed from the tile [66] by erosion. Deposition was found at the tile wing positions [11, 66, 69]. Untouched marker layers occurred symmetrically between wing deposition and erosion centres [66]. The deuterium retention found at the mid-plane tile was 2.81 x 10^{20} D atoms [69]. The integrated D atom inventory for outer poloidal limiters was 5.22 x 10^{22} D atoms [7].

Typical D retention per castellation area, were approximately 5.2 x 10^{17} at the centre and 3.5 x 10^{18} at the left wing, for plasma energies up to 100eV [8].

Unfortunately only a detailed breakdown of ILW2 TDS data from the outer poloidal limiter are published, however total retained isotopic hydrogen values between IBA and TDS are maintained between ILW1 and 2 campaigns [8]. Nevertheless, some evidence of isotopic exchange, (replacement of D by H), is suggested [8, 11, 69] (figure 2.7), and explained by the campaigns switch to a final round of H plasma loadings.

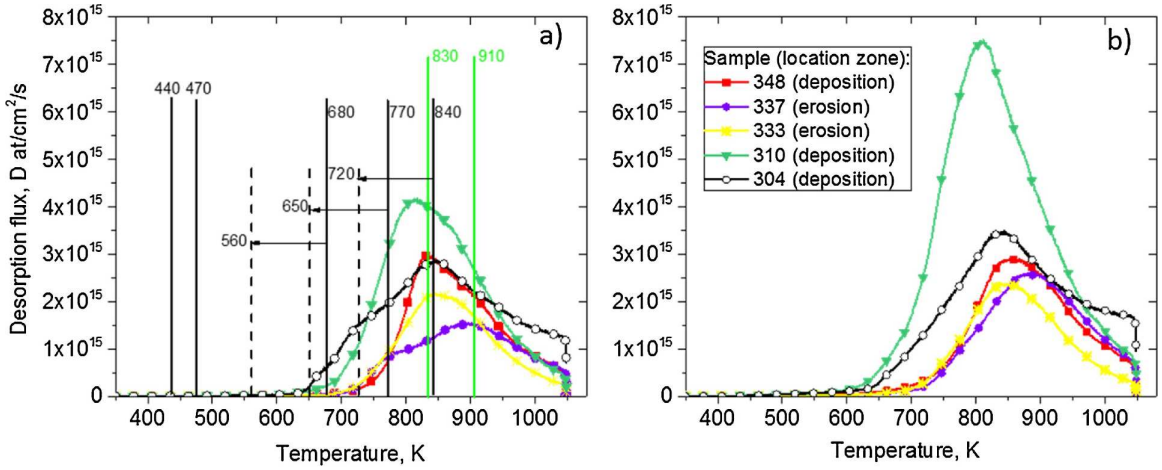


Figure 2.7: A comparison of TDS data for the outer poloidal limiter mid-plane for the second ITER-like wall campaign [8].

Desorption occurs at temperatures greater than 480K (figure 2.7), and inferred either the result of higher implantation temperatures (reducing the ability of D to be held in low energy traps), or implantation fluences greater than saturation (reported saturation fluences are 1 x 10^{17}cm^{-2}) [8].

These desorption characteristics are presented as differing from laboratory literature implantations, and instead the result of codeposition or chemical bonding at eroded beryllium surfaces [8]. Three D_2 desorption peaks are presented for central erosion locations: 780, 835, and 910K. Release from deposited wing regions occurs at higher temperatures still (795K), with the largest integrated area [8]. Comparison

to the laboratory experiments [8] are plagued by differences in: thermal ramp rates, thermal cycling, materials (model versus JET in service), and incident flux.

Inner limiters mirrored the traits of outer poloidal limiters with central erosion and wing deposition regions [11, 69]. Howevever, a minimum of $\sim$60μm erosion is quoted [66]. Inconel components of Ni, Mo, Cr, Fe and additionally W are reported present in the deposited layers [66]. The mid-plane inner limiter, displayed the lowest retention, accounting for 6.76 x 10^{19} D atoms. The inner wall limiters integrated inventory was 1.4 x 10^{22} D atoms [7, 69], 5 times lower than the outer limiter.

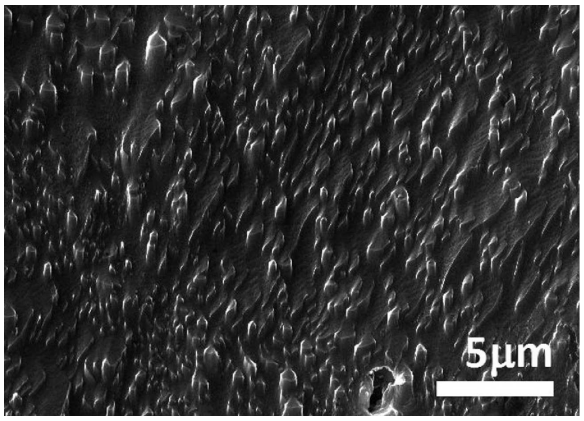


Figure 2.8: SEM SE image showing the inner wall limiter midplane erosion region; the morphology has been linked to light ion plasma exposure [9].

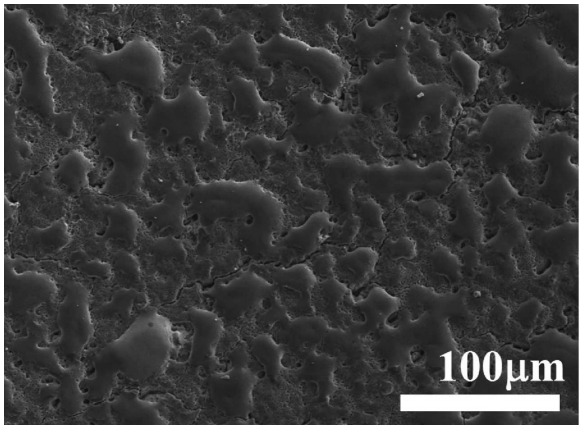


Figure 2.9: SEM SE image showing the inner wall limiter midplane at the outer wing edge; the morpghology is described as "cabbage-like" and linked to molten materials arriving at the tile [9].

Figures 2.8 & 2.9 show the only JET surface SEM images of eroded filamentary morphology comparative to globular deposit morphology, respectively.

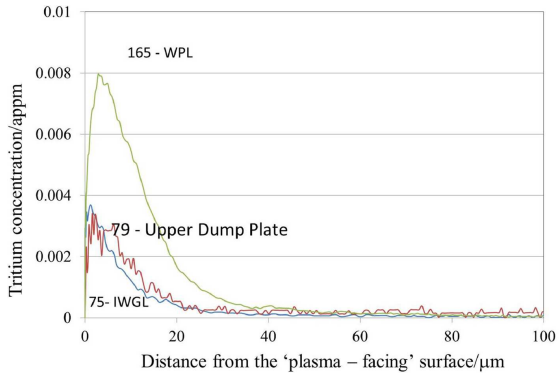


Figure 2.10: Tritium depth profile of beryllium samples from the inner wall limiter (IWGL) erosion zone, the outer poloidal limiter (WPL) deposition zone, and the upper dump plate tile (away from the melt ridge) [9].

Figure 2.10 presents tritium depth distributions from JET Be dissolution studies. Comparative to depth profiles of $\sim 20\mu$m at erosion and dump plate locations; deposition zones occur with a factor of 2 increase at $\sim 40\mu$m [9] at the outer poloidal limiter. Tube furnace TDS measurements found fractional release rate kinetics varied most for outer limiter deposits (165 WPL) (figure 2.9). Overall, D retention increased at the outer poloidal limiter by a factor of 2-5 [7]. Midplane tiles also represented the greatest deuterium retention [66], and therefore are a good sampling site for comparison to future ITER loadings.

JET literature presents charge exchange neutrals as a sizeable source of long distance erosion [11]. Recessed wall areas without beryllium cladding, act as impurity sputtering sources [11]. Impurities have unfortunately become part of the erosion and deposition processes around JET, and therefore affect the final microstructural compositions of codeposits, into which hydrogen is trapped. These effects are particularly relevant compared with modelled laboratory clean conditions of implantation experiments. Recent results across 3 years of campaigns with a variety of plasma operating conditions has shown consistent material migration trends [10]. The main components of the deposited divertor materials were: Be, C, O, D, W, Mo, Ni, Cr, and Fe [10]. Ni, Cr, and Fe; components of Inconel alloys, form JET's structural components. The ILW3 (2015-2016) campaign was marker layer free; and therefore the only data available to separate codeposit Ni impurity contributions from marker layer and Inconel sources. Higher Ni levels occurred at wing positions (figure 2.11), consistent with codeposit and deuterium retention trends. The relative Ni ratios correlated to Inconel. It is possible similar processes were present for ILW1-2 but masked by marker layer presence. Tungsten impurity was also correlated to deposition regions [10].

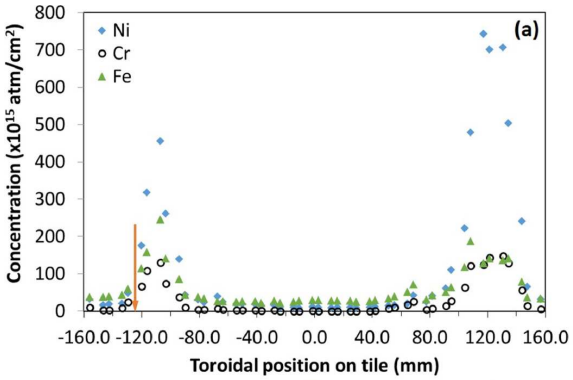


Figure 2.11: Ion Beam Analysis showing the Ni, Cr, and Fe impurities present at the inner midplane poloidal limiter from the 3rd ITER-like wall campaign (the same position as the inner poloidal limiter tile from ILW1 analysed in this thesis) [10].

There remains no microstructural cross sectional imaging of JET main chamber beryllium deposits. A divertor cross section governed by beryllium deposition is given in figure 2.12 [7], showing horizontal layer formation. The main components of the deposited materials present were: Be, O, C, and D [7], with traces of W, Ni, Mo, Cr and Fe [66]. D/Be ratios were considered between ∼0.1 and ∼0.5-1.0 [70]. Deposit thickness [69] correlated with deuterium retention. It remains unclear whether D retention is composition or thickness dependent.

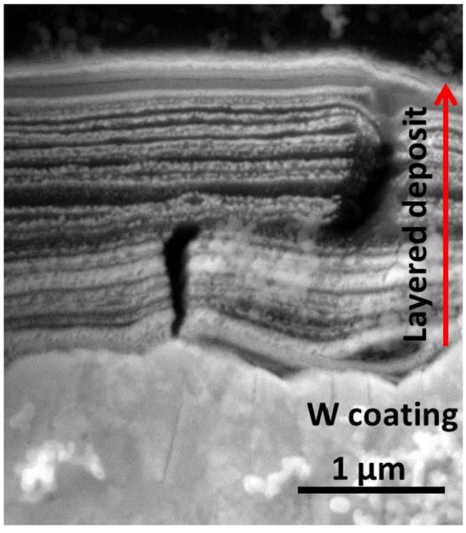


Figure 2.12: A cross section of deposit on tile 6 at the outer divertor (just beyond the strike point location) [11].

The general trends of central beryllium tile erosion, and wing deposition; occur consistently at both the inner and outer mid-plane poloidal limiters. Melting and

arcing patterns were also reported. The greatest hydrogenic retention correlated to deposit layers. Composition and chemistry remain in contention with deposit thickness for mechanistic understanding of trapping. Material mixing across the three ITER-like wall campaigns, suggests Inconel components deposit additionally to Ni marker layers at wing regions. There is an extremely limited level of microscopy presenting main chamber beryllium.

2.5 Thermal desorption and microstructural results of laboratory implanted beryllium

What follows in the next two sections is a description and analysis of the modelled experiments undertaken in laboratories. Early work centred around Be implanted by deuterium (D) ions, with subsequent work implanting deposit-like grown Be layers. The effects of implanting species (neutrals versus ionic) [71], fluence, and implantation temperatures are presented.

2.5.1 A summary of the general trends of laboratory produced and implanted tokamak-like beryllium materials

Fluence effects are most clear to researchers in this field. Implantation at fluences greater than 2.0 x 10^{17}ions cm^{-2} overcomes the threshold for supersaturation behaviour to occur. Bubble and micro-channel formation is reported above this fluence [14]. Variation in quoted saturation fluences occurs with reported saturation capped at $10^{22}Dm^{-2}$ [17, 72, 73].

The effects of implantation temperature is stated repeatably in beryllium materials. As implantation temperature increases, D/Be ratios reduce [17]. TDS Desorption at temperatures below the implantation temperature results in low hydrogen signals. Total hydrogen retention reduces at higher implantation temperatures, whilst higher temperatures are consequently required for desorption to occur. Authors suggest chemistry (BeH_2 and BeOH) effects govern mid range implantation temperatures, whilst implantation induced defects are thought to govern at the highest implantation temperatures [17].

Loading scenarios have been applied carefully to produce (in laboratories) tokamak-relevant materials. JET literature suggests a maximum of 2-3 microstructures: eroded, deposited and melted beryllium. Laboratory techniques used to produce relevant

tokamak materials include: linear plasma devices, vapour deposition techniques (magnetron sputtering, chemical vapour deposition, thermionic arc vapour deposition), and ion beam implantation, often with combinations of these techniques applied.

Unfortunately the scale of these technique's parametric space remains large producing significant potential error. Studies investigating the effect of loading sequences, utilising IBA type accounting of hydrogen depth profiles and stoichiometries, failed to investigate microstructures post implantation; leading authors to believe that either preparation route would suffice [27, 74]. Different deposit production routes also produced significant sputtering rate deviations, (especially comparative to TRIM predictions) [75]. Some authors suggest these differences occur from differences between Be and BeD_2 sputtering rates. Limited microstructural analysis remains a hallmark of these papers.

Surface preparation also affected retention measurements [76]. Whilst JET samples are produced via TVA techniques and described as 'fully dense'; the consequences of porosity is clearly shown via initial retention of: H, H_2O, N_2, and Ar; prior to D operation [76]. Increased surface recombination rates was thought linked to columnar grain growth and enhanced grain boundary diffusion.

Caution should be taken with cross literature comparisons. Careful scrutiny of the methods of implantation, production of the beryllium or co-deposit layer; relative implantation energies; implantation fluence and temperature; as well as final TDS ramp rates; all effect the conclusions drawn. This is most true to conclusions drawn modelling (with FEM) 'trap energies' to match the desorption spectra.

2.5.2 Hydrogenic implantation into crystalline beryllium

Care has been taken to describe the methods taken when assessing trends from eroded 'model' papers. This section discusses the results seen in crystalline beryllium without co-deposit.

Many of the hallmark issues studying hydrogenic isotopic implantation into beryllium can be seen in the earliest studies [77]. Beryllium cleanliness and the success of modelling TDS desorption trends, are intrinsically linked with material production methodologies. The less clean the implanted material is, the less certain standards of hydrogen permittivity and diffusivity, can be in both the final material and its modelled desorption curve. Early papers demonstrate this variation of measurement in the hydrogen diffusion coefficient between: $2x10^{-15}cm^2s^{-1}$ at 500eV, and $2x10^{-14}cm^{-2}s^{-1}$ at 1500eV [77]. Permeability has been found to vary by over 7 orders of magnitude between published data [12].

Bubble formation, was originally provided as a solution to changes in Be/H saturation ratios at fluences greater than saturation. The D/Be ratio was estimated at 0.3 and activation energies of proposed traps as 1eV and 1.8eV for the 125 and 400 degree desorption peaks [12, 18, 78]. This microstructural and mechanistic conclusion occurred without microscopy; and reasoned solely through theoretically shortened diffusive pathways. Isotopic cyclical loading was applied to rule out diffusion into depth [12]. H, D and He were implanted at different energies (presenting different implantation depths) to isolate surface chemistry effects. The NRA results show (figure 2.13) deuterium preferentially migrated to surface He/H traps over its own depth sites.

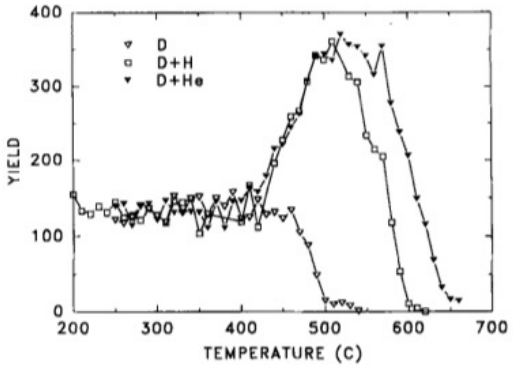


Figure 2.13: NRA yield of Deuterium release on 2K/s thermal ramps between samples implanted to high depth with D at 60keV, or implanted with D at 60keV with additional implantation at 15keV of He, or a final sample implanted with D at 60keV with additional H implantation to 10keV [12].

Experiments producing deeper high energy traps from He implantation at 700keV (micron depths) followed by subsequent implantation with D at 7.5keV (at 100nm); showed only 3% of deuterium migrated into depth (He traps) [12]. This result is often in contention to others showing trailing implantation depths of 10-100μm [18, 78] despite TRIM predictions of 14nm. It is clear that subtle mechanistic behaviours divide results with no single clear indication of effects. Modelled activation energies of traps varied between 1-1.8, and 2.3eV/atom [18, 78].

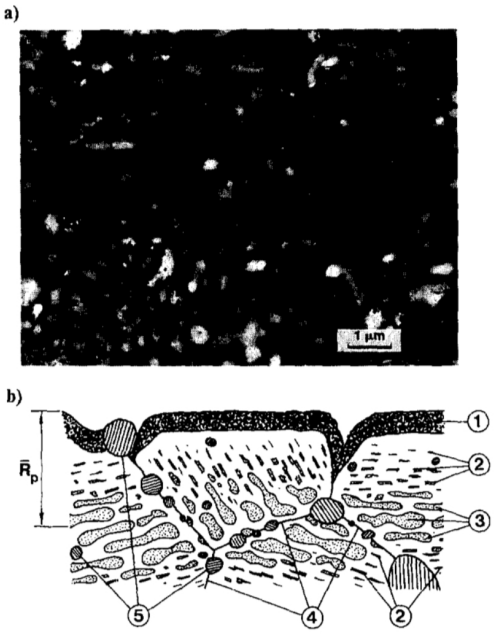
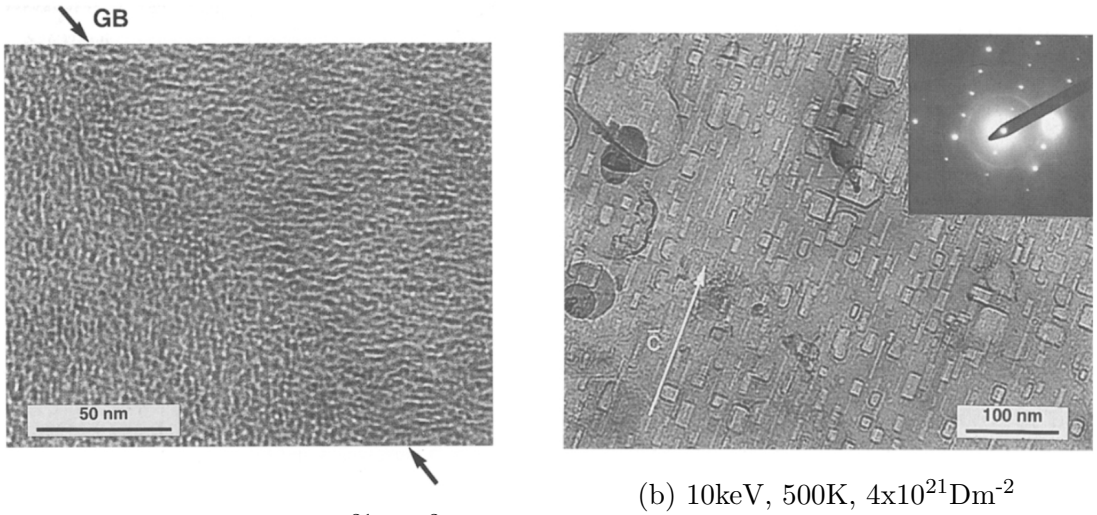


Figure 2.14: Deuterium bubble formation from implantation of beryllium at 700K with 10keV D ions to a fluence of $4x10^{21}Dm^{-2}$. (a) TEM image showing the bubbles present in the structure; (b) a schematic showing the proposed composition of the bubble formation in a cross section of the beryllium (1) BeO layer at the surface; (2) small prismatic D_2 bubbles; (3) larger oblate D_2 cavities; (4) grain boundaries and (5) grain boundary oxides [13].

Only three apparent papers [13, 14, 79], present actual microstructural evidence of bubble formation. Surface modification (SEM), alongside nanometric bubble formation (TEM); are alluded to in [79]. Figure 2.14 shows TEM micrographs of bubble formation [13], for high fluence implantations at 18-20keV D_2^+ ions, (well beyond possible JET ion energies). Figure 2.15a and 2.15b present clearly the findings of bubble morphology and distribution at very high implantation energies. Some indication of coarsening may be present between the 300K and 500K implantations. These results mirror the schematic in figure 2.14(b).

Chemistry and the potential for beryllium deuteride formation in crystalline beryllium, implanted with a linear plasma device (PISCES-B), was investigated [80]. A powdered standard of BeH_2 was measured via XPS; however, BeD_2 was not present in the deuterium exposed sample. Hydride formation was further highlighted in results seen from implantation insitu with sputtering measurements. Self-sputtering results during implantation experiments, appear contradictory with temperature, between plasma and ion beam implantation methods. Some experiments showed at temperatures above the 'decomposition temperature'; hydride species could no longer be



(a) 3keV, 300K, 3 x 10^{21}Dm^{-2}

(b) 10keV, 500K, 4x10^{21}Dm^{-2}

Figure 2.15: TEM images (bright field) showing bubble formation and coarsening between (a) 3keV 200K, and (b) 10keV 500K, D ion implantations undertaken by Chernikov [14]. (b) Dense prismatic bubbles are seen along the hcp c-axis; larger oblate bubbles are also seen at these conditions.

formed in front of the implantation target [80]; others the exact opposite [75, 81].

Conn [82] used sputtering experiments to show the relative effects of high energy plasmas on surface quality. Two Be grades were investigated, S65-B: prepared with surface machining; and MSC-100 (similar to JET S65) with machining and chemical etch. The MSC-100 showed a smoother surface finish. Both grades at room temperature displayed surface smoothing post high energy plasma exposure, with the addition of oxide islands at the surface. At elevated temperatures all grades, whilst in high sputtering environments formed a black non reflective surface film linked to plasma impurities; and a reduced sputtering yield. Plasma impurities ranged from 1-10%. Whilst Doerner [15] further decreased impurity levels to 0.2% for C and below for O; a surface film was still produced. This cleanliness exceeds the JET plasma; providing critical evidence for the persistence of oxidation at the surface of JET samples [83]. At high temperature surface roughening was apparent; increasing with fluence, showing consistency with micro-channel formation [13, 14, 15] (figure 2.16). The effect of surface roughening from plasma interaction at high temperature was explained via competition between recrystallisation and overall surface modification [16].

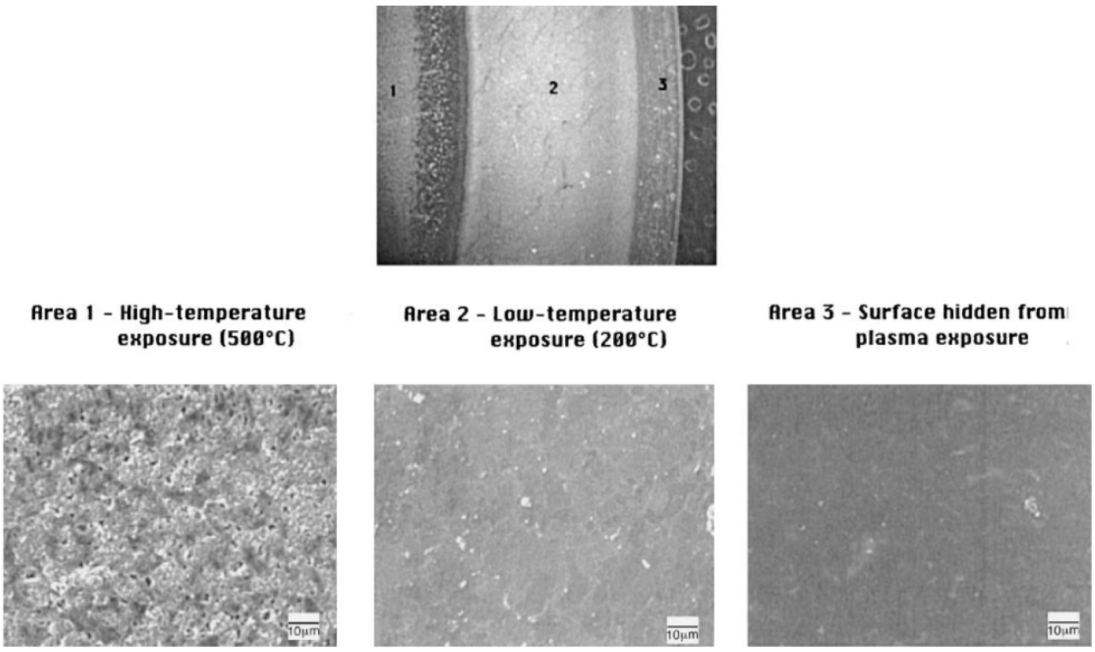


Figure 2.16: An overview surface image of the S65 grade Be subjected to (left to right) high temperature exposure, low temperature exposure and no plasma exposure [15]

Overall micrographic evidence of beryllium response to both plasma and ion beam implantations are few. Both implantation systems have shown surface modification to significant depths, greater than implantation depths predicted via SRIM/TRIM. The three TEM cross sections provided show prismatic small high density bubble formation; with larger oblate bubbles forming at higher implantation temperature and fluence. The same may be true for linear plasma conditions; however plasma ion energies are at least a tenth of ion implanted TEM experiments. It is unclear how great an impact ion energy and implantation method have on the defects created. It is not clear how chemical desorption interacts with bubble formation, and whether surface effects are the difference in retention kinetics between saturation type behaviour or recombination limited release [72]. It is clear that surface chemistry and plasma impurity provide increased complexity over ion implantation via competition between erosion and deposition, forming oxide film growth. A full summary of retention against impurities and Be grades can be found here [72].

Results published here [16, 73], provide some of the final insights into trap behaviour. Three figures: 2.17, 2.18, and 2.19 summarise all characteristic traps in single crystal implanted beryllium. The first describes behaviour at specific desorption temperatures (overlaid). The second describes trap filling with increasing fluence; and the third, trap filling with increasing implantation temperatures for an oxidised sample.

The effects of crystal orientation and oxidation were mitigated in the first two experiments by implantation into single crystal of (11-20), alongside Ar sputtering (the surface oxide was maintained at 0.2 mono-layers), and same chamber TDS analysis.

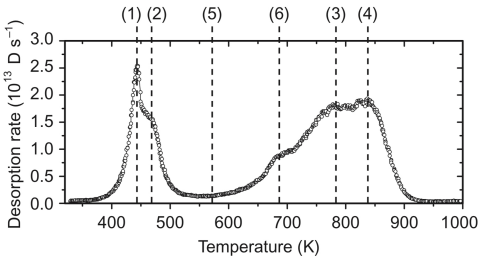


Figure 2.17: Thermal desorption spectra showing D_2 signal when heated at $1Ks^{-1}$ (the JET TDS ramp rate) after a fluence of 3keV D_3^+ ions at 2 x $10^{17}cm^{-2}$ at room temperature [16].

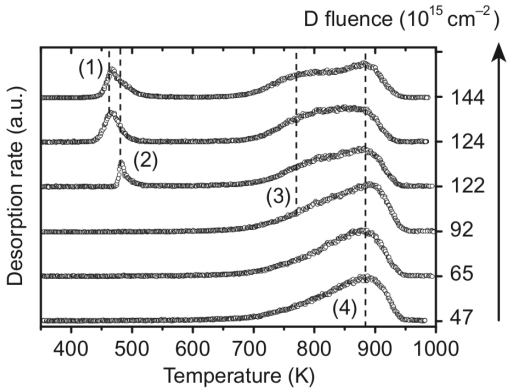


Figure 2.18: Thermal desorption spectra showing D_2 signal changes between release states; when heated at $1Ks^{-1}$ (same conditions as JET samples) on increasing fluence of 3keV D_3^+ ions at room temperature [16].

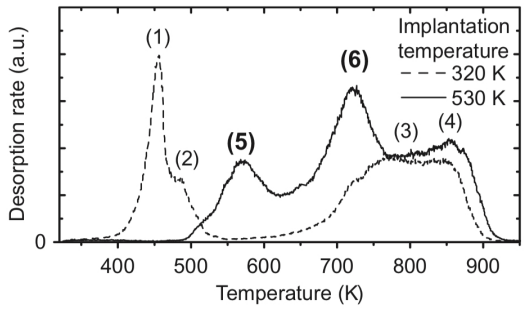


Figure 2.19: Thermal desorption spectra showing D_2 signal changes between release states; when heated at $1Ks^{-1}$ (same conditions as JET samples) at two implantation temperatures of 320K and 530K for 3keV D_3^+ ions [16].

Figure 2.18, shows that at lower fluence (below saturation), higher energy traps

are filled, requiring higher desorption temperature release. As saturation occurs, lower energy traps are progressively filled, requiring respectively lower temperature desorption. The transition between sites (4) to (3) is argued the transition from sole filling of ion induced traps in the ion stopping range, to some further diffusion to point defects into depth. This idea is in agreement by measurement of 3% diffusion into depths [12]. States (2) and (1) are explained upon saturation; shifting from near surface and surface morphology release to a near surface modified beryllium lattice (from intense ion bombardment). This conclusion introduces the possibility of chemical ordering in the modified super saturated beryllium lattice. However disagreement exists between the conclusions drawn between these release kinetics [16] and the morphology found under the TEM in figure 2.15a [14]. Release at 470K is argued insufficient for bubble dissociation, and argues features seen in the TEM are a destabilised Be/D amorphous material, more bound via surface mechanics than chemistry. Alternatively it is possible that TEM beam damage creates a non-equilibrium structure relative to macroscopic release.

Deliberate oxidation is presented in figure 2.19 at stage (6). Release is argued as non recombination limited whilst no other desorption peak shift occurred. BeOD bonding at the surface is tentatively posited. Implantation at temperatures greater than 480K (ITER wall operation) present peak (5). Once more BeH_2 decomposition is suggested [16, 80]. Modelling with TMAP7 of the system for sites (3) and (4) give activation energies of 1.88eV and 2.05 eV respectively, consistent with previous estimates.

Zalkind [84] undertook initial measurements of hydrogen, oxygen and water absorption onto crystalline beryllium surfaces to identify rate determining states.

Oxide formation was argued via initial chemisorption, island nucleation, followed by lateral growth to full BeO wurtzite coverage [84, 85, 86]. Increases in temperature reduced oxide nucleation requirements, and thus increased overall oxide thickness. Oxidation reduced total hydrogen coverage [84].

Pre-adsorbed hydrogen covered beryllium surfaces; subsequently exposed to O_2, impeded surface oxidation [87]. However, on application of higher oxygen exposure, greater oxide thickness resulted.

Pre-adsorbed H_2O covered beryllium surfaces, deviate from O_2 and H_2 behaviour. At room temperature, H_2O monolayer growth was double oxide monolayer thickness, with indication of H penetration and trapping in the sub-surface oxide layers [85, 87, 88, 89]. At elevated temperature, H_2O adsorption and oxidation reduced, with possible surface dissociation to OH and H. Oxide thickness and rate, grew at

elevated temperatures. Hydrogen retention reduced at higher temperatures from desorption [89].

H_2O oxidation followed a parabolic rate equation; whilst O_2 oxidation followed a logarithmic rate equation indicative of diffusion through the growing oxide [88]. The electric effect was confirmed by increased oxidation due to electron beam stimulation [90], and should be considered when undertaking JET Be TEM.

The differences in reported sputtering rates maybe explained [86]. Sputtered samples showed faster oxidation kinetics than annealed samples. Sputtered samples were argued to provide greater defect densities, from which ad-atoms could nucleate [86].

Application of modelling studies to Reinelt's [16, 73] experimental results concludes this section, providing possible mechanistic explanations from first principles, via energy reduction on super cells, produced via Density Functional Theory (DFT).

Energy minimisation of hydrogen species in a Be super cell occurred at H/Be ratio of 3 [16]. However, studies also showed hydrogen atoms stabilised basal tetrahedral and octahedral sites for up to 5 atom occupancies [91, 92]. The presence of multiple hydrogen atoms, did not lead to diatomic hydrogen formation in vacancy complexes.

Both intrinsic and extrinsic defect sites were investigated. Di-vacancies were found less energetically stable than beryllium monovacancies [93, 94]. Self-interstitial vacancies had very low formation energies (0.12eV); indicative of easy diffusive pathways; whilst single vacancies were anisotropic [93]. Energetically favourable hydrogen diffusion in beryllium (via basal tetrahedral to octahedral sites) occurred via an 0.39eV activation barrier [93]. These figures provide insight into the trailing depth profiles, seen previously. Clearly the extent to which thermal vacancy creation can occur in Be, suggest (irrelevant of plasma or ion beam implantation) defect production will increase dramatically [91].

This review is small, and is by no means an exhaustive list of all modelling papers submitted. Literature results have been presented that represent the current understanding of hydrogen retention in crystalline beryllium materials.

2.5.3 Thermal desorption and microstructural analysis of deposited laboratory beryllium materials

The literature surrounding deposited layers is now presented. Layers form under favourable plasma conditions. The production rate of co-deposited layers must exceed erosion due to sputtering [95]. Even less co-deposit literature exists with no micrographic investigation of layers produced. Nevertheless, the discussion is subdivided into Be interaction with hydrogenic species and then inclusive of impurity effects.

2.5.3.1 Thermal desorption of Be-D layers

The current knowledge of co-deposited traps is summarised here [23] via well structured parametric testing. Be/D co-deposited layers were produced via magnetron sputtering, covering W spheres. Experiments modelling loading and unloading of cyclically laid down (tokamak-like) co-deposit, were undertaken. Rounds of Be-D deposit layer production and TDS desorption culminated in saturated surface layers (b) and unsaturated deep layers (a). Total thickness of layers (a) and (b) were varied, and compared both structurally, and via pre and post TDS desorption rounds.

In line with JET findings (divertor deposits), layer thickness increases, decreased effective desorption. Reproduction of the overall deposit's TDS curve, was unsuccessful via combination of the 2 TDS ramps applied. A superposition [23] of the surface layer and total layer thickness effect, was needed. Diffusion of D species into the non-saturated (a) layer dominated, over surface (b) layer desorption into vacuum, concluding that diffusive drive to balance hydrogen content over the total layer thickness was primary.

Application of 900K holds on (a) deposits, showed structural crystallite grain growth. A second wave of testing involved intermediate oxidised layers considering oxidation as a primary retention mechanism. Modelling of the overall desorption curves improved yet with greater uncertainty over the system's D diffusivity. The standard metric [96] was considered too low to represent smaller crystallites with higher grain boundary surface area's. However, non stoichiometric oxides could equally be present.

Beryllium deuteride was also investigated in co-deposited layers produced via in situ plasma sputtering [80] at PISCES-B. Every effort was made to produce JET relevant samples, matching JET divertor sputtering rates [75]. The Be-D co-deposits had high qualitative amounts of BeD_2 present in both XPS and TDS signals comparative to the BeH_2 standard. BeD chemistry was suggested the primary retention mechanism.

So far it is likely that BeD_2 will contribute largely to JET co-deposits; depending on layer temperature and erosion/deposition flux balance. However, it is highly unlikely that these deposits form in purely D plasmas (or isotopic plasma) [95]. More likely, local impurities will complicate co-deposit chemistry and therefore hydrogen retention mechanisms.

2.5.3.2 The effect of other impurities in co-deposited layers: O, C, W, N

Oxidation of beryllium is something that cannot unfortunately be avoided [82, 97], and has been discussed previously via surface adsorption on beryllium 0001 single crystals [84, 85, 86, 88, 89, 90]. High temperature oxidation in vacuum has been shown alongside mixed material layer growth from plasma impurities [82]. Enhanced high temperature oxidation [16, 82, 85] is argued via Be^{2+} ion diffusion through growing oxide layers. Radiation enhanced diffusion is also reported [95, 98]. Reinelt argues this process only occurs above 900K [16]. However, once oxide formation occurs, retention appears greatest under midrange implantation temperatures [73, 99].

Measurements of films grown with D, Be, and C [95], showed Be-D films were in fact BeO films with almost 1:1 stoichiometry, producing D/BeO ratios of 0.3-0.35. Vacuum conditions in JET will therefore dictate whether co-deposit retention is mechanistically dominated by oxide or beryllium deuteride. From the literature it appears more likely that oxygen will play a part. It is even more likely for ITER with a larger plasma and vacuum volume.

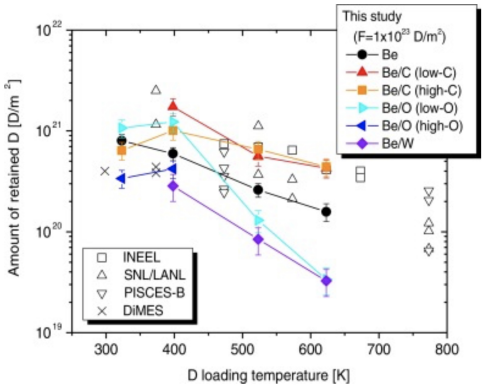


Figure 2.20: The results from TVA co-deposits implanted with high energy deuterium ions with the amount of retain fraction shown against the implantation temperature, of different mixed materials [17]. For comparison the author has also shown literature values [12, 18, 19, 20].

Studies [17] of co-deposits incorporating Be, O, C and W, implanted with high energy D_3^+ ions, showed D retention only increased under high temperature implantation, for Be-C formation (figure 2.20). This was argued the result of deuterated hydrocarbon chemistry at the sample's surface. These results were confirmed [99] when Be-C-D layer combinations retained greater deuterium content (2-4 times) than C-D layers alone. Carbide presence reduced BeC layer sputtering [99], stabilising D retention to higher desorption temperatures, alongside stable layer growth. Desorption

temperatures commenced at 800K and ceased at 1000K. Inclusion of the remaining impurities failed to increase retention above 'pure' Be.

Further work investigated compound formation against amorphous layer formation in impurity deposits of Be-W and Be-C [21]. Figure 2.21 displays these results for (a) the magnetron sputtered Be, BeW and BeC compounds and (b) the deposited Be, BeW, and BeC layers. Figure 2.21(c) shows two further carbon layers at higher and lower atomic %; whilst (d) compares implantation temperatures for Be only layers.

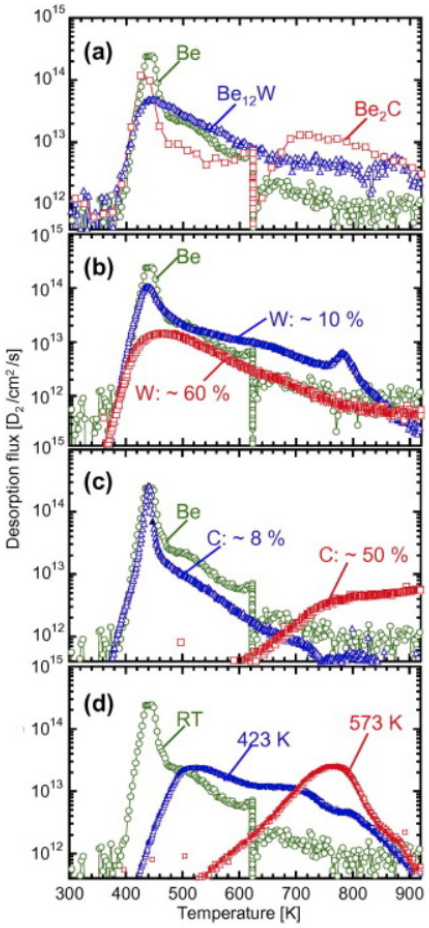


Figure 2.21: (a) thermal desorption of room temperature compounds of Be, Be_12W, Be_2C samples; (b) thermal desorption of room temperature mixed layer deposits of Be, with W at 10%, 60%; (c) thermal desorption of room temperature mixed layer deposits of Be with C 8% and 50%, (d) thermal desorption for beryllium layer implanted at room temperature, versus 423K, and 573K [21].

Sharp release at 430-470K for room temperature implantations where linked to saturated amorphous Be:D layer retention. The shoulder at 500-600K was linked to BeD_2, whilst desorption peaks at 650-900K were related to BeC sp^3 hybridised

bonding (CH3) [21]. $Be_{12}W$ samples displayed lower intensity broader 430-470K desorption peaks.

The Be_2C TDS peaks at approximately 400K and 700K can be described by combination of the two C mixed layers (8% and 50%). The early desorption peak is likely a feature of low temperature implantation damage. The last graph of beryllium TDS spectra implanted between room temperature and 573K, shows peak narrowing and shift to higher desorption temperatures. The author presents this as the result hydride or hydroxide formation, without any presented physical microscopy.

The results from mixed material experiments presented, can be condensed to having a large retention impact in Be-C layers; slightly less in BeO layers; and almost no or reduced retention from other impurities compared with 'pure' beryllium.

2.6 TMAP, applied to hydrogenic trapping in beryllium

This section reviews applications of the Tritium Migration Analysis Program (TMAP7) to thermal desorption spectra. TMAP7 analysis remains the typical approach to desorption curve interpretation, and inference of trap release energy (eV).

The TMAP7 code [100], is a finite element model comprising a one-dimensional system divided into enclosures (the vacuum chamber) and structures (the sample). The sample's structure can be further subdivided into multiple structures, for different component compositions and properties (diffusivity, solubility, trap populations, trap occupancies, recombination surface rates or Sievert's law governance). Only 1 hydrogenic species can exist in a single trap. No provision allows for defect recombination during annealing ramps. Successful authors apply TMAP7 to produce modelled spectra matching experimental thermal desorption curves.

The most simplistic trap release model is governed by equilibrium release of a trapped species (within the material's microstructure) from a surface devoid of chemical sinks. The activation energy for that trap release is that required by the species to detrap, migrate to the surface, and desorb [77]. TMAP7 follows this remit with available addition of chemical sinks and recombination limited surface release.

Well known solubility and diffusivity material constants are therefore, an important aspect of desorption modelling processes; culminating in inferred trap activation energies. Figures 2.22-2.24, show the systemic level of variation among diffusivity [22, 23]. Solubility also suffers similar variability [101].

Summary of published data on diffusion, solubility and permeation of hydrogen isotopes in beryllium

Reference		Diffusion coefficients		Solubility coefficients		Permeation coefficients		Temp. range [K]
		D_0 (m^2/s)	E_D (kJ/mol)	S_0 ($mol/m^3\sqrt{Pa}$)	E_S (kJ/mol)	K_0 ($mol/m\,s\sqrt{Pa}$)	E_K (kJ/mol)	
Pemsler and Rapperport [3]	H	3×10^{-13}	0	–	–	–	–	1123–1173
Jones and Gibson [4]	T	3×10^{-11}	18.47	1.964×10^{-3}	-1.82×10^{-3}	5.795×10^{-14}	18.47	673–1173
Al'tovskiy et al. [a] [5]	H	–	–	–	–	4.24×10^{-7}	86.96	773– 873
	H	–	–	–	–	3.39×10^{-11}	26.70	773– 923
Fromm and Jehn [6]	H	–	–	2.24×10^{-3}	−1.818	–	–	523–1123
Swansiger [7]	T	–	–	7.484×10^{-4}	112.8	–	–	713– 783
Billone et al. [8]	T	1.73×10^{-9}	18.47	–	–	–	–	573–0873
		1.35×10^{-10}	0	–	–	–	–	> 873

[a] Two different types of beryllium were studied.

Figure 2.22: Table displaying the variation in experimentally measured and reported diffusivity and solubility data for beryllium by Abramov [22].

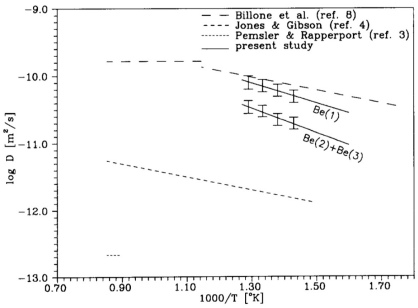


Figure 2.23: Diffusion coefficients calculated by multilayer permeability approach between an ultra purity beryllium grade (1) and a further less pure comparison at two different thickness (2) and (3); in comparison to previous reported literature values [22].

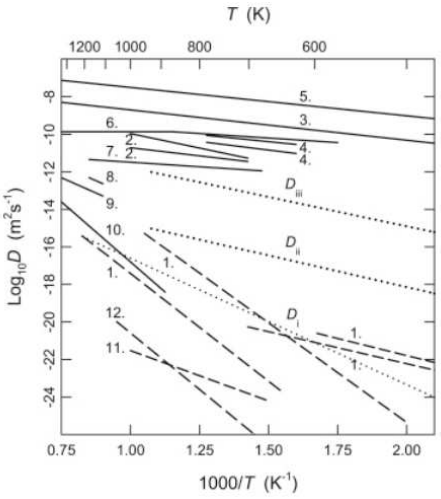


Figure 2.24: The variation of reported diffusivity across the literature in Be and BeO respectively. Dotted lines refer to measured hydrogenic species diffusivities in BeO; whilst solid lines refer to hydrogenic diffusivities in Be [23].

Further contention exists in the mechanistic assumptions used in modelling of diatomic gaseous desorption from the sample's surface. Recombination limited release is often argued for over diffusion limited release. These approaches are often largely numerical fixes, in order to better match measured desorption curves.

These manipulations are especially prevalent in studies concerning co-deposits [102]. Whilst TMAP7 has the ability to model complex multilayers; the greatest successful agreement between TDS spectra and modelled TMAP7 desorption curves, occur from application of a single homogeneous Be-D codeposit layer (structure) [102, 103], despite studies having grown and desorbed layers cyclically.

The same occurrence is also applied to oxidation, despite attempts to accurately measure oxide parameters. Desorption of samples with 80nm oxide layers were not successfully described by either trap energy adaptation, or a suitable surface oxide boundary [23, 103]. The most successful attempts to reproduce co-deposit TDS spectra still require diffusivity and solubility adaptations (figure 2.25); even in studies exploring cyclic deposition of co-deposited layers relevant to ITER [102] and JET divertor co-deposit [104]. These results still represent a mathematical fitting to recorded spectra. In the case of JET, non negligible impurity levels complicate the assumptions made. In these situations the model reflects even less accuracy to the real material under analysis.

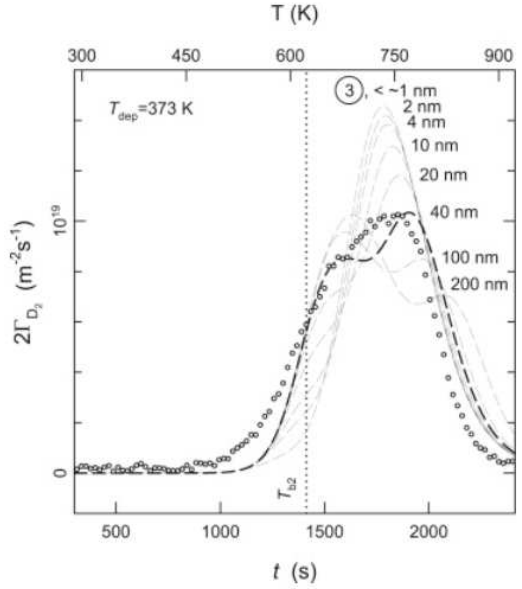


Figure 2.25: The application of a free parameter of the D diffusivity in BeO to create a good fit to under and overlayer co-deposits superposition in the applied TMAP7 model is shown [23].

Whilst some level of successful implementation and fitting of these codes has been made against the most complicated of tokamak materials (co-deposits), it cannot be ignored that these findings are largely a result of numerical fitting. Fundamentally, the process of TMAP7 application must be currently limited in validity. The process applies a model, with many simplified assumptions, utilising a wide parameter field, with high degrees of parameter uncertainty, to infer trap activation energies on materials, which have not been microstructurally evaluated. In the worst instances these inferred trap energies are then used to comment on the materials' real microstructure and bonding.

It is difficult to conclude, under the current understanding that any validity is provided in this approach, given the level of uncertainty and the number of assumptions. Some small improvement can be seen in a more sophisticated model including trap development during the annealing process, alongside trap occupancies reflective of DFT results [105]. However, true, thorough microstructural investigation is necessary to further apply these models for successful interpretation.

2.7 Beryllium binary phase diagrams

The S65-H grade has been discussed in detail in relation to first wall material choice in section 2.1. These discussions outlined the properties which led to the ILW choice. The high temperatures alluded to in JET ILW1 operational literature suggest that material mixing is a real possibility. Phase diagrams of binary beryllium systems have been provided for the readers' convenience and reference. The copper-beryllium system (due to machining impurity presence) and the nickel-beryllium system (due to marker layer presence) are shown in figures 2.26 and 2.27, respectively.

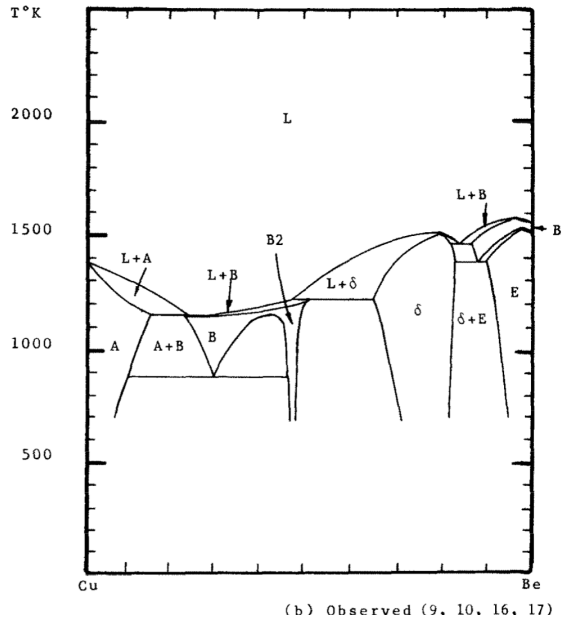


Figure 2.26: The beryllium-copper alloying system [24].

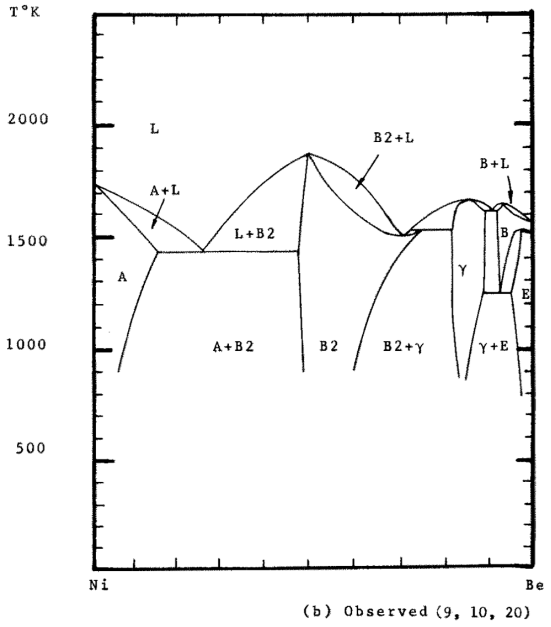


Figure 2.27: The beryllium-nickel alloying system [24].

2.7.1 EELS of beryllium materials

Exceptionally limited evidence of Electron Energy Loss Spectroscopy (EELS) applied to beryllium can be found. Only one paper was found concerning BeD_2 and Reflection Electron Energy Loss Spectroscopy (REELS) [106]. The REELS low loss region,

for a sample implanted by D ions under vacuum conditions and monitored for oxide production (by XPS), is shown in figure 2.28. The low loss region is indicative of plasmon energies relating to matrix bonding. In this region, small amounts of interstitial deuterium could potentially be measured. Whilst the experimental set-up does deviate from standard Transition Electron Microscope (TEM) with EELS; limiting the findings; the figures do give characteristic indication of beryllium low loss spectra.

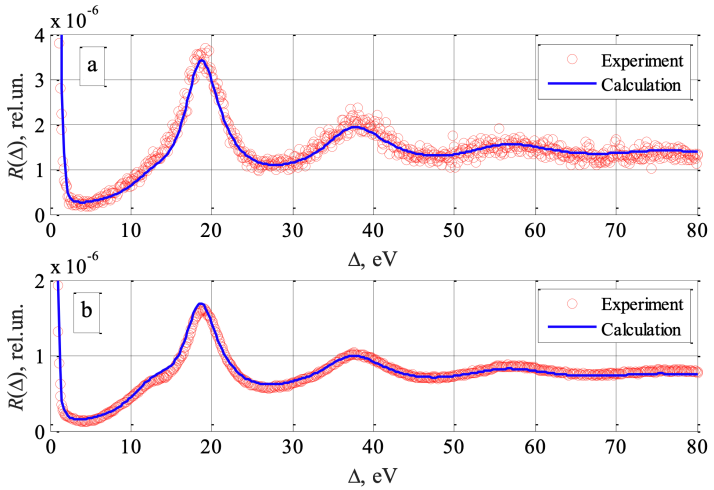


Figure 2.28: The low loss region via REELS of a beryllium MaTeck sample (99.8%) implanted by D ions without oxygenation. A comparison between experiment and modelling for two angular geometries.

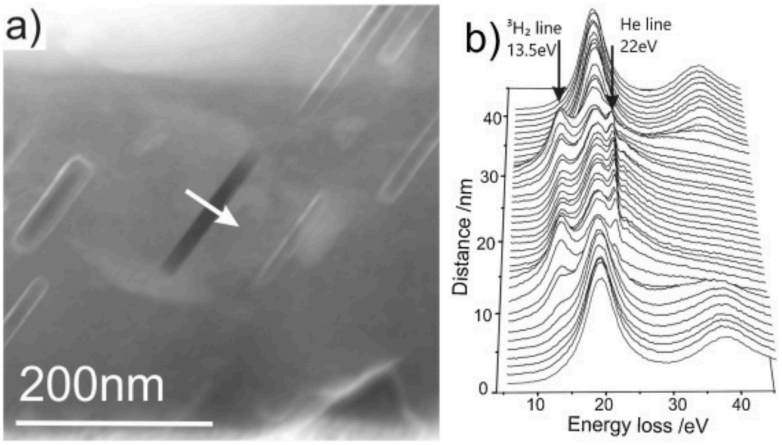


Figure 2.29: STEM with EELS in standard geometry with a Gatan GIF detector, of samples under neutron, T and He implantation at the Petten high flux reactor in the Netherlands under the HIDOBE II program. (a): STEM HAADF image of the region, (b): Low Loss EELS spectra of a linescan across the HAADF feature [25].

Figure 2.29, shows the only other EELS recorded of beryllium materials implanted

by hydrogen (T). Only the low loss spectra are recorded. Furthermore the materials were implanted under high neutron load with He (closer to ITER than JET conditions). Some indication of a low loss peak at ∼13eV is assigned by the authors to bound tritium, which only precipitated at He bubble interfaces. Unfortunately, neither the Be core loss or O core loss was recorded. As a result it is exceptionally difficult to isolate other low loss spectral contributors (like oxidation) from the results. It is exceptionally difficult to isolate hydrogen signals in most common experimental techniques. This is particularly true when measuring plasmon behaviour and attributing peaks. A high degree of controlled measurement is necessary. Nevertheless, these results show some level of reproducibility to results presented later in this thesis.

2.7.2 Atom probe tomography of beryllium materials

Similar to the discussion surrounding EELS application to beryllium materials containing hydrogenic species; very few papers are present on the application of Atom Probe Tomography to tokamak relevant beryllium materials. The only paper found concerns accelerator irradiation damage [26]. Nevertheless, characteristic non Gaussian peak trailing at higher Da is greater for samples with higher dpa damage. These features are shown in figure 2.30.

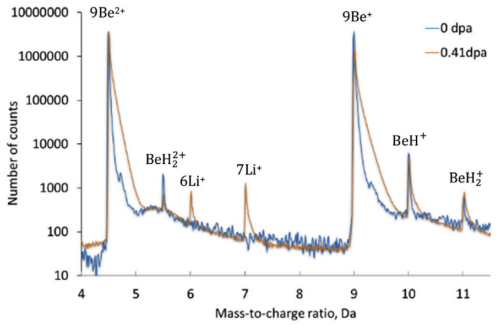


Figure 2.30: Trailing APT time of flight Da peaks for beryllium with no dpa damage and 0.4dpa from neutron bombardment and He production [26].

2.7.3 Literature summary

Observations from post-mortem analysis of ILW1 Be tiles, alongside microstructural findings from laboratory testing of modelled 'erosion' and 'deposit'-like beryllium materials, is presented. Where present, the few papers applying unusual techniques to this niche system were presented.

Chapter 3

Experimental Methods

In this chapter the experimental methods employed to acquire data will be discussed in order of the equipment use.

3.1 Sample preparation

At the end of every experimental campaign series in JET, a shutdown of the facility occurs. The shutdown enables checking of machine components and diagnostics; as well as sample retrieval for post-mortem analysis. Figure 1.2 in section 1 shows a complete 'poloidal' cross section of the tiles removed at the end of a campaign. As stated in chapter 1, the materials analysed in this thesis, called 'castellations' (see figures 1.3 and 1.4) are taken from a midplane Inner Wall Guard Limiter (IWGL) 2XR10 tile; a mid plane Outer Poloidal Limiter (OPL) 4D14 tile, and a Dump Plate (DP) 2B2C tile. All of these tiles were exposed singularly to the first ITER-like wall campaign (ILW1).

Each whole tile is made up of segments of bulk beryllium attached onto an Inconel back plate, a schematic of which can be seen in figure 2.1 (section 2.1). Each segment has machined grooves that cut the surface of the beryllium segment into 12 x 12 squares, to a depth of ∼3mm, to relieve thermal and magnetic stress during campaigns. These features are called 'castellations' and are the basis of sample preparation. The two, inner and outer, wall mid plane tiles are displayed in figure 1.2, to aid visualisation. Due to their dimensions, castellations are an efficient size for Thermal Desorption Spectroscopy (TDS), and are prepared via cutting, from the back tile face, in a controlled manor; to avoid hydrogen isotope desorption. This process is described in detail here [67]. The final castellation sizes are approximately 12 x 12mm and 2.5mm in depth.

The castellations discussed in this thesis, and tiles from which they originated, are 'marker layer' tiles. These tiles were specifically prepared for JET operation to measure deposition and erosion processes. The tiles were produced with S65 beryllium powder which was consolidated via hot-isostatic pressing. Further layers were prepared on the S65H surface via Thermionic Vacuum Arc (TVA) deposition. A 3μm Ni layer was produced on the surface of the beryllium bulk substrate, followed by a further 8μm Be layer. The process is described in [107], and [108]. A schematic of the final 'starting' microstructure is shown in figure 3.1.

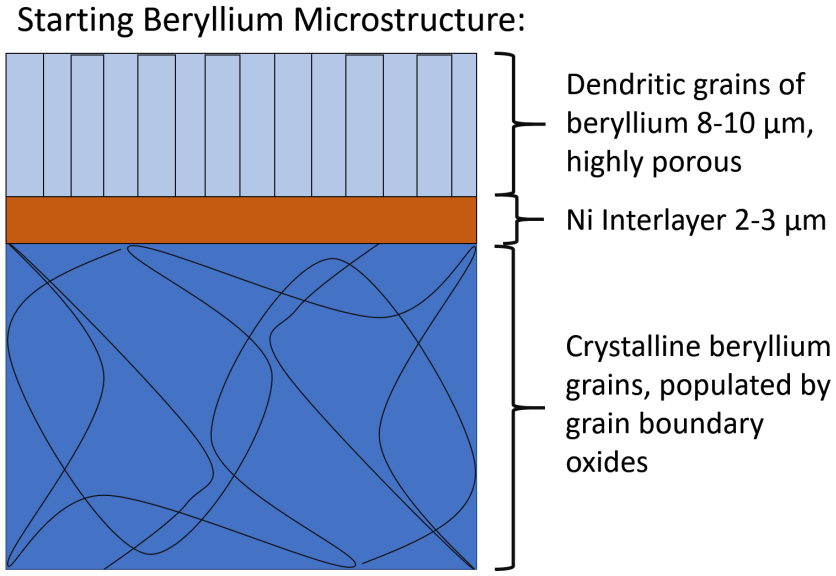


Figure 3.1: A schematic cross section of the starting tile microstructure, from top to bottom showing the bulk crystalline beryllium, the nickel TVA 3μm interlayer and the beryllium 8μm TVA surface layer.

All samples were mounted for microscopy purposes using 20mm SEM pin stubs and attached to similar diameter carbon sticky pads. The samples were prepared several days prior to vacuum ingress. This reduced drift due to both movement and charging in a Scanning Electron Microscope (SEM). Care was taken to avoid any damage to sample surfaces, most especially due to the toxicity of beryllium dust formation. The samples were held in tweezers via the sides of the castellations. Care was also taken to avoid surface damage. Samples were pressed into the carbon layer via the castellations' sides. Carbon 'sticky' pads were chosen so that later removal prior to TDS did not require polar solvents to remove any adhesives. It was feared, this would directly influence the retention in the samples and was therefore unacceptable. Instead the samples were mechanically levered off the sample stub holders again

via gentle application of force with tweezers acting at the sides of the castellation. Sample 163 from the Outer wall poloidal limiter proved the only sample providing any difficultly owing to its greater surface area.

3.2 Microscopy

What follows is a description of the microscopy methods used to asses the castellations isotopic hydrogen retention.

3.2.1 Scanning Electron Microscope and Energy Dispersive X-Ray

A Tescan Mira XMH SEM equipped with an Oxford Instruments X-Max 80 EDS detector was used for imaging and analysis of the individual castellations surfaces. The samples were prepared as discussed in section 3.1. The mounted samples were placed into the chamber and held via grub screws across SEM pin stub inserts. The chamber was then evacuated and analysis proceeded.

In standard Imaging mode with primarily use of secondary electrons, samples' surfaces were investigated and a broad sense of the surface conditions attained qualitatively. The beam was set at an accelerating voltage of 20kV and a beam intensity of 18.00, corresponding to a beam current of 1600pA. This process also gave an indication of the sample's uniformity across the $1cm^2$. Some castellations showed a greater extent of non uniformity across their surface areas.

Further analysis occurred via application of Energy Dispersive X-Ray (EDX). Here the samples' characteristic X-Rays were collected and analysed to obtain elemental compositions. Since the samples are predominantly beryllium and more-over beryllium is the largest elemental contributor, some care was taken to evaluate these results. Only a qualitative comparison was used. Several accelerating voltages were used on the layered deposited samples in particular and also when oxides were thought to be present to compare relative compositions at different depths corresponding to different interaction volumes. These voltages were 5, 10 and 20kV and corresponded with the use of modelling via the Casino software [109] to, approximate to the maximum depths of which an X-Ray can be measured leaving the surface. The voltages were: 5kV, which corresponded to a maximum of 250nm depths; 10kV corresponding to 400nm depths; and 20kV corresponding to a maximum of 2000nm depths. The beam intensity and current were optimised to (22.0 and 2nA) due to the low X-Ray production of beryllium.

Image analysis of EDX maps was utilised via ImageJ (Fiji) [110] to give an indication of the number densities present of oxides in the eroded materials, and film thickness in the deposited materials.

3.2.2 Focused Ion Beam and sequential milling

Each sample was loaded one at a time into the vacuum chamber of a Focused Ion Beam (FIB) on a dual beam FEI Helios. A protective platinum layer was deposited via the electron beam at 22nA to provide a clean and non-damaging surface layer to 0.5μm. A further Pt layer was deposited using the ion beam to achieve a total depth of 2μm of protective platinum. This is a necessity to prevent surface damage via Ga ion implantation to the substrate material under investigation. It is likewise important to start the process with the least destructive beam (here the electron beam) for the initial protective layer. This process is optimum given the fundamental constraints of the FIB device and time, to prevent surface damage and changed retention in the surface region under investigation. Ultimately, the microstructure responsible for hydrogen isotopic trapping in beryllium materials exposed to working plasmas is present in the first few microns of material. The general FIB process to describe 3D milling sections, large and small lift-outs is almost identical, the differences exist in the final surface quality steps, and the initial surface area required for the protective platinum layer. The next sections will discuss the process for 3D serial milling and from there the differences in approach to techniques such as Raman and Transmission Electron Microscopy (TEM) with Electron Energy Loss Spectroscopy (EELS); will be outlined. For the purposes of serial milling studies a 1μm depth platinum layer is deposited on the surface of the material, 0.5μm depth is achieved through electron beam deposition and the final 0.5μm depth via ion beam. The surface area of the region of interest is generally 30μm in length by 20μm in width.

For lift-outs that were analysed by Raman and standard TEM, as well as EELS the initial platinum layer was 30μm in length, 3μm in width and a total of 2μm in depth, including both electron beam and ion beam deposition.

3.2.2.1 The FIB process: "trenching" for serial milling studies

The next process for any preparation is termed "trenching". A 65nA beam was used with a rectangular milling cross section, to produce a 50μm long and 15μm wide trench. This occurred 3μm away and in front of the protective platinum layer, and was milled to a depth of 15μm. The side trenches were then roughly cut to the left

and right of the protective layer. This occurred again at a distance of 3μm away from the protective layer and at a length of 8μm and width of 20μm and again to 15μm depth. Figure 3.2 shows the initial rough milling region in navy blue when looking at the schematic SEM surface from above.

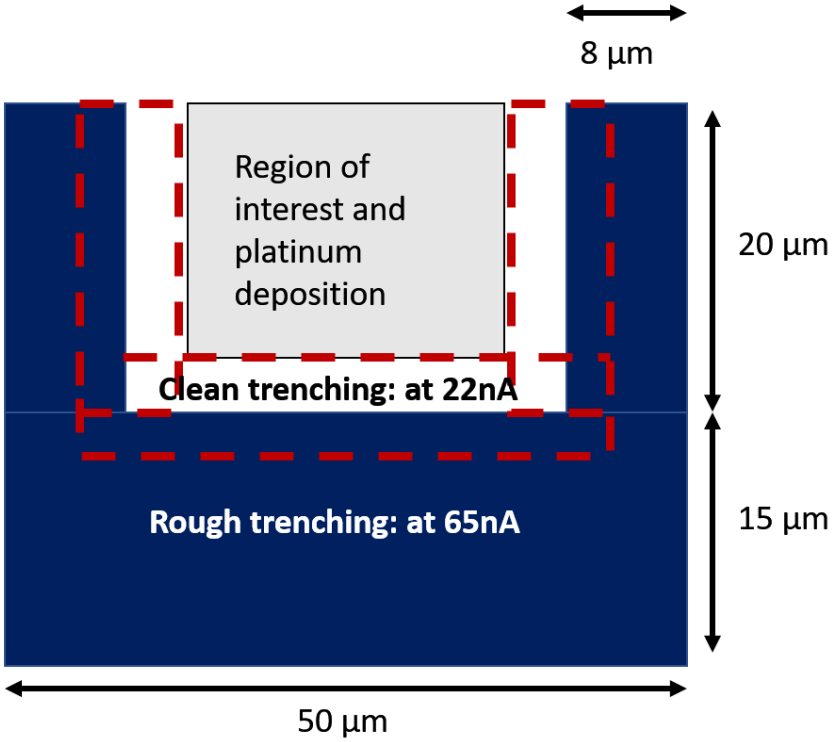


Figure 3.2: A schematic of the trenching process for serial milling studies. The image displays the SEM surface area from a bird's eye vantage point. The navy blue boxes surrounding the region of interest (on which platinum is deposited) represent the rough cut trenched regions to 15μm depths; note the white spacing left around the region of interest during this step. This was to reduce any chance of beam drift interacting with the region of interest at high current. The inset red boxed regions represent the finer mill of the trenching process to abut the region of interest. This is done at 22nA for greater accuracy and milling precision.

A lower beam current was then applied at 22nA to approach the sample directly. This process enables the trench to abut the platinum layer. The beam is moved in. At the front of the lift-out, a milling rectangle is created of 50μm length, 10μm width and 10μm depth; outlined in red boxing in figure 3.2. Care must be taken that the beam doesn't eat away at the platinum, nor redeposit. The same process occurs at the sides of the region of interest. The beam is stepped inwards and placed optimally to mill the remaining material present between the last trench and the platinum (figure 3.2, outlined in red).

If the surface finish does not yet reveal the crystalline structure of for example: eroded regions with lighter contrasted oxide features, or the layers of deposited materials, a further 9.5nA beam is used to clean the surface; until a uniform gray scale is present for the matrix (in the case of the eroded regions). The length of the rectangular cross section will be the same as the above 50μm in length but only 5μm in width and only 5μm in depth. The milling process is monitored by the user until the front depth surface is uniform and clear.

An example of an acceptable surface is shown in figure 3.3. 8-10μm of beryllium from the base of the white platinum layer (the beryllium surface) into depths is shown, with white precipitates (primarily oxide) present at the grain boundaries, some of which are a result of the powder consolidation process.

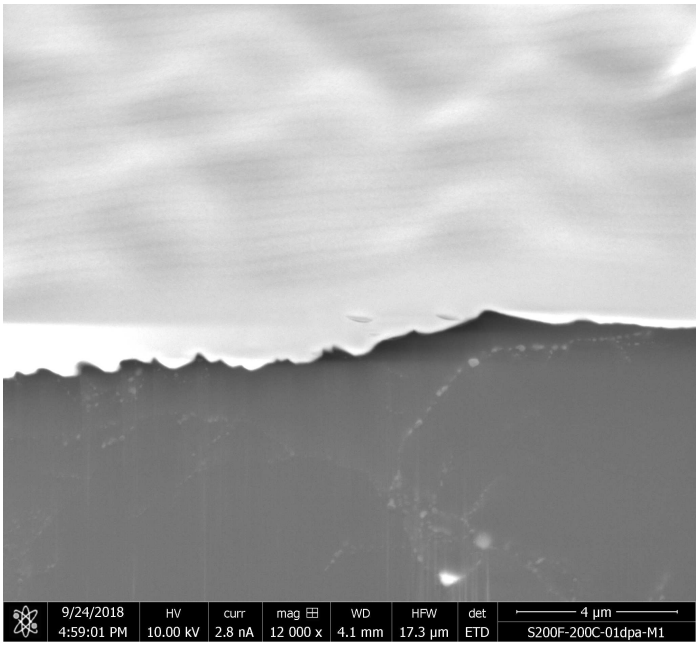


Figure 3.3: A SEM secondary Electron (SE) image of the cross section of the sample's surface. From top to bottom the regions seen are: white - the platinum protective layer; mid grey scale - the beryllium surface abutting the protective platinum layer. The bottom of the image corresponds to approximately 8-10μm depths into the beryllium surface. The beryllium region is smooth and uniform, with white precipitates (oxides) present primarily at the grain boundaries. This is an example of the surface finish needed for a serial milling study.

Once this surface uniformity is achieved, the set up for 3D milling can occur.

3.2.2.2 Serial Milling studies

Prior to the serial milling, a fiducial, shown in figure 3.4, is made. A small square of platinum is deposited of 8 x 8μm on the surface to 0.5μm thickness. A circular cutting tool is then fitted within the square with a diameter of 8μm, and a further eccentric circle fitted within with a diameter of 4μm. The inner circle is disabled so that a disk type pattern is milled to 2μm depth. This process produces a unique, well contrasted, fiducial on the surface.

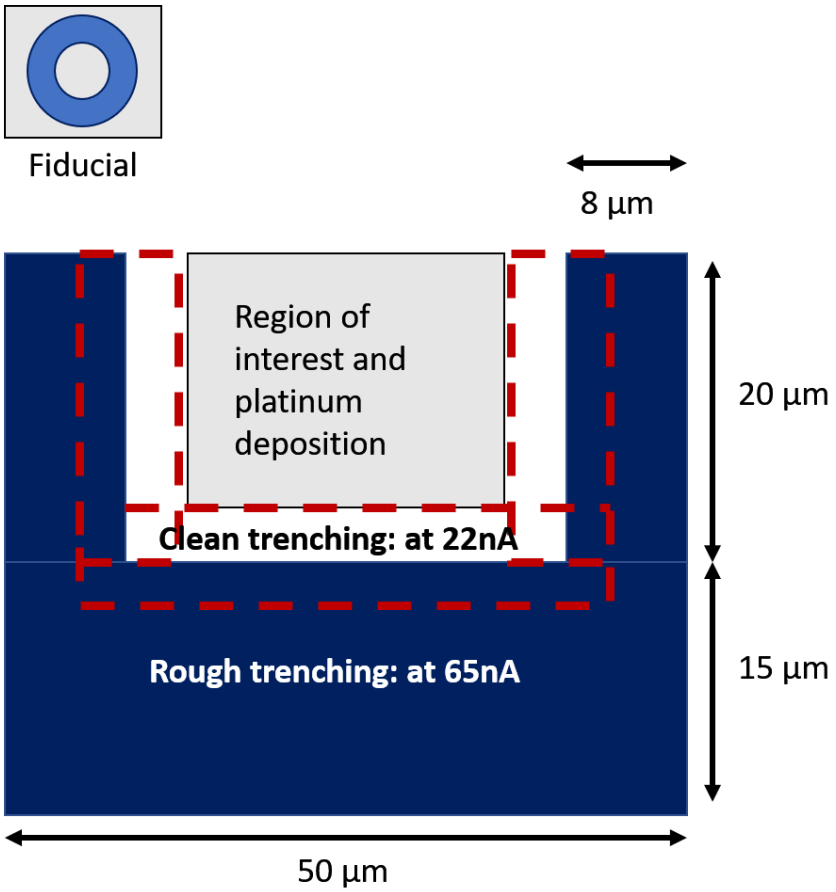


Figure 3.4: A schematic showing the optimum design and position of a fiducial to the top left corner of the region of interest, as perceived from a bird's eye vantage of the sample's surface.

The serial milling undertaken utilised the licensed FEI "slice and view" software. The user sets the software up via the following method. The user confirms that the microscope is at eccentric focus and aligned (this is correct since without which the platinum deposition and trenching could not occur). The user proceeds to deselect the automated options for trenching and fiducial production, and proceeds to: im-

age selection, auto focus, and, brightness and contrast settings. Figure 3.3 shows the contrast optimised for beryllium (which produces a very low signal/few SE). The necessary matrix contrast to grain boundary precipitates, necessitates saturation at the edges of the region of interest due to platinum sputtering or the platinum protective layer. The optimum SEM secondary electron detector is the "ETD" detector. The electron beam is set at 10kV to reduce the signal produced from depth. The SEM images in the stack are selected at 2048 x 1768 pixel resolution. The dwell time is 10μs and the SEM current 2.75nA. The ion beam settings are: 9.3nA current, 30nm slice thickness, and the maximum total thickness of the region probed is 15μm if the run is successful and autofocus remains optimal. In order to initiate autofocus after brightness and contrast are optimised, the current focus is set to the mid plane of the region of interest (into the page, milling direction) so that the greatest chance of success can occur across the whole of the probed region. The auto focus is then optimised. The image resolution in terms of the scanning dwell time across the autofocus range is reduced to reduce the overall serial milling time. The range of focus is selected to include equidistantly the mid plane focus discussed previously. The rough auto focus establishes the layer's current relative focus and then a further fine focus is applied within that smaller range. The fine focus has a higher resolution and a greater dwell time (3μs) to achieve a crisp image that is recorded after each milling slice. The optimum conditions optimise image quality whilst reducing focusing time to the greatest extent. These settings were saved to the user profile and applied to all datasets.

A serial milling study was produced at lower magnification in a minimum of two surface locations across the 1cm^2 castellations' surface areas. This approach assessed the uniformity of depth profiles and surfaces across the castellations' surface areas. Once an understanding of each castellation's uniformity was understood a further higher magnification serial mill was produced so that greater resolution was achieved, and if possible image analysis could occur, utilising grey scale thresholding to account for precipitate number densities, and average particle diameters.

After successful completion of the serial mills at higher magnification, the final regions of platinum left were extracted via the lift-out method, described in sections 3.2.2.3-3.2.2.4, in this chapter, and EDX applied on the last face milled, to gain an understanding of the compositions present in the whole serial mill.

3.2.2.3 The FIB process: "undercutting" for lift-out production

Whether the lift-out process is occurring after serial milling studies have been undertaken, or whether it is a "standard" lift-out for TEM, the process is very similar. If occurring after the serial milling, a minimum region of protective platinum of: 30μm (L) x 2μm (W) x 2μm (D) must remain. If this process is begun solely for lift-out purposes, the same area of platinum is required. Once again the platinum protective layer is produced by electron beam followed by ion beam deposition. Once the trenching process occurs as described in section 3.2.2.1, a further trench is required to reveal the final side of the lift-out as shown in figure 3.5, by a rough cut region of navy blue, and a finer cut abutting the platinum surface outlined by red boxing. These cuts are again undertaken at 65nA and then 22nA ion currents.

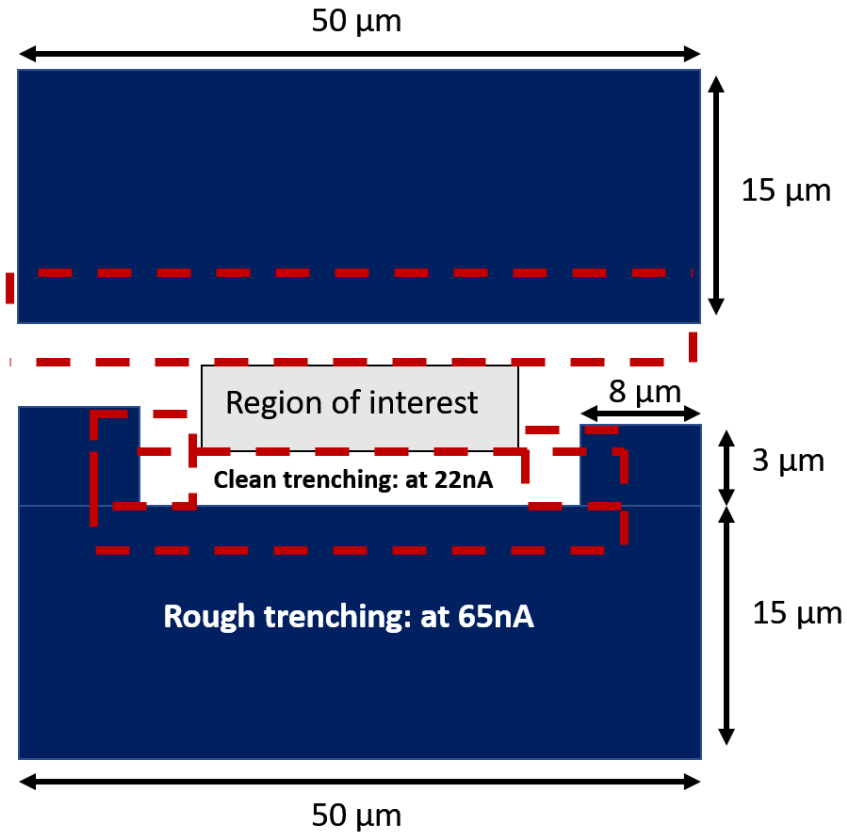


Figure 3.5: A schematic showing the lift-out surface from a bird's eye vantage. A further rough cut (navy blue boxing) and fine cut (red boxing) at 65nA and 22nA ion beam currents is undertaken (relative to the figure above the region of interest), completing the trenching process.

The region can then be rotated globally to zero degrees, producing an ion beam at

52 degrees relative to the sample's surface. This enables the underside of the region of interest to be removed. This process is called "undercutting" and occurs at 22nA, which produces the quickest and least redeposited beryllium. Figure 3.6 shows the view when undercutting at zero degrees. A bridge on the right side still connects the surface to the liftout.

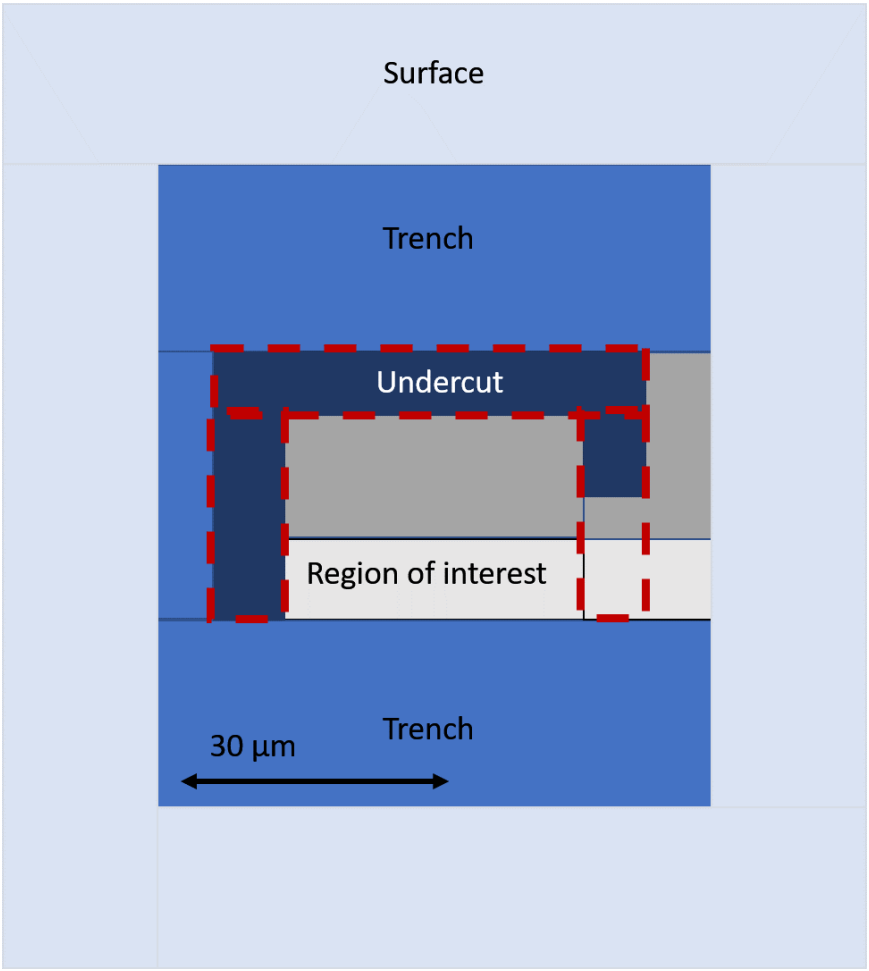


Figure 3.6: A schematic showing the relative view present in the FIB beam (relative to the surface at 52 degrees). The surface is displayed in sky blue, whilst the trenched royal blue regions would appear shaded in the 'real' image due to the material removed in these areas. The region of interest would be displayed as suggested with the platinum (white) facing outwards at the surface and the depth profile of the beryllium lift-out retreating into the page slightly. The undercut region is outlined by rough cut in navy and then on attachment of the lift-out to the micro-manipulator needle, the 'bridge' remaining, attaching the sample to the surface would be removed at smaller currents as indicated by the red boxed regions.

3.2.2.4 The FIB process: "Lifting out" the sample

The next process to produce a TEM or Raman lift-out is to remove the region of interest from the surface of the material substrate. A micro-manipulator needle is inserted towards the sample's surface, which is orientated at zero degrees globally. The micro-manipulator needle is moved into position. For these samples to assure that they were in fact undercut and free from the surface the manipulator needle was positioned at the bottom left leading edge of the region of interest and brought to a slight overlap with the sample in the z direction (into the page). The needle was then pushed gently up against the region of interest and if a slight movement/flexion occurred, the needle was moved back slightly in the y direction and an area of platinum 5 x 2.5 x 2μm deposited overlapping the needle and lift-out. Once the platinum securely attaches the needle to the sample, lift-out can occur. The last bridge point of the region of interest to the sample's surface (figure 3.6 RHS, where the red boxing overlaps the white platinum region) is removed by a 9.5nA rectangular mill. Both the needle and 'lift-out' can be removed from the surface by retracting the needle.

3.2.2.5 The FIB process: Attaching the lift-out to an omniprobe grid

The needle with lift-out attached is now moved to a TEM omni-probe grid. The sample and needle is positioned opposite a 'v' position of either 'A' or 'C' depending on space availability. Each grid is reserved for samples originating from the same castellation and filled accordingly in the 'v' positions. Once the size of the lift-out is positioned opposite the 'v' position of for example 'A', it is retracted once more and a small rectangular mill is performed at 65nA to widen the position into a rectangular shape, in which the sample lift-out can reside. This process is done via eye, until the image in the SEM approaches the correct shape.

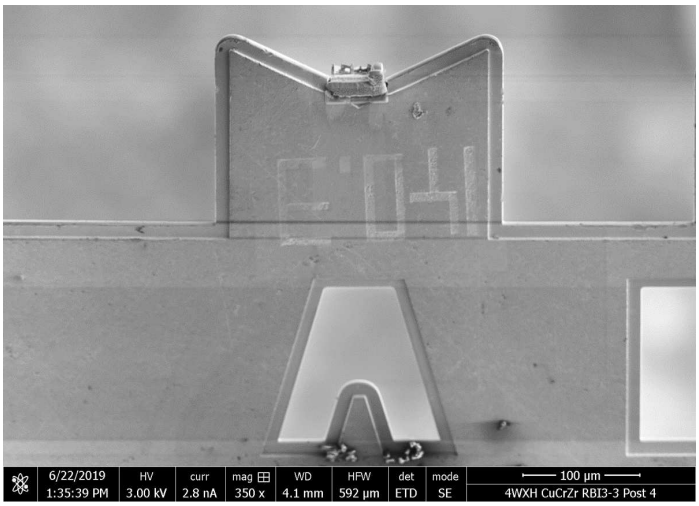


Figure 3.7: An SEM SE image of the omni-probe grid at position A with the lift-out attached in the 'v' position for added structural stability. The face of the lift-out seen is the depth profile of the lift-out from top to bottom relative to the top of the image.

Once the mill has occurred the sample is repositioned in the now rectangular field similar to a lock and key structure, and platinum is laid down once more. Platinum is laid to support and fill the bottom edge and sides of the lift-out to the omni-probe grid. Figure 3.7 shows the lift-out fixed to the omni-probe grid for a sample from the inner wall limiter erosion zone. Once the lift-out is secured the needle can be removed via a quick 22nA mill to remove platinum attaching needle to lift-out; and be retracted. The sample is then rotated 180 degrees and further platinum matching the first face is deposited at the sides and base of the lift-out in contact with the TEM omni-probe grid.

3.2.2.6 The FIB process: smoothing the lift-out sides for Raman analysis

In order to undertake both Raman analysis and EDX on the depth profiles of JET materials, the lift-out's sides must be smooth and polished. A 9.5nA beam is used to gently mill any redeposited Be off the surface of the lift-out's two faces (figure 3.8(a)). This step occurs at an 'over tilt' of 56 degrees such that the tailing edge of the beam used to trench the surface is accounted for, to remove any wedge shaped profile.

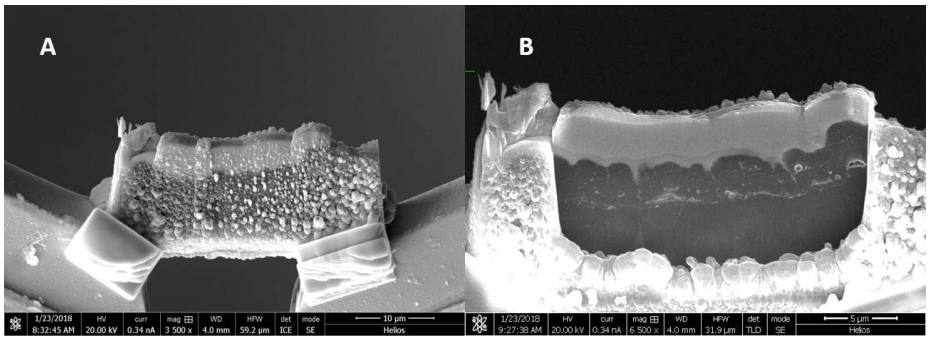


Figure 3.8: An SEM SE image of a lift-out from the dump plate (melted) material. (a): showing the redeposited surface after undercutting where the wedge profile remains. (b): From top to bottom; the platinum protective surface region (white/light grey); the darker grey beryllium sample whose global surface abuts the platinum layer, going into depth; surrounded by a platinum and beryllium (high contrast/white saturated region) - a sputtered window to give added strength to the thinned region. The smooth uniform sides are appropriate for Raman or EDX analysis, showing microstructural features.

This step ensures that the sides of the lift-out are parallel and not sloping into depth with varying thickness. A further 2.5nA beam is then used on each side of the lift-out to ensure that the surface is smoothed and polished to produce resolved microstructural features (figure 3.8(b)). The TLD (in-lens) detector gives an excellent indication of surface finish, with any changes in dark contrast (beneath the white platinum protective layer) of the crystalline beryllium (of eroded regions) being due to surface finish. The final lift-out which is still 1-1.5μm thick, must have a dark beryllium grain structure with white precipitates of oxides around the grain boundaries when originating from eroded regions. This sample is now ready for Raman and/or EDX analysis. An example of the surface finish typical for a Raman lift-out, is given in figure 3.8(b).

3.2.2.7 The FIB process: smoothing the lift-out sides for TEM analysis

The surface finish of TEM samples are always preferred to be as smooth as possible with the least amount of beam damage. The finish is also thinner than that of a Raman sample. If the sample is used for diffraction purposes and EDX then on average it will be approximately 100nm in thickness. However, if the sample is being produced for STEM with EELS, the sample must be equal to or less than 50nm thickness, and as uniform as possible. The initial description of the process, will be concerning samples for standard TEM and EDX, with a further explanation for EELS analysis.

The goal of any TEM sample must always be at every thinning step to remove the last step's Ga ion beam damage, or to have sufficient thickness remaining, so that removal can occur at a later step. The initial thinning steps still require a 30kV ion beam and further reduce the thickness of the lift-out to sub 500nm. This is done with a 2.5nA beam removing 200nm on each side, whilst improving surface finish. The lift-out remains at 56 degrees and the bottom of the liftout thins slightly preferentially.

On completion, the lift-out is tilted to 54 degrees and a further 60-80nm is removed on each side. This time the beam will mill higher into the face off the lift-outs depth profile (half way up). An eye must be kept on the surface contrast so that the base of the lift-out approximates the contrast of the regions being milled towards the surface. This milling step occurs at 0.3-0.69nA and 30kV. The lift-out should now be approaching 100nm thickness.

The lift-out is then tilted to 52 degrees and directly milled from a perpendicular angle. This steps removes any wedge that has been formed at the top surface of the lift-out directly onto the platinum layer. The platinum will start to erode. Care should be taken so that the surface contrast approaches that of the mid and base of the lift-out. This step is undertaken on each side.

The beam's current is now stepped down to a sub 100pA range. Both SEM and FIB detectors are changed to 'ETD' to have an indication of thickness by eye. The brightness and contrast are set to average for the background vacuum. An intensity profile measurement can be drawn through the sample and overlap the background signal to aid the operator in achieving electron transparency. The SEM beam can now be stepped down to 10kV, 5kV and 3kV as the mill proceeds. The timing of this change should occur when the intensity of the beryllium surface appears brilliant white in the previous SEM beam's voltage (figure 3.9). For example, when the SEM image appears white at 10kV, step the SEM beam down to 5kV and so on. For a standard TEM and EDX sample, it is sufficient to stop this process at 8-5kV SEM beam. From there the sample can be cleaned gently of beam damage. To remove beam damage, the sample is tilted to 45 degrees globally. The FIB beam is lowered to 5kV and a low current of 600pA. The face of the lift-out is milled with a diffuse beam and rectangular mill. This occurs on each side for a maximum of 5 minutes, depending on the sample's thickness. At any sign of a hole expanding, the process should stop and the sample rotated with the final step completed on the opposing side. This process should remove a maximum of $\sim$10nm on each side.

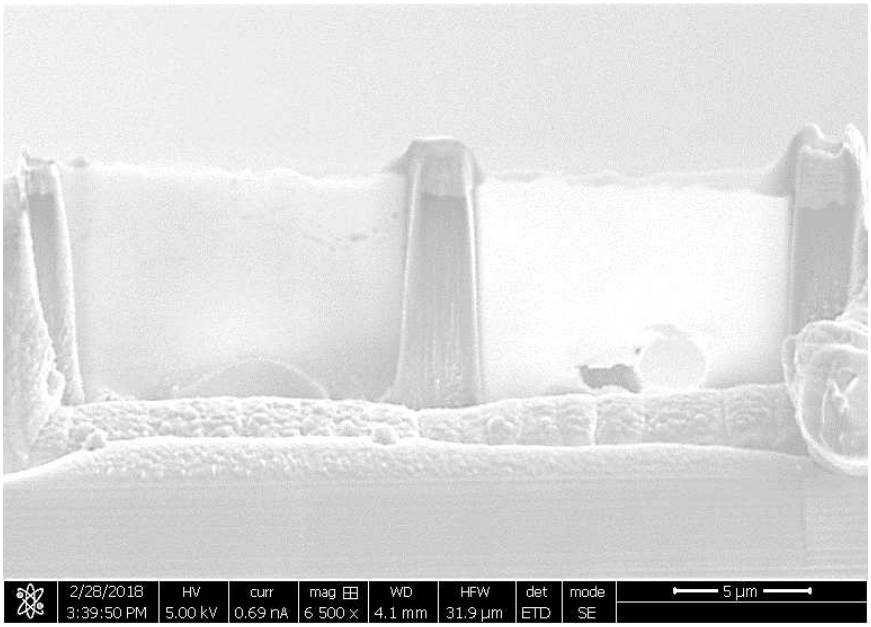


Figure 3.9: An SEM SE image of an inner wall eroded region lift-out prepared for EELS and transparent at 5kV in the SEM beam. The platinum signal at the top of both windows is almost completely gone. The milled window on the right of the lift-out is more transparent than the left (from contrast). A hole can be seen in both lift-outs at the base.

For EELS transparency, the SEM image must appear brilliant white (saturated) in the 5kV and semi transparent in the 3kV. Once this has been achieved the sample is rotated to 45 degrees globally and a diffuse 5kV FIB Ga beam used to 'clean' the surface of damage similar to that described for a standard TEM and EDX sample. This process removes 10-15nm on each side. During this step for an EELS sample, an eye should be kept on the platinum surface layer. The beam should be stopped immediately when the platinum has completely gone. Figure 3.9 shows an example of the typical contrast at 5kV required for a successful EELS sample. The window on the right of the image (with greater white contrast) is more transparent than the milled window on the left.

These samples are now ready for Transmission Electron Microscopy and Electron Energy Loss Spectroscopy.

3.2.3 Raman Microscopy

Initial Raman Microscopy occurred on the surface of samples on secondment in Marseille. Samples were placed on the stage of a Horiba-Jobin-Yvon HR LabRAM apparatus in backscattering geometry. The surface maps were collected with a x100 ob-

jective lens, a numerical aperture of 0.9, utilising wavelengths of 514.5 and 632.8nm. The laser power was kept at 1mWμm^{-2}. Further details of this set up can be found here [28], with published results here [111, 112].

Due to the restrictions of beryllium toxicity, further Raman work in the UK could only occur on samples reduced to 'cleared' via FIB lift-out production. Samples were prepared as described in section 3.2.2.6. FIB lift-outs produce, pieces of beryllium with implanted tritium, that are sufficiently small such that the tritium inventory and beryllium toxicity are below detection levels and deemed as low as reasonably practicable. Remaining Raman work continued on samples which had been lifted out from the surface, and furthermore probed the depth direction of the lift-outs in mapping mode. This second level of investigation with Raman utilised a Witec alpha300 ARS correlative, Atomic Force Microscopy, Raman, and Scanning Near-field Optical Microscope. After many surface tests optimising the power and integration time to avoid sample heating and any resulting Raman peak shifts, the beam power was set to 5mW, utilising the green laser (532nm), whilst the integration time was 0.1s. All investigations occurred in mapping mode with the EMCCD detector. Spectra were collected per 50nm increment, from which a 9 x 9 spacial average could be taken. This process maximised the signal received from the surface and beryllium, after cosmic ray removal.

Data analysis was undertaken in the Witec process software. Cosmic ray removal was utilised with a filter size of 4 and a dynamic factor of 1. This produced the most thorough, sensitive, and effective cosmic ray removal across the samples. Noise was reduced via Gaussian smoothing method with an average spectral filter size of 9 and a average spatial filter size of 9. Any background gradient was then removed with a "rolling ball" method, the diameter of the rolling ball was 150cm^{-1} and the dynamic factor 1. A thorough search of the literature was undertaken to eliminate any possible contributions from Ni, Fe, W and any other impurities likely to be present on the Raman cross sections. EDX of these surfaces was also undertaken to establish the likelihood of any bonding due to impurities.

3.2.4 Transmission Electron Microscopy and Electron Energy Loss Spectroscopy

Lift-out samples described in section 3.2.2.7 were transferred to a Jeol-ARM200F TEM (cold-FEG operated at 200kV). Scanning TEM (STEM) was used with Jeol High Angle Annular Dark Field (HAADF) and Annular Dark Field (ADF) detectors using a 8cm camera length, to survey the lift-out areas at lowest magnification. The

ADF detector covers angles of 33-51 mrads, whilst the HAADF detector cover angles of 72-235 mrads, which correspond to images of diffraction contrast; and mass contrast respectively. EDX measured in conjunction to STEM was recorded in a Jeol Centurio detector. EDX and EELS occurred wherever possible in conjunction with the following settings. Electron Energy Loss Spectroscopy (EELS) was recorded in a Gatan Quantum GIF, with a 2mm aperture, covering an angular range of 82-194 mrads, corresponding to a mass contrast image. A schematic of the set-up is provided in figure 3.10.

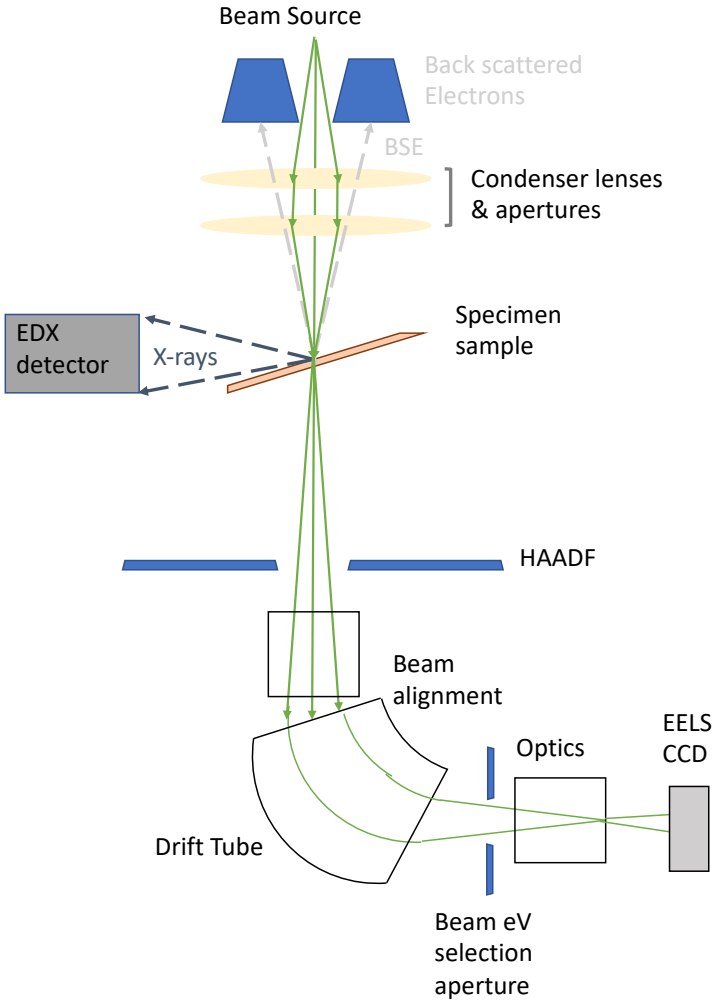


Figure 3.10: A schematic showing the STEM mode with EELS and the orientation of EELS and EDX detectors

Zero loss spectra were recorded at 0eV for 0.0001s per pixel. The beryllium core loss edge was recorded at 111eV with 0.01s per pixel. The oxygen core loss was recorded at 532eV with 0.05s per pixel. On average the number of frames were 5 per map, unless a fault occurred. The maps were normalised during post processing to account for the different total integrated pixel times. EDX was, where possible, recorded in-situ with EELS (figure 3.10), such that the sample could be checked for higher element contamination. Nitrogen was also acquired for, due to the presence of N puffing discharges in JET, however it's signal was not observed.

Electron Energy Loss Spectroscopy (EELS) maps were analysed using both hyperspy software and Gatan Digital Micrograph software. The hyperspy approach is described in detail here [113]. The first process is to remove spikes originating both from cosmic rays, and produced from column X-Rays hitting the detector. This is a simple process and easily remedied due to the typical Full Width Half Maxima (FWHM) of these spikes being substantially different to the EELS core and low losses. The second stage of data processing is, noise reduction. This can occur in two parts, with differing assumptions applied. The first step is defined as Principal Component Analysis (PCA). The signal is decomposed into orthogonal components. The system's components are assumed linear, and the noise lower than the variance. From these assumptions the components' eigenvalues are ordered largest to smallest, with a cut-off applied; such that all signals beyond the cut-off are discarded as noise. Since this treatment is purely mathematical and not based on 'real' physics, a further step can occur to reduce noise and identify cleaner signals by undergoing Independent Component Analysis (ICA). This step is similar to the previous, however it occurs with a relaxation of the restraint of orthogonality. Independent components can then be extracted from mixtures of component eigenvalues present in PCA spectral images.

The third stage of analysis is background removal and curve fitting. Background removal occurs by estimating the exponential background around the signal's edge. Once removed this enables a truer area under the core loss to be interpreted. Care was taken to record all edge losses with the same onset energy, such that the background estimation and fit occurred on the same pre-edge window when in the Gatan Digital Micrograph software. The Gatan curve fitting process is limited to the physical edge structure calculated from a theoretical cross section. The cross section is the Hartree-Salter model, however no fine structure is taken into account [113].

Curve fitting, via hypserspy, is much more accurate, accounting for the fine structures present. Here, the whole spectral window is used to estimate the background subtraction. All of the spectral points are then reproduced as a linear combination

of components including polynomial components used to describe the fine structural features fully. A much greater accuracy can be found of the core loss integrated area via this method. Examples of these fits can be found in Appendix A.

The hyperspy approach, utilising all spectral points, substantially reduces errors associated to Gatan pre-edge background removal, if for instance there is variation in the pre-edge region across data sets. The algorithm also incorporates the effect of plural scattering. Stoichiometries extracted from this technique are therefore more reliable. Further details of the hyperspy methods and approach can be found here [114]. All of these steps were undertaken in hyperspy [114], including methods to optimise data processing times and reduce computational loads. After accurate extraction of the signals via curve fitting; two matrices of intensity (Be and O) can be extracted. Careful consideration of their total integrated pixel time with normalisation, enables a percentage map of each component to be produced.

These binary maps of stoichiometric compositions alongside their background subtracted, decomposed and curve fitted fine structure (Be or O true EELS) spectra can be extracted and compared with the help of modelling, using Density Functional Theory (DFT), to better understand any unique structures found.

3.2.5 Atom Probe Microscopy

Atom Probe Tomography (APT) is one of many techniques that exploit field evaporation of materials on the nanometric scale length, and was used in this case to exploit the presence of deuterium in these samples and investigate whether there was any spacial clustering present in these materials. In conjunction to both EELS and Raman, APT explored beyond the chemical environment of deuterium in the samples to deuterium's spacial positioning.

The system employed in these experiments was the Cameca LEAP 5000. Samples were prepared via FIB as described to the end of section 3.2.2.6. Further preparation occurred subsequently which deviated from that used to produce TEM foils. The cantilever extracted after section 3.2.2.6, was not adhered to an omniprobe grid and instead moved to Si posts and positioned on an individual Si post centrally. Once orientated correctly the Cantilever was adhered to the Si post via platinum deposition. Once adhered, the remaining section of the cantilever was removed by rectangular mill and retracted. This process is repeated across all available Si posts until no further cantilever is left. The average cantilever produced approximately 10 needle specimens. Similar to the TEM preparation route in section 3.2.2.7, these needles needed to be milled to less than 50nm tip diameters to be successfully evaporated. It was soon

found that sharp needles with a higher shaft angle produced longer lasting specimens. A series of circular milling tools was used in conjunction to a 30kV FIB milling beam. Two circular cross sections were required, a large cross section and a smaller cross section positioned inside to blank the beam so that the outside edge of the mill could become smaller and smaller on subsequent milling turns. Care was taken to mill the needle with increasing gentleness and precision, starting with a 2.5nA ion current and finishing the final pre-cleaning mill at 30kV with a 40pA ion beam. One further pre-cleaning step occurred by stepping the voltage down to 8kV with a 24pA current. This step enabled the sharpest needles to be formed with an average tip diameter of 20-30nm. At these currents and voltages, greater accuracy can be achieved however, further care has to be taken to 'find' the sample again due to poorer alignment and therefore difficulty imaging the sample in the FIB beam. As such when a change in current or beam voltage occurs, depending on the severity of misalignment, both circular cross sections must increase in diameter and then be considered during a short mill to see where the mill is taking affect and adjust inwards accordingly. Across all of the samples, milling ceased once the protective platinum at the tip approached 200nm. At this stage the FIB beam is lowered to 5kV and a cleaning diffuse beam utilised to remove the remaining cap of platinum and any beam damage associated with the procedure. If done correctly, Pt should not be present in the recorded Time Of Flight (TOF) spectrum produced by the Atom Probe. Likewise the Ga ion TOF spectrum should be significantly reduced if not eliminated entirely.

Once the samples are prepared, the Si atom probe 'coupon' is moved swiftly to the LEAP 5000 and placed under vacuum in the loading chamber for a minimum of 1 day prior to analysis. This step reduces any off gassing from adsorption onto the surface in transport. Many samples will produce larger hydrogen (mass to charge ratio (m/q) 1) peaks if this does not occur. The samples are then moved into the analysis chamber and pumped down to a minimum of $1x10^{-10}$ Pa.

Once loaded and pumped down the samples are aligned by slowly raising the voltage to a point at which meaningful evaporation starts to occur, and the hit map can be seen. The needle under investigation is further aligned to the electrode so that the hit map fills the screen centrally in the x and y plane, and via the z direction, fills the field of view. For beryllium samples this occurred around 3000V. The samples were then run in purely voltage mode. Early efforts showed significant artefacts present from preferential laser heating and preferential release resulting from it; when run in laser mode. As a result laser mode was discarded. Samples were run in voltage mode, with 200kHz pulses, a 20% pulse fraction, until either fracture or

the upper voltage limit of the detector, was reached. Crystalline samples from eroded regions could produce significant and repeatable runs of between 3 and 30 million ions. Deposited samples proved extremely difficult and unfortunately unreliable, resulting in difficulty repeating results.

The evaporation and field ionisation of the atom probe is a complex process. Early simplification assumed the ions left the surface by overcoming the surface energy barrier due to the evaporation field at the tip without intermediate ionisation steps. Later work suggested the ions could be field ionised during their TOF to the detector. The true mechanism of ion(s) leaving the surface and reaching the detector is still an area of ongoing research [115], and whilst there appear similarities between APT and TDS techniques, they are in fact significant differences in the evaporation process. TDS assumes that diffusive ions meet at the surface to recombine as molecular release, whether from two substrate surface atoms, or whether one atom is provided from vacuum impurity gasses (mainly hydrogen). During APT however, singular ion release can occur and does (for example Be^{+}). Care should therefore be taken when comparing these techniques. Likewise, it is difficult to make clear statements concerning the true mechanism of ions detected in the APT due to field evaporation, and whether those exact ions existed in the surface in an equilibrium state prior to evaporation. Careful consideration of the peaks associated to hydrogen ions is similarly required in the atom probe during analysis.

All atom probe results were analysed in the Cameca LEAP 5000 IVAS software and underwent a series of steps that will now be described. All steps described, occurred with un-sampled data, this is particularly important when trying to see lattice parameters in the reconstruction. The first step assesses the voltage history and removes counts both associated with initial tip positioning and reshaping due to fracture at the end of a run (shown as a significant dip in voltage). The background history is checked and saved for future use. The second step reduces the field of view to so that no xy region without counts is associated on the detector. The third step utilises a time of flight correction consisting of a bowl correction alongside a time of flight voltage correction. The TOF empirical fit relates the mass to charge ratio (m/q) to the time of flight.

$$m/n = \frac{2eVt^2}{d^2} \tag{3.1}$$

$$t = \frac{d\sqrt{m/n}}{\sqrt{2eV}} \tag{3.2}$$

A semi-empirical fit for t is then used to correct for tip dulling and the resulting voltage increase to achieve the same evaporation rate.

$$t = \frac{a_0}{\sqrt{a_1 + V_{DC} + a_2 V_{DC}^2}} \tag{3.3}$$

The result produces peaks that are much sharper with significantly reduced tailings at the higher mass to charge side. Whilst this correction is good, it is not perfect and tailings in these experiments remain greatest around the beryllium peaks. The second fit is a bowl correction which remedies the flight path that hits the outer rings of the detector to the centre of the detector for a given m/n and voltage. This equates essentially differences in trajectory of ions released at the same time. The fitting is an average of the flight time projected onto a polynomial function of position.

The fourth step of data analysis is mass calibration. Here all the peaks of unsampled data, that the software associated as peaks were defined. If, for example, complex ions such as BeH^+ were found, they were manually input as 11. Unfortunately, this process is less reliable to lighter elements, and the most effective for higher mass to charge ranges. Therefore some inherent error will be present and unavoidable when investigating beryllium, whose significant peaks are m/q 4.5 and 9; alongside implanted hydrogen and deuterium at 1 and 2 m/q respectively.

The fifth step, formally ranges all ions including complex ions by name. This step is manual and undertaken at the users discretion. However, without all ions ranged the volume calculated by the ranging is inaccurate. For this reason every attempt was made to range and associate all m/q peaks.

The final step prior to reconstruction is to estimate the tip radius and shaft angle. This can be done several ways, with varying degrees of accuracy and success. The method chosen here, particularly for crystalline eroded regions was to observe the lattice parameter in conjunction to assessing whether the tip radius seemed reasonable. SEM images of the needles were taken prior to run in the FIB. A measurement of their "as prepared" tip radius was taken. It should be noted that the tip radius will always be greater than this measurement on commencement of the experiment due to the positioning steps necessary at the start of the experiment to align the needle to the electrode. Therefore any settings that produced tip radii, which were less than the measured starting radius were discarded and approached again. Fortunately many of the eroded regions displayed a C zone axis along the center of the needle and could therefore be measured more precisely. These settings were assessed in the IVAS expert module. The Image Compression Factor (ICF) was set between 0.55-0.7

for all needles. The X and Y centres adjusted such that the atomic planes were perpendicular to the evaporation direction. Finally the initial tip radius was adjusted and the typical lattice parameter spacing for the C-axis assessed. This method will have some degree of uncertainty, however all samples were treated the same way, and therefore a consistent and systematic approach was applied.

Finally the experiment was reconstructed and its total volume and statistics recorded. Further processing occurred to assess any clustering present. Initially isosurfaces were used as a visual aid to assess the likelihood of ion species clustering. If present at greater than 2% enrichment, the isosurface was processed and a proxigram created showing the ion species percentage concentration into all isosurfaces of such concentration averaged across the sample. A further method was then employed with more mathematical rigour. Solute analysis was performed consisting of several steps. At each step the result was compared to a randomised version of the data so that a null hypothesis could be created. If no variation was seen between the randomised data set and the same ordered experimental data, no clustering was considered present. The steps of solute analysis are: a nearest neighbour analysis, cluster size distribution analysis, cluster count distribution analysis, and finally cluster solute analysis. All of the parameters required in the solute analysis: d_{max} pair, N_{min} (the minimum number of ions in the cluster), L and d_{ero} are all found via the steps of the solute analysis, and occur at the point where randomised data intersects with the real data. In this way, the approach is consistent across all sample data sets.

3.2.6 Thermal Desorption Spectroscopy

The Thermal Desorption Spectroscopy (TDS) system was manufactured by Hidden Analytical Ltd (TPD Workstation type 640100) [116]. The system can be described in two sections, including the load lock system and the main vacuum chamber, where analysis occurs. Nitrogen gas is used as a purge gas in the load lock system between sample exchanges. Thermal Desorption Spectroscopy (TDS) is a macroscopic technique which occurs on samples of approximately $1cm^2$ and 2.5mm thick. All samples were treated the same way during the experiment.

A background measurement of the main chamber was taken prior to all runs. The background measurement is taken when the vacuum is below 5.0 x 10^{-9} torr in the main chamber. The sample stage is positioned approximately 10mm below the pins of the mass quadrupole spectrometer and heated at a standard ramp of 10K/min until 1050K and held here for 1hr. The stage then cools down via an integrated water

cooled system at approximate 10K/min. This data is saved for the four runs of the eroded and deposited regions which then occurred.

The sample is then placed in the load lock atop a aluminium nitride (AlN) interlayer of approximately 1cm^2 by 2.5mm to avoid sample adherence to the heated stage post experiment. Samples are pumped down in the load lock with two sequential pumps, an Edwards XDS dry pump and a turbo pump to achieve 5.0×10^{-6} mbar pressures. The load lock gate is then opened to the main chamber for 5mins. This is to enable any loosely adsorbed atmospheric hydrogen to desorp from the surface prior to the run. The gate to the main chamber is then closed and a preheat in the main chamber occurs. This preheat is similar to the background taken. The stage is heated at 10K/min until 1050K and then cooled at the same rate. This data is saved to assess the background hydrogen associated to the sample and inside of the main chamber.

The load lock gate is then opened. The sample and AlN interlayer (to avoid sample adhesion to the heated stage), is then moved via the load lock arm into the main chamber and positioned above the molybdenum stage. The stage is moved up flush into the center and hollow of the load lock arm. A manipulator needle on the opposite side of the main chamber pushes the sample and AlN layer centrally onto the stage. Once positioned centrally the stage is lowered and both the load lock arm and manipulator arm retracted. The stage is then repositioned and moved up so that the sample is held down by pins orientated from the Quadrupole Mass Spectrometer (QMS) above. A second set of turbo-pumps and Edwards XDS dry pumps separately enable the Ultra High Vacuum (UHV) conditions in the main chamber, achieving pressures of approximately 1.0×10^{-9} mbar. The heated Molybdenum stage has both an integral water cooled shroud to enable careful management of cooling rates at the end of a run, and a built in resistive heater and thermocouple. A second thermocouple is in direct contact with the sample. Each sample is then individually heated to 1070K at a ramp of 10K/min and held at maximum temperature for 1 hour. The sample is then cooled slowly by the integrated stage and once cooled removed using the same steps in reverse.

The masses of gas species released from the sample on heating during a run, are analysed in direct line of sight by the Hiden Analytical HAL/3F RC 1051-9 PIC mass spectrometer with Burle 4871H channeltron electron multiplier. The position of the mass spectrometer to the sample, maximises the efficiency of desorbed species detection. Background signal is monitored via the triple-filtered QMS system. For the purposes of later modelling the sample's thermocouple measurement was taken to be

the surface temperature. Calibration of the deuterium, hydrogen and HD masses were performed via three calibrated leak tests and a factor extracted enabling conversion of counts to atoms.cm^{-2}. A calibration was then obtained. This calibration is carried out every 10-12 months due to changes in the TDS system overtime, such as the PIC voltage in the QMS system.

Chapter 4

Microstructural analysis of eroded JET materials

4.1 An introduction to eroded materials in JET

This chapter explores microstructures seen at eroded limiter tiles in JET. The positions of the two tiles from which the eroded regions originate are the inner and outer midplane tiles, 2XR10 and 4D14, respectively (figure 1.2, chapter 1). The central eroded castellations analysed in this chapter are presented in figure 1.3. Eroded regions sit furthest into the plasma, receiving the highest levels of material removal. All Density Functional Theory modelling in this chapter and subsequent chapters 5 & 6, enabling comparison between experimental JET EELS results and theoretical EELS core losses of relevant Be compounds, were kindly provided by, and the sole work of, Xinlei Liu (University of Oxford). Xinlei, thank you for all your work.

The chapter starts analysis at the macroscopic with increasingly incremental steps towards sub-microscopic length scales. Figure 4.1 shows the sampling locations where experiments took place. Experiments were repeated for statistical relevance.

Scanning Electron Microscopy (SEM) and Focused Ion Beam milling techniques, present observations of surface morphology. Transmission Electron Microscopy (TEM) alongside Electron Energy Loss Spectroscopy (EELS) primarily analysed samples' oxidation. DFT modelling of theoretical Be-O-H systems producing predictive EELS curves; were compared to experimental EELS results, to enable comment on the presence of hydrogen isotopes in the samples. Atom Probe Tomography (APT) determined the spatial distribution of hydrogen isotopes within the sample at the smallest length scales. The chapter concludes by comparing hydrogen isotopic ratios measured between APT and Thermal Desorption Spectroscopy (TDS). All comparisons made

in this chapter occur between the two eroded JET positions and the non-exposed beryllium (NE-Be) sample.

The microscopy work presented, is novel to this field.

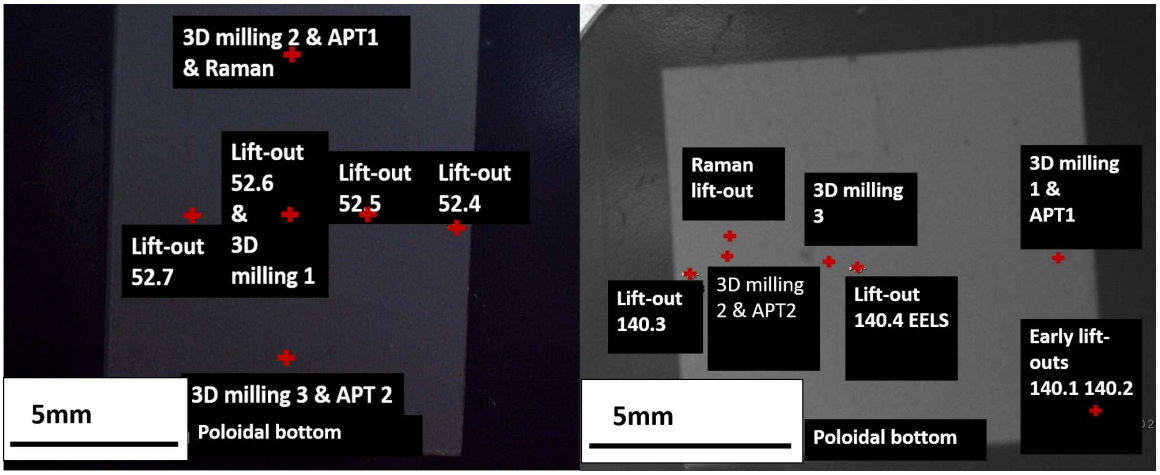


Figure 4.1: Left: Navcam image (optical) from the FIB: showing a schematic of the sampling locations for the inner eroded wall castellation. Right: Navcam image (optical) from the FIB: showing a schematic of the sampling locations for the outer eroded wall castellation. (The abbreviation 'APT' stands for Atom Probe Tomography samples.)

4.2 Scanning Electron Microscopy of eroded JET surfaces

This section compares the typical surface finishes seen after JET plasma exposure at inner and outer wall eroded zones, to a NE-Be sample manufactured to JET specifications. These images are a subset of many. Figure 4.2 shows the NE-Be sample. The surface has micron level roughness and uniform variance in surface features. Figure 4.3 of the inner wall eroded surface, shows sharper angular features (described elsewhere as 'fillaments' [15], figure 2.16); relative to the NE-Be sample. Figure 4.4 shows the outer wall eroded surface. Similar features are present between inner and outer wall exposed samples, however some reduction in filamentary feature size could be argued at the outer eroded sample.

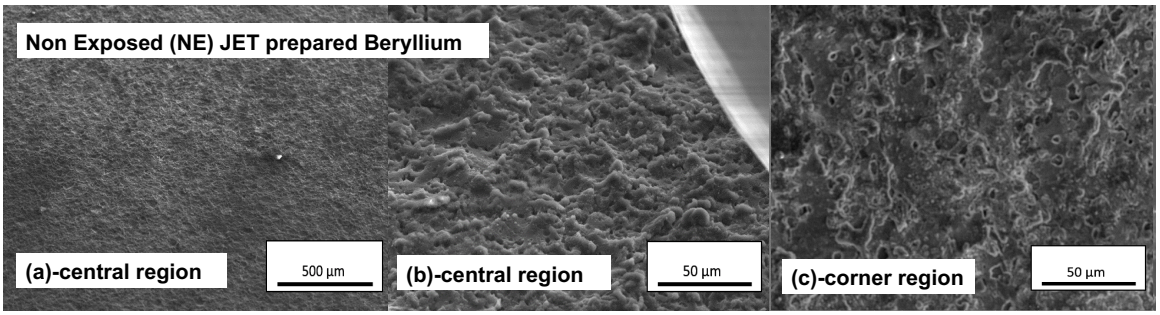


Figure 4.2: Overview surface Scanning Electron Microscope (SEM) secondary electron images of a NE-Be sample: (a) central location at low magnification; (b-c) central and corner location at high magnification.

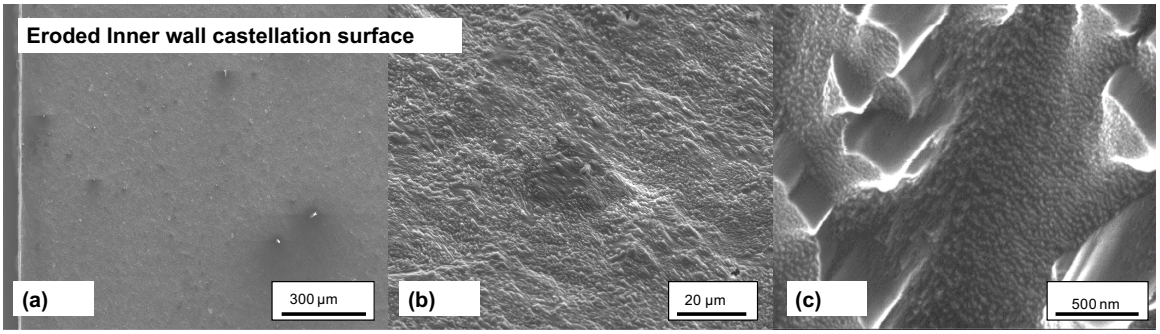


Figure 4.3: Overview Scanning Electron Microscope (SEM) Secondary Electron (SE) images of the surface of the inner eroded limiter castellation at increasing magnification.

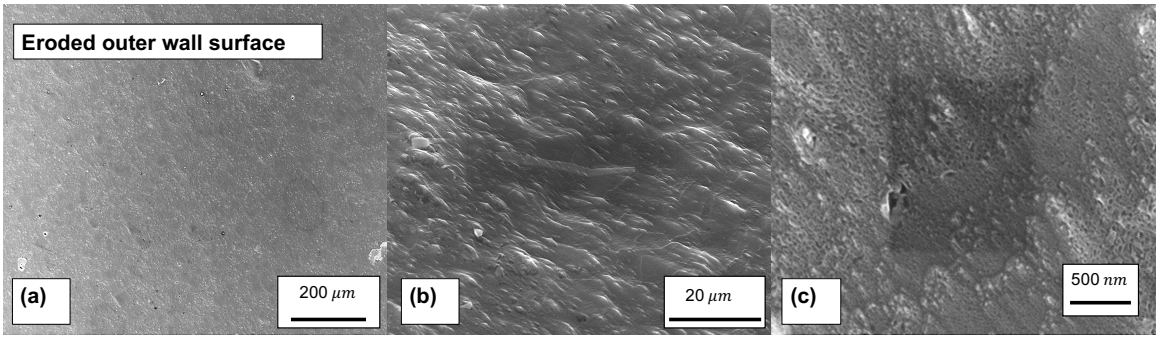


Figure 4.4: Overview Scanning Electron Microscope (SEM) Secondary Electron (SE) images of the surface of the outer eroded limiter castellation at increasing magnification.

4.2.1 Energy Dispersive X-Ray and 3D milling of eroded cross sections in JET produced via Focused Ion Beam (FIB) milling

Following surface morphology results; regions were sampled across the toroidal direction of the NE-Be, inner eroded, and outer eroded samples; to investigate the subsurface microstructure. The eroded exposed sampling regions are shown in figure 4.1.

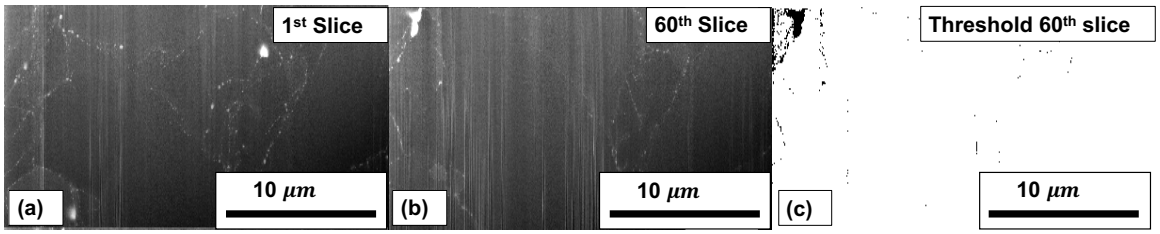


Figure 4.5: (a) & (b): The first and 60th slice, SEM secondary electron images of the NE-Be produced from FIB 3D milling at the centre of the castellation. (c): The thresholded 60th slice produced via FIJI, showing particles decorating grain boundaries.

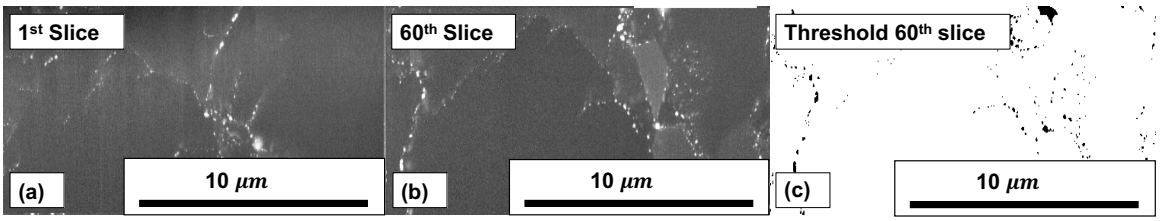


Figure 4.6: (a) & (b): The first and 60th slice, SEM secondary electron images of the inner wall eroded sample, produced from FIB 3D milling at the centre of the castellation. (c): The thresholded 60th slice produced via FIJI, showing particles decorating grain boundaries.

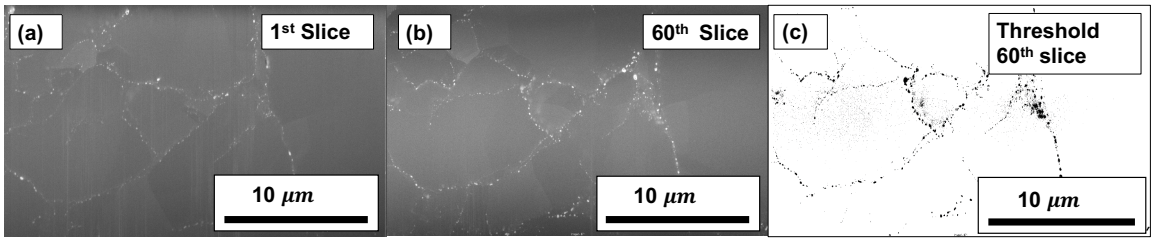


Figure 4.7: (a) & (b): The first and 60th slice, SEM secondary electron images of the outer wall eroded sample, produced from FIB 3D milling at the centre of the castellation. (c): The thresholded 60th slice produced via FIJI, showing particles decorating grain boundaries.

The results of 3D-milling studies (from central regions) on: NE-Be, and, eroded inner and outer walls; are displayed in figures 4.5-4.7. Many images were generated (see appendix A). The 1^{st} and 60^{th} slice are printed for each sample, alongside the thresholded output of the 60^{th} slice (black and white).

For each sample, there is little discernible difference between the 1^{st} slice and 60^{th} slice. These results are representative of the other locations, whereabouts 3D serial milling took place across the samples' surfaces; suggesting that random sampling satisfactorily represents the whole. This result validated subsequent use of randomised sampling for TEM analysis. Figures 4.5, 4.6 and 4.7; show grain boundaries decorated with precipitates. The (c) of each figure is the thresholded image result, from which, precipitate statistical analysis occurred.

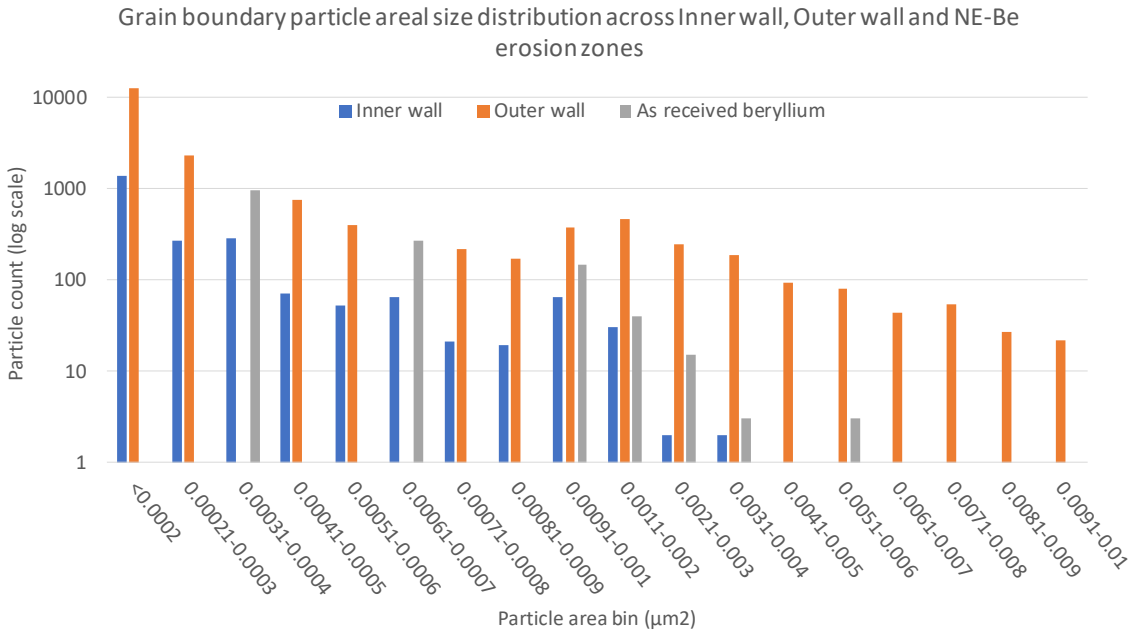


Figure 4.8: A logarithmic frequency distribution. Particle areas have been binned into size distributions. The results compare the inner and outer eroded sample with the NE-Be sample.

Figure 4.8 shows frequency distributions of precipitates, binned by area; between the outer and inner eroded zones, and the NE-Be sample. The outer wall eroded zone has a higher number of precipitates present generally. The outer wall also has a more continuous distribution to higher particle areas, suggesting some precipitate growth. The inner wall eroded zone has fewer large precipitates relative to the outer wall, but a greater number and wider distribution relative to the NE-Be sample. The NE-Be sample has the smallest and least continuous distribution of particles.

The percentage area of precipitates were: 0.05 +/- 0.09% present at the inner wall, 0.43 +/-0.02% at the outer wall and 0.03 +/-0.2 % for the NE-Be. Both the number of particles and their percentage contribution to the total area measured (across slices), remain small. Nevertheless, these values remain within similar orders of magnitude to the error. Qualitatively the outer wall appears to have a greater number of precipitates.

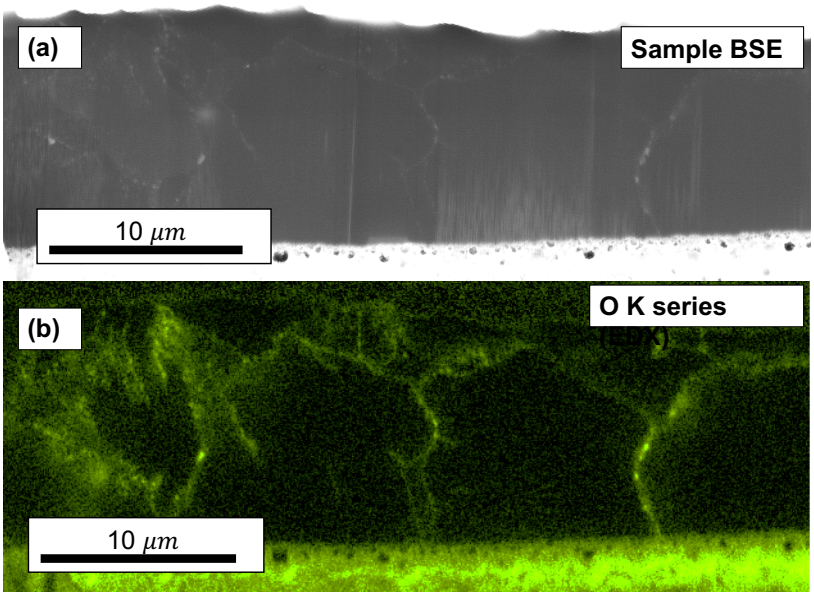


Figure 4.9: Scanning Electron Microscope, Secondary Electron image of the inner wall eroded depth profile, and corresponding Energy Dispersive X-Ray map of the Oxygen K-series.

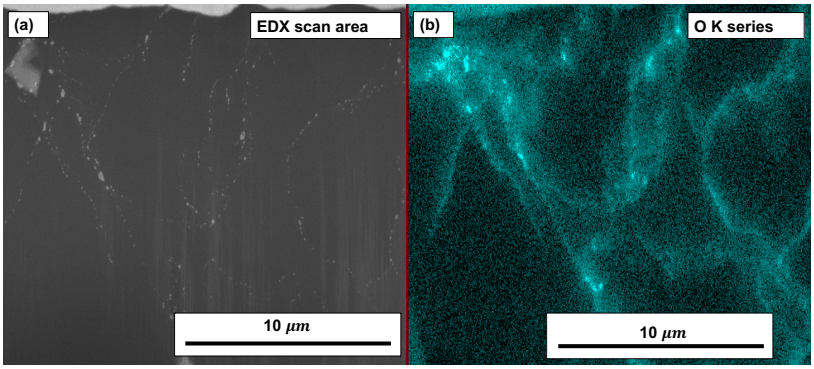


Figure 4.10: Scanning Electron Microscope, Secondary Electron Image of the outer wall eroded depth profile and corresponding Energy Dispersive X-Ray map of the Oxygen K-series.

Post 3D serial milling, a lift-out was produced of the inner and outer wall eroded zones; and Energy Dispersive X-Ray (EDX) undertaken on the exposed face, to anal-

yse precipitates' composition. Figures 4.9 and 4.10 show precipitates largely formed from oxidation at, or around the grain boundary. An occasional larger aluminium silicon iron beryllide was present and is reported in the literature as a grade and powder methodology contaminant [117]. Grain boundary oxidation is also reported from the powder consolidation process.

The EDX results at this length scale cannot distinguish compositional differences between outer and inner wall positions, and cannot measure stoichiometry between Be and O, due to Be windows remaining the preferred component in EDX analysis systems. Higher resolution techniques were therefore used to further explore oxidation in JET materials.

4.3 Transmission Electron Microscopy of eroded materials with application of Electron Energy Loss Spectroscopy (EELS)

Lift-outs prepared for Electron Energy Loss Spectroscopy (EELS) will now be discussed, comparing the inner and outer wall eroded regions to those signals from the NE-Be sample. EELS will investigate the effect of oxidation in these samples. Energy Dispersive X-Ray (EDX) collected in-situ, investigated any other higher atomic number components present, which could alter Be:O stoichiometries.

The lift-outs presented of the inner and outer wall eroded zone, occur from the centre of the castellation, close to the presented 3D milling studies. The NE-Be lift-out was produced from a random location roughly 0.25mm in from a corner in both directions. The central location failed in transit between the FIB and TEM.

All three lift-outs in figures 4.11-4.13, are indiscriminate from each other on inspection. All have large crystalline Be grains, whose grain boundaries are decorated with oxides. Any marker layer produced prior to JET exposure has been removed fully. The NE-Be sample was not produced with a marker coating.

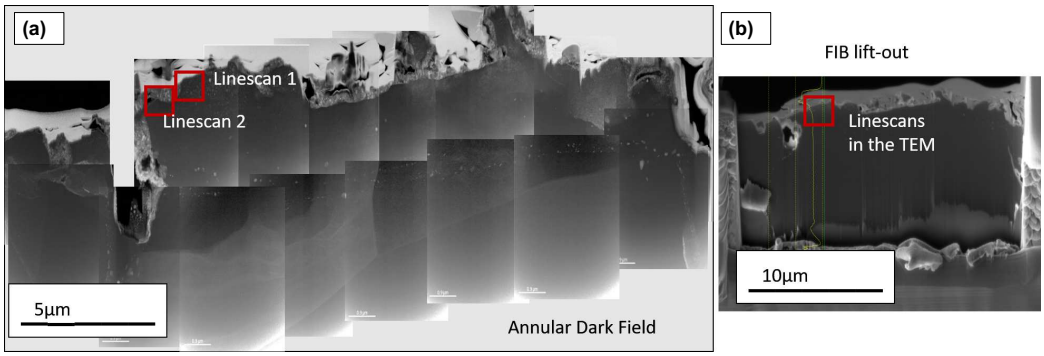


Figure 4.11: (a): High Angle Annular Dark Field (HAADF) STEM images montaged, showing Z contrast of the NE-Be sample. (b): The corresponding FIB image prior to electron transparency.

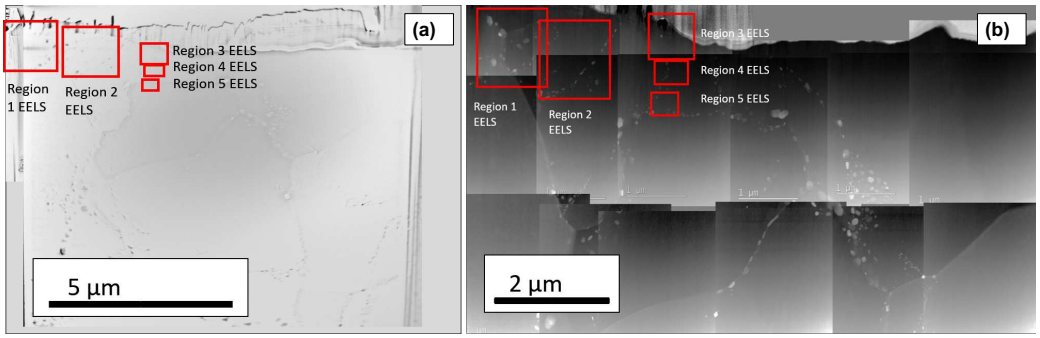


Figure 4.12: The inner wall eroded TEM lamella. (a): Lower magnification Bright Field STEM overview image. (b): STEM High Angle Annular Dark Field (HAADF) images montaged at higher magnification showing the Z contrast.

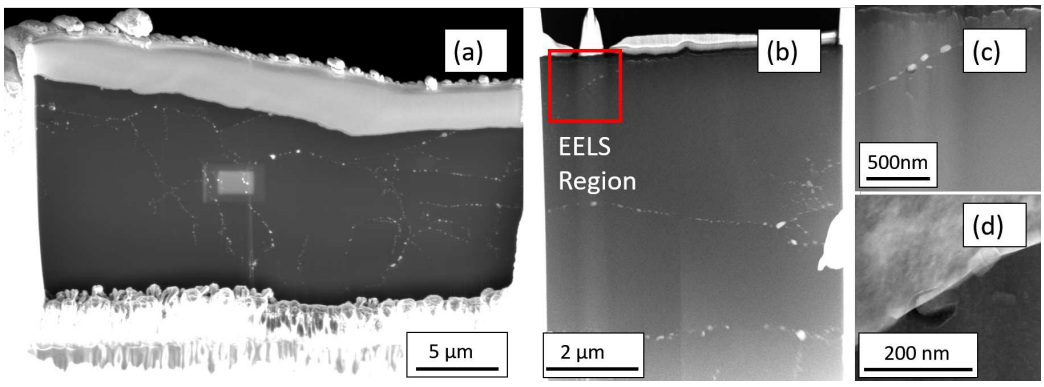


Figure 4.13: The outer wall eroded TEM lamella; (a) FIB lift-out prior to electron transparency (white square from SEM C contamination, subsequently removed), (b) STEM HAADF Z contrast image. (c) Higher magnification HAADF of the EELS area, (d) Annular Dark Field STEM image of EELS area, showing diffraction contrast.

4.3.1 STEM with EELS and EDX of non-exposed beryllium

Figures 4.14- 4.17, show EELS results for the NE-Be sample. This material has not been exposed to plasma wall interactions or hydrogen of any kind. It was prepared in the same way as all JET beryllium. These EELS results were used as a benchmark against exposed Be results.

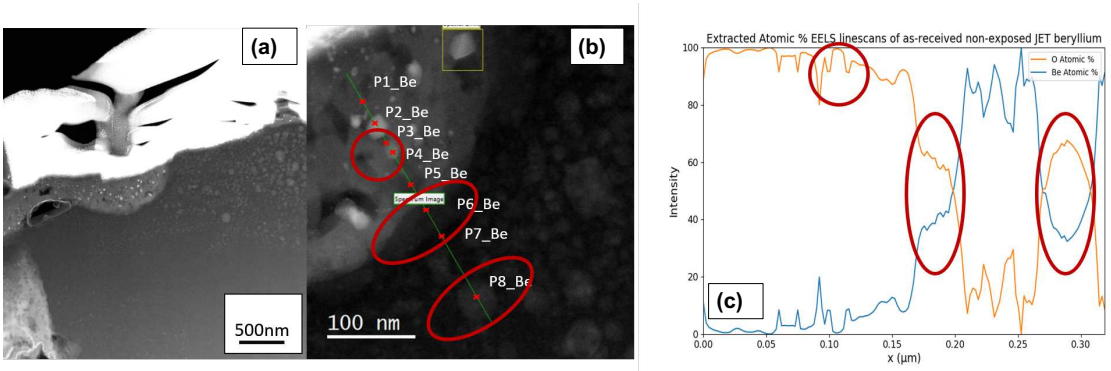


Figure 4.14: Figure displaying the as-received beryllium material; (a): STEM HAADF image overview of regions of interest. (b): STEM HAADF EELS linescan. (c): Atomic % beryllium and oxygen along the linescan via curve fitting.

Figure 4.14 shows an overview of the area under examination. Several similar regions were profiled. All exposed samples were eroded down to the original surface Be S65-H, due to plasma interaction. As a result, NE-Be surfaces were prioritised for analysis. It was argued that this surface, was most like the resulting exposed microstructure without hydrogen interaction. Figure 4.14(c) presents beryllium-oxygen stoichiometries into depth along the line scan. In the first 150nm oxygen (orange) appears exceptionally high ∼90-100 at%, implying a missing component from the ratio calculation. EDX was applied to the same region to identify if further components were present (figure 4.15).

Figure 4.15(b) shows the EDX signals corresponding to the two integrated regions (in figure 4.15a). The region with higher oxygen (measured via EELS and EDX) has one further component present above the baseline, Cu. It is suggested this is the cause of the unrealistic oxygen stoichiometry calculated, and a residue of the surface preparation method discussed in the literature review, from EDM cutting [43].

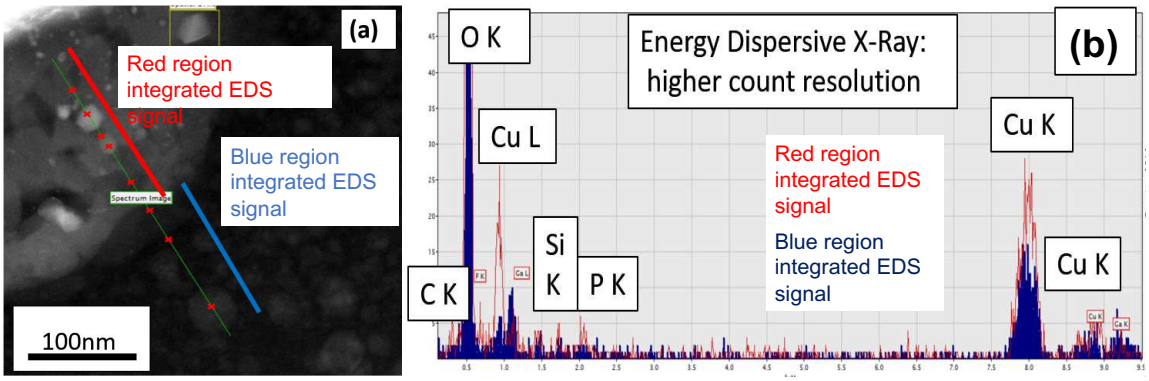


Figure 4.15: (a): Following EELS results, two integrated areas were analysed by EDX along the linescan, those with higher oxygen levels - concern the red region, those with lower oxygen levels, the blue region. (b): The EDX spectra of the two regions.

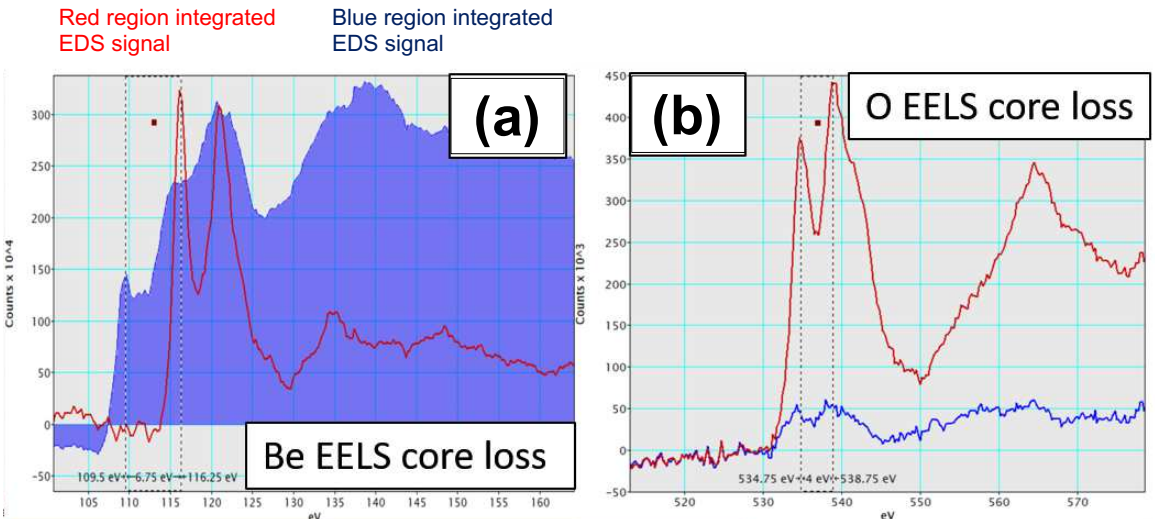


Figure 4.16: Extracted EELS curves of the same integrated areas displayed in figure 4.15(a). (a): The Be core loss for the red and blue regions. (b): The O core loss for the red and blue regions.

Background subtracted EELS data of the Be and O core losses are provided of the same region in figure 4.16. The red integrated region clearly displays a large oxygen signal in (b) as expected, however most notable is the shift to higher energies in the Be core loss onset energy in (a).

Point ($P8_Be$) from figure 4.14b, a lighter precipitate in the dark matrix, does show ~1:1 Be:O ratios approaching the wurtzite structure, and therefore is likely a good reference for future oxide precipitates found in exposed samples.

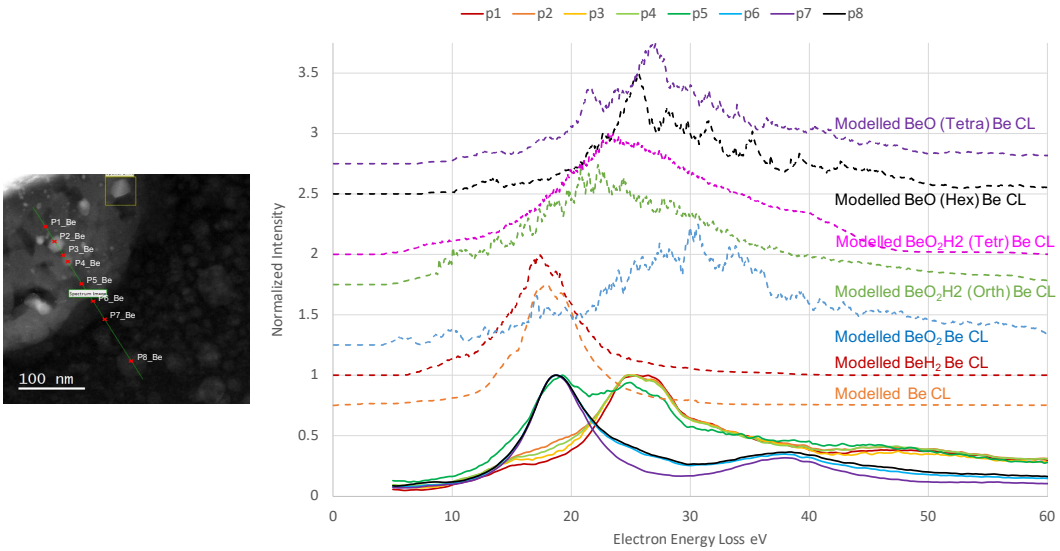


Figure 4.17: Left: STEM HAADF image of the as-received beryllium material, with sampled positions marked along a linescan. Right: Normalised low loss spectra of marked positions, with addition of DFT modelled EELS data (dotted lines).

Figure 4.17 shows extracted normalised low loss spectra of the NE-Be sample, alongside DFT modelled spectra of relevant Be-O-H structures for cross comparison to this, and future data. Low loss spectra, represent a region of signal where lattice vibrations (plasmons) produce spectra effected by their local bonding environment. A sealed hydrogen cell's edge occurs at ~13eV (EELS ATLAS). Despite a high degree of overlapping signals, the low loss region remains a potential area for interpretation of hydrogen presence in exposed samples.

Figure 4.17 shows the extent of copper presence in the sample's near surface region by changing plasmons. Points 1-5 (Cu presence) show distinctively different features. Points 6-8 refer closely to the modelled Be metal spectra. A small amount of oxidation in points 6 & 8 produce Be plasmon broadening, and is likely due to a small presence of hexagonal oxide. The NE-Be matrix without oxidation (point 7) shows a 18.75eV plasmon peak.

4.3.2 STEM with EELS and EDX of the JET Inner wall eroded beryllium sample

EELS results for the inner wall eroded zone are presented. The results present atomic percentage graphs of Be and O increasing into depth. Several similar regions were profiled. The results are representative of the many regions analysed.

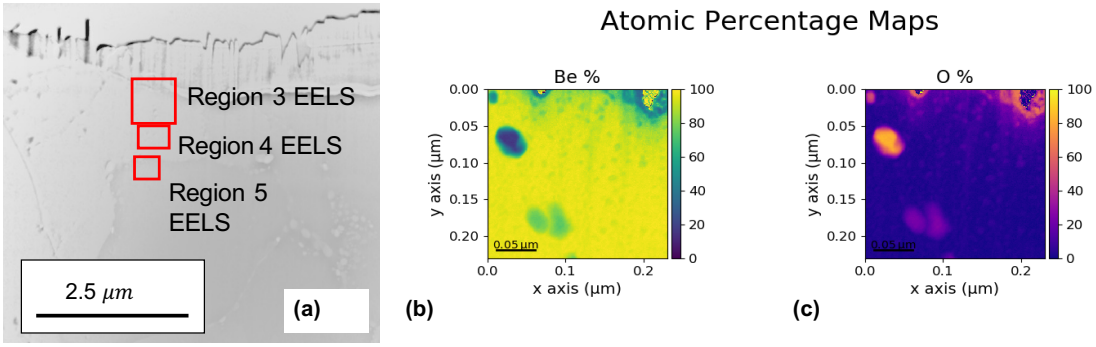


Figure 4.18: The inner wall eroded region. (a): STEM Annular ADF1 overview image, with regions of interest. (b): Be EELS at% map at region 3. (c): O EELS at% map at region 3.

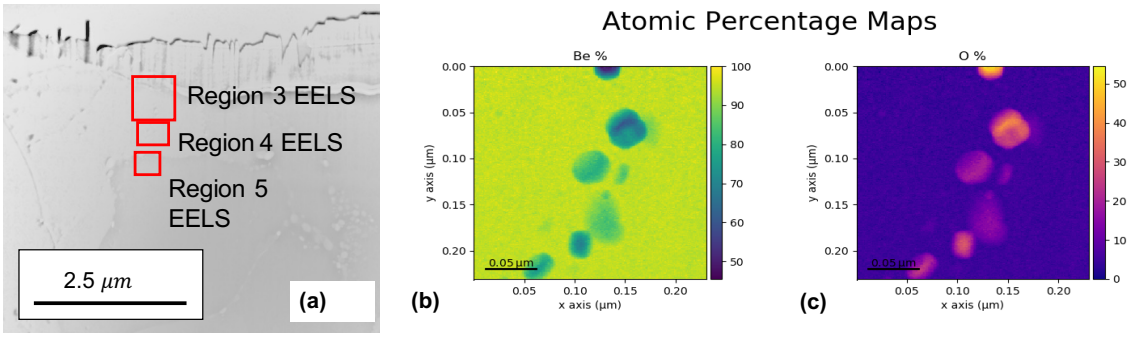


Figure 4.19: The inner wall eroded region. (a): STEM Annular ADF1 overview image with regions of interest. (b): Be EELS at% map at region 4. (c): O EELS at% map at region 4.

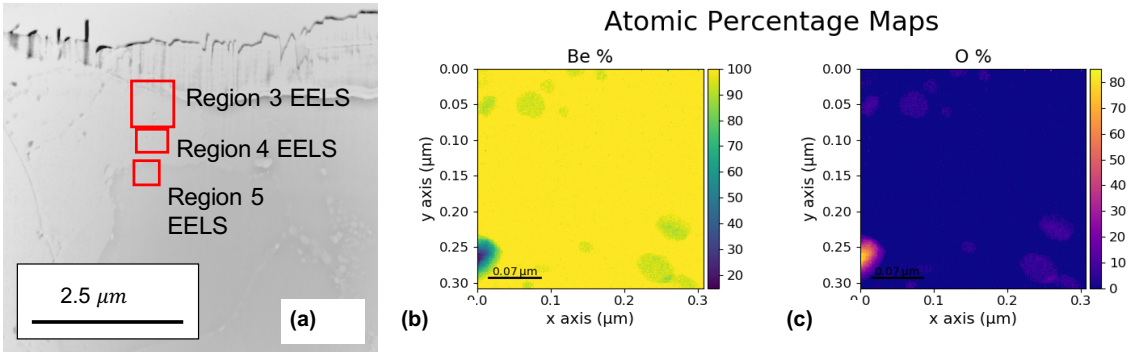


Figure 4.20: The inner wall eroded region. (a): STEM Annular ADF1 overview image with regions of interest. (b): Be EELS at% map at region 5. (c): O EELS at% map at region 5, furthest into depth.

Figure 4.18 presents the level of oxidation in the near surface region. These results are contrasted against figures 4.19 and 4.20 increasing into depth.

The atomic percentage map of region 3 at the surface of the lift-out displays one solitary oxide particle with particularly high levels of oxidation (∼80-100%) (left hand side of the maps). A problem with in-situ EDS acquisition meant Cu contamination (from EDM) cannot be ruled-out. All other particles shown display 40-60% oxidation, mirroring those seen in the NE-Be sample. The relative at% Be into depth increased, showing greater oxidation at the surface. No discernible differences can be seen between the surface (region 3) and the subsurface (region 4). These regions are likely to have both received some plasma interaction.

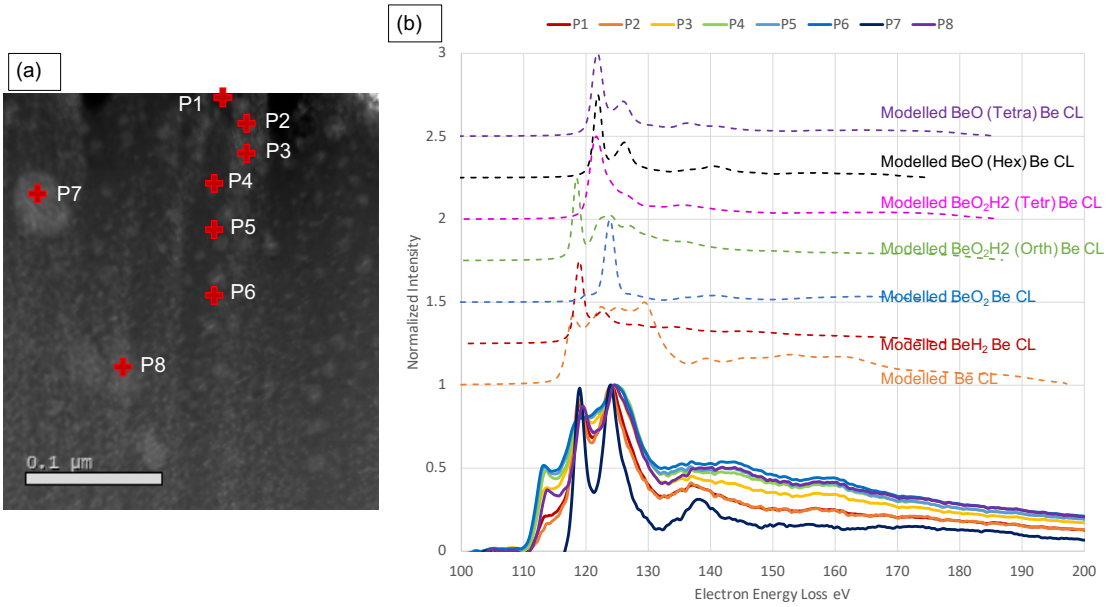


Figure 4.21: Figure displaying region 3 of the inner wall; (a) STEM HAADF image at the surface, and (b) Background subtracted normalised Be core loss point spectra, compared against the DFT modelled spectra.

Figure 4.21 shows extracted normalised Be core loss spectra from the surface compared to modelled Be-O-H DFT structures. Point 7 with high oxidation (∼80%), shows Be onset at higher energies. Unfortunately the DFT modelled spectra concerning Be and O core losses, are precise in fine structural shape, but not yet in position (modelling work remains ongoing). Nevertheless some mixing of oxides or hydroxides seems likely to form at point 7. Two extremes appear present in the beryllium core loss onset energy and fine structure. Those occurring with onset at ∼110eV, and those with onset at ∼118eV. It appears that spectra from points 1-2, can either be described as a linear combination of these two extremes, or have some level of Pt contamination at the surface. This suggests only one type of oxide is present from this data alone.

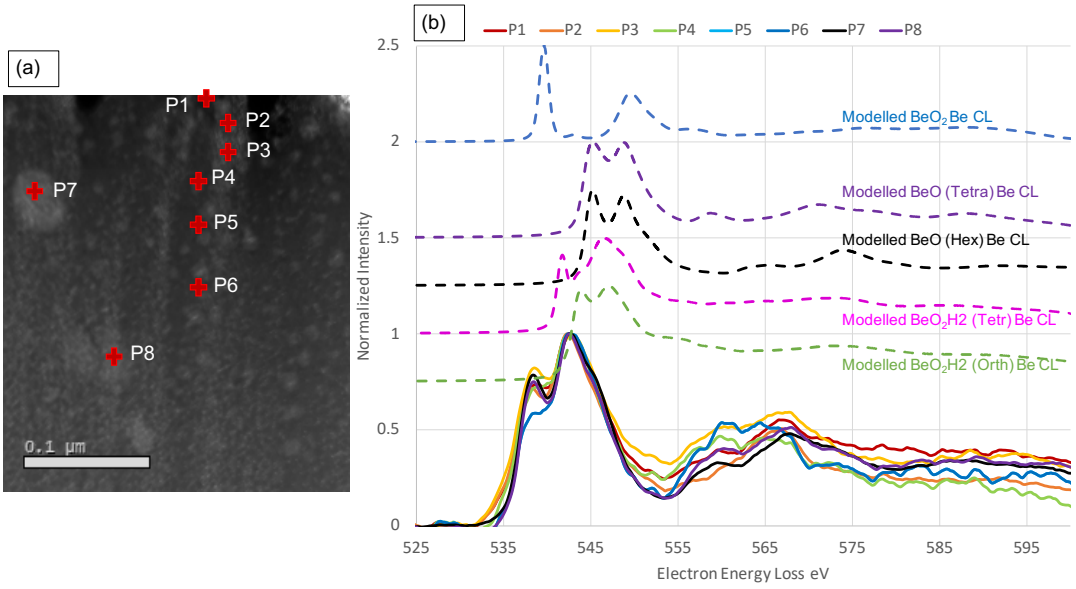


Figure 4.22: Figure displaying region 3 of the inner wall. (a): STEM HAADF image at the surface. (b): Background subtracted normalised O core loss point spectra, compared against the DFT modelled spectra.

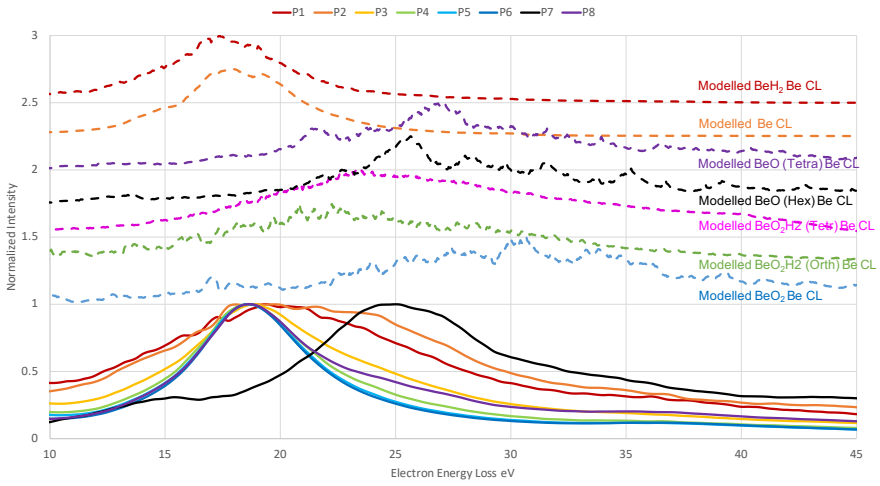


Figure 4.23: Figure displaying the corresponding low loss spectra relating to figures 4.21 & 4.22. Low loss point spectra are compared against the DFT modelled Be-O-H structures.

Figures 4.22 & 4.23, present the corresponding O and low loss spectra. The O loss shows all spectra save point 6, have similar fine structure; resembling modelled orthorhombic beryllium hydroxide. Point 6 appears more similar to the tetragonal hydroxide. The low loss comparison between spectra and the DFT models, remains accurate for both position and fine structure. The results suggest points 4-6 remain

lower in oxygen with some broadening. Points 1-2 are suggestive of BeD_2 as well as a tetragonal and/or orthorhombic hydroxide. Point 7 however, most closely resembles a hexagonal beryllium oxide. The higher value O at.% at point 7, therefore is explained as a variation in through thickness; where sequential layers of Be and BeO change relative to the sample's thickness and beam direction.

4.3.3 STEM with EELS and EDX of the JET Outer wall eroded beryllium sample

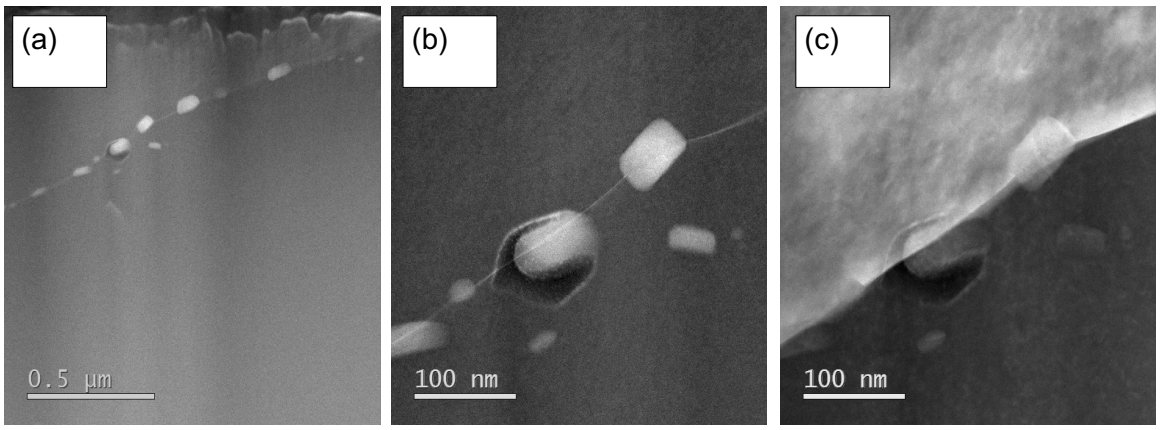


Figure 4.24: The outer wall eroded region. (a): STEM HAADF image of the region of interest. (b): STEM higher magnification HAADF image. (c): STEM ADF image showing diffraction contrast at the grain boundary.

EELS results for the outer wall eroded zone are now presented. Figure 4.24 shows a region of interest (along a grain boundary) presented across increasing magnification. Several similar regions were profiled. The results submitted are representative.

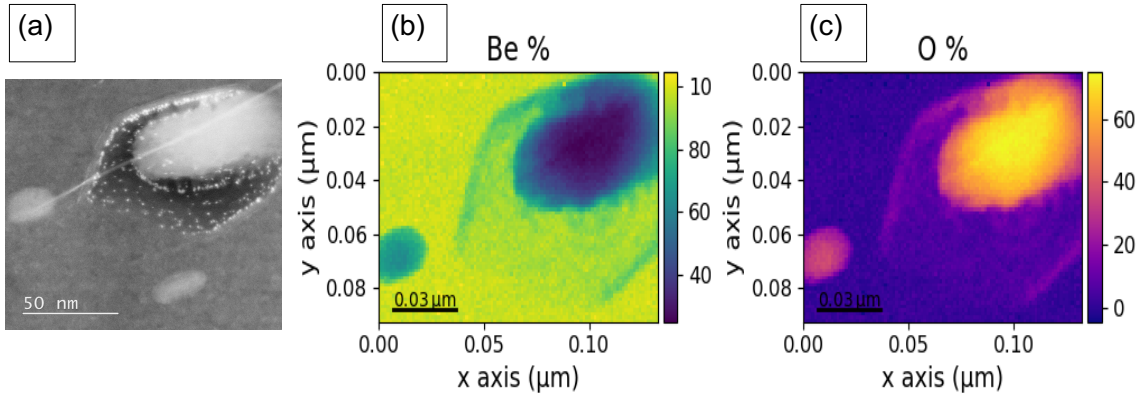


Figure 4.25: The outer wall eroded region. (a) STEM HAADF EELS area scan. (b): Be EELS atomic % map. (c): O EELS atomic % map.

Figure 4.25 presents the HAADF EELS scan image alongside, Be and O atomic % maps. The oxide map shows a particle of significantly greater oxidation (∼70-80%), and a smaller oxide particle (∼40-50%), likely wurtzite, approaching 1:1 stoichiometry. EDX was recorded during the EELS scan and used to account for any heavier element presence.

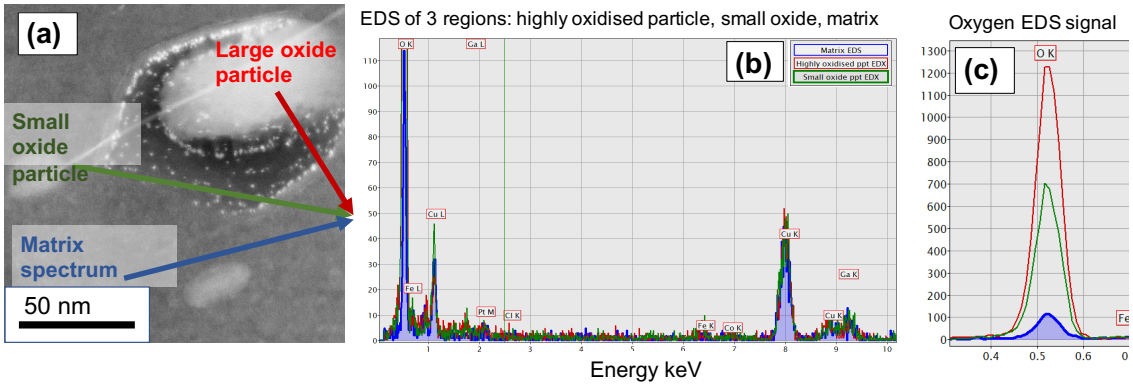


Figure 4.26: The outer wall eroded region. (a): STEM HAADF EELS area scan region. (b): EDS overview of the 3 equivalent count integrated regions: red - the large oxide, green - the small oxide, and blue - the matrix region. (c) the Oxygen EDS peak of the 3 regions.

Three regions of the same pixel count were integrated, and are compared across their EELS and EDS spectra. Figure 4.26 shows the results of the EDX integrated scans. The only observable difference in EDX signal, is that of the oxygen K peak intensity. The Cu L line is negligible (Figure 4.26(b)) in relation to the K line, suggesting here that the copper signal originates from the Omni-probe grid.

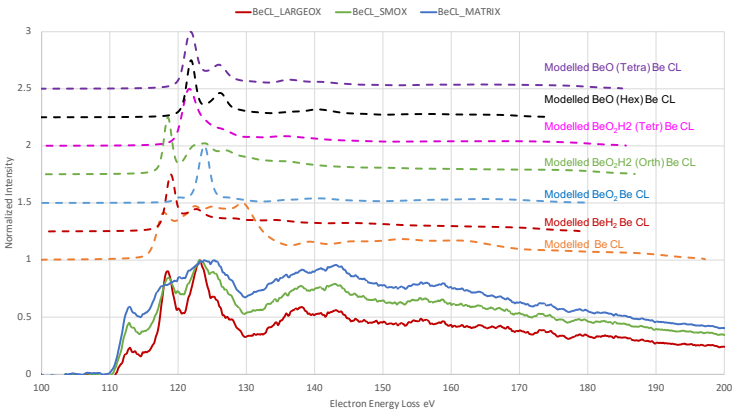


Figure 4.27: Figure displaying normalized Be core loss spectra of the three averaged regions discussed in figure 4.26(a), compared to DFT EELS models of Be-O-H systems.

Figure 4.27 displays the Be core loss comparison of the three averaged areas to the modelled data. The small oxide appears a linear combination of the Be loss from the matrix and large oxide. Figure 4.28 displaying the oxygen core loss, with comparison to the modelled spectra, appear closest to orthorhombic or tetragonal beryllium hydroxides. The oxygen signal from the matrix contained only noise, and was not included.

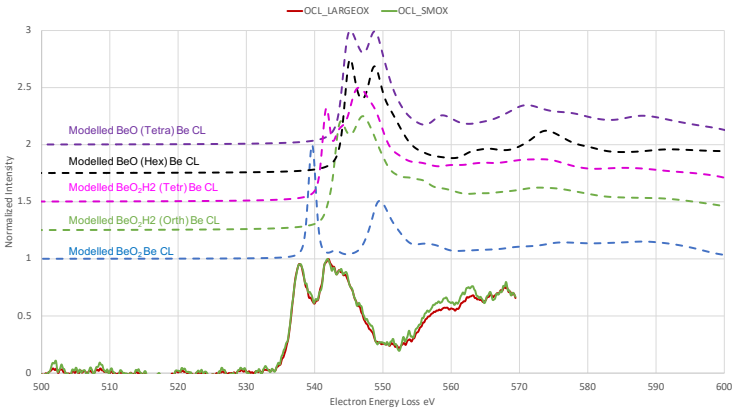


Figure 4.28: Figure displaying normalized O core loss spectra of the three averaged regions discussed in figure 4.26, compared to DFT EELS models of Be-O-H systems.

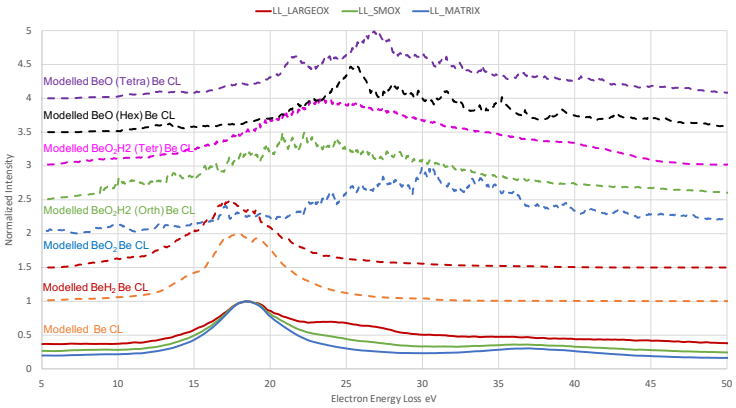


Figure 4.29: Figure displaying normalized low loss spectra of the three averaged regions discussed in figure 4.26, compared to DFT EELS models of Be-O-H systems.

The low loss spectra (figure 4.29), give the most accurate comparison. The matrix appears largely Be and BeD_2, whilst the small oxide shows some broadening indicative of orthorhombic hydroxide presence. The large oxide, however, displays further peak broadening in the range ~23-30eV. It is suggested that this is due hexagonal and tetrahedral BeO presence additionally. Once more from EDX and EELS spectra in

figures 4.26-4.29, there is little evidence of an oxide which cannot be explained by a linear combination of Be and BeO ratios; where stacked layers of oxide and Be grains exist through the thickness of the sample (through thickness variations) perpendicular to the beam.

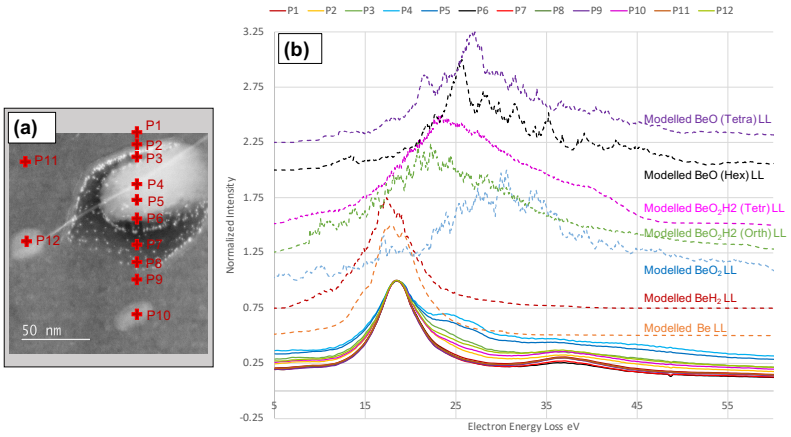


Figure 4.30: The outer wall eroded region. (a): STEM HAADF EELS area scan with extracted points. (b): low loss spectra and DFT model comparison.

Figure 4.30 shows a final example of low loss point spectra throughout the area scan. Throughout there is evidence of BeD_2 alongside orthorhombic hydroxide presence. However in the region of the large oxide there appears to be an added component of hexagonal BeO.

Finally, the observed grain boundary in the HAADF image, led to integrated EDX of the interface showing increased levels of Fe, Si, and O at the grain boundary; in line with expectations from the powder processing route. However, the grain boundary may have enhanced oxidation. Residual Ga from the FIB process created the speckles of atomic contrast in the HAADF image around the large oxide. These features suggest the opening of a cavity from the FIB milling process. The result may be the remnants of an oxide surrounded by a cavity filled with isotopic hydrogen.

4.4 Atom Probe tomography findings from eroded materials in JET

Atom Probe Tomography (APT) was applied to the JET samples for the first time, and compared to the Ne-Be sample; to investigate the spatial orientation of deuterium (and tritium). APT measurements enabled inspection of nanometric length scales and highlighted whether clustering was occurring. These results are the first of their kind.

Atom probe lift-outs, each producing 6-10 separate APT needles, were run from locations along the surface of all samples (with a minimum 3-5mm between successive runs) for statistical relevance. The results discussed below are a selection of larger data sets.

Mass spectra results (from whole needles) enabled bulk composition analysis to compare retention. The average decomposed atomic % of beryllium were: 99.905% at the inner wall, 99.228% at the outer wall, and 99.326% for the NE-Be. A comparison of both the average impurities seen in these materials and the summed hydrogen content are given in figure 4.31.

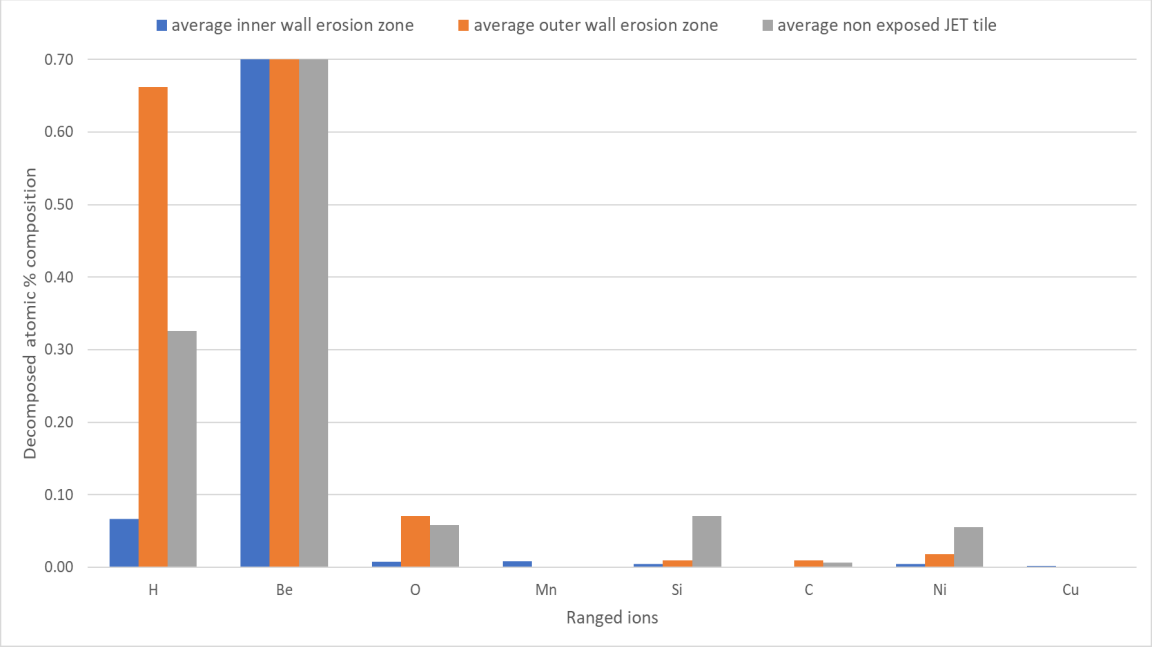


Figure 4.31: Comparison of decomposed ion ranges in atomic % across JET erosion regions

On average the outer wall erosion zone shows a 90% increase in retained isotopic hydrogen compared to the inner wall, and a 50% increase above the non-exposed Be reference sample. The outer wall retains twice as much hydrogen in isotopic form, compared to a randomised NE-Be background, which cannot be accounted for by vacuum hydrogen contamination alone. The outer wall also contains significantly more hydrogen than the inner wall eroded material. Further information is gained from decomposition of hydrogen into its relative H(1Da):D(2Da):T(3Da) ratio.

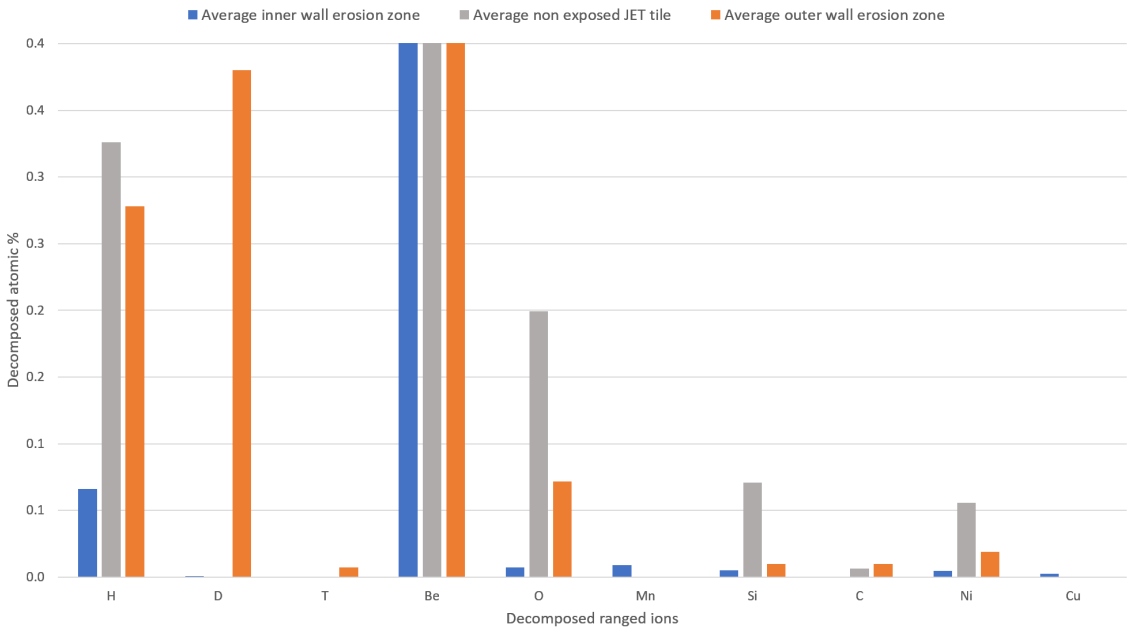


Figure 4.32: Comparison of decomposed ion ranges in atomic % across JET erosion regions: showing H isoptopic changes between samples

The decomposed at.% H, from peaks: 1Da corresponding to H, and its constituent molecular ions (10Da BeH, 17Da OH, 18Da H2O, 13Da BeH4, 26Da BeOH) are compared to the same decomposed peaks accounting for total D, and T separately, in figure 4.32.

Given the limitations of the technique: tailing peaks via TOF measurement, ion detection deficiency (40%), bowl assumptions, and evaporation under uniform fields; it is difficult to completely rule out hydrogen from vacuum contaminants against H originating from JET plasma H exposure. However, figure 4.32 presents a clear distinction in H isotopic contents; between outer and inner wall positions, compared against the NE-Be. The H (1Da) peak, (likely vacuum contamination) is similar in both the NE-Be and outer wall Be.

The 2Da peak (D related), clearly presents deviation from vacuum contamination. There are clear signs of plasma exposure at the outer wall, against no 2Da peak presence in the NE-Be. 0.001 at.% D is accounted for at the inner wall, whilst 0.380 at.% D resides at the outer wall. A reduced global retention at the inner wall is put forward. The spatial orientation of D and BeD can now provide further insight from reconstruction.

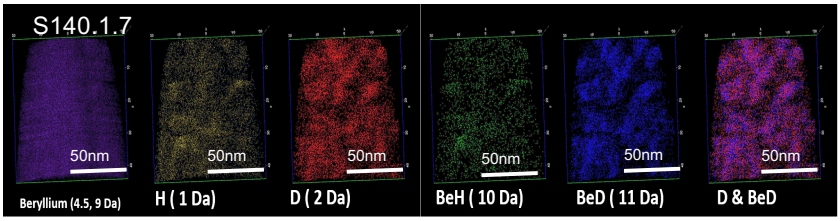


Figure 4.33: A three-dimensional reconstruction of the first atom probe measurement of the outer wall erosion zone

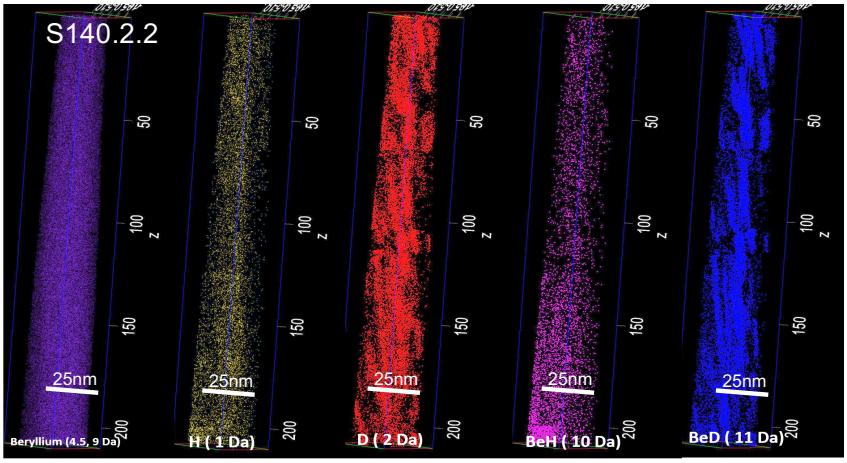


Figure 4.34: A three-dimensional reconstruction of the second successful atom probe measurement of the outer wall erosion zone

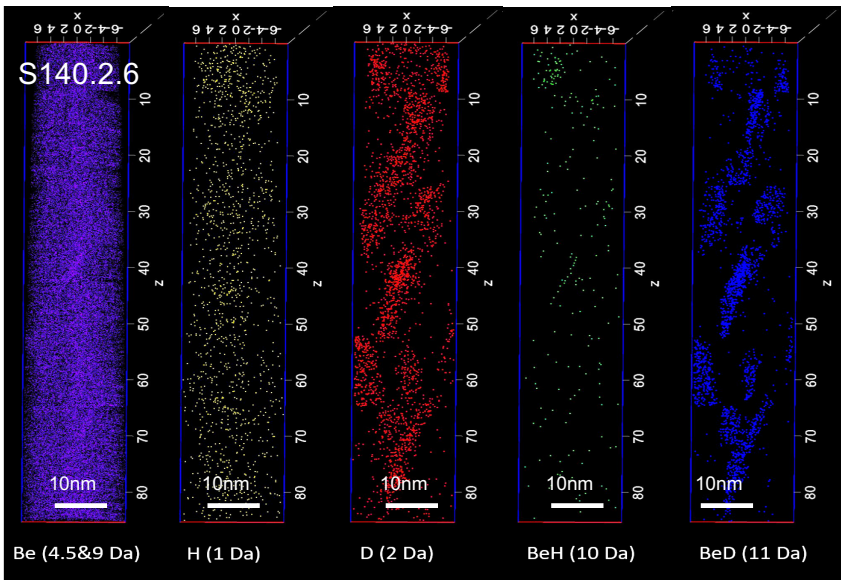


Figure 4.35: A three-dimensional reconstruction of the third successful atom probe measurement of the outer wall erosion zone

Figure 4.33 shows the first successful atom probe run on the outer wall eroded sample. The reconstruction contains ∼3.3 million ions in a volume of ∼0.04 million

nm^3. Figures 4.34 and 4.35 present reproducibility across the $1cm^2$ sample's surface area. The different APT sampling locations are shown in figure 4.1. Sample 140.22, (figure 4.34) corresponded to ∼8.6 million ions and ∼0.1 million nm^3. Sample 140.26, (figure 4.35) corresponded to ∼1.5 million ions and ∼0.02 million nm^3.

Figures 4.33-4.35, all show unique clustering between the D(2Da) peak and the BeD(11Da) peak. The behavioural link between D and BeD peaks is most evident when overlaid in figure 4.33. In comparison to D; peaks corresponding to H(1Da) and BeH(10 Da) have reduced correlation. This enhances the argument that the deuterium peaks were not falsely assigned, and represent real D^+ ions escaping the sample, and not H^{2+} from the vacuum.

This is the first experimental evidence of its kind to report on tokamak in service materials. The results here add to the literature surrounding DFT [91, 92] predictions and TEM bubble evidence [14].

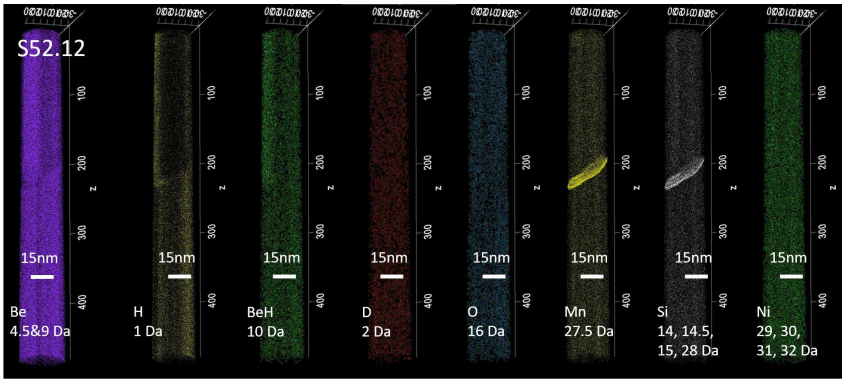


Figure 4.36: A three-dimensional reconstruction of the first successful atom probe measurement of the inner wall erosion zone

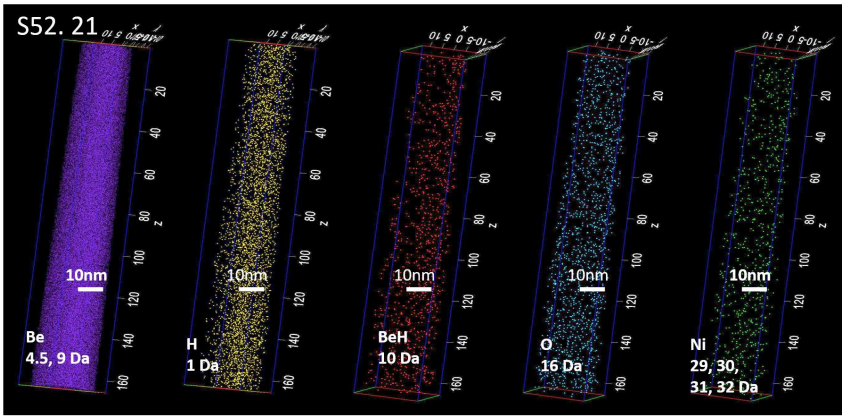


Figure 4.37: A three-dimensional reconstruction of the second successful atom probe measurement of the inner wall erosion zone

In comparison to the outer wall, the inner wall eroded regions show no perceivable clustering. Application of a randomisation algorithm to the inner wall APT data, produced no statistically significant deviation between the real data and a randomly produced matrix; confirming no clustering.

Sample 52.12, corresponded to ∼100 million ions and ∼1.3 million nm^3. Sample 52.21, corresponded to ∼4.7 million ions and ∼0.07 million nm^3. Higher ion count was possible at the inner wall, prior to needle fracture. The results suggest that higher H levels embrittle beryllium materials. Figures 4.36 and 4.37 show low levels in both H(1Da) and D(2Da) peaks, consistent with the bulk analysis.

Finally, figure 4.36 presents a Mn and Si grain boundary. A localised increase in H(1Da) peak concentration occurs at the interface. The D(2Da) peak remains unaffected. The APT H contamination is therefore low, and governed by releasing surface effects. Equally, D retention does not occur preferentially at the grain boundary. D clustering appears intra granular. This result is consistent with low loss EELS measurements. No changes were seen at the grain boundary for the outer wall map.

It remains currently unclear which operational environments could produce clustering at the outer wall and none at the inner wall.

Following clustering observations from the 3D data sets; concentration curves were extracted from iso-surfaces. An iso-surface defines a volume where the concentration of the component is above a percentage composition limit, thereby defining a cluster's minimum concentration limit. Deuterium iso-surfaces were produced for the outer wall samples. All iso-surfaces are averaged; and a central compositional profile extracted.

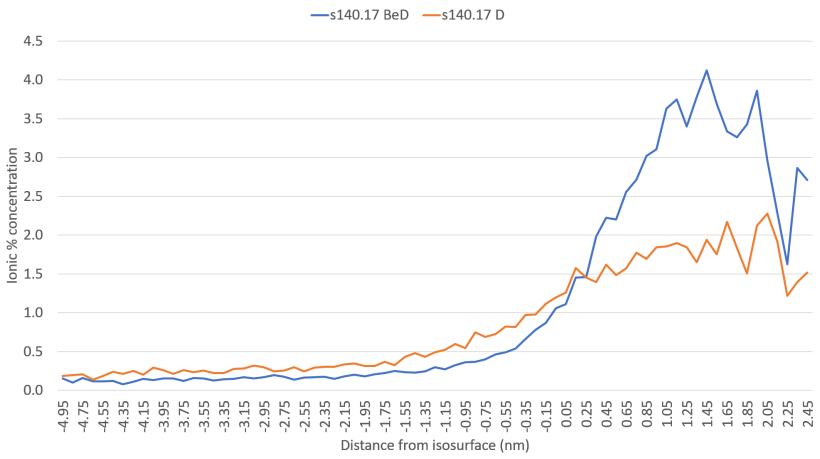


Figure 4.38: The BeD (11Da) isosurface of sample 140.17 extracted from sample 140.17's APT reconstruction; showing the ionic percentage concentration gradient of BeD (11Da) and D (2Da) into the surface

Figure 4.38 shows an outer wall (s140.17) example, of a deuterium iso-surface. This figure is characteristic of all eroded outer wall samples. Background levels of D, throughout the sample are ∼0.25 ionic%. The D cluster has a maximum of 1.5%, whereabouts a release of BeD occurs from the surface, at a peak concentration of ∼4%.

APT surface ionisation and evaporation does not occur via equilibrium thermodynamic release. Molecular ion release is less likely than monatomic ion release, during high evaporation field and tip stresses. The opposite to these results is what would be expected. Alongside reproducibility, this leads credibility that the results are real.

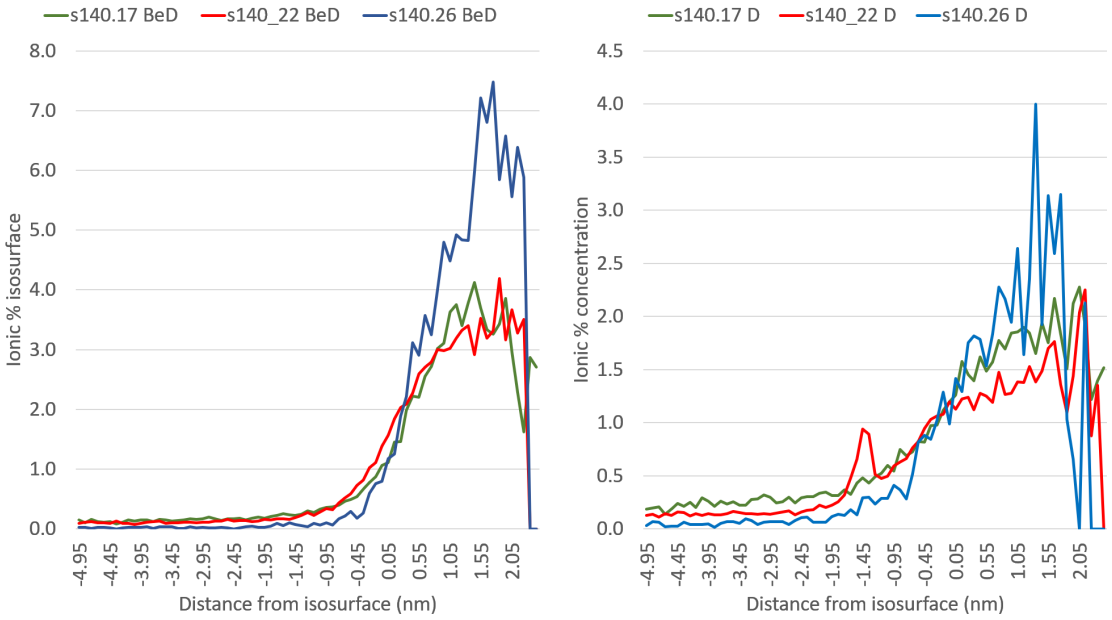


Figure 4.39: Left: A comparison of extracted Atom Probe BeD (11Da) isosurfaces of samples 140.17, 140.22, and 140.26, into the surface. Right: A comparison of D concentrations in the BeD isosurfaces of samples 140.17, 140.22, and 140.26.

These APT results are reproducible across all successful runs and summarised in figure 4.39. Even across successive needles of varying volumes and ion counts; the peak BeD level only ranges from ∼4% to ∼8% in the final needle. The release position remains extremely reproducible. Maximums in D release remains more coincident between ∼1.5-2.0%. Sample 140.26, reaches a maximum of 4% peak concentration, however this appears noisy.

As discussed earlier, iso-surfaces for the inner wall eroded regions were not possible. No indication of clustering was present and therefore no further analysis or comparison to the outer wall can occur.

4.5 Integrated TDS data comparing relative H isotopes present at the Inner and Outer wall eroded regions

A short analysis of raw TDS data converted from mass spectrometer counts to atoms cm^{-2} is provided in comparison to Atom Probe results.

Figure 4.40, shows a brief overview of the desorption seen. Hydrogen has several release peaks, whilst deuterium and HD appear with linked release, most particularly at the inner wall. At the outer wall two release mechanisms appear present for D_2 release.

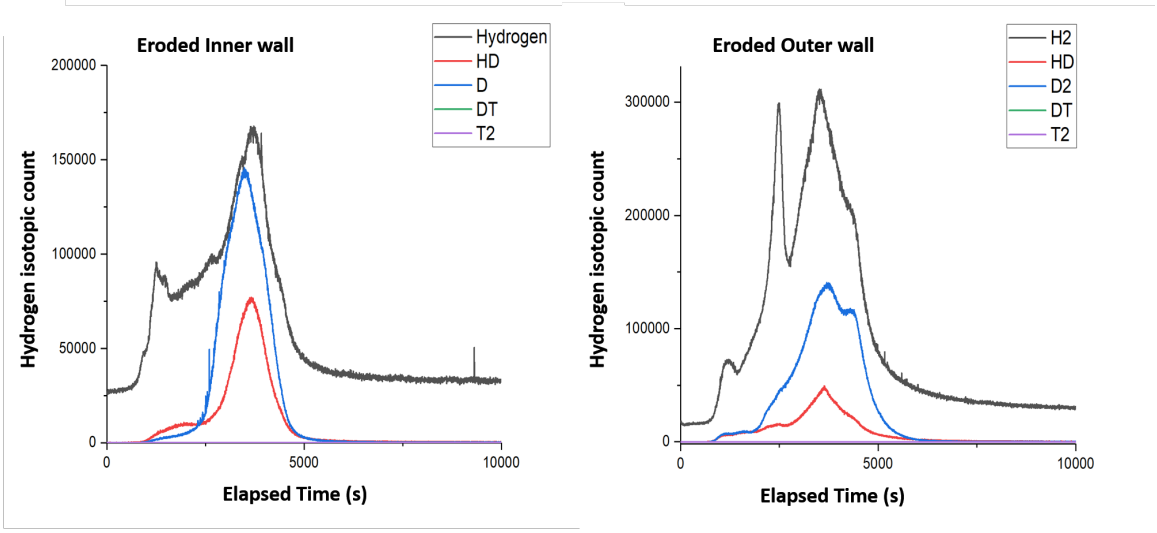


Figure 4.40: Comparison of hydrogen isotopic release for the inner and outer wall eroded materials as a function of elapsed time. Left: inner eroded sample results. Right: outer eroded sample results.

Table 4.41 confirms that the total retention is greatest at the outer wall. Table 4.41 compares % hydrogen isotopes across the inner and outer wall eroded samples, measured via Thermal Desorption Spectroscopy (a macroscopic approach) and Atom Probe Tomography (a microscopic approach), respectively. Significant issues with this comparison should be considered due to the differences in the techniques' scales; however if consistent the results could bridge the gap for modelling the behaviour of nanometric surface layers (APT) against macroscopic bulk samples (TDS); alongside providing mechanistic understanding of retention.

Sample	TDS data				APT data		
	Total retained Hydrogen - all isotopic forms	% of Hydrogen isotopes			% of Hydrogen isotopes		
		H	D	T	H	D	T
Non-exposed sample	6.56E+17	99.92	0.08	0.0005	100.00	0.00	0.00
Inner wall eroded	7.86E+17	81.71	18.29	0.0000	99.13	0.87	0.00
Outer wall eroded	9.22E+17	83.59	16.41	0.0010	41.80	57.13	1.08
Inner wall deposit	1.93E+18	71.46	28.54	0.0000	16.20	13.20	70.60
Outer wall deposit	3.93E+18	44.41	55.59	0.0030	50.90	25.50	23.60
Melted dump plate	1.89E+18	88.81	11.19	0.0000			

Figure 4.41: A comparison of APT and TDS data considering atomic % of hydrogen isotopes from the two techniques.

Table 4.41 shows the inner wall eroded APT data is composed almost exclusively of H. The TDS data at this site, by comparison, shows a slight reduction. Measured H% was 99.13% via APT, and 81.71% via TDS. Considering the difference in scale, these measurements appear consistent.

APT outer wall results agree less to TDS data. Outer wall APT (surface) data shows considerably higher D retention, comparative to bulk TDS D measurement. These results could be explained by the first 100-200nm (APT measurement) of surface, saturated with D; alongside a D concentration gradient reducing with increasing depth (averaged TDS measurement).

APT breakdown of the NE-Be shows all hydrogen present to be H, and is thus assumed vacuum contamination. The NE-Be TDS results also show 99.92% H with 0.08% D, suggested contamination from previous runs. Neither eroded sample has any significant T present, via TDS or APT.

4.6 A results summary from eroded JET inner and outer wall samples; and a NE-Be sample

This chapter discussed the microstructure of beryllium materials from JET's eroded regions. The microstructure was crystalline, and decorated by oxides at the grain

boundaries (via SEM-EDX).

TEM and EELS in conjunction with modelled EELS results of Be-O-H structures, suggested samples contained BeD_2 (largely towards the surface at the inner wall) and $Be(OH)_2$ (tetragonal and orthorhombic) contributions throughout the samples, with addition of hexagonal BeO at specific oxide features with higher O at.%. Oxide coarsening appeared likely at the outer wall, alongside suggestion of large oxides surrounded by hydrogen filled cavities.

APT results presented novel findings of D/BeD clustering at the outer wall eroded zone. Iso-surface analysis suggested BeD release occurred on opening the D bubble. APT release occurs under non-equilibrium conditions and therefore may be in less agreement mechanistically to in service tokamak release. It remains unclear whether BeD/D are held in ionic or gaseous form within the sample. Sufficient evidence concluded that the samples' D peaks were containing D^+ and not vacuum contaminated H^{2+}. No APT clustering occurred at the inner wall. Grain boundary presence showed no preferential D grain boundary retention.

Comparison between APT and TDS, showed overall lower retention at the inner wall. Some discrepancy between the first 200nm of surface retention (via APT) and macroscopic retention at the outer wall (via TDS), was posited the result of an extremely saturated D surface.

These results question which operating conditions led to the stark differences seen between inner and outer wall erosion retention. Unfortunately, JET is a dynamic environment. Several pulses occur a day, all of an experimental nature, investigating the variance and boundary of operational space. Machine and hydrogen environment potentially change hourly. Relating post-mortem microstructures to machine operation remains a challenging task. Published TDS results from the second ITER-like wall, which finished in purely hydrogen pulses, have shown retained isotopic exchange possible [11].

The literature suggests implantation temperature and fluence to be the primary factors determining retention [16, 89]. Unfortunately, wall measurements are governed by inaccuracies, which can be seen by the data included in the appendix C. The differences measured in temperature between inner and outer walls are insufficient to explain those seen in the microstructures recorded. Wall fluence data remains unavailable at this time. These machine uncertainties make concluding statements determining which wall conditions governed post-mortem results, elusive.

Chapter 5

Microstructural analysis of deposited JET materials

5.1 An overview of the chapter's analysis of deposited JET materials

This chapter discusses the results seen from deposited regions in JET. The deposited regions from the mid plane tiles (outlined in figure 1.2, chapter 1) under discussion in this chapter, originate at the wings of the inner and outer wall limiters, (figure 1.3). The starting microstructure of deposited sample regions are illustrated in the methods section, figure 3.1. Any deposit investigated post-mortem is formed at the surface. The structures under the deposit in descending order are: columnar layers perpendicular to the surface of TVA deposited Be (8-10μm); TVA deposited nickel (2-3μm), and below this structure the original powder formed S65-H grade.

The same methodology undertaken in the previous experimental chapter 4 was undertaken here, proceeding from macroscopic to sub-microscopic. SEM was used in conjunction with FIB techniques to survey both surface and sub surface morphologies. TEM and EDX combined with EELS were utilised to examine the elemental compositions of the subsurface microstructures. High-Power Impulse Magnetron Sputtered (HiPIMS) samples provided through EUROFusion laboratories alongside DFT predictions of Be-O-H structures were compared to EELS JET results; and the nature of hydrogen isotopes in the samples commented on. APT was applied to the samples to determine whether finite deposited layers could be understood sequentially in terms of thickness and composition. Finally retained isotopic ratios measured via APT and TDS were compared.

The work presented here is the first of its kind examining the post-mortem microstructures of tokamak deposited beryllium materials.

Sampling locations are displayed in figure 5.1. Any numbering refers to the chronology of sampling and repetition for statistical validation.

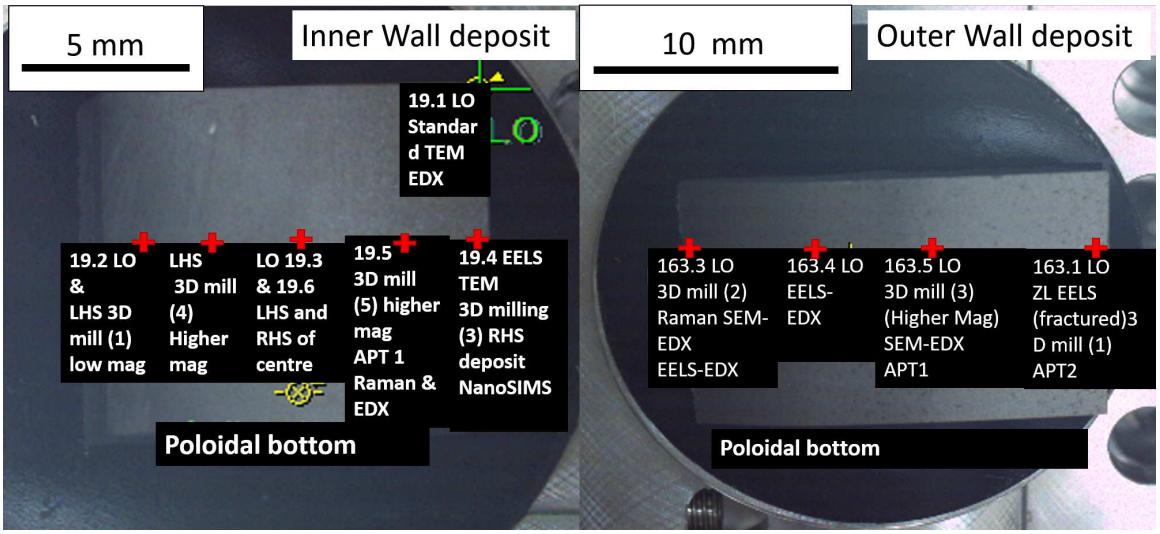


Figure 5.1: A Navigational optical image. Left: the inner wall deposited castellation. Right: the outer wall deposited castellation. The notation 'LO' stands for lift-out produced via FIB milling. 'APT' stands for atom probe microscopy. The navigational image shows the locations and techniques applied on sampling.

5.2 Scanning Electron Microscopy (SEM) of deposited surfaces and sub-surfaces in JET

For the ease of the reader, inner wall limiter deposited JET samples will hence forth be defined as IW-deposit; and outer wall limiter deposited JET samples as OW-deposit.

5.2.1 The Inner wall deposit

Figure 5.2, presents the IW-deposit surface with a medium wave form, alongside finer scale roughness. Some variation between RHS and LHS poloidal positions may be discernible. Figure 5.3 presents the subsurface microstructure of LHS and RHS poloidal edges of the IW-deposit. No surface deposit is present at the LHS poloidal edge. The layers present are: the FIB protective Pt layer, dendritic TVA Be, TVA Ni, and S65-H beryllium. The RHS poloidal edge has an additional $\sim 5\mu$m of plasma deposit.

Comparison between figures 5.2 & 5.3 at the LHS IW-deposit, suggest, the surface circled in figure 5.2(a), described as a concentric 'cauliflower-like' structure, indicates the TVA Be layer with no deposit presence.

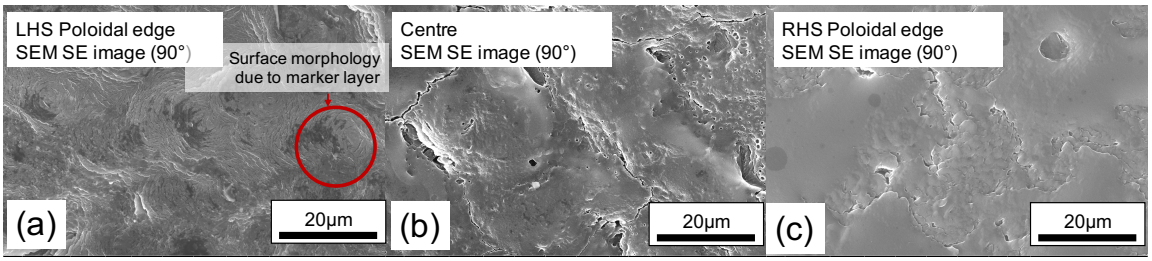


Figure 5.2: SEM SE images of the IW-deposit showing: surface morphology perpendicular to the sample surface at LHS (a), centre (b) and RHS (c) poloidal positions.

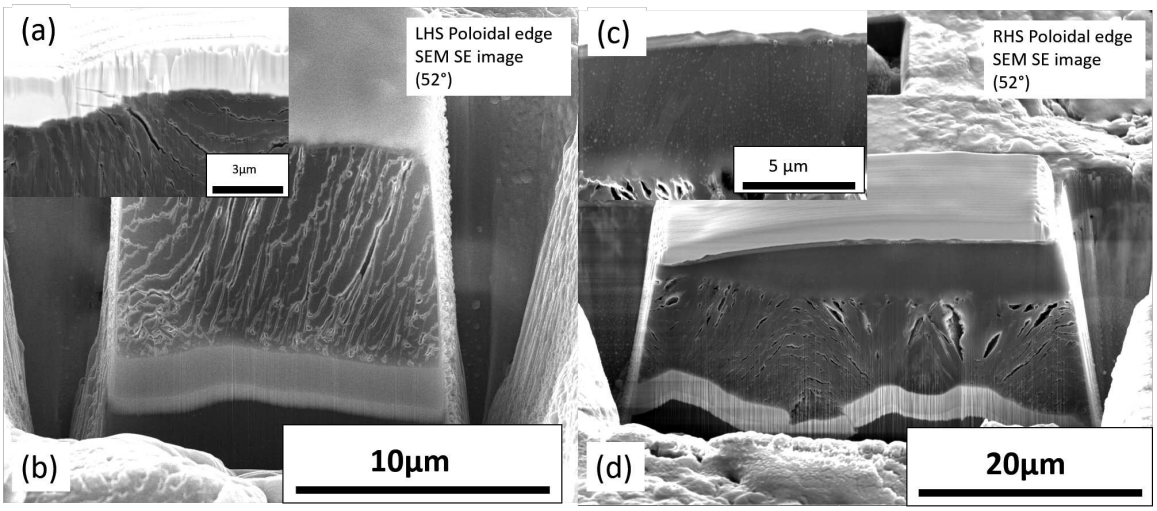


Figure 5.3: SEM SE images. (a-b): LHS IW-deposit sub surface with no deposit present. (c-d): RHS IW-deposit sub surface with $\sim$5μm of plasma deposit additional to the starting structure: TVA Be, TVA Ni, and S65-H Be.

These observations enabled future sampling success where the likelihood of sampling deposit increased. It was estimated that the deposit covered $\sim$75% +/$-$20% of the surface; its depth measurements ranged from $\sim$1-6 μm and commenced $\sim$25% in from the LHS poloidal edge (in the toroidal direction). This calculation assumes no variation was present in the poloidal direction.

5.2.2 The outer wall deposit: SEM imaging

The outer wall deposits appear more irregular and non-uniform.

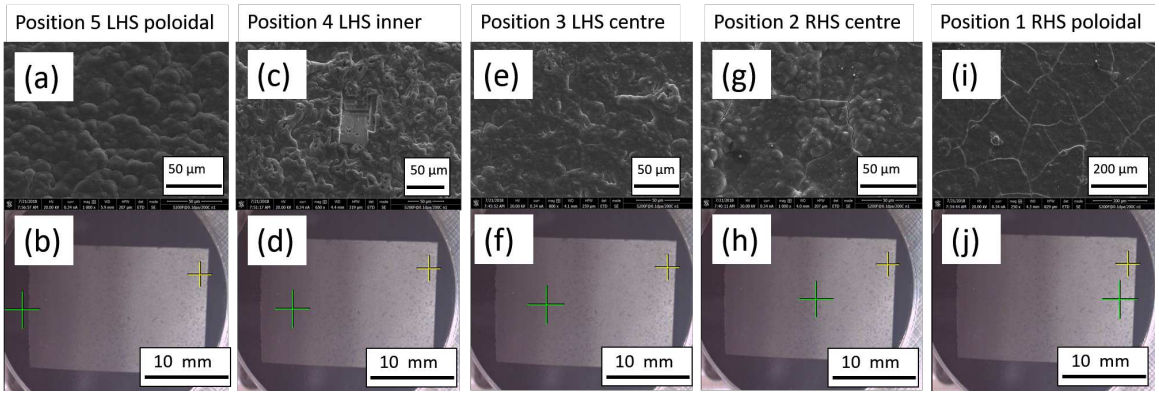


Figure 5.4: A figure displaying (b-j): optical positions along the toroidal direction (LHS-RHS poloidal edges) of the OW-deposit indicated by the green cross. (a-i) Respective SEM SE images of those positions.

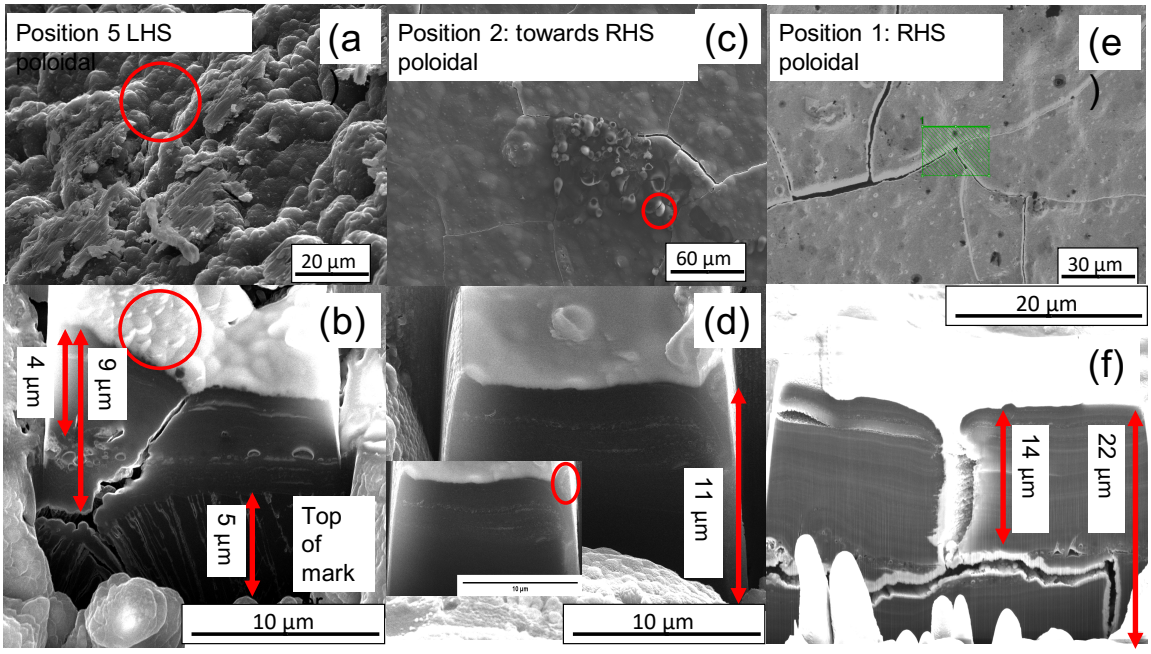


Figure 5.5: (a-b): Figure showing the surface and depth profile at the LHS poloidal edge, position 5. (c-d): A RHS intermediate surface and subsurface, position 2. (e-f): The RHS poloidal edge, position 1.

Representative surfaces are shown in figure 5.4. OW-deposit surface morphology changes, occur across the toroidal direction. The LHS poloidal edge has mushroom-like bulbs of deposit. More filamentary structures occur at the centre, whilst the RHS poloidal positions show smoothing and transition into cracked surfaces with bubble-like growths.

Similar horizontal 'sedimentary-like' layer cross sections occur at positions 1 & 2 (figure 5.5) to depths ranging from ∼11-14 μm. Cracking occurs between layers up to the surface, and suggested the result of residual thermal stresses from deposit build up.

Position 5 deposit is thinner. The top of the beryllium marker layer is present at ∼9 μm into depth (figure 5.5(b)). Bubbles are present at the layer/deposit interface. Bubble formation via gaseous retention under continued high heat loads, may propagate to crack formation at the interface. This mechanism may explain progression from positions 5-1 (figure 5.5(b)-(f)).

5.3 Energy Dispersive X-Ray of deposited cross sections in JET produced via Focused Ion Beam (FIB) milling

5.3.1 The inner wall deposit: EDX

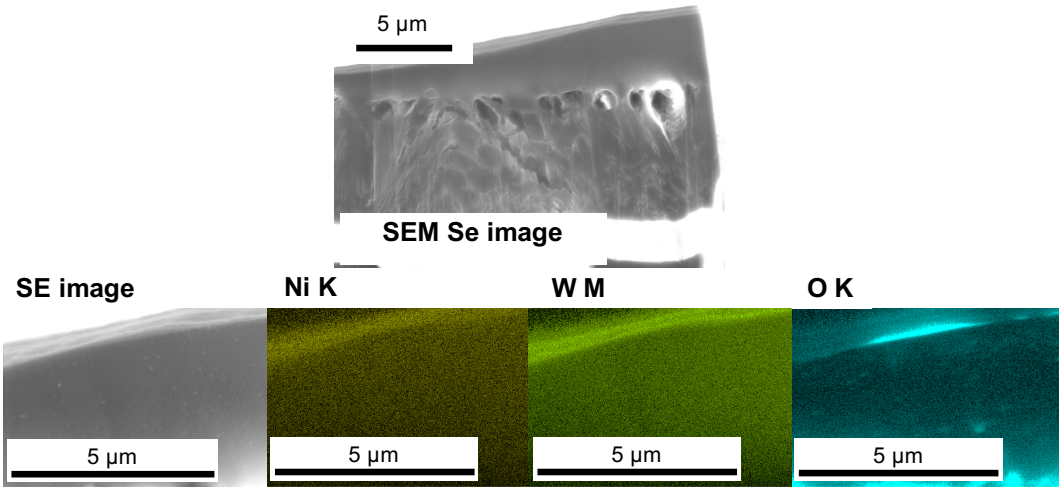


Figure 5.6: Background subtracted SEM SE EDX images: low magnification overview SEM-SE image; high magnification SEM-SE image of EDX scan area, Nickel K line elemental map, Tungsten M line elemental map, and Oxygen K line elemental map.

The EDS maps produced in figure 5.6, shows the IW-deposit at high magnification. Two deposit structures are apparent, sedimentary-like layers of ∼1μm and a larger 3-4μm subsurface deposit. The sedimentary-like horizontal deposit is composed of Ni and W layers with some small trace of Cu. Beneath this layer, at the interface, is likely a beryllium oxide, and below a beryllium rich matrix with oxygen precipitation.

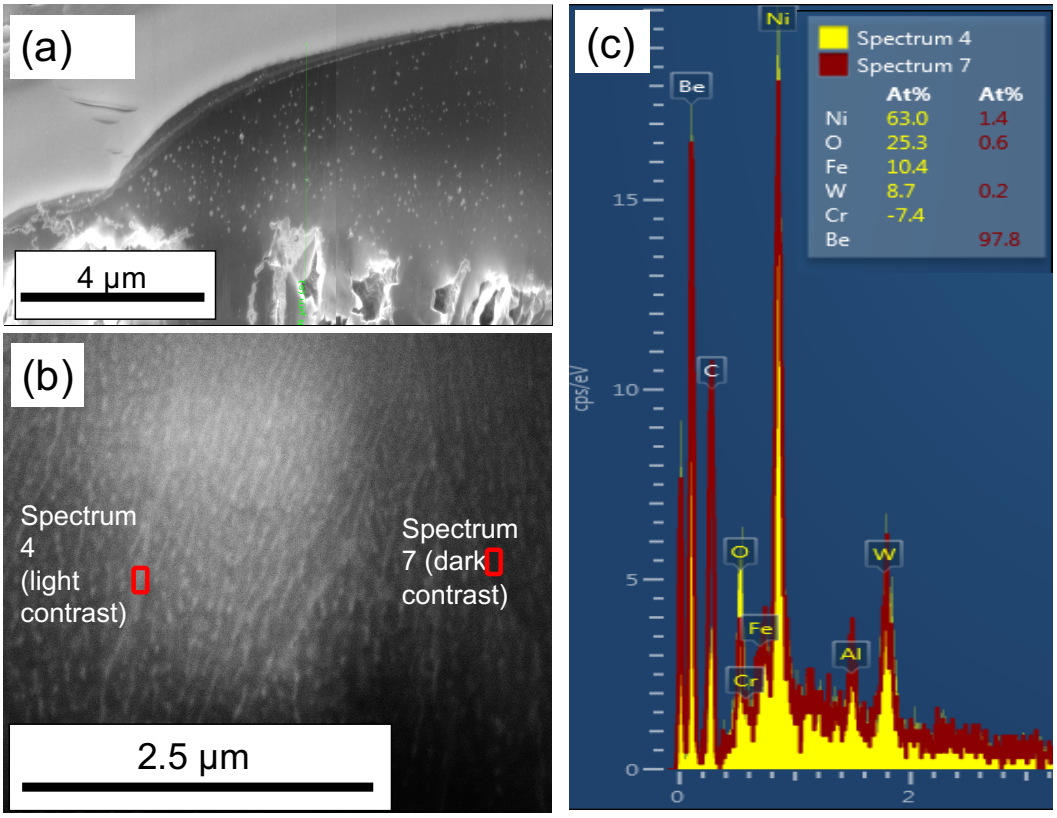


Figure 5.7: SEM SE image (a) showing the top of 'marker layer' Be with oxidised surfaces; (b) SEM SE at higher magnification of sub surface deposit layer with two apparent microstructural features white contrast precipitates, and a dark contrast matrix; (c) Background subtracted EDX spectra of the two extracted areal regions: spectra 4 (light contrast) rich in nickel, iron and oxygen; spectra 7, beryllium matrix with small nickel contributions.

Figure 5.7 shows this last region at higher magnification. Two spectral areas of equal count are directly compared: a lighter region, spectrum 4; and a darker region, spectrum 7. Spectrum 4 measures ∼63% nickel, ∼25.3% oxygen, ∼10.4 % iron, and ∼8.7% tungsten. Comparatively, spectrum 7 (likely the matrix) is predominantly beryllium with only ∼1.4% nickel. EDS is notoriously difficult to apply to beryllium materials due to its lack of precision of the lighter elements due to beryllium windows on most detector systems. These measurements are not quantitative. However, the regions of lighter contrast are due to Ni, O, Fe, and W presence.

It is concluded two deposition processes are occurring, to explain the two distinctive microstructures seen. Whether this is due to changes in machine operation: limiter plasma configurations initially followed by diverted plasmas, is unclear.

5.3.2 The outer wall deposit: EDX

The same pattern of analysis is repeated at the outer wall deposition zone.

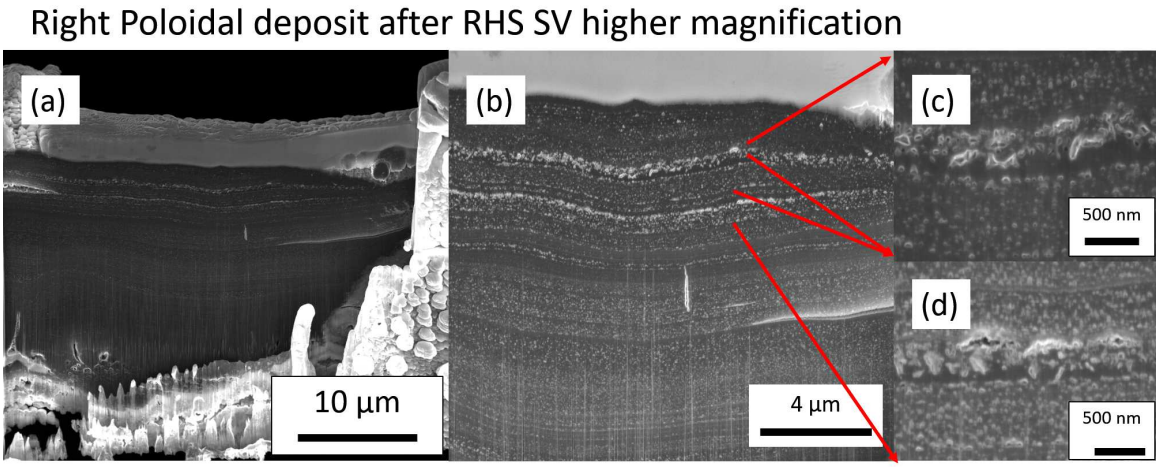


Figure 5.8: SEM SE images from (a-d) at increasing magnification; showing a right poloidal edge liftout after the higher magnification 3D milling study. Images (c) and (d) show the intense variability of feature densities at the 500nm scale from two regions less than 3 μm apart.

A lift-out taken from the higher magnification 3D milling series study in figure 5.1, is shown at the different length scales in the FIB SEM SE image in figure 5.8. The level of intricacy increases with magnification. The lift-out displays $\sim$15μm depth of consistent horizontal 'sedimentary-like' deposition atop 8-10μm beryllium marker layer and; at the base of the lift-out, a Ni marker layer of higher contrast.

Pores occur sandwiched between layers at different frequencies associated to depth (images (c-d)). Unfortunately, the resolution achieved in the SEM in-situ with the FIB Helios is greater than that of the Tescan SEM with EDS. Figure 5.9 shows the output EDS maps of the region. Nickel and oxygen appear coincidently in many of the layers, whilst carbon appears more dispersed and less intense. Al, W, Cu and Fe appear consistently together at a lower intensities.

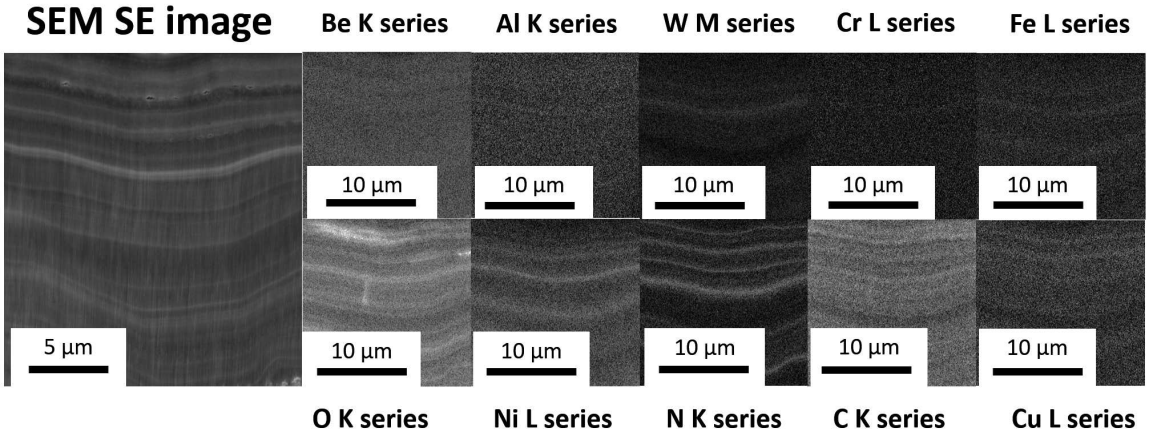


Figure 5.9: SEM-EDX maps of the lift-out from figure 5.8, showing the horizontal 'sedimentary-like' deposit structure with rich alternating layers of nickel oxide, nitrogen associated with Cu, and fewer layers of aluminium, iron and tungsten associated elements.

Results from EDX analysis show significant changes of deposit along the toroidal direction between left and right poloidal edges in both IW-deposits and OW-deposits.

The inner wall has significantly less deposition coverage, and two microstructural phases. A matrix with precipitates of Ni, W and O, lies sandwiched between the beryllium TVA marker layer and a second smaller sedimentary deposit at the surface. The deposition of the inner wall is greatest at the right poloidal edge and indicated by smoothing surface morphology.

The OW-deposit is sedimentary-like and continuous along the toroidal direction, with some slight variation in depth and surface morphology. The OW-deposit is thicker in all instances than the IW-deposit. Bubble formation appears prevalent at the beryllium marker layer/deposit interface. Surface cracking is seen at the right poloidal edge, correlated to greatest deposit thickness. On increasing magnification, the morphology of the deposit appears exceptionally complex, with no definable finite layer start and end.

5.4 Transmission Electron Microscopy of deposited materials with application of Electron Energy Loss Spectrosocpy (EELS)

This next section concerning TEM results utilising EELS and EDS will be discussed in terms of all lift-outs concerning IW-deposits; and compared to all OW-deposits.

Unlike for the eroded results, where considerable uniformity of base structure occurred again and again; deposited materials show greater variation. A greater number of example data sets were therefore presented.

This section aims to understand whether any averaged composition and microstructure can be presented of deposited materials, to assist global machine-scale retention predictions for ITER.

Because beryllium is such a light material, there remains no perfect technique available to satisfactorily quantify all components present. EELS was applied to deposited phases, to investigate Be and O components and potentially, deuterium. EELS is limited when investigating heavier element presence (Ni, W). Acquisition times for these materials becomes increasingly impractical. EDX was therefore captured wherever possible in-situ. EDX of beryllium still remains qualitative.

5.4.1 The inner wall deposit: STEM with EELS and EDX

Figure 5.10, provides a 'map' of positions explored at the inner wall deposited region. Deposition is reported to have the greatest weighting responsible for hydrogenic retention. Since investigation of the IW-deposit surface showed no deposit present in some areas, only lift-outs with deposit are analysed. Non-deposited marker layers with columnar grains open to the surface [76] were thought unlikely to retain hydrogen.

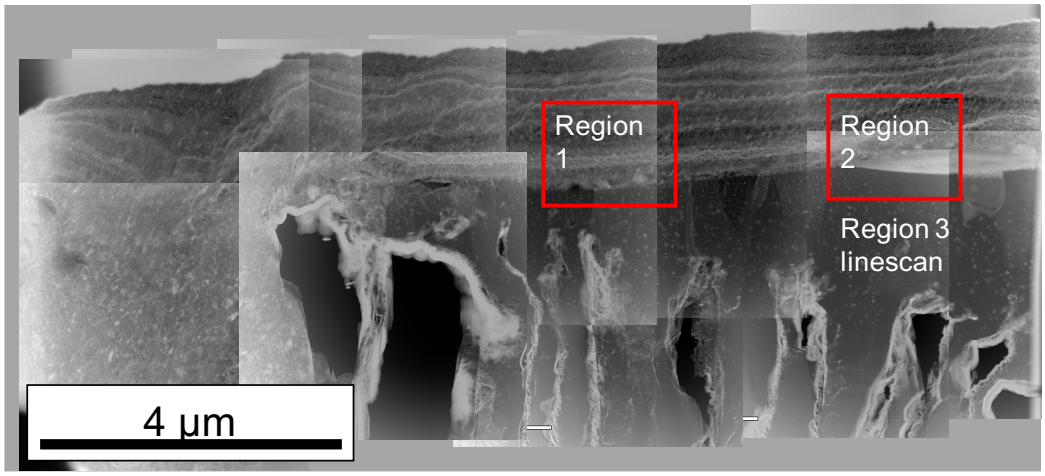


Figure 5.10: A High Angle Annular Dark Field (HAADF) STEM image of the deposited inner wall at the right poloidal edge, where deposition is most frequently seen. Those regions indicated are further explored via EELS and EDS.

Figure 5.11 presents low magnification EDX maps of region 1. Nitrogen can be seen at this scale semi-continuously. Oxygen occurs almost uniformly. Nickel and

Tungsten are apparent but at low concentration. Further components of Inconel [66]: Mn, Cr and Fe; were present at the limit between resolution and noise, at this magnification.

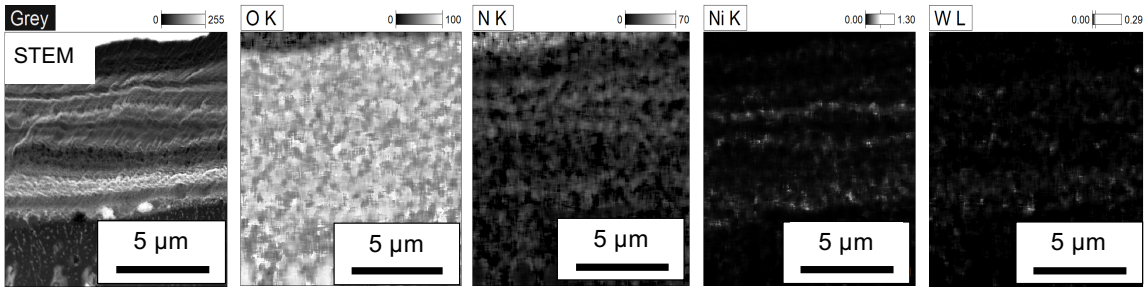


Figure 5.11: A HAADF STEM image and associated EDS spectra at low magnification of region 1 defined in figure 5.10, showing low resolution changes in deposit composition. All images are background subtracted

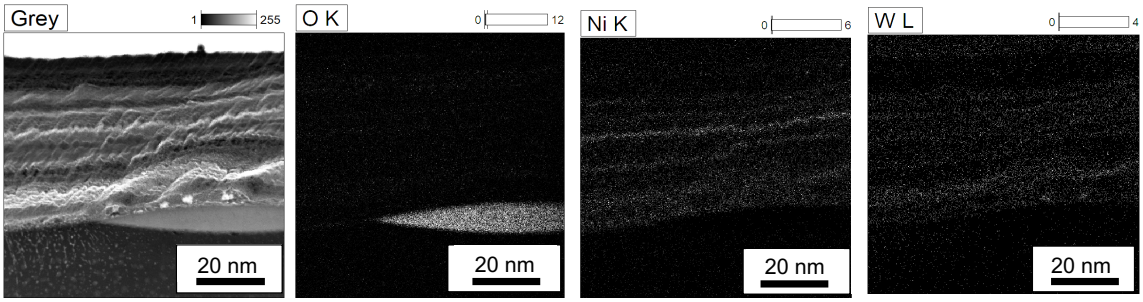


Figure 5.12: Higher resolution EDS spectra and HAADF STEM image of Region 2 outlined in Figure 5.10, showing the deposit compositional changes and both a surface oxide as well as the second deposit layer beneath. All images are background subtracted.

Figure 5.12 presents an EDX overview of region 2, analysed subsequently with EELS. An oxide island lies at the interface between the two deposit microstructures, in the O K map. Ni and W occur disparately at the limit of discrete layers. Some variation is evident even within $\sim 4\mu$m toroidal deviation between figures 5.11 and 5.12.

Figure 5.13, shows a higher magnification linescan of figure 5.12. Regions of the linescan were integrated to extract EDX and EELS signals at those positions, and are numbered from the second beryllium microstructure at depth towards crystalline beryllium oxide and further into the sedimentary layers in increasing order (Be, BeO, D1-9). The EDX signals are presented in figure 5.13b, and EELS low loss and Be core loss in (c) and (d), respectively.

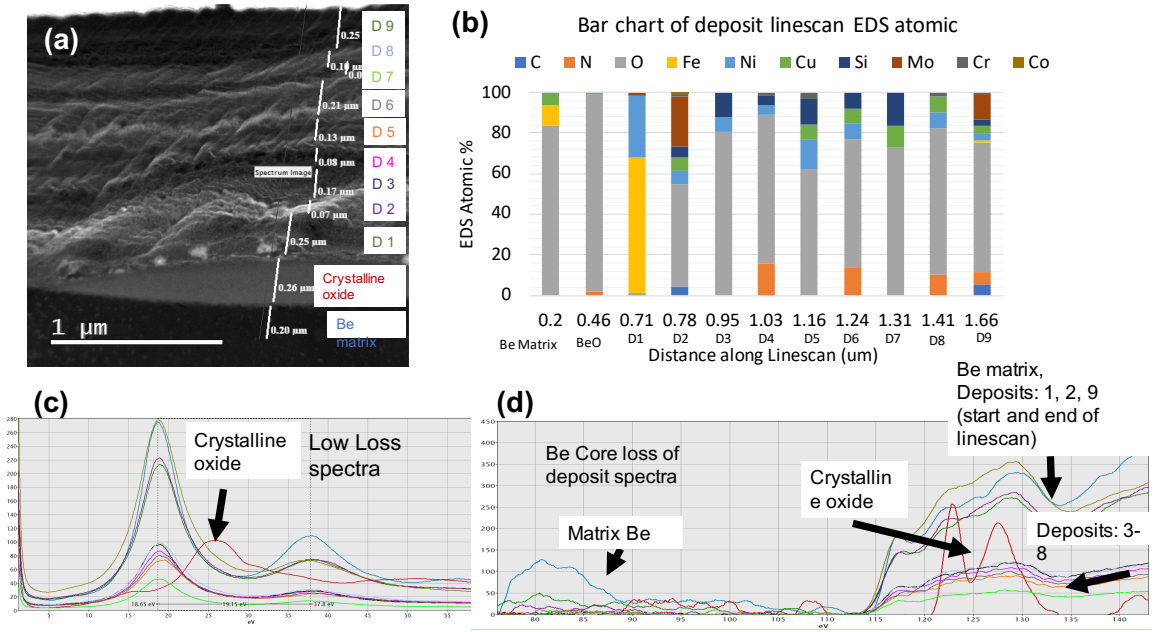


Figure 5.13: Linescan of Region 3 at the inner wall deposit. (a): STEM HAADF image with atomic contrast, with integrated regions marked. (b): extracted EDS at.% bar chart. (c): EELS low loss extracted spectra. (d): EELS Be core loss extracted spectra.

EDX results suggest the sedimentary-like deposit is predominantly high in oxygen, with a reasonable degree of continuous Ni, alongside smaller contributions of Si, Cu, Fe, Mo, N and C, intermittently. EELS Be core loss and low loss results show the sedimentary-like deposit signals are consistent into depth, with repeatable and consistent fine structures. Only the oxide present between the sedimentary layers and second deposit microstructure, shows any change in either the Be low loss plasmon, or Be core loss fine structure. Here, the Be core loss fine structure, changes to features reminiscent of wurtzite, reported in section 4 for eroded samples. This region likely contains some BeOD. EDX measurements therefore underestimate Be and overestimate O. Overall, the sedimentary layer surface deposit appears largely formed via Be co-deposition, with little BeO co-deposition present.

Three further EELS, EDX linescans are now presented to investigate sedimentary layers at higher magnification, at 3 different regions of the sample. The final comparison investigates the features of the second deposit microstructure in further detail.

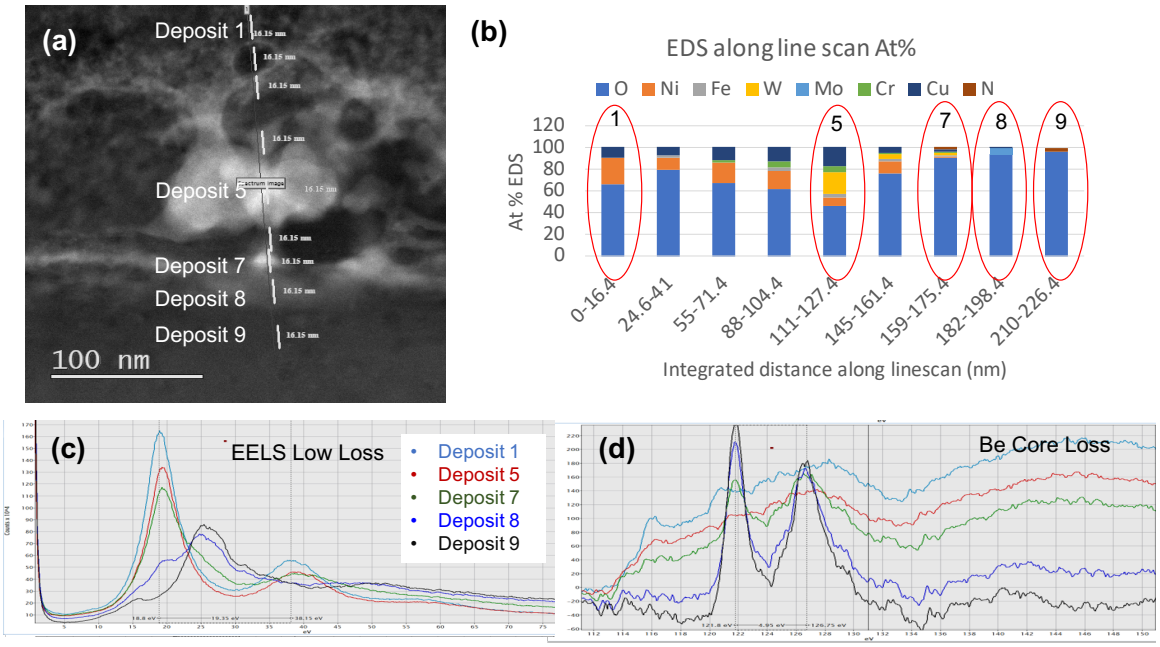


Figure 5.14: (a): HAADF STEM image of the inner wall Region 3 deposit, right poloidal edge at higher magnification. (b): EDX linescan results, as a bar chart with distances along the scan numbered. (c) Low loss EELS of extracted numbered regions. (d): Be core loss EELS of numbered regions.

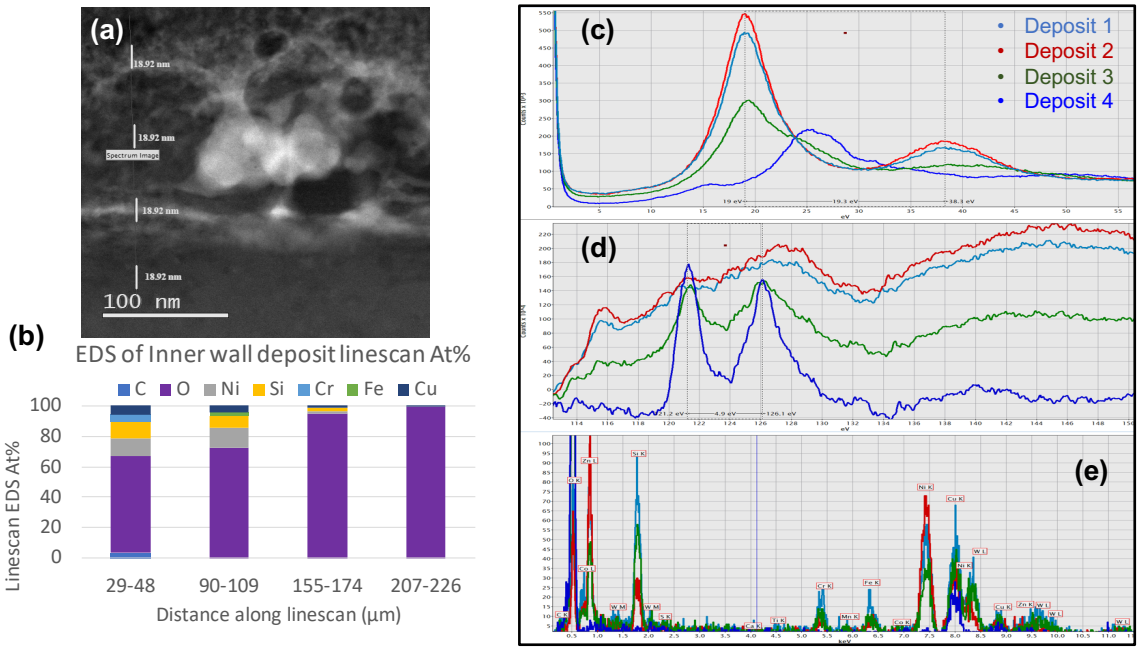


Figure 5.15: (a): HAADF STEM image left of the inner wall region 3 deposit at higher magnification, investigating the sponge-like matrix. (b): EDX extracted linescan at.%. (c): EELS low loss extracted spectra. (d): EELS Be core loss extracted spectra. (e): EDX extracted spectra.

Figure 5.14, shows a higher resolution scan of a particle at the interface between the sedimentary-like deposit and BeO. Ni and Cu appear coincidentally in EDX, between 0-160nm depths, in the sedimentary layers. Bright contrast (in the HAADF image) is due to a tungsten rich precipitate. At point 8, the interface between tungsten rich sedimentary-like deposit and oxide; Mo is present (EDX). Impurity presence is most noticeable in the low loss plasmon at this position. The Be core loss, fine structural changes denoting oxidation; occur as early as point 7, with Be edge onset delaying to higher energies at 8 and 9.

A comparative line scan is given of the same area; off the particle's position in the surrounding sponge-like microstructure in figure 5.15. EDX shows: O, Ni, Si, and Cu, are largely stable compositionally, across the sponge-like deposit. EELS measurements across the boundary of the sedimentary-deposit into the full BeO, show a gradient of oxidation evident by the changes of the Be core loss fine structure (Be onset delay and intensity changes).

A final deposit linescan is given of region 1 in figure 5.16, $\sim 4\mu$m away. This example compares local environments, across a lift-out; whilst also investigating the second deposit structure, without a BeO interface present.

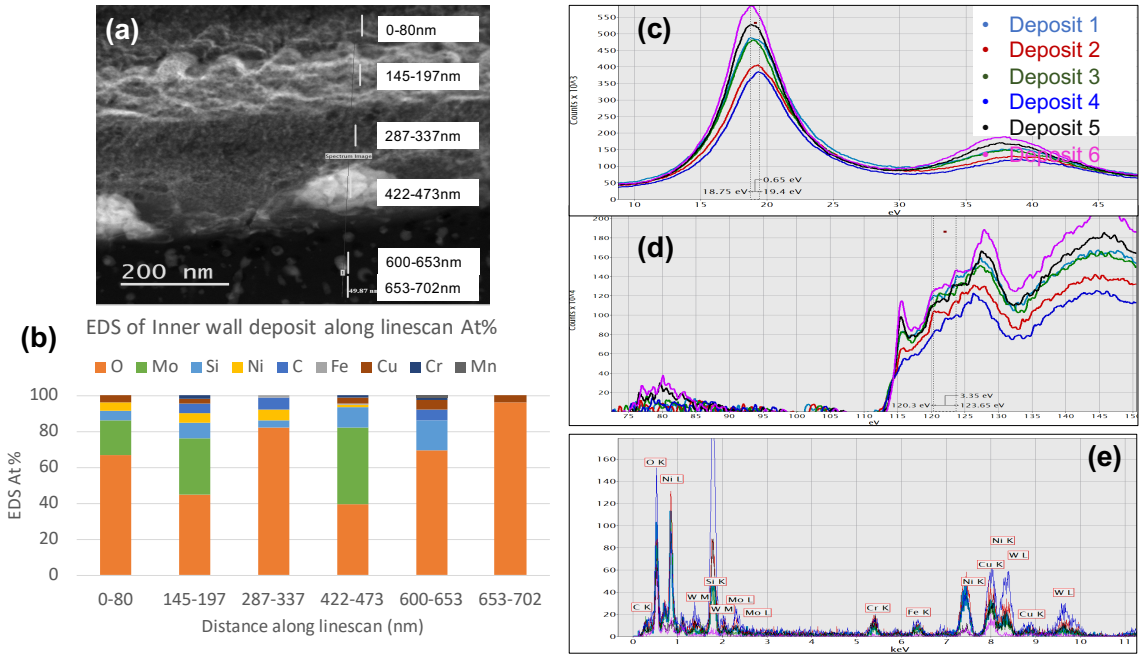


Figure 5.16: (a): HAADF STEM image of the inner wall at region 1, deposited right poloidal edge of the castellation at higher magnification investigating a linescan intersecting sedimentary-like deposit at the surface; and the second deposit structure into depth. (b) EDX ectracted at.%. (c): EELS low loss and (d): Be core loss are presented alongside EDX extracted spectra (e).

EELS results present, low loss and Be core loss fine structures as uniform, with almost no variation, across both deposit microstructures; suggesting that Be is present in chemically similar environments irrelevant of the deposit microstructure. EDX presents the second deposit structure with lower impurity presence. Small fractions of Si, C, Cu, and Cr occur alongside O. Sedimentary layers measure the same impurities with additional: Ni and Mo. EDX comparisons between point 5 (on a precipitate) and point 6 (in the matrix) of the second deposit microstructure; show a Be and Cu matrix with: Si, Cr, and C precipitates. Both Ni and Cu can alloy with Be [118, 119]. Copper is soluble up to ∼15 at% at high temperatures; and forms an alpha phase of $CuBe_3$ [119].

The pattern of deposit structure: type 2; Be-Cu grains with Si, C, Cr, and Cu precipitates; may suggest alongside literature that high heat loading occurred on these inner wall beryllium tiles. The surface co-deposit suggests subsequently reduced heat loads. The differences in deposit structures could indicate a change in machine operation between early limiter plasmas (high levels of novel neutral beam injection) versus divertor plasmas later. IW-deposits' codeposition appears largely governed by Be in the presence of D; and not BeO codeposition with D.

5.4.2 The outer wall deposit: STEM with EELS and EDX

5.4.2.1 The outer wall deposit; left poloidal edge

Outer wall deposits (OW-deposits) will now be assessed. Due to the microstructural variation presented via FIB and SEM, three different OW-deposit lift-outs are presented, starting at the left hand poloidal edge, centre, and right poloidal edge.

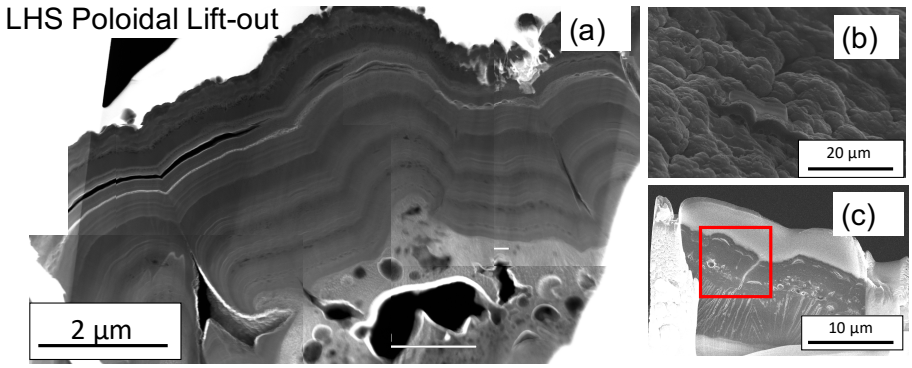


Figure 5.17: Overview of the outer wall left hand poloidal edge deposit. (a): STEM HAADF image, (b): SEM SE image of the original surface morphology. (c): SEM SE lift-out image, prior to thinning. The region of interest in (a) where EELS and EDX occurred, is indicated by the red box in (c).

Figure 5.17 shows an overview HAADF image of the LHS poloidal edge deposit. Image (c), shows from depth to surface: the Ni layer (higher contrast at the lift-out's base); above which resides the beryllium marker layer (columnar grain structure); closer to the surface still, a region of bubbles/pores; and at the surface, the co-deposit. The final two surface regions, are a result of plasma interaction. The HAADF image, via atomic contrast, suggests some compositional difference between the porous region and sedimentary co-deposit.

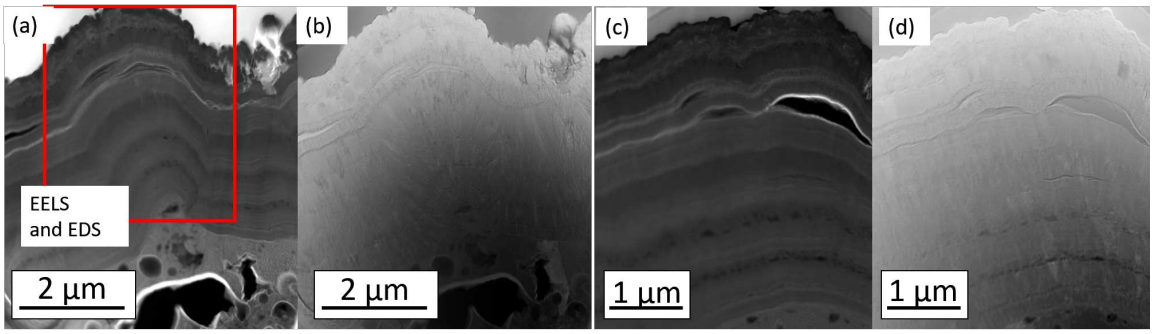


Figure 5.18: STEM HAADF images (a and c), and ADF images (b and d) showing atomic weight contrast in the former and diffraction contrast in the latter. These images are from the outer wall left hand poloidal edge deposit. The STEM-EELS region of interest scanned, is indicated by the red box in (a).

Figure 5.18(b) & (d), with diffraction contrast, present exceedingly fine structures perpendicular to the layer direction; whilst HAADF images (a) & (c) suggest horizontal layer directions. The EDS and EELS region of interest is indicated in figure 5.18(a) (via the red box).

Figure 5.19 presents the EDX maps of this region. Maps are granulated due to kernel size and background subtraction, and should not be interpreted as discrete precipitation. Caution is applied to interpretation of beryllium, which remains highly qualitative within most EDX systems.

Many of the features seen at the inner wall, are similarly repeated in figure 5.19, with the appearance of sedimentary-like compositional layers. There is however a greater degree of discrete N horizontal layering, alongside high levels of semi continuous oxidation. The extracted EDS graph of positions along the Nitrogen areal map, show consistent levels of Be, C, N, O, F. Interestingly, Al, W and Ni increase towards porous regions at the base of the sedimentary layers.

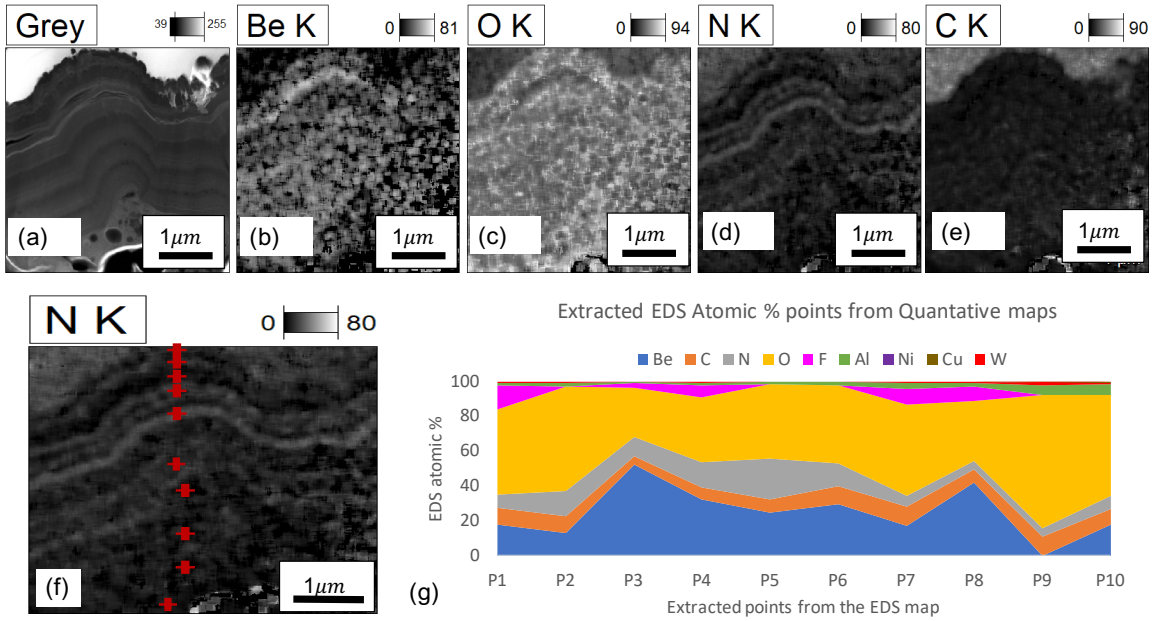


Figure 5.19: (a): STEM HAADF image at low magnification of the outer wall left hand poloidal edge deposit. (b-e): EDS maps of: Be (K), O (K), N (K), and C (K). (f): Nitrogen EDX map, with extracted EDX positions marked in red numbered 1-10 from top to bottom. (g): EDX atomic % compositions of extracted points.

5.4.2.2 The outer wall deposit, sample centre

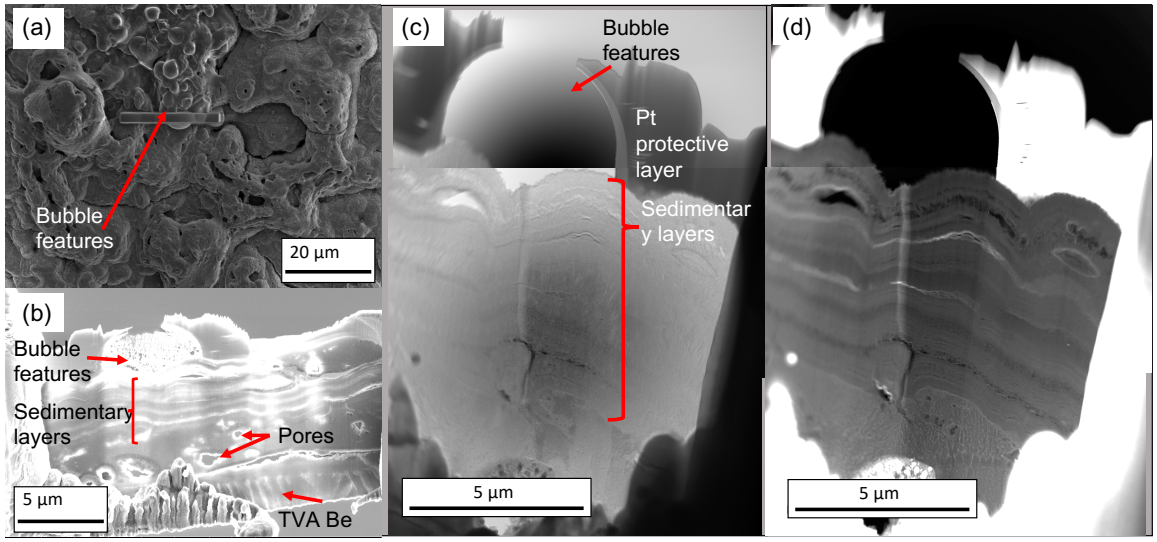


Figure 5.20: (a): Overview of central poloidal OW-deposit surface morphology. (b): FIB lift-out thinning process showing four microstructures: surface bubbles, sedimentary layers, pores, and TVA Be. (c): STEM ADF diffraction contrast image. (d): STEM HAADF atomic contrast image.

Figure 5.20 displays an overview of deposit taken towards the sample centre. Similar features are present to those seen at the left hand poloidal position (figure 5.17). Surface bubbles in image(a) (figure 5.20), confirmed by FIB image(b), were destroyed in transit; evident by the Pt negative space in images (c-d).

EDS and EELS were recorded in-situ and presented in figures 5.21-5.22.

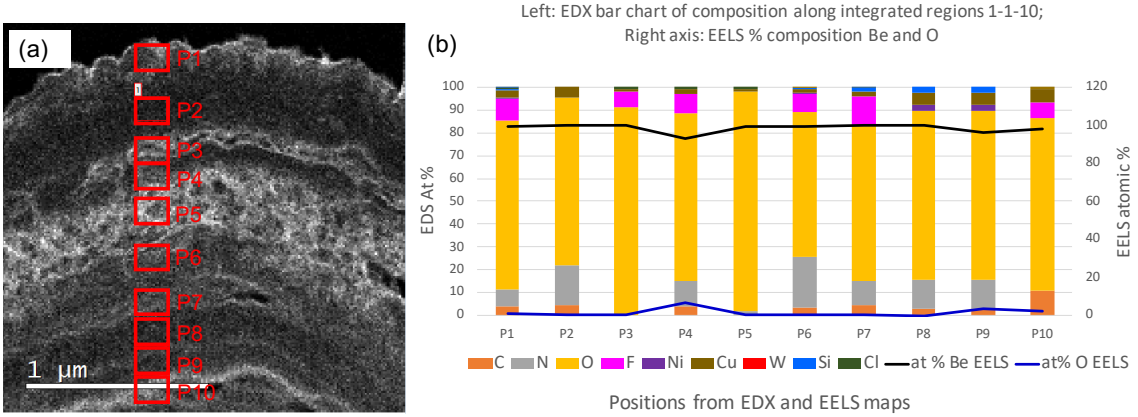


Figure 5.21: (a): STEM EDS map of the region, integrated normalised pixel areas from which spectra were extracted for EDS and EELS are indicated. (b): Graph showing, left axis: EDX at.% composition measured in situ, right axis: EELS curve fit at.% Be and O.

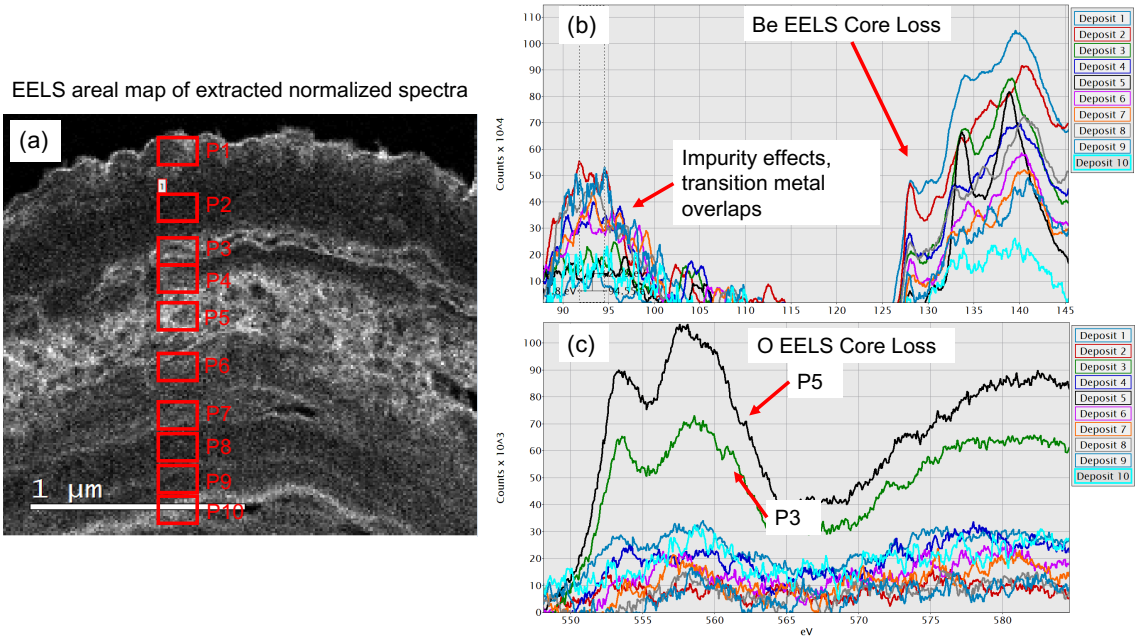


Figure 5.22: (a): STEM EDS map of the region probed. (b): EELS Be core loss extracted spectra. (c): EELS O core loss extracted spectra. Points 3 and 5 have greater oxidation.

Figure 5.21(b) shows the variation of EDX (left axis); superimposed with EELS quantified Be and O at.% on the right axis. Trace impurity components (via EDX): N, C, F, and Cu; are compositionally stable across the $\sim 3\mu$m map. The levels of Ni, W and Cu increase towards the base of the sedimentary layers, consistent with other OW-deposit results.

EELS results show that beryllium is the major deposit component, ranging between $\sim$92-100 at%. Oxygen appears present in non-stoichiometric quantities; mostly at porous interfaces in the deposit. No literature can be found describing the crystal structure for BeO at 92:8. It remains possible that this phase is stabilised by deuterium presence.

The EELS Be core loss fine structure shows some variation. Features linked to oxidation reflect those seen in eroded regions at intermediary oxidation levels. However, impurity presence is seen in both via Be fine structure and the pre edge region, which overlap M edge energies of transition elements. Despite low at% oxidation levels, oxidation is clearly present in the EELS O edge. Overall, it suggests that the outer wall is governed by a greater degree of Be-O codeposition with D, than inner wall deposits.

5.4.2.3 The outer wall deposit; right poloidal edge

The final lift-out presented in this chapter is the right hand poloidal edge of the outer wall, shown in figure 5.23. Unfortunately this lift-out fractured during transport to the TEM. What remained of the lift-out was the bubble surface feature, indicated in figure 5.23(a-b), and the bottom fractured layers, in image (c). Only EDX could be taken of this sample, since the pieces that had broken off, were the regions of greatest electron transparency.

Figure 5.23 presents two areal scans of equal count of the two remaining regions; the bubble and fractured sub surface layers. The bubble surface feature occurs with a high degree of N, alongside (O, Na, C, P, and Al). The fractured surface is rich in O, (C, N, and Be). Nitrogen is likely present as a result of gas puffing reported in the literature surrounding machine loading conditions. EDX, remains a qualitative measurement of beryllium samples, and no further conclusion is possible. The sedimentary plasma deposited layers appear greater than 10μm, since no indication of the original TVA Be is present in the lift-out. Greater deposit thickness correlates to the right poloidal edge of deposited samples, irrelevant of inner or outer wall origin. Lastly, large sedimentary layer growth appears to correlate to increased sample fragility.

Bubble top right		
Element	Atom %	Atom % err
Be K	0.0	
C K	2.48	0.28
N K	37.35	0.8
O K	47.01	0.99
Na K	9.06	0.13
Al K	0.34	0.04
P K	3.44	0.12
P L		
Cl K	0.07	0.01
Cl L		
Fe K	0.01	0
Fe L		
Co K	0	0
Co L		
Cu K	0.12	0
Cu L		
Ga K	0.08	0
Ga L		
Pt L	0.04	0
Pt M		
		2.38

Fractured surface		
Element	Atom %	Atom % err
Be K	14.72	4.06
C K	8.85	0.48
N K	8.99	0.67
O K	67.09	0.7
Al K	0.23	0.02
Cr K	0.01	0
Cr L		
Fe K	0.01	0
Fe L		
Ni K	0.03	0
Ni L		
Cu K	0.06	0
Cu L		
Ga K	0.01	0
Ga L		
W L	0	0
W M		
Pt L	0	0
Pt M		
	100	5.93

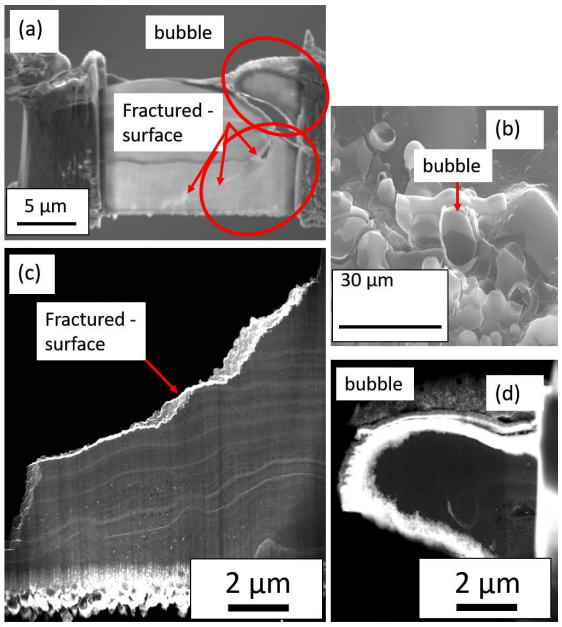


Figure 5.23: (a): SEM SE image, showing the right poloidal OW-deposit lift-out. (b): SEM SE surface morphology image at the region of interest. (c): STEM HAADF image of the remaining lift-out post fracture in transit. (d): The remaining surface bubble morphology of the lift-out after transport. Two EDX integrated spectra of the bubble surface and fractured bottom surface respectively.

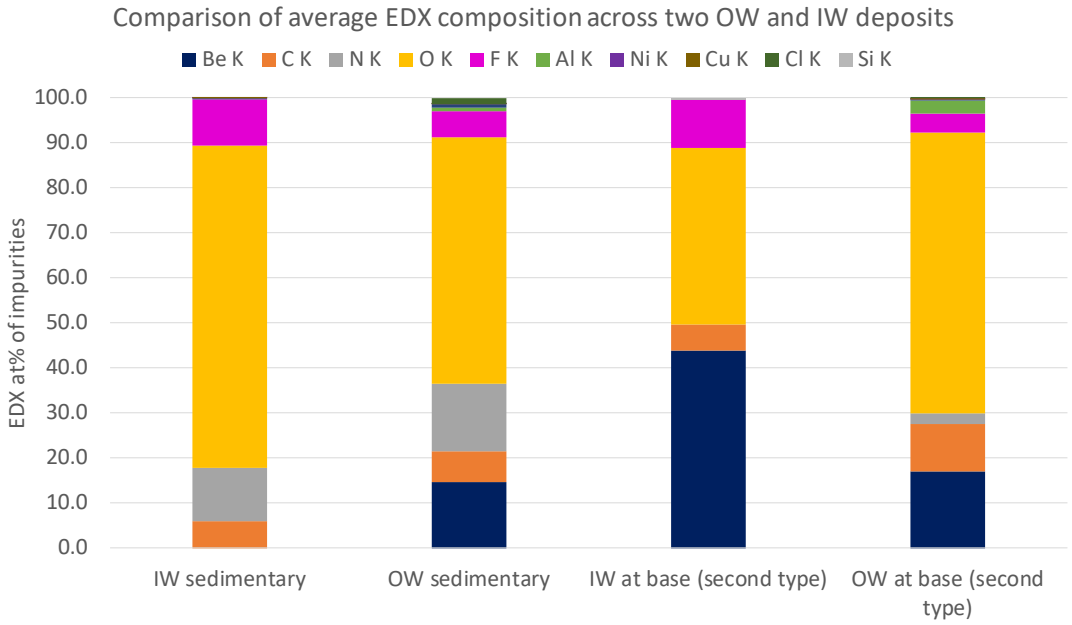


Figure 5.24: A comparison of EDX elemental impurity at%, between inner and outer wall deposits. 2 deposit structures appear at the inner wall; some variation in heavier elements at the base of OW-deposits could classify a second OW-deposit structure.

A final graph is given in figure 5.24, comparing EDX averaged integrated areas from the deposit structures presented. This method does not quantify beryllium and remains only qualitative of impurity concentrations. There is low overall compositional variation by EDX. Oxygen stoichiometries via EELS are greatest within OW-deposits. N appears relatively higher at the OW-deposit position. Carbon remains relatively consistent. However, an increase in heavier element trace impurities occurs at OW-deposits, most especially at the base of the sedimentary-like layers, indicative of the original TVA Be surface prior to plasma interaction. Some relative increase in impurity composition is also seen at the base of the IW-deposit microstructure; suggesting the presence of higher heat loads during early campaign pulses. Ni presence is likely the result of diffusion from the Ni interlayer through columnar Be grains to the surface.

5.4.3 EELS of EUROFusion samples produced via HiPIMS

One further comparison of EELS averaged data is provided of the sedimentary-like IW and OW deposit, compared to a set of lab grown (High-Power Impulse Magnetron Sputtering (HiPIMS) [27]) samples from the EUROFusion; alongside a final comparison with DFT modelled spectra. The EUROFusion standards were presented as BeO, BeD, and BeOD.

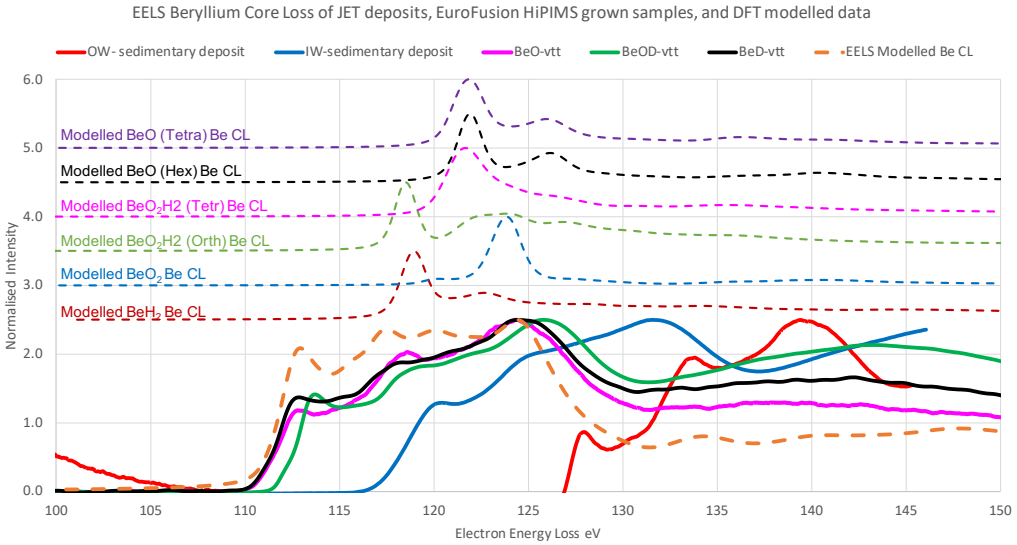


Figure 5.25: An EELS Be core loss comparison of averaged normalised spectra of: JET IW and OW sedimentary deposits; EUROFusion BeO, BeOD, and BeD samples (via the HiPIMS method [27]); and DFT modelled spectra. Those spectra showing closest affinity are plotted at the same y-height.

Figure 5.25 shows experimental normalised intensity Be core loss JET results against EUROFusion samples, and the DFT modelled spectra. All experimental graphs underwent alignment and exponential background subtraction in the same pre-edge window. The OW-deposit has a pre-edge feature (not shown here) at∼90-96eV, thought the result of transition element contamination. Both JET samples have delayed Be edge onset to higher energies. Only fine structural differences are present among the EUROFusion samples. All data appears closest to that of the Be Core Loss DFT modelled spectrum. Unfortunately, whilst the shape of the modelled fine structures are precise, on-going work continues perfecting calculation methodology to confirm exact onset positions. Via fine structure comparison of experimental results alone, the IW-deposit appears more similar to the BeD EUROFusion sample; whilst the OW-deposit appears most like BeOD.

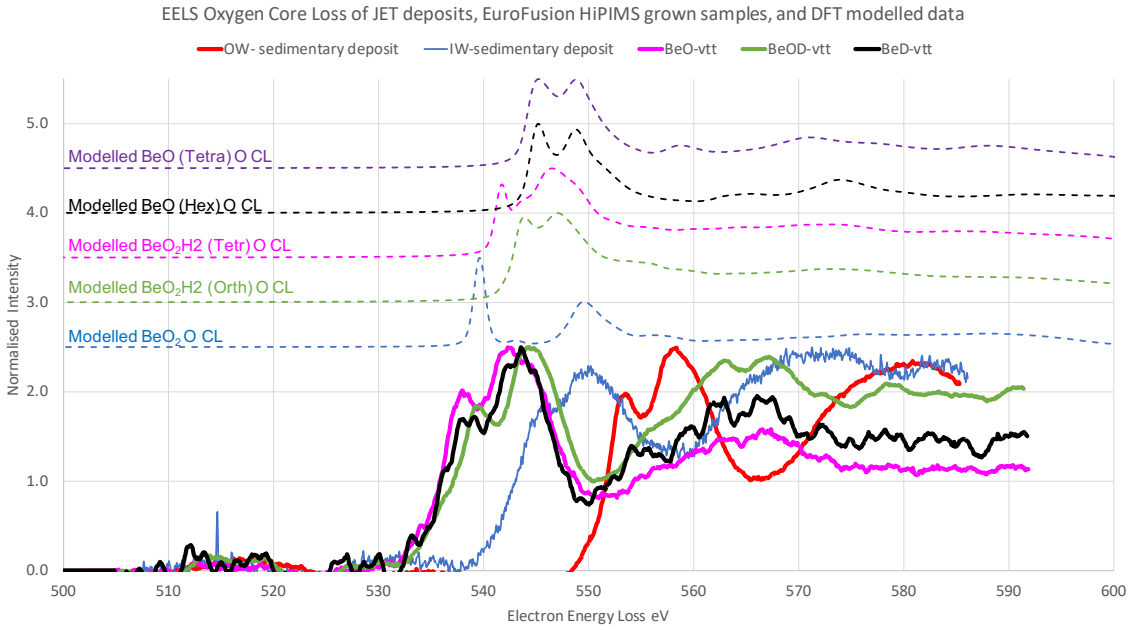


Figure 5.26: An EELS O core loss comparison of averaged normalised spectra of: JET IW and OW sedimentary deposits; EUROFusion BeO, BeOD, and BeD samples (via the HiPIMS method [27]); and DFT modelled spectra.

The same methods have been applied to the oxygen core loss EELS data, comparing IW and OW deposits; EUROFusion HiPIMS samples, and DFT modelled spectra. The experimental results' comparison between JET samples and EUROFusion samples does not provide much insight. All samples appear similar when comparing fine structure. Comparison between experimental results and DFT modelled spectra, suggests the fine structures resemble most that of BeO_2H_2 tetragonal, with some mixing

of orthorhombic presence possible. It should be noted that the original IW signal was exceptionally low, and therefore remains noisy after normalisation. JET onset energies remain delayed and are assumed a result of higher impurity levels.

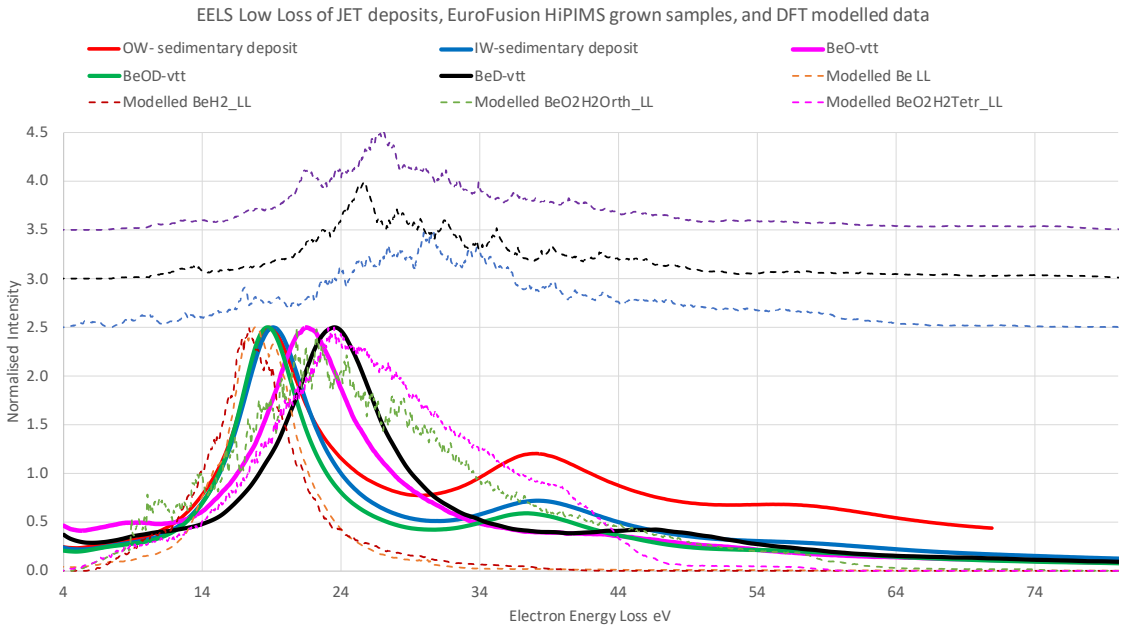


Figure 5.27: An EELS low loss comparison of averaged normalised spectra of: JET IW and OW sedimentary deposits; EUROFusion BeO, BeOD, and BeD samples (via the HiPIMS method [27]); and DFT modelled spectra. Those modelled spectra showing closest affinity are plotted at the same y-height.

Figure 5.27 shows the final comparison between experimental and modelled low loss results. Here the low loss modelled spectra are accurate in both position and fine structure. The experimental results appear that JET samples resemble most closely the EUROFusion BeOD. Comparison between DFT and JET results, suggests there is a high degree of BeH_2, here BeD_2; in the large area averaged spectra. Small fine spectra fluctuations at ~10eV on some JET samples seems indicative of orthorhombic deuteroxides; alongside a degree of broadening at the OW-deposit, resembling features seen at the OW-eroded region. However, features of BeO_2H_2 orthrombic and textragonal appear most present in the EUROFusion samples: BeO and BeD. These samples do not appear to be stoichiometrically precise, however do appear relevant for comparison to tokamak materials under core loss comparisons constraints.

5.5 Atom Probe tomography of JET deposits

Atom Probe Tomography (APT) was applied to these samples, to investigate any spatial segregation of hydrogen isotopes to nano-metric layers; and further investigate layer compositions. Unfortunately, and consistent to issues seen on transport to the TEM; deposit fragility was especially compromised under APT high electric fields. Needle fracture occurred often, and failed to allow long runs to be completed. The result reduced statistical accuracies, and restricted the conclusions drawn.

Only two reasonable reconstructions, one IW-deposit and one OW-deposit were obtained. The data sets are given for completeness in figures 5.28 & 5.29, however any potential spatial conclusions of layer thickness or deuterium presence, was not possible.

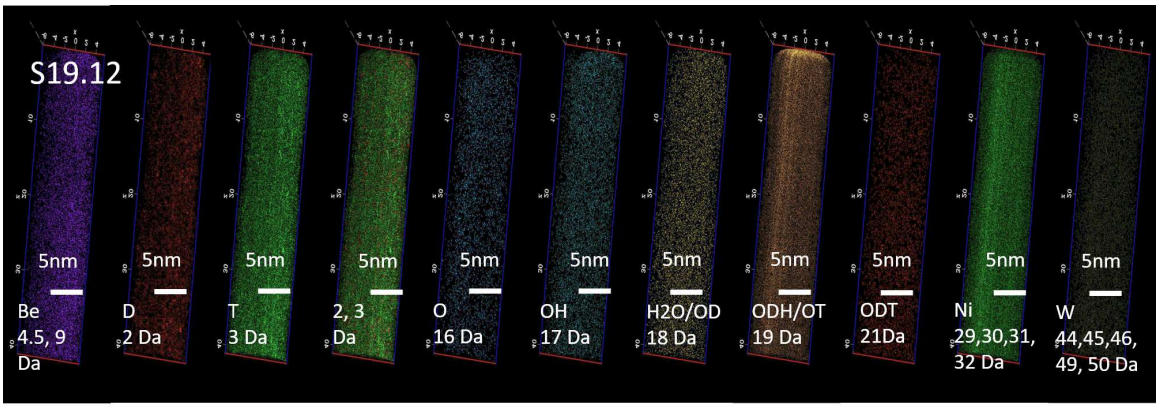


Figure 5.28: A three-dimensional reconstruction of the first atom probe measurement of the inner wall limiter deposition zone

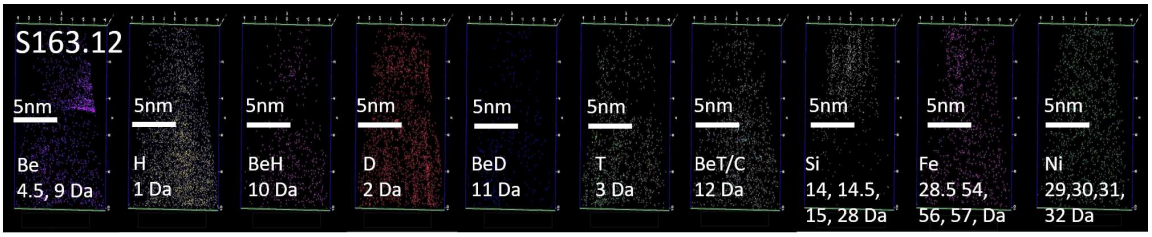


Figure 5.29: A three-dimensional reconstruction of the first atom probe measurement of the outer wall limiter deposition zone

Both IW and OW deposits, unlike eroded regions are seen here with both D(2Da) and T(3Da) peaks. These runs were analysed for global compositional analysis; and are presented in figures 5.30 & 5.31.

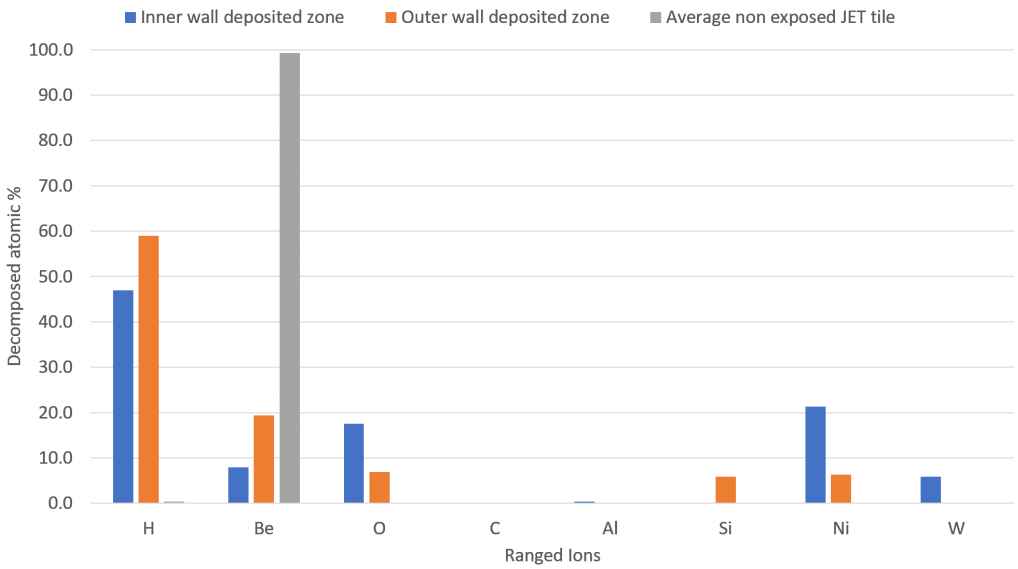


Figure 5.30: Comparison of atomic % composition of all ions decomposed between outer and inner wall deposited zones and a NE-Be JET sample.

Comparison of total integrated hydrogenic isotopes (figure 5.30) shows both deposited locations contain significant retention: 46.95 at% IW-deposit and 58.97at% OW-deposit, far above the reference NE-Be at 0.33at%. Consistent to experimental results, the OW-deposit retains greatest hydrogenic levels; correlated to increased deposit thickness [69].

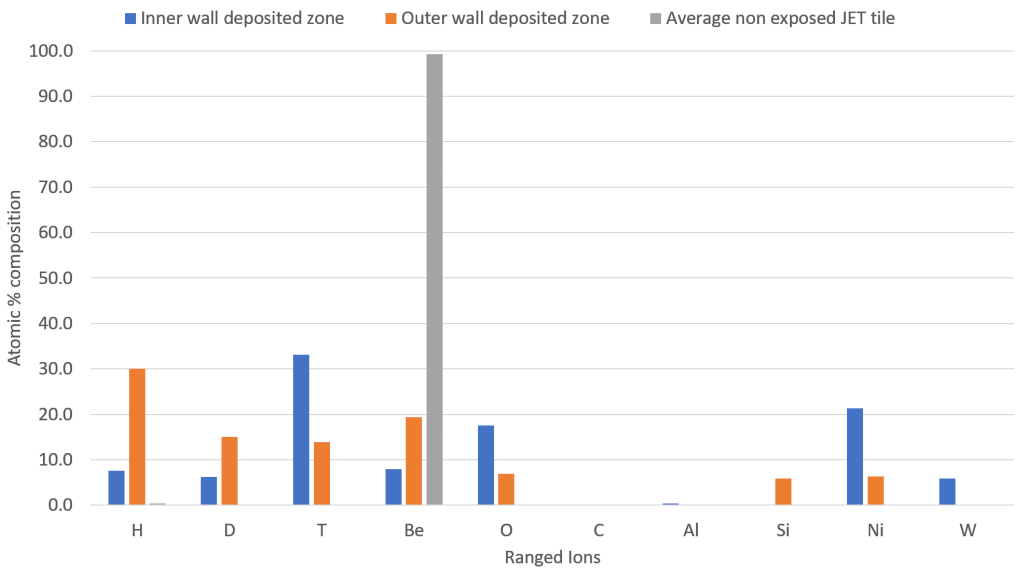


Figure 5.31: A comparison of all decomposed H isotopes present in outer and inner wall deposition zones alongside a NE-Be JET sample.

Individual integrated H, D and T isotopic peaks were decomposed and the results shown in figure 5.31. The IW-deposit accounts for H:D:T of 7.59:6.20:33.17 at%. The OW-deposit accounts for H:D:T of 30.01:15.06:13.90 at%. Relative Be levels are significantly reduced, compared to eroded samples. These results highlight the limitation of EELS in respect of hydrogen quantification; without the ability to quantify H, stoichiometries will be skewed. Be measures ∼7.96at% at the IW-deposit and ∼19.41at% at the OW-deposit. The ratios of retained H isotopes shown here, exceed those recorded in the literature. Oxygen levels for the deposited regions are elevated relative to erosion zones. IW-deposit O is recorded as higher.

Overall, some calculations are possible utilising this technique, on these fragile samples. The conclusions drawn are limited by: the varying depths of the regions probed, and lack statistical repetition; resulting in a high degree of uncertainty.

5.6 Integrated TDS of relative H isotopes present between IW and OW JET deposits

A short analysis of hydrogenic retention comparing TDS data (atoms.cm^{-2}) to nanometric APT ratios is provided, to observe whether differences in retention are present among different length scales.

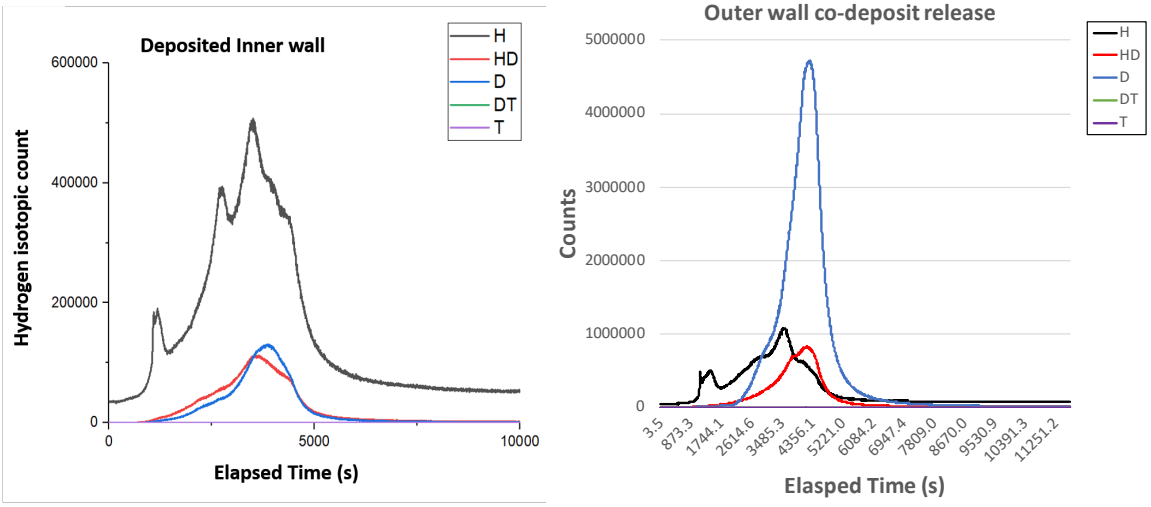


Figure 5.32: Comparison of hydrogen isotopic release for the inner and outer wall deposited materials as a function of elapsed time. Left: Inner wall deposited castellation results. Right: outer wall deposition castellation results.

Figure 5.32, shows a brief overview of the desorption seen. Hydrogen has several release peaks, whilst deuterium and HD occur with linked release. The outer limiter

retains a far greater contribution of D (mass 4).

	TDS data				APT data		
	Total retained Hydrogen - all isotopic forms	% of Hydrogen isotopes			% of Hydrogen isotopes		
Sample		H	D	T	H	D	T
Non-exposed sample	6.56E+17	99.92	0.08	0.0005	100.00	0.00	0.00
Inner wall eroded	7.86E+17	81.71	18.29	0.0000	99.13	0.87	0.00
Outer wall eroded	9.22E+17	83.59	16.41	0.0010	41.80	57.13	1.08
Inner wall deposit	1.93E+18	71.46	28.54	0.0000	16.20	13.20	70.60
Outer wall deposit	3.93E+18	44.41	55.59	0.0030	50.90	25.50	23.60
Melted dump plate	1.89E+18	88.81	11.19	0.0000			

Figure 5.33: A comparison of APT and TDS data considering atomic % of hydrogen isotopes from the two techniques.

Figure 5.33 compares percentage hydrogen isotopes at the IW and OW deposits, between APT and TDS. IW-deposit APT data shows exceptionally high T; unlike the TDS data. Either the APT data has failed by incorrect peak identification (possibly carbon contamination); or T is present in the very surface atomic layers. Greater agreement is seen between the two techniques at the OW-deposit. Overall, greater agreement between techniques, has occurred at the deposited regions than for eroded sample. This may be due to the overall increase in hydrogenic saturation at many more length scales. Deposit retention may also be more homogeneous throughout its depth profile. The OW-deposit records the highest retention of all samples, supporting correlation between greatest retention, and greatest deposit thickness.

5.7 Summary JET IW and OW deposits

This chapter presented a significant quantity of novel material and insight into reactor grown co-deposited materials for an ITER relevant Be wall.

SEM surface morphologies varied and were linked to sub surface deposit thickness. The inner wall overall, had less deposit, 1-5μm with an estimated $\sim$75% surface

coverage. The outer wall had complete deposit surface coverage; alongside cracking correlated to increased thickness. Thermal stresses were considered the cause. Surface bubble/blistering and was found at the OW right poloidal edge.

EDX and SEM subsurface investigations showed IW-deposits had two distinct phases. An intermediate phase sandwiched between the TVA marker layer and a fine scale sedimentary-like co-deposit. The intermediary phase was $\sim 5\mu$m, and the co-deposit surface phase sub 1μm. The OW-deposit displayed only the sedimentary-like co-deposit, $\sim$8-15μm in thickness. Bubbles occurred at the interface between the co-deposit and TVA marker layer; culminating in crack propagation at the right poloidal edge where thickest co-deposit occurred.

TEM with EDX suggested the deposits were less varying in impurities than first expected and had some degree of continuity across length scales. Trace components included Ni, Cu, C, N, F, Fe, Si, and Al.

EELS provided novel insights into JET co-deposits and tokamak beryllium chemistry. EELS showed less oxidation present at the IW-deposit relative to OW-deposit. Early speculation of the mechanism suggested, IW-deposits were largely governed by Be codeposition with D; whilst BeO co-deposition with D, governed the OW-deposit. The highest, non stoichiometric quantity (8 at%) was measured for OW-deposits.

Comparison of JET results to EUROFusion grown samples (BeO, BeD, and BeOD) muddied the water somewhat. At the Be core loss spectra, the OW mirrored most the BeOD sample, with elements of other grown samples. Comparison of O core loss, showed 3 very similar grown spectra to the OW-deposit. Low loss comparisons also suggested BeOD as the main component; with a viable conclusion that BeOD bonding was present in both samples but higher at the OW-deposit.

Unfortunately, experimental comparison to DFT modelled results, provides another layer. At the Be and O core losses, the modelled DFT results are accurate for fine structural shape, but not position (modelling work remains ongoing). The low loss DFT results are accurate in both. Considering Be core loss results; here the DFT Be spectra reflect well the fine structure of both IW and OW JET results. BeH_2, BeO_2H_2 orthorhombic, and BeO_2 presence is suggested via fine structure comparisons. Considering O core loss results, the BeO_2H_2 orthorhombic system most reflects the OW-deposit, by the relative peak heights. However, in the low loss region, correlation between JET samples; EUROFusion samples; and the DFT results; most suggests BeH_2, alongside some evidence of oxidation via broadening at the OW-deposit. The DFT results, raise the possibility of both BeD_2 and a small component of BeO_2H_2 orthorhombic presence in these samples.

Overall, the JET samples likely contain a significant portion of BeD_2, alongside varying degrees of BeO_2D_2. Of interest to those creating EUROFusion lab grown tokamak relevant samples; is that these samples do reflect JET tokamak grown materials well, however the differences between BeD, BeOD, and BeO, are less discernible. Greater precision needs to be developed in production methodologies to achieve greater disparity and accuracy in BeO, BeD, and BeOD.

Atom Probe tomography of these samples, could not present the spatial distribution of discrete layers, nor spatial preference of deuterium; however, it did calculate the relative ratios of Be:O:D. The results, presented a much higher degree of D present, the missing piece in the Be:O EELS stoichiometries; and a final piece of evidence suggesting the presence of BeOD was likely real, alongside BeD_2 presence.

Literature authors [17] have suggested D retention remains lower in oxidised samples. This does not seem the case here. TDS data showed the OW-deposit held the greatest retained total hydrogen, (and deuterium). Enhanced TDS release occurred at the OW. Increased OW-deposit retention, could either be due to BeOD presence and/or greater overall deposit thickness.

Chapter 6

Microstructural analysis of melted JET materials

6.1 An introduction to melted materials in JET

With the upgrade in JET's neutral beam injection, during ILW1; melting occurred at regions along the dump plate [4, 55, 63], and Be splats were found in the divertor. These samples underwent high thermal loads from plasma interactions, where the plasma mid-plane was 'vertically displaced'.

This chapter investigates melted materials for chemistry, microstructure and composition. The dump plate sample is shown in figures 1.2 & 1.4. The poloidal left edge of the castellation has a macroscopic region of melted material.

SEM investigated the surface morphology across the castellation length. Two distinct morphologies were present; a melted (macroscopically mounded) region and non-melted area. The chapter treats these materials separately, focussing first on the melted material, and secondly on the remainder of the surface (the second microstructure).

Raman microscopy across the surface of this sample found BeOD bonding present, only in the melted region. Confocal microscopy estimated surface roughness. FIB 3D milling of the melted region, investigated subsurface deviations in BeOD bonding regions. SEM-EDX depth analysis was performed on lift-outs. Raman lift-outs were thinned for STEM with EDX and EELS.

The second microstructure was investigated repeatably. SEM with EDX was applied to the subsurface depth profile, and further thinned for STEM with EELS and EDX. EELS was expanded spectrally, to include C and Ni; and employed on surface microstructures linked to desorption.

TDS of a surrogate sample, one poloidal position away, occurred due to size incompatibility.

6.2 SEM of the surface morphology and microstructures present

Only one castellation of the melted dump plate was available for examination.

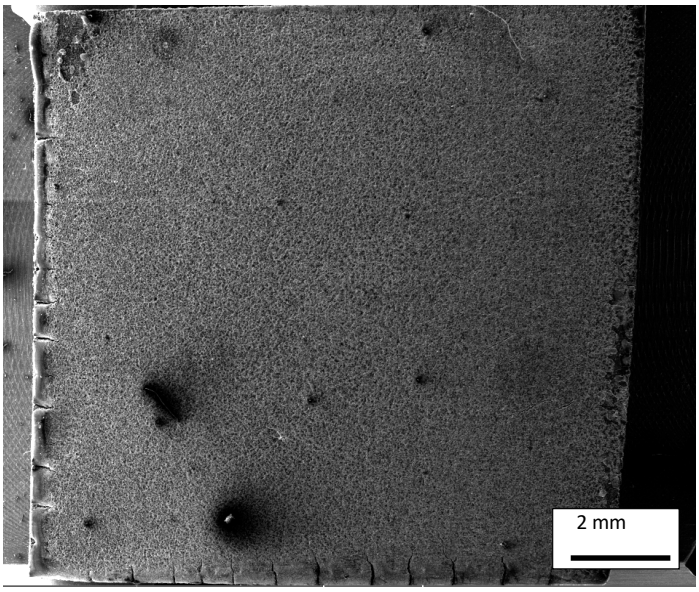


Figure 6.1: A SEM SE image of the dump plate castellation; providing an overview image of the whole surface area.

Figure 6.1 shows the typical two microstructures seen on a macroscopic scale. At the left poloidal edge, and to a lesser extent the base of the tile, is a region of melted material, mounded and cracked. The top left poloidal corner is displayed in figure 6.2, showing the melted region and remaining surface of: high surface roughness rounded globular features. The lightest regions (figure 6.2(b-c)) refer to higher elemental weight, likely uncovered Ni marker layer, originating ∼8-10μm into depth. Two microstructures are present. Figure 6.2(c) represents the rest of the surface area and majority of the surface microstructure. Using image tools, the melted region accounts for ∼7.7mm^2 +/- 3.5mm^2. The second microstructure accounts for ∼126mm^2 +/- 2.2^2. The standard deviations here represent pixel gray scale variation, which are higher at melted sample edges, due to contrast effects. The proportion of melted material is ∼5-6% of the total surface area.

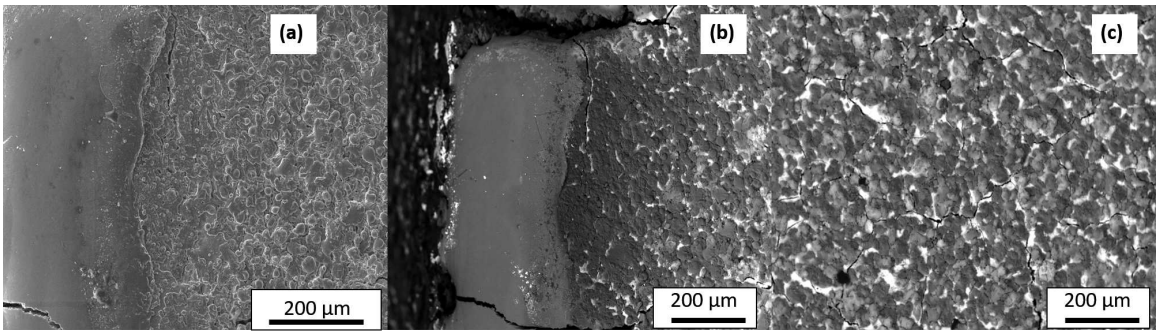


Figure 6.2: Three SEM images. (a): SE image of the left poloidal melted mound and to the right, the secondary microstructure. (b): the same position via a backscattered electron image. Lighter regions refer to heavier elements. (c): BSE image of the sample's surface at the centre. White regions are valleys. Dark spots occur from de-lamination.

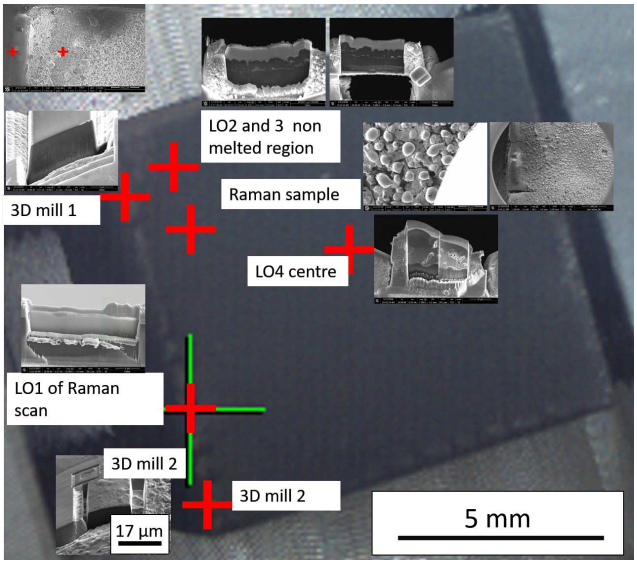


Figure 6.3: A (FIB) optical image, via the navigational camera; overlaid with sampling locations and their typical microstructural SEM SE images.

Figure 6.3 presents those regions where sampling occurred across the castellation's surface area.

6.3 The melted ridge microstructure

6.3.1 Subsurface SEM and 3D milling studies

Several regions were probed in the melted, mounded region and are presented in figure 6.4.

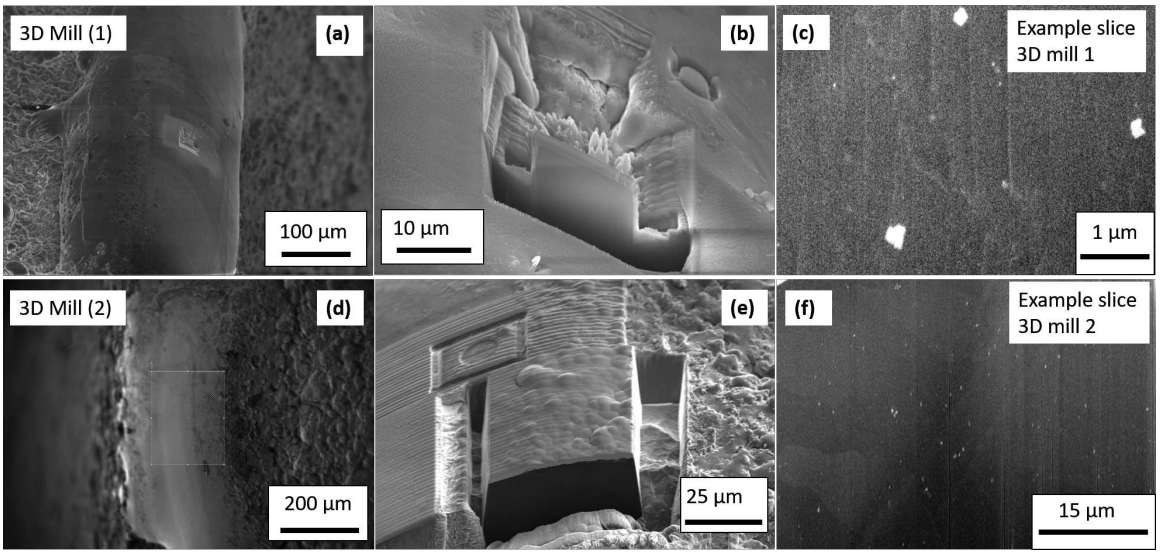


Figure 6.4: Top (a-c): three SEM SE images of the melted mound at the top poloidal LHS sample edge. (a): Overview of a Raman region which identified BeOD bonding. (b): The final slice of the 3D milling study. (c): A 3D milling slice of the exposed face with high contrast precipitates in a low contrast Be matrix. (d-f) Three identical examples of at the sample's left poloidal base. (d): region of interest, (e): 3D milling study, (f): representative slice.

Figure 6.4 shows representative microstructures of the exposed faces seen during the 3D milling studies. Slight qualitative differences can be seen in white precipitates present in (c) & (f). Thresholding image analysis was applied to every 10th slice with Fiji (appendix B). The average white precipitate area was $\sim$270 nm^2 with a standard deviation of 0.5 nm^2. The particles incorporate $\sim$0.15% +-0.001 of the whole exposed facial area. These errors are double the standard deviation of the data set. There is additionally, a substantial human error present from thresholding, alongside errors from changing background contrast (from (FIB) milling and local surface roughness). The error is likely closer to 30%. Features thresholded at the poloidal base region were two small (nanometric) to be measurable relative to the pixel size.

6.3.2 Surface: Raman Spectroscopy & Confocal microscopy

Raman spectroscopy of the surface is briefly introduced here to present a summary of the results published in [112, 111]. Figures 6.5 & 6.6, present a sequence of SEM images, at the surface, increasing in magnification to outline the position of the Raman scan area relative to the macroscopic area.

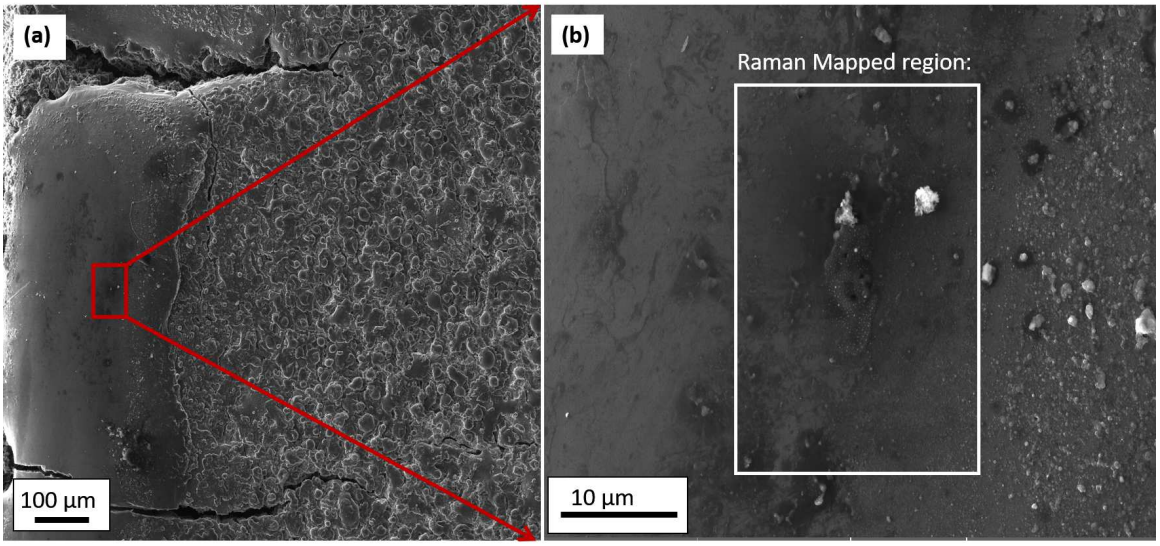


Figure 6.5: Two SEM SE images showing the area of the Raman mapped surface region at increasing magnification from (a-b)

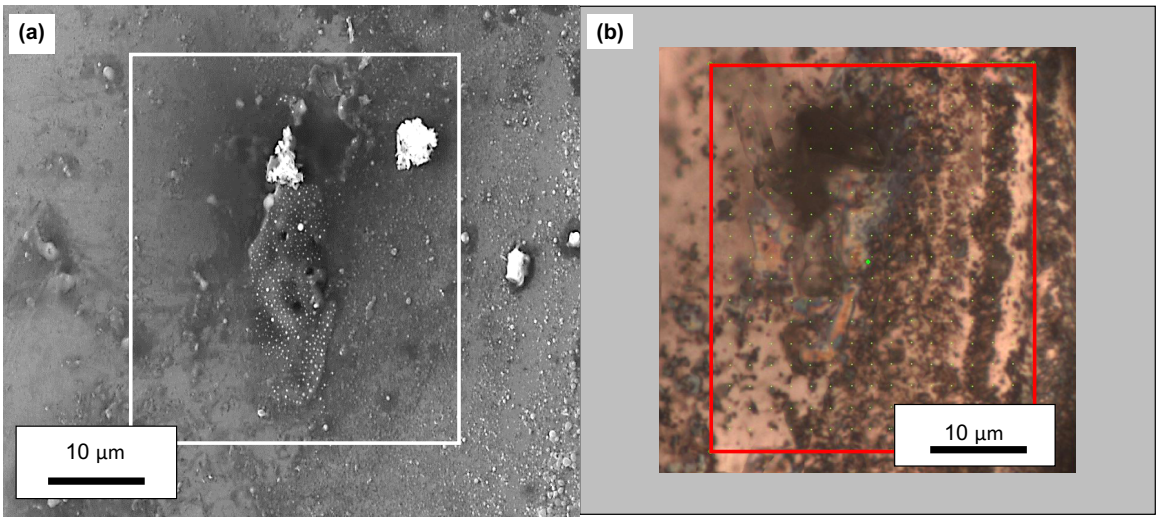


Figure 6.6: (a): SEM SE image showing the Raman mapped surface region. (b): The corresponding Raman optical image with the mapped region marked in red.

Figure 6.7, shows a complex picture of the melted beryllium JET surface. The component bands present are shown in figure 6.7(a), and the complete representative JET spectra in figure 6.7(b).

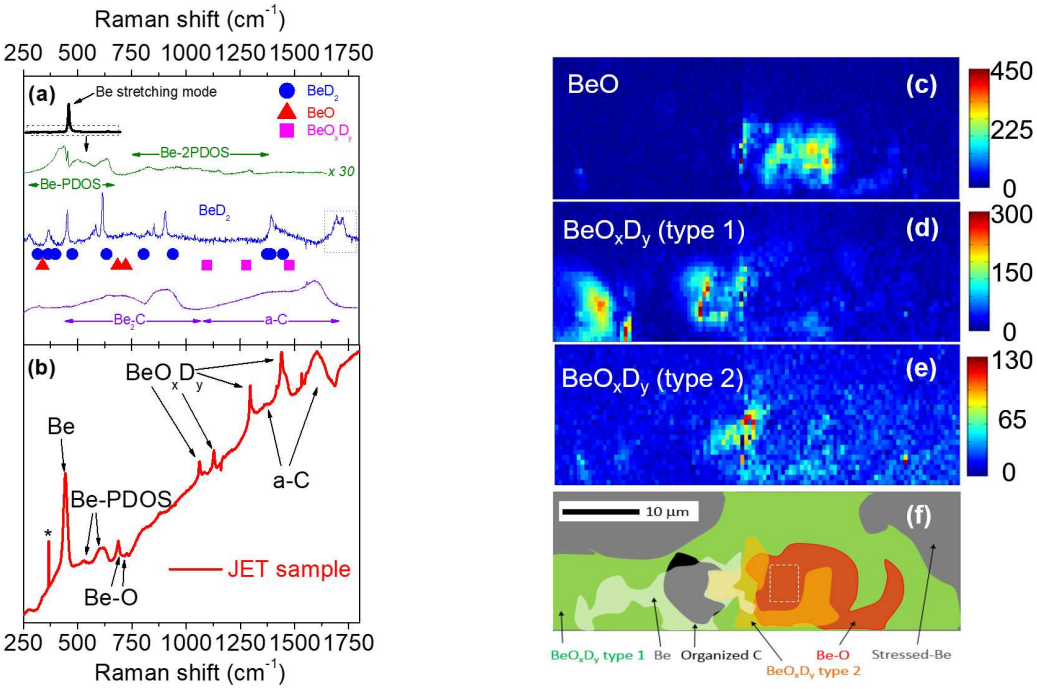


Figure 6.7: (a) Graphed prospective spectral bands: Be stretching mode at $\sim$450cm^{-1}, the Be phonon densities of states (PDOS), correlate to defect number densities; BeD_2 spectra [28], BeC_2 and amorphous carbon B&G bands [29]; BeOD and BeO positional spectral bands [30]. (b): A typical JET spectrum from the melt region. Increasing background is due to carbon contamination. Areal maps (c-e): show areas where spectral regions have high associated intensity of BeO and BeOD bonding. (f): A schematic marking those surface areas with highest intensities of relative component bands, Be up-shifted, Be, BeO, C, and two suggested types of BeOD.

The results presented in figure 6.7 were compared to literature of BeOH under infra-red spectroscopy [30]. IR has different quantum selection rules to Raman spectroscopy, and have been taken into account in figure 6.7(a). Only those peaks corresponding to Raman selection rules have been marked. These are novel results and show BeOD bonding present at the surface of the region shown in figure 6.6.

Figure 6.7(c-e) presents the spatial orientation of oxide and deuteroxide at the surface. The overlap of islands suggests segregation and growth linking one-another. The red beryllium oxide region is suggested an island, from which type 2 (orange) and thence type 1 (white) BeOD regions grew.

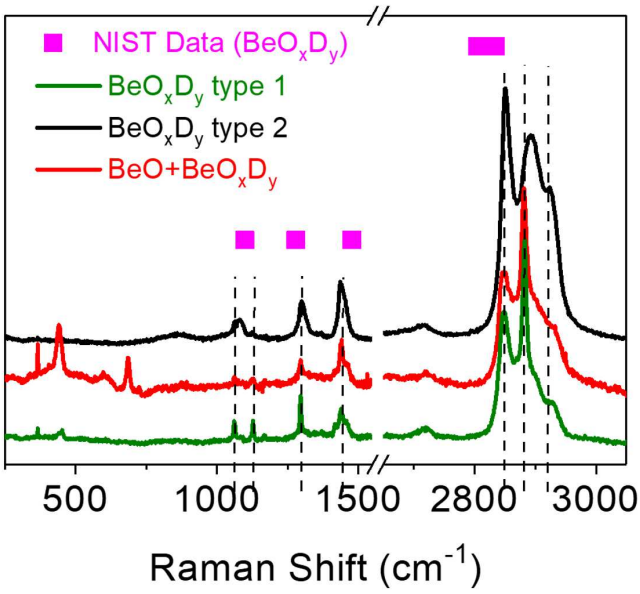


Figure 6.8: Three extracted Raman spectra from an additional map of the same region, with expanded spectral range showing: a highly resonant band correlated to the BeOD and smaller bands at 1040, 1110, 1240, and 1460 cm^{-1}. Changing relative intensities of the bands: 2840, 2880, 2910 cm^{-2}, alongside 1040, 1110, 1240, and 1460 cm^{-1}; suggests presence of multiple BeOD stoichiometries.

Extracted spectra from a map of the same region as that presented in figure 6.7, are shown with an extended spectral range, in figure 6.8. Figure 6.8, provides the argument for suggesting two possible Be-OD bonding stoichiometries.

The evidence promotes correlation between spectral intensities of representative bands. Where there is greatest intensity in the 2840cm^{-1} band, 1040 and 1110cm^{-1} bands, appear condensed and unresolved to one another. At higher intensity, a 2880cm^{-1} band appears alongside all four smaller bands of BeOD. The shape of the shoulder present at 2910cm^{-1} also varies. These results were repeated at several melt regions, each sampling 10s of μm^2 per map. A distribution of this bonding across the samples is shown in figure 6.9(a)-(b).

Figures 6.9 & 6.10, suggest BeOD is highly sensitive to the local plasma environments; and melt direction. Across the length of the sample, on average BeOD occurred most, towards the sample's base and poloidal left edge; left of the melt pool. The sample was not square. Shifts in plasma direction, may explain the number of successful identifications in this region. These results suggest BeOD bond formation has either thermal or plasma optimum conditions; represented spatially on the

substrate. At higher magnification (figure 6.9 (b)), plasma shadowing could likely explain the position of BeOD. This explanation assumes that local mound shape does not affect Raman detection efficiencies via scattering. Sub-surface investigation of the region by Raman and EELS would rule out surface effects.

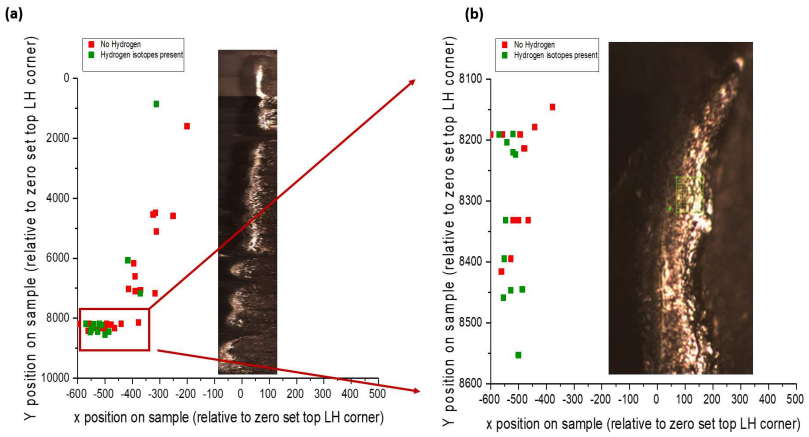


Figure 6.9: Two montaged Raman optical images. (a): The total length of the melted region, areas where BeOD was present are marked in green. Regions in red had no BeOD bonding present. (b): The region with greatest BeOD density at higher magnification. BeOD appears sensitive to the plasma direction, relative to the mound.

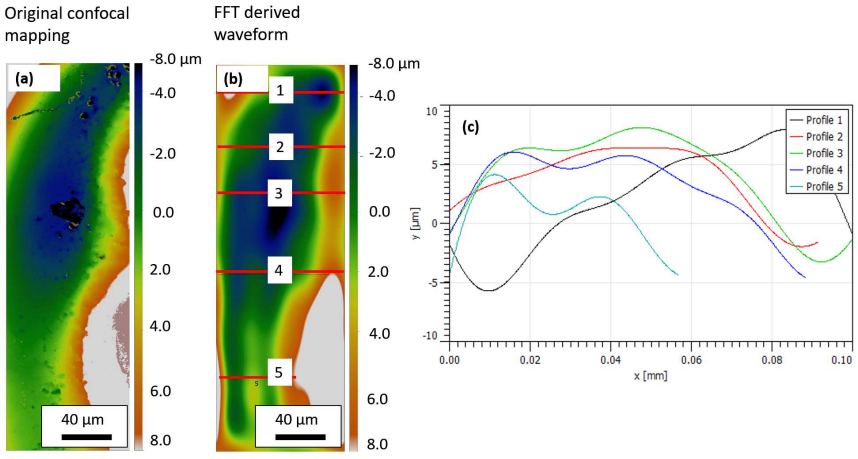


Figure 6.10: (a): Confocal microscopy heat map results of the area (figure 6.9). Fast Fourier Transforms (FFT) were applied to separate large waveforms, of macroscopic gradients, from changes in local roughness. (b): FFT results of the mound's local waveform and height. The mound is $\sim 10\mu$m higher than the remaining sample surface. Other extracted waveforms from their line profiles are also presented. The central maxima shifts spatially, from sample top to bottom.

A final surface comparison is provided of the second microstructure, which rep-

resents approximately 94-95% of the surface area (in figure 6.11). A larger waveform and extracted mid-line profile; is displayed in figure 6.11(a-b); alongside local roughness in (c-d). The surface height varies by $\sim 10\mu$m from valley to peak, with smaller localised areas with additional roughness spanning a further 8μm from valley to peak. No BeOD Raman bands were identified anywhere in the second microstructure, probed across the toroidal midplane. Confocal microscopy suggests the total roughness extremely high; and sufficient to reduce Raman scattering below detectable limits. Pardanaud [29] showed the relative interaction volume of the laser light probes maximally $\sim$300nm of the surface depth. Local roughness greatly exceeds this.

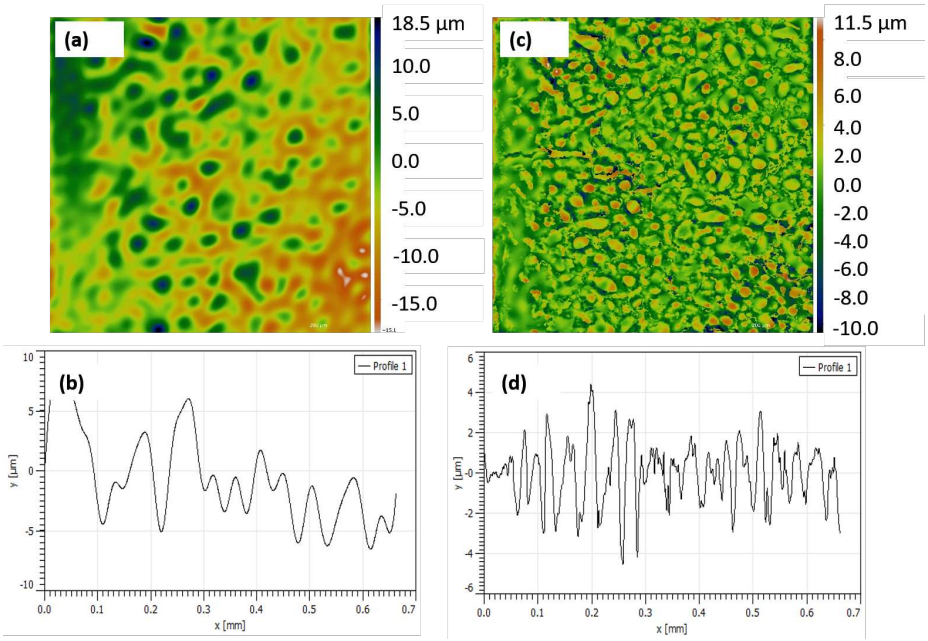


Figure 6.11: Figure (a-b) the second microstructure's localised waveform, right of figure 6.10's melt pool; and FFT extracted profile. Figures (c-d) FFT areal roughness map and, respective midplane profile.

6.3.3 SEM-EDX of melt region lift-outs

The surface region, identified with BeOD bonding via Raman, was subsequently examined under SEM with EDS. The results of Be(qualitative) and O maps are presented in figure 6.14. The region was examined with increasing SEM accelerating voltages: 5keV, 10eV and 15keV. Their interaction volumes were subsequently modelled using the casino software [109]. The modelled maximum beam penetration depths were $\sim$250nm, $\sim$400nm, and $\sim 2\mu$m. Progressive O maps at different depths enabled a rough estimation of the extent of oxidation. Figure 6.12, shows (quali-

tatively) the oxide present down to $\sim 2\mu$m; far exceeding the assumed nanometric oxidation resulting from vacuum impurities [71, 84, 85, 86, 88, 89].

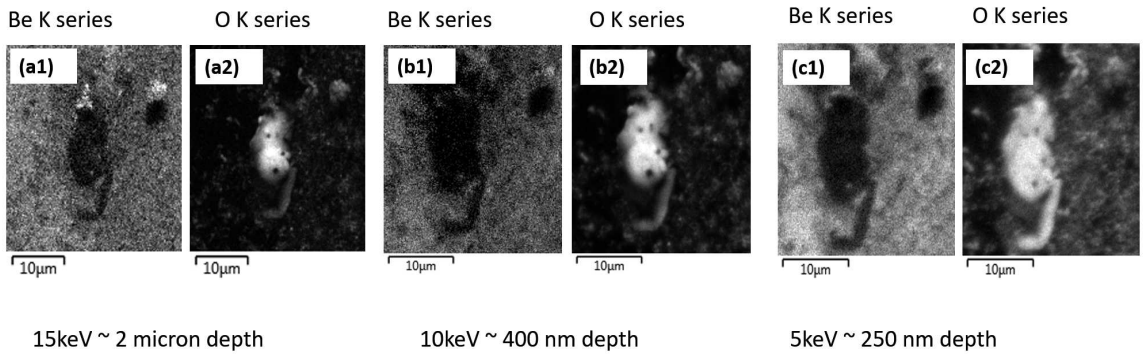


Figure 6.12: Three pairs of figures showing the relative beryllium and oxygen EDS maps (left to right): 15keV, 10keV, and 5keV, with signals corresponding to interaction volumes of approximately 2μm, 400nm and 250nm respectively.

A lift-out of the region, taken from the oxide's central length, was produced for SEM-EDS analysis. A surface oxide present atop a region, rich in Be and Ni was found. Beneath the oxide region, the Be/Ni rich region occurred with precipitates rich in Ni, Al and O; shown in figure 6.13.

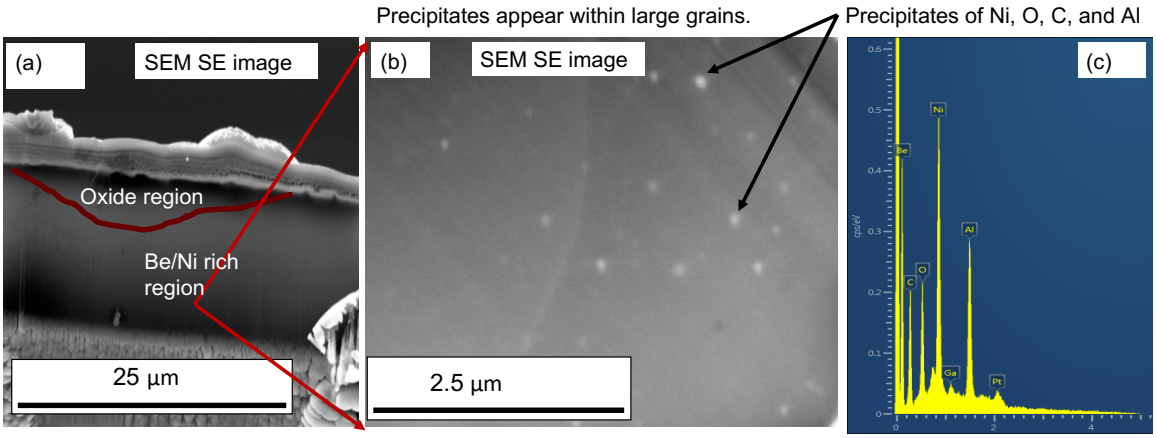


Figure 6.13: Higher magnification SE image. (a): The lift-out. (b): Higher magnification of the lift-out beneath the oxide region. (c): EDS spectra of higher contrast white precipitates rich in Ni, Al, C, and O.

6.3.4 Scanning Transmission Electron Microscopy of the melted lift-out with EELS and EDS

The same lift-out was milled to electron transparency, and examined under STEM with EELS and EDS; to determine stoichiometric ratios of oxidation. Figure 6.14, shows a STEM HAADF overview showing atomic weight contrast (top image). The oxide region is clearly displayed with little to no C or Ni contamination, versus the Be/Ni/C matrix region beneath.

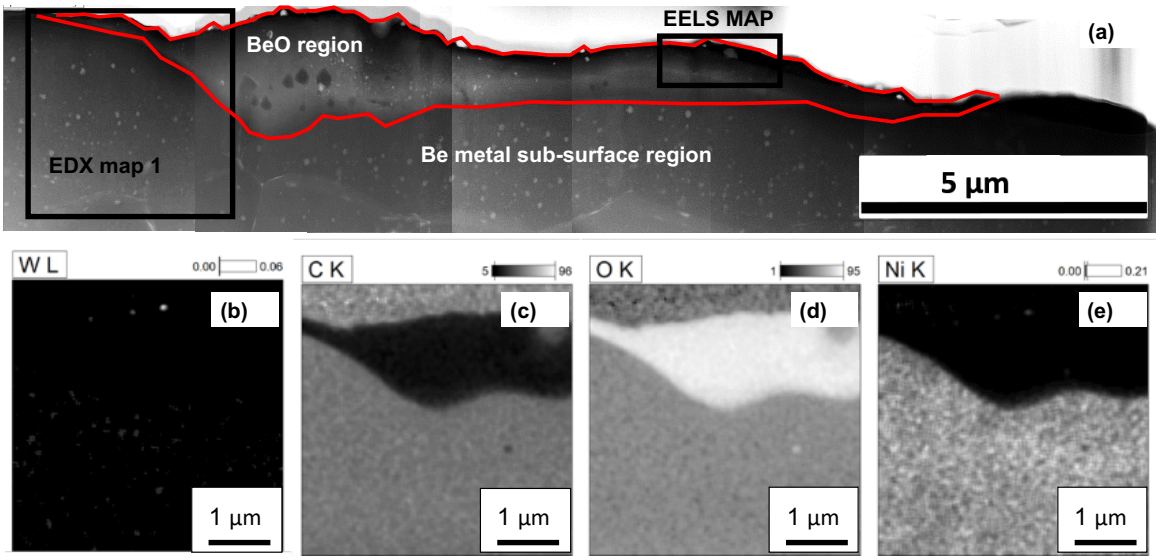


Figure 6.14: (a): STEM HAADF overview of a central slice of the melted BeO Raman region, showing the subsurface BeO seen with low magnification EDS, marked in red. The EDS region indicated by 'EDX map1' is displayed in (b): W (L) map, (c): C (K) map, (d): O (K) map, and (e): Ni (K) map.

6.3.4.1 STEM and EDS

A Detailed EDS survey is presented in the following figures 6.15–6.17, showing relative compositional changes between the surface oxide and subsurface matrix region. These comparisons are given to understand the regions of the lift-out prior to EELS stoichiometry measurements, where applicable.

Figure 6.15 clearly displays a 2 phase region, between the oxide devoid of metallic impurities at the surface; and the subsurface Be-Ni rich region. The Oxide region displays exceptionally high O with fractional impurities (N and Ni). The matrix beneath registers Be, C, N, O, F, and Ni. As always, regarding EDX of Be materials, this analysis is qualitative and only comparative between regions. The cleanliness of

the oxide region, suggests the Raman analysis correct, confirming the highly resonant ~2880cm^{-1} peak, as likely BeOD and not another component.

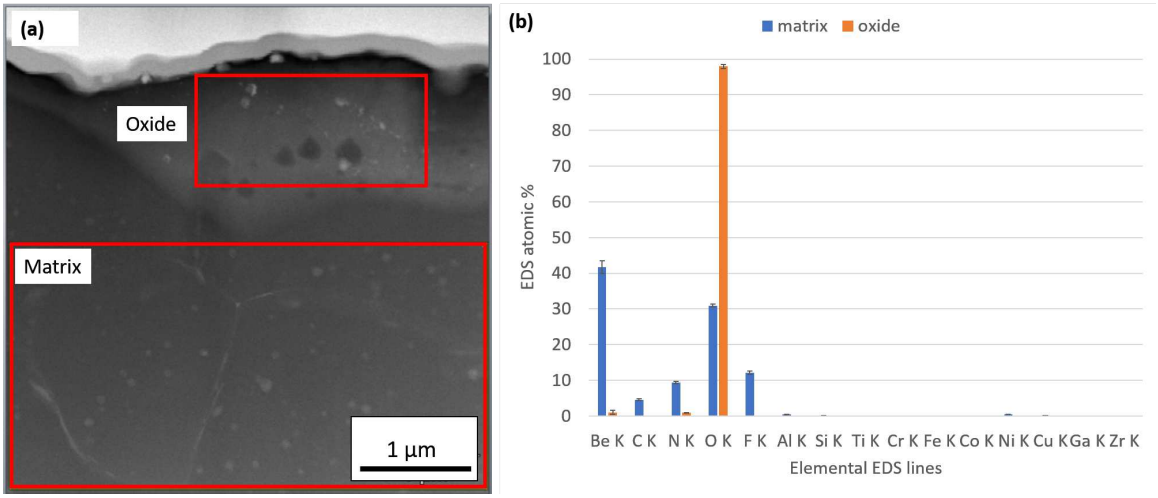


Figure 6.15: A comparison of EDS composition between the two regions seen in the overview; that of the surface oxide and the subsurface matrix region. (a): STEM HAADF image of the regions. (b): EDS spectral compositions of the respective areas.

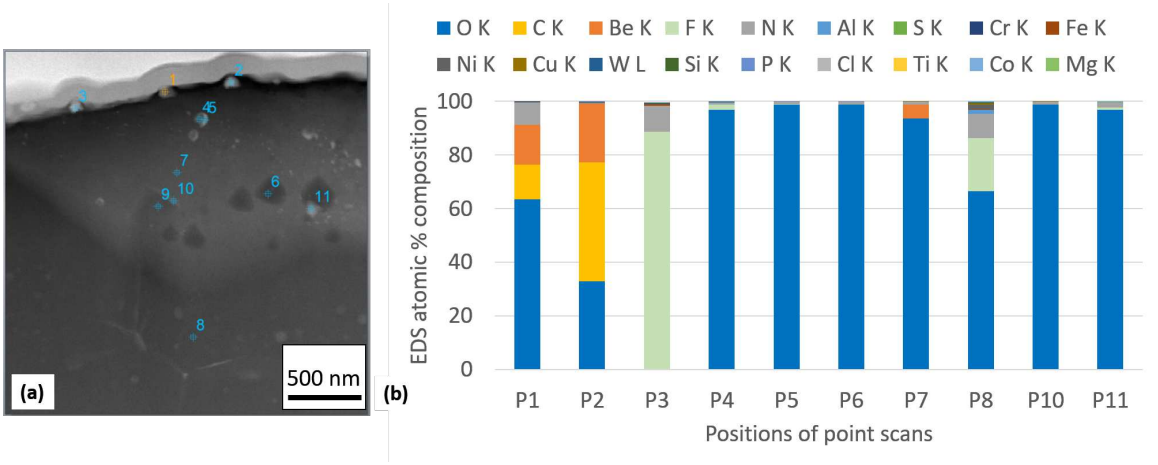


Figure 6.16: Point scans extracted from the oxide region in (a): the STEM HAADF image. (b): The extracted stacked bar chart of the points' EDS compositions.

Figure 6.16, shows extracted point scans of the oxide region. These were used to investigate precipitation mechanisms within the oxide and impurity inclusions. Points nearer the surface (1, 2, and 3) show higher relative levels of C and N. Point 3, with high F, is likely due to the protective Pt raising the spectral background. C is also linked to platinum during FIB production. N, was used to enhance plasma

detachment, and likely a remnant of operation. Points 4-6, and 10-11, are almost purely oxygen (via EDX). Point 8 shows the subsurface matrix with F, N, Ni and Al, contributions.

Some elemental compositional changes are present in the oxide, with inclusion of Nitrogen at the surface. The subsurface matrix rich in Al and Ni, suggests material mixing from marker layers. Presence of N in the subsurface region indicates a time where N was available during the melt formation, and oxygen was not. Literature suggests oxidation to the levels of μm seen here, could only occur from repetitive material melting. This combined with EDS evidence suggests the subsurface region comprising the mounded area formed ahead of the subsequent iterations of oxidation.

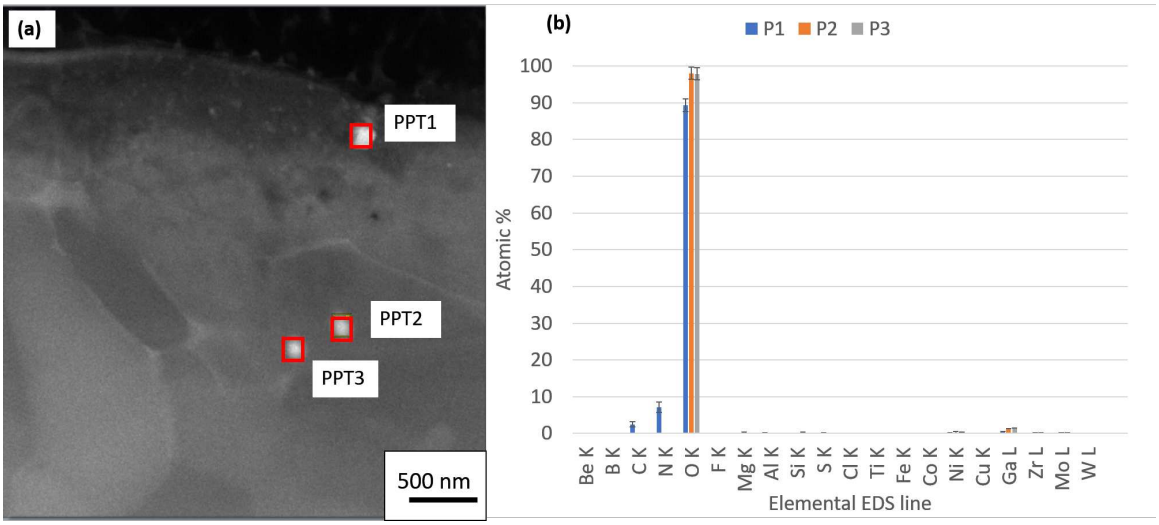


Figure 6.17: (a): Area EDS scans of bright precipitates present in the STEM HAADF image (the same area was investigated with EELS). (b) The corresponding EDS compositions.

Greater inclusion of N at the oxide surface under higher magnification conditions in figure 6.17 confirms the results seen thus far.

6.3.4.2 STEM and EELS

Figure 6.18 displays the results of hyperspy curve fitting to produce a Be at.% and O at.% map of the region. The exported stoichiometries are displayed in figure 6.18(c). The EELS measurements show a small Cu contamination at the surface, likely due to platinum deposition or neutral beam injection impurities in JET. EELS results at points 3 and 7, show an oxide approaching 1:1 stoichiometries. Similar impurities: C, and N, appear present, in the EDS bar chart, in all but point 8, a largely Be grain,

which may be approaching the second microstructure. The results show even within the oxide island, that there are differing extents of oxidation.

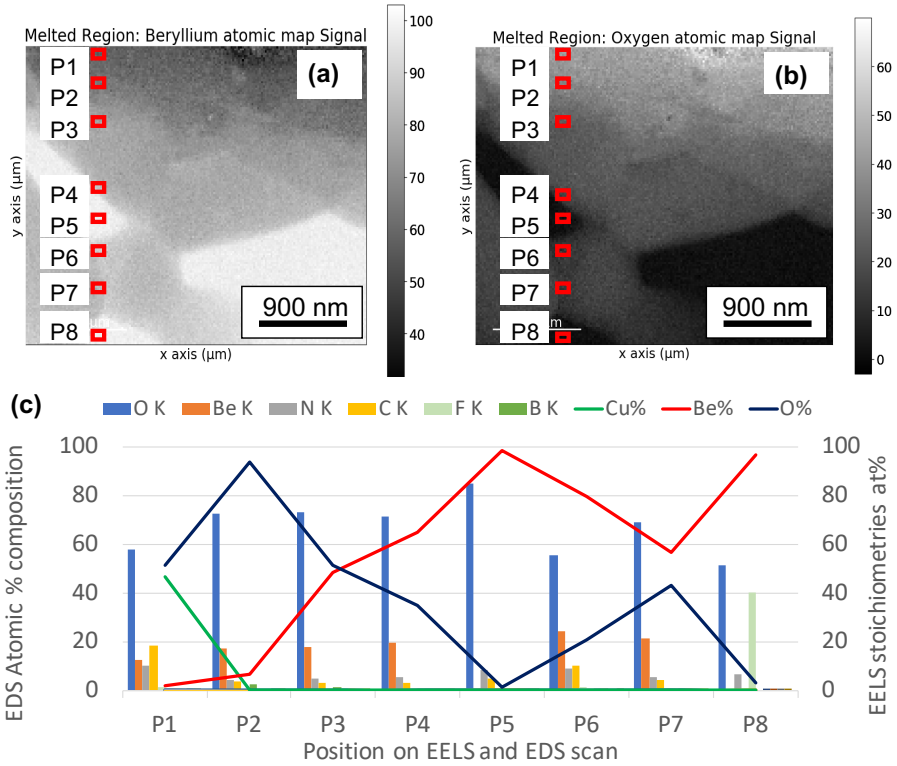


Figure 6.18: The melted lift-out region. (a): EELS Be at.% map. (b): EELS O at.% map. Regions marked in red are presented in (c): graphing EELS Be and O stochiometries (line) against EDS impurities (bars). Cu (M) (green) was also calculated in the EELS stoichiometries, because of a pre-edge region indicative of a transition element impurity.

Be core loss spectra are extracted from the points displayed in figure 6.18 and shown in figure 6.19, alongside DFT modelled EELS Be core losses of relevant structures. It is important to note, at this time, the shape of the modelled spectra are accurate, whilst the peak position work remains ongoing for the core loss calculations. However, from the modelled spectra it is easy to validate the pure Be curve. It is suggested that at phases where Be onset remains, alongside an increase in fine structure intenstiy at ~120eV, some elements of BeH_2 and/or BeO_2H_2 is apparent, due to both peak shape and broadening at ~125-130eV. The respective tetragonal oxide seems also likely. At phases where the onset occurs at ~118eV, BeO_2H_2 may account for the whole phase.

The O core loss and modelled spectra are presented in figure 6.20, points 5 and 8, were not plotted here, since signal normalisation resulted in a noisy, flat line, due

to the absence of O in the position. Some small discrepancies seem to be occurring between oxidised regions in the samples, by the relative shape and ratios of peaks ~538 and 543eV. This difference may be explained by presence of both orthorhombic BeO_2H_2 and hexagonal BeO. Both tetragonal and hexagonal oxides seem likely culprits of the increasing intensity between 555-580eV.

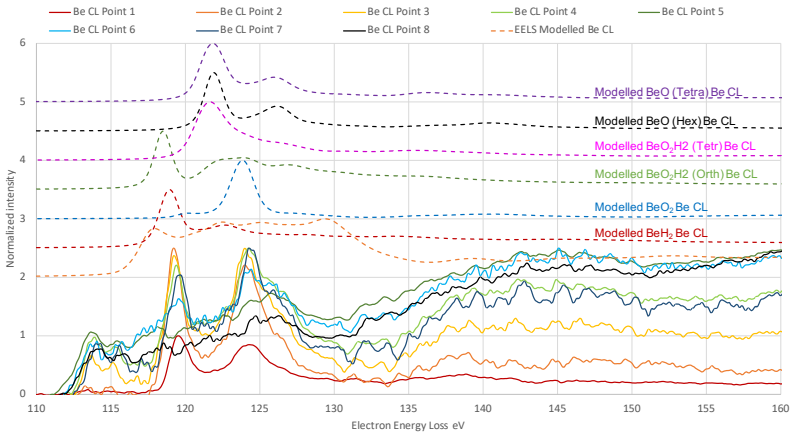


Figure 6.19: EELS Be core loss spectra of points displayed in figure 6.18, the JET positions are plotted normalised to 2.5 times, DFT modelled EELS spectra of different structures containing Be, O and H are graphed iteratively. Only the fine structural shape is accurate

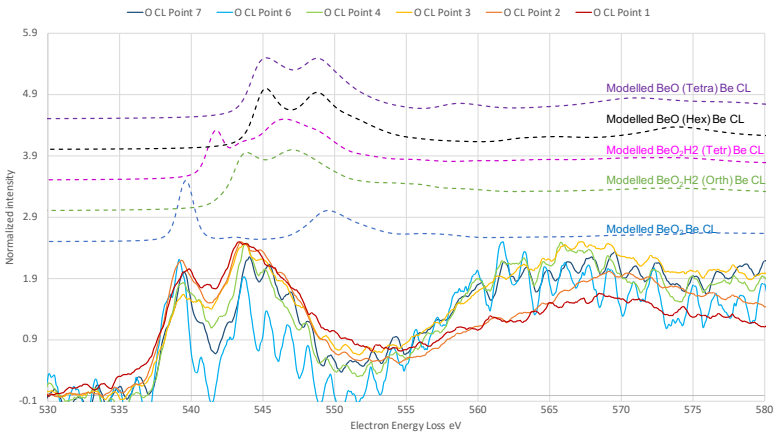


Figure 6.20: EELS O core loss spectra of points displayed in figure 6.18, the JET positions are plotted normalised to 2.5 times, DFT modelled EELS spectra of different structures containing Be, O and H are graphed iteratively. Only the fine structural shape is accurate

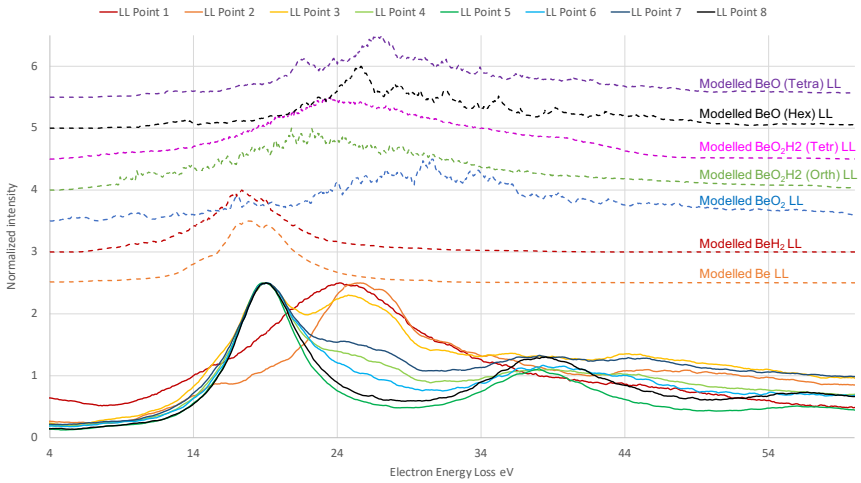


Figure 6.21: EELS low loss spectra of points displayed in figure 6.18, the JET positions are plotted normalised to 2.5 times, DFT modelled EELS spectra of different structures containing Be, O and H are graphed iteratively. Both shape and onset energies are accurate.

The final comparison is made between the extracted JET low loss spectra and the DFT modelled low loss. There appears to be 4 features in the JET data: a repeatable peak at ∼18.8eV; a separate structure at 24.5eV; a double peak between ∼18.8 and ∼24.5eV and finally a peak at ∼26.5eV. When comparing these results to the modelled results, there may be some overlay occurring between the Be plasmon and BeH_2 peaks, accounting for 18.8eV; however this is only present by peak broadening at 18.8eV.

The experimental peaks at ∼24.5eV and ∼26.5eV, including the double peak, occur most at the surface of the sample, but correlate most with both tetrahedral and hexagonal oxides, and tetragonal and orthorhombic hydroxides. The increased background intensity in a particularly broad peak at points 2-3 are suggestive of the tetrahedral BeO_2H_2. This component also appears present for positions 4,6, & 7, and absent at 5 & 8, indicative of absence in solely Be grains. The outcome of the comparison suggests the Raman results could be explained by differences between tetrahedral and orthorhombic hydroxide presence.

The effects of increasing lamella thickness was ruled out by further thinning and re-examination. Low magnification results of both EELS and EDX are displayed of regions of normalised area count, in figures 6.22-6.25.

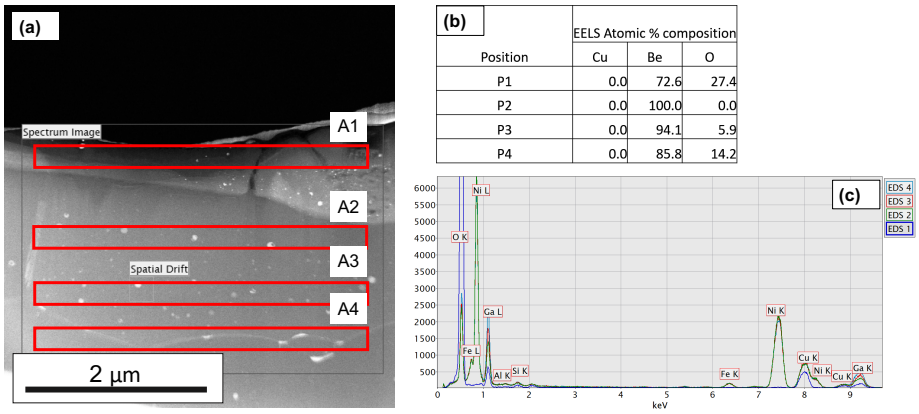


Figure 6.22: Raman lift-out region after second thinning ruling out thickness effects. (a): STEM HAADF image at low magnification, with integrated areas marked in red from A1(oxide)-A4 (into depth). (b): Be and O at.% via curve fitting. (c): EDX of the 4 regions.

Figure 6.22 shows at lower magnification, the same liftout, after thinning. The results are as expected over larger area comparisons. Region 1, the oxide, has an averaged 27.% O and 72.6% Be, with no Cu presence in the EELS calculation. EDX shows significantly higher oxygen in the region with only Ga, and a small Cu impurity. Regions 2-4 have significant quantities of Ni, implicit of material mixing with the marker layer.

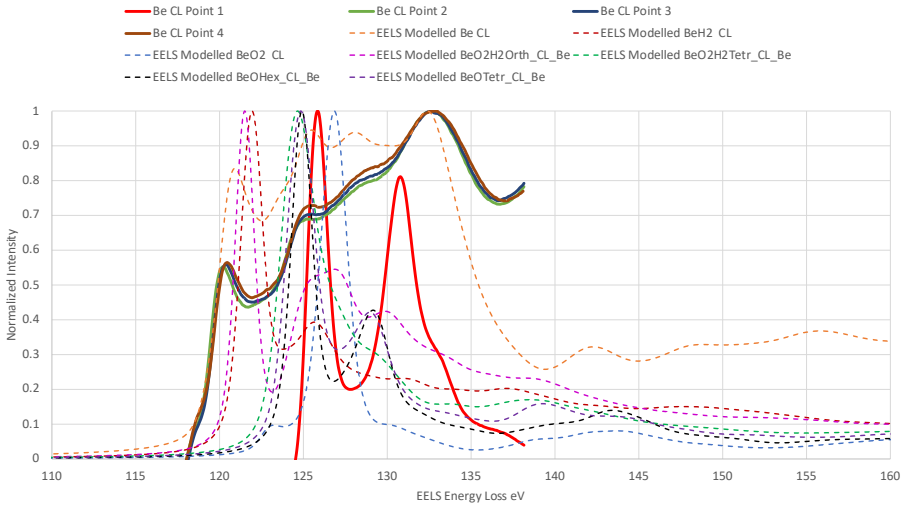


Figure 6.23: EELS Be core loss for regions 1-4 of figure 6.22, with DFT modelled spectra superimposed. The modelled spectra are accurate in shape but less in position. Some energy adjustment has been utilised +/- 1-2eV to show, where overlay could occur.

Figure 6.23 shows the Be core loss against the DFT modelled spectra. The greatest

accuracy exists between the modelled fine spectral shape, rather than position. Some energy adjustment has been routinely applied for the reader's convenience. From the comparison, the oxidised region 1, correlatives well to both tetrahedral and hexagonal oxides, alongside tetrahedral beryllium hydroxide.

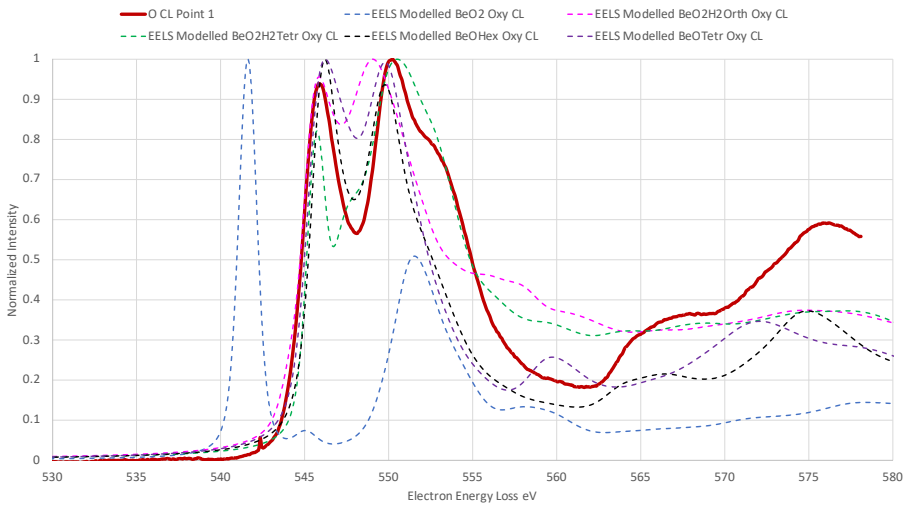


Figure 6.24: EELS O core loss for region 1 (figure 6.22), vs DFT modelled spectra. Modelled spectra are accurate in shape but less in position. Some energy adjustment has been utilised +/- 1-2eV to show, where overlay could occur.

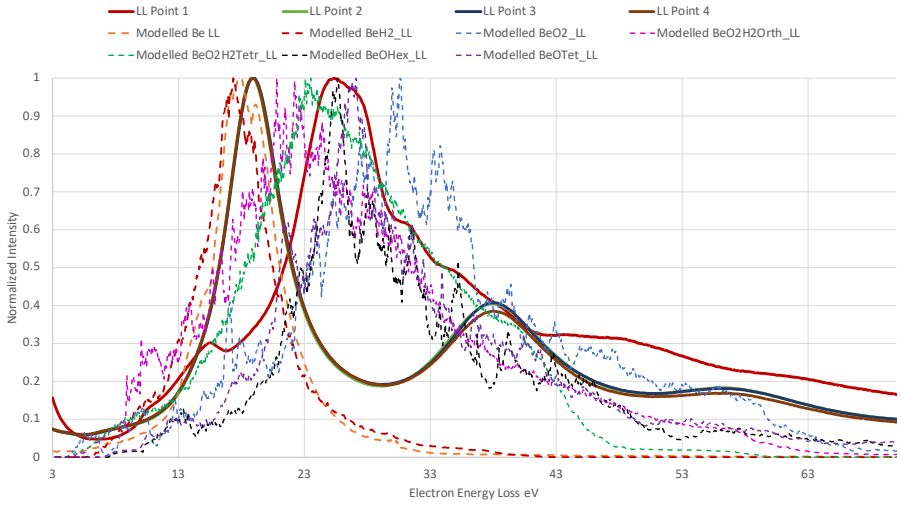


Figure 6.25: EELS low loss for regions 1-4 (figure 6.22), vs DFT modelled spectra. Modelled spectra are accurate in shape and position.

The DFT structures are only compared to region 1 in figure 6.24, due to very little oxygen presence in the sub oxide regions. The comparison of structures here suggest

the intensity ratio of the orthorhombic beryllium hydroxide with the broadening of the tetrahedral hydroxide. Some contribution from the tetrahedral oxide is also likely.

The final comparison between JET regions 1-4 and the DFT modelled low loss is presented in figure 6.25. Here both position and shape are accurate for modelled spectra. The results show reginos 2-4 beneath the oxide likely trap some BeH_2 or BeD_2 -for JET materials. Region 1 can be described by a combination of BeO_2H_2 tetrahedral, with both tetrahedral and hexagonal beryllium oxides.

Two further graphs of this region, at greater magnification, post second thinning, show the repeatability of the features presented in figures 6.23-6.25, and are attached in the appendix B.

6.4 The second microstructure at the surface:

What follows in this section, is an investigation of the second microstructure (accounting for ∼94 at% of the surface area); specifically, to ascertain the extent and effect of material mixing between the Be and the Ni marker layer.

An argument could be made that this material does not represent the ITER case, being far from beryllium implanted with hydrogen isotopes; nevertheless it does provide important understanding of the outcome of high power loads during operation in a tokamak environment. The marker layer is a source, providing a secondary metallic component with the potential to alloy, but not the only source. JET's Inconel armour plates, are not far from beryllium limiters, nor material sources from neutral beam injection.

Retention has been measured by TDS. Knowledge of material mixing in this case, can add to TDS interpretation in understanding desorption features outside the norm.

6.4.1 Subsurface SEM-EDX of lift-outs of the second microstructure

Figure 6.26 shows a complex many layered material found at the dump plate in this second microstructure. Raised surface globule features (figure 6.26(b)) consist of Ni, O and Cu at this magnification under SEM-EDX. Pt from a FIB deposited protective layer, shows the roughness of the surface. Ni diffusion appears present across a minimum 12μm.

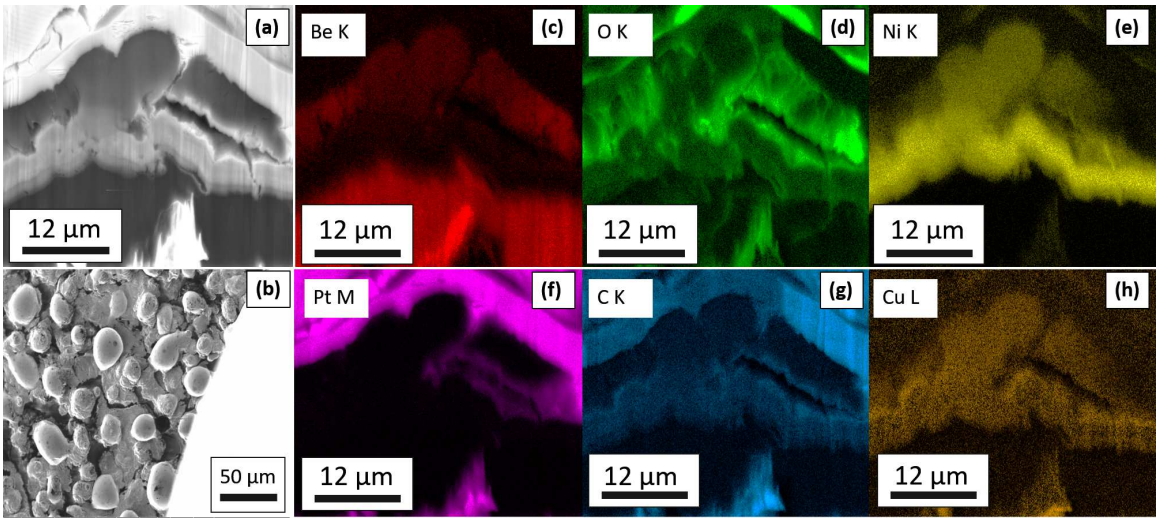


Figure 6.26: SEM SE images (a) from a central region, of the second microstructure of the dump plate; and (b) the lift-out region of interest, perpendicular to the surface. (c): Be K EDS map into depth. (d): O K EDS map into depth. (e): Ni K EDS map into depth. (f): Pt M EDS map into depth. (g): C K EDS map into depth. (h): Cu L EDS map into depth.

6.4.2 Scanning Transmission Electron Microscopy of the second microstructure

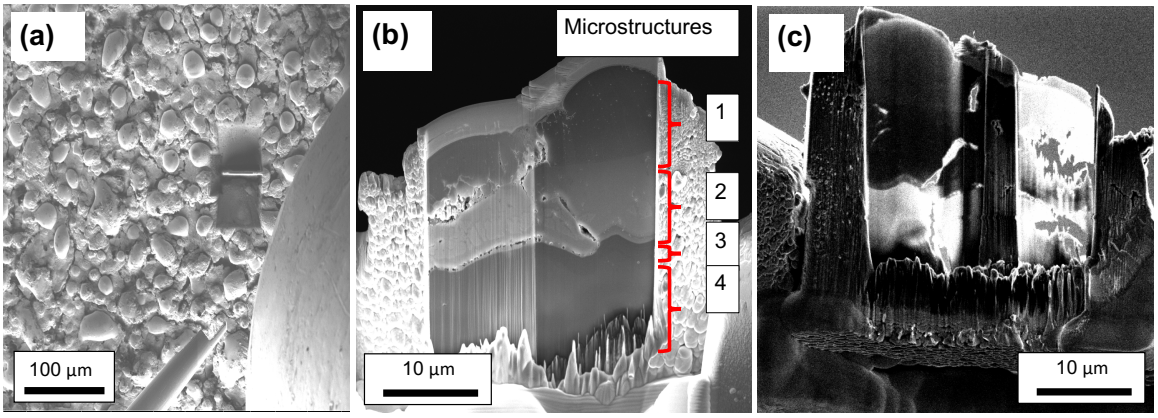


Figure 6.27: (a): SEM SE image of the lift-out region of interest from the sample's centre (second microstructure). (b): SEM SE lift-out during thinning. A schematic of 4 potential microstructures is shown. The lift-out spans ~25μm into depth. (c): SEM SE image at 3kV highlighting regions of electron transparency, implying differing atomic weight.

Figure 6.27, presents FIB production of the central lift-out, discussed in this section. Image (b) shows a schematic of 4 potential microstructures present as atomic contrast

in image (c). These phases will be analysed compositionally by EDX iteratively from 1-4 into depth

6.4.2.1 STEM-EDX, lift-out surface into depth:

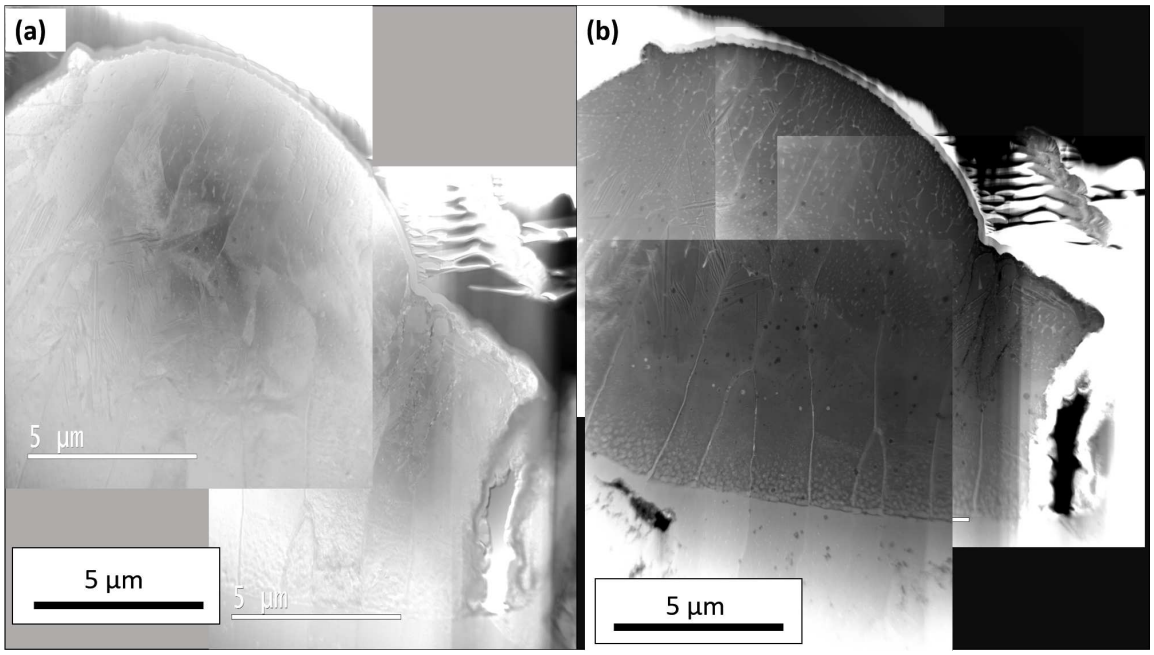


Figure 6.28: STEM ADF image (a): displaying diffraction contrast of the first two surface microstructures of the lift-out. STEM HAADF (b): displaying atomic weight contrast. Lighter regions represent higher Z elements.

Figure 6.28, shows the complexity of the first two surface microstructures (from figure 6.27(b)). The HAADF image (b) contrast distinguishes the two regions.

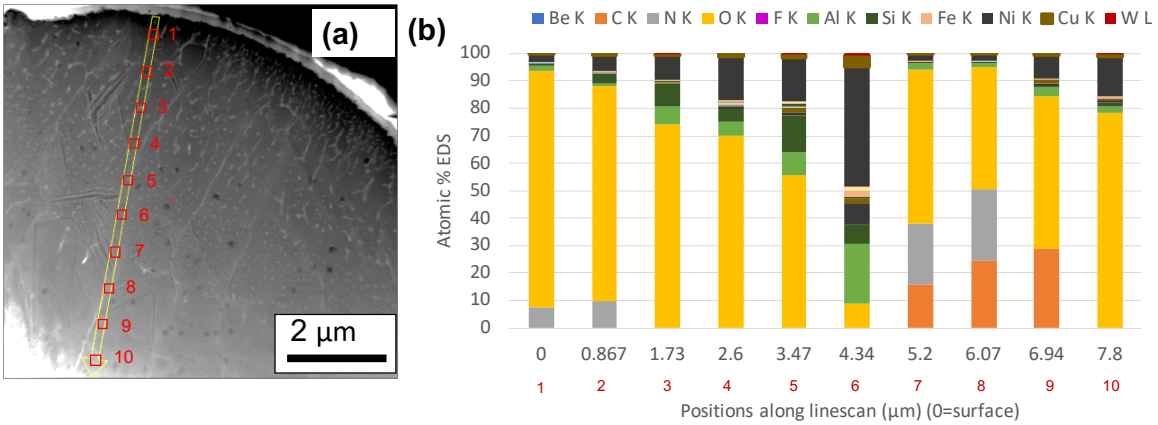


Figure 6.29: (a): HAADF image of the surface microstructure with (b): EDX line scan results presented as a bar chart.

Figure 6.29(b) displays an EDX linescan of the first surface microstructure. O and Ni are the main components. Ni increases in at% up to point 6 alongside many other metallic impurities: Cu, Fe, Al, Si, and W. Larger grains at points 7-8 appear less impurity laden with larger degrees of C, N and O; however Ni increases again into the second microstructure.

A higher magnification linescan was taken of the first 600nm of the surface in figure 6.30(a), to investigate closer the composition of features. The surface features, points 1-6, contain mostly N, C and O. The feature at point 7, with lighter contrast is richer in Ni; whilst Al, appears responsible for atomic contrast of filamentary features at points 9-10. Points 18-20 further into the surface are again richer in Ni.

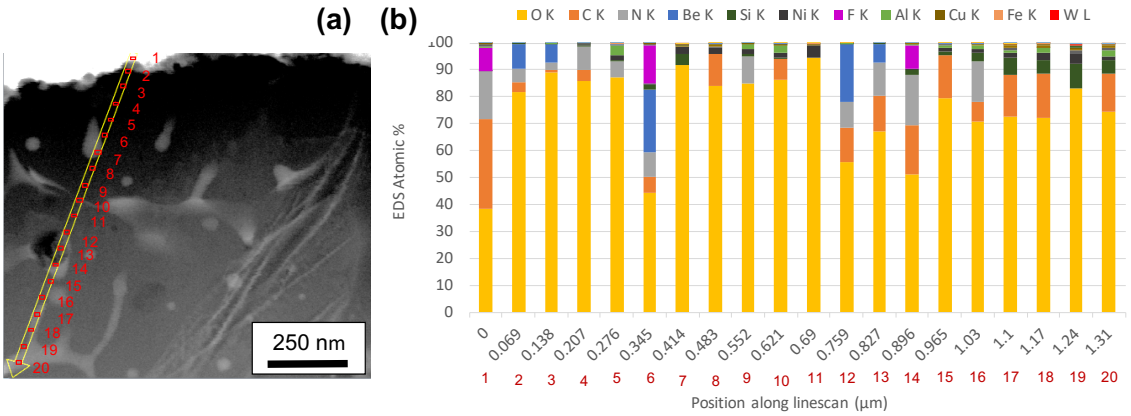


Figure 6.30: (a): HAADF image of the first 600nm of the surface microstructure of figure 6.29 with EDX line scan results presented in (b): the bar chart.

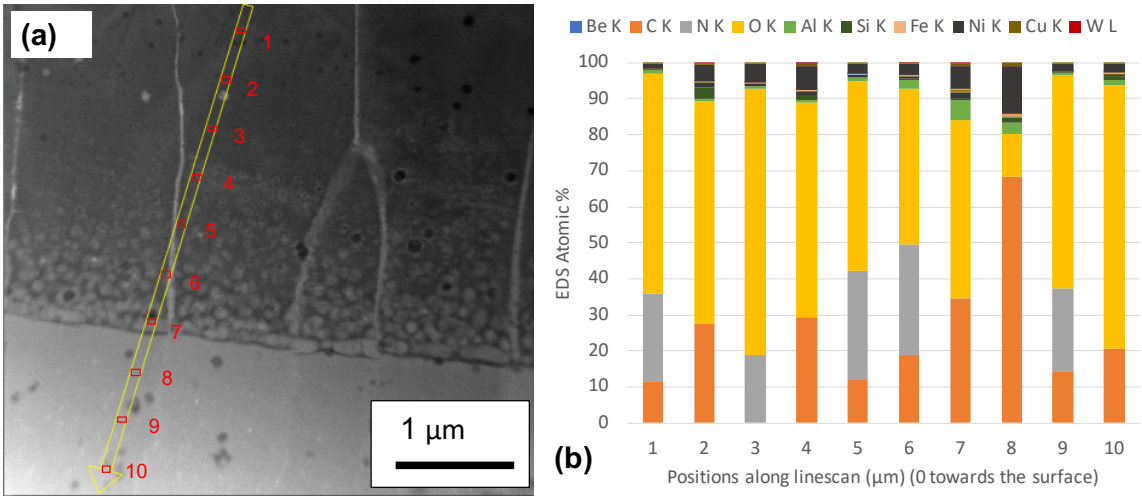


Figure 6.31: (a): HAADF image of the transition between microstructures 1-2, in figure 6.27(b), with EDX line scan results presented in (b): the bar chart.

Figure 6.31 presents the interface of the first two microstructures. The EDS bar chart shows an increase in carbon and nickel at the interface. Oxygen once again remains a significant compositional component; perhaps suggesting beryllium presence.

Points 6-7 show the filamentary structures richer in C. Despite the changing contrast of the HAADF image, the phases appear only the result of composition variation in: O, N, C, Ni, Al, Si, Fe, and Cu.

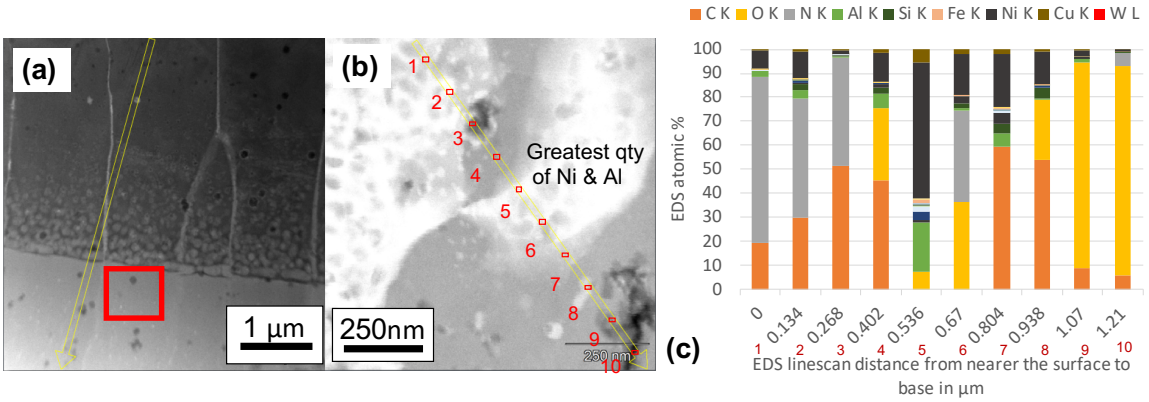


Figure 6.32: (a): HAADF image of the 2nd microstructure in figure 6.27(b), with EDX line scan results presented in (b): the bar chart.

The second microstructure is displayed at higher magnification in figure 6.32(a-b). These linescan results show a much more varied, complex composition. Light regions 1-3 (in (b)), appear high in: N, C, with no O presence. Lower contrast regions: 4, and 7-10; show substantial oxidation. Point 5 measures a significant portion of Ni.

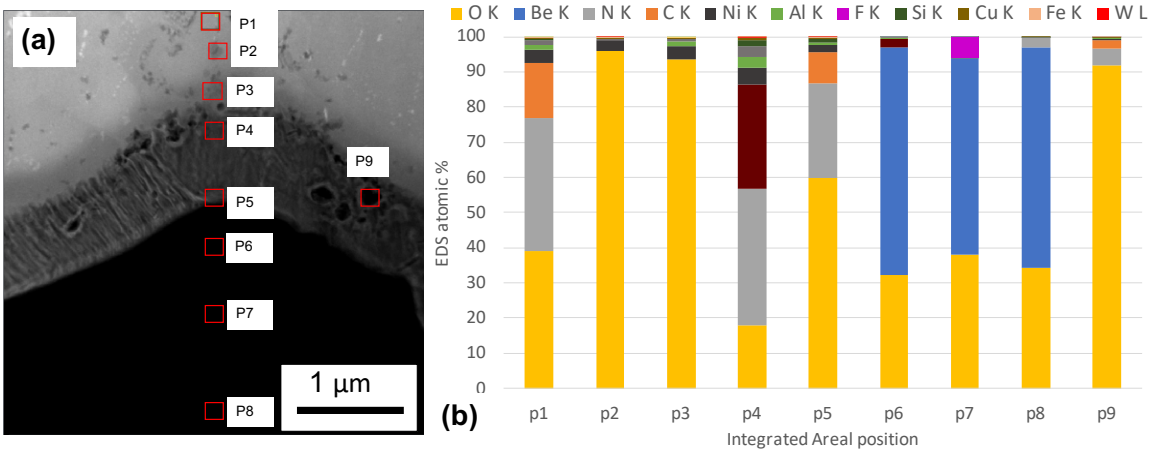


Figure 6.33: (a): HAADF image of the 3rd and 4th microstructures in figure 6.27(b), with EDX point scan results presented in (b): the bar chart.

The final microstructural intersection is displayed in figure 6.33(a), from the bottom of the lift-out at $\sim 20\mu$m depth. A three phase region is present. Points 1-3 display the variation seen in the previous microstructure, high in O, with C, N, Al, and Ni impurities. Point 4 appears the remnant of the original Ni marker layer, however with Na, N, C, and O presence. This suggests that at some point during operation, this layer has been present to the surface or at the very least molten. Points 6-8 are presumed the S65-H Be substrate upon which the marker layers were prepared. This is presumed from EDX with uncertainty without EELS measurement.

The complexity and many phases present in the depths probed, implies high thermal loadings under different time periods, occurred on this sample and is the result of many plasma events.

6.4.2.2 Scanning Transmission Electron Microscopy with EELS, of the second microstructure found at the dump plate tile

The surface microstructure (1) in section 6.4.2 was analysed with EELS via an expanded spectral window, including C in the Be core loss; and Ni in the O core loss region. EELS only examined the surface, where hydrogen retention was thought most probable. Figure 6.34, shows the two EELS areas, analysed.

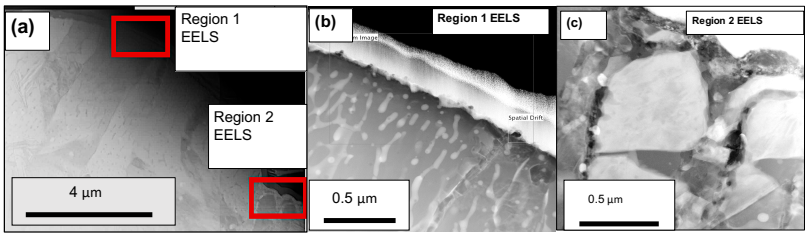
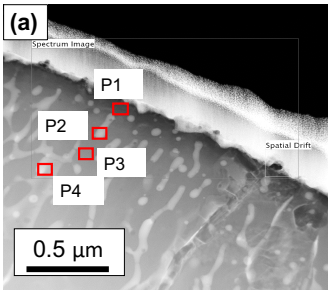


Figure 6.34: (a): STEM ADF overview image of the two surface lift-out regions where EELS mapping took place. (b): STEM HAADF image of the first EELS region. (c): STEM HAADF image of second EELS region.



(b)

	EELS hyperspy quantification at.%					
	Fe	Cu	Be	C	O	Ni
P1	0.0	0.0	71.2	0.0	8.2	20.6
P2	0.0	0.0	78.6	0.0	7.9	13.6
P3	0.0	0.0	83.0	0.0	3.5	13.6
P4	0.6	0.0	78.2	0.0	6.9	14.3

Figure 6.35: (a): STEM HAADF EELS map region 1, with standard count areas 1-4. (b): spectra were fitted and at% extracted.

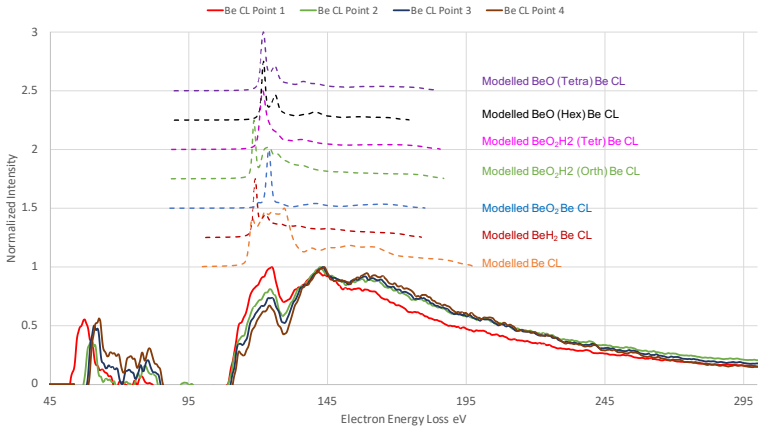


Figure 6.36: Carbon and Beryllium core loss EELS spectra 1-4, with modelled DFT results overlaid.

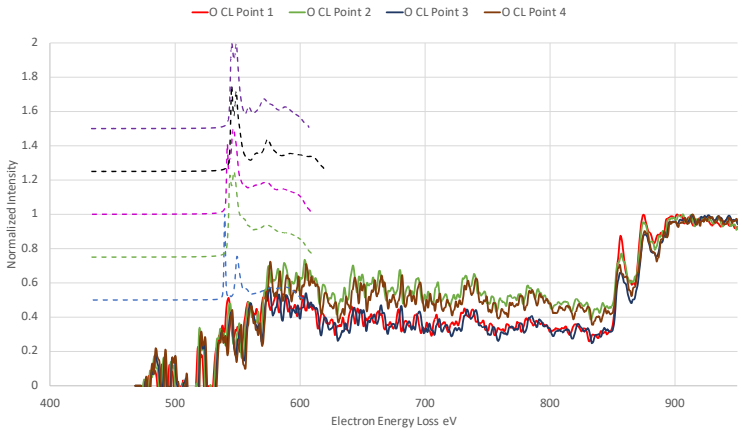


Figure 6.37: Oxygen and Nickel core loss EELS spectra 1-4, with modelled results overlaid.

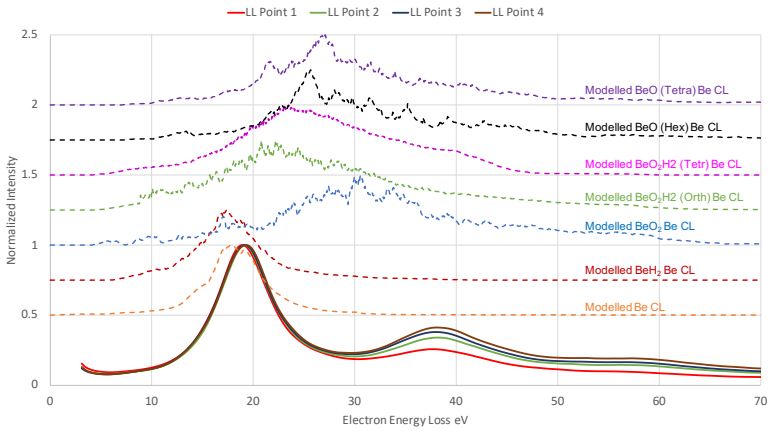
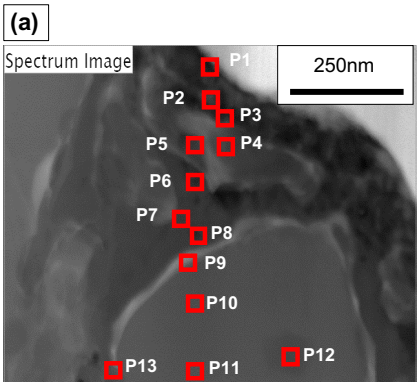


Figure 6.38: Low loss EELS spectra 1-4, with modelled DFT results overlaid.

Irrelevant of position in figure 6.35, atomic % compositions do not differ significantly. All positions range between 71-83 at.% Be, 13.6-20.6 at.% Ni, with greatest Ni present at the surface; and 3.5-8 at.% O. Oxygen appears the component most responsible for the phase contrast in the HAADF image. These findings are consistent with the EELS spectra presented in figures 6.36-6.38. In figure 6.38, in particular, the low loss structures are exceptionally repeatable, and most alike to the Be core loss model. Some broadening and higher energy shift could be indicative of a orthorhombic or tetrahedral hydroxide, however to very low levels.



(b)

Positions	Atomic % from EELS curve fitting					
	Fe	Cu	Be	C	O	Ni
P1	0.0	0.0	32.1	0.0	60.7	7.1
P2	0.0	0.0	84.1	0.0	13.9	2.0
P3	0.0	0.0	60.0	0.0	20.0	20.0
P4	0.0	0.0	60.0	0.0	20.0	20.0
P5	0.0	0.0	60.1	0.0	38.8	1.1
P6	0.0	0.0	13.6	0.0	86.4	0.0
P7	0.0	0.0	16.3	0.0	83.7	0.0
P8	0.0	0.0	16.5	0.0	83.5	0.0
P9	0.0	0.0	66.2	0.0	31.2	2.6
P10	0.0	0.0	77.6	0.0	7.9	14.5
P11	0.0	0.0	75.3	0.0	8.2	16.4
P12	0.0	0.0	76.9	0.0	9.2	13.8
P13	0.0	0.0	62.7	0.0	28.4	9.0

Figure 6.39: (a) STEM HAADF EELS map region 2, with standard count areas 1-13, (b) spectra were fitted and at.% extracted.

This second region appears to have far greater oxidation present, at the surface (point 1) and in the second phase region surrounding grains (points 6-8, & 13). A largely beryllium grain can also be seen in points 9-12, with Be at% ranging between 66.2-77.6; and O at% between 7.9-31.2; and Ni at% between 2.6-16.4 at%. This region appears to have larger grains and greater levels of oxidation; perhaps due to a slower cooling regime, with prolonged diffusion time, and grain coarsening.

These results are mirrored in the EELS spectra, in figures 6.40-6.42. Both Be and O core loss shows more of the fine structural features observed throughout JET samples, due to oxidation. In the low loss region, (figure 6.42) at points: 5, 7, & 8; a mixture of tetrahedral and hexagonal oxides by comparison to DFT modelling appear present. Points 1-3, & 13, all appear present with the broadening linked previously to orthorhombic hydroxides. Point 5 appears indicative of some level of tetrahedral hydroxide in the shape of the trailing peak at $\sim$50eV.

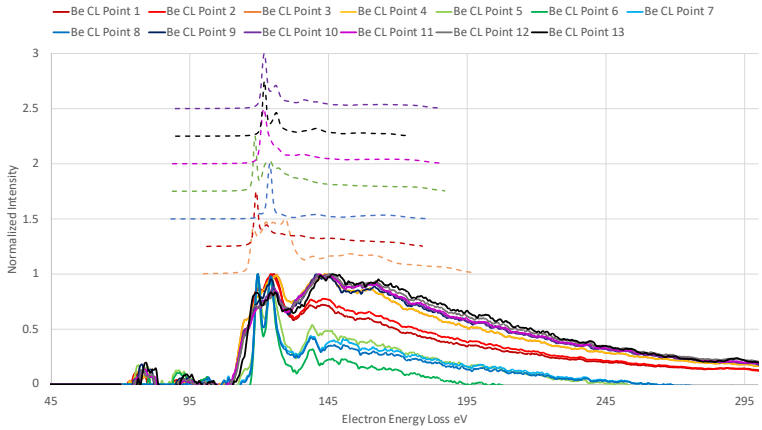


Figure 6.40: Carbon and Beryllium core loss EELS spectra 1-13, with modelled DFT results overlaid.

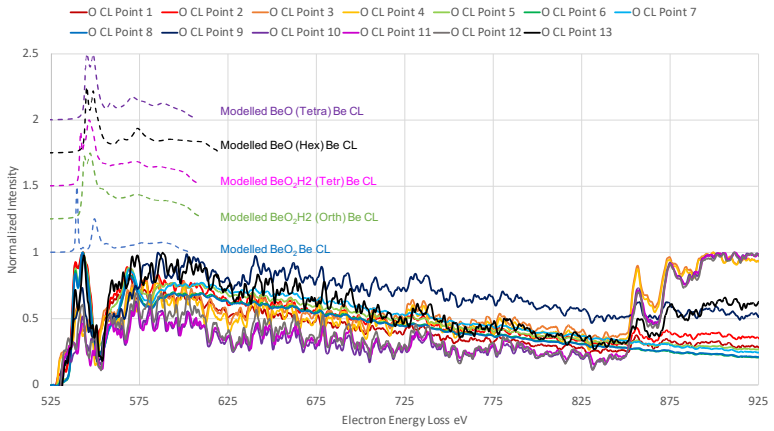


Figure 6.41: Oxygen and Nickel core loss EELS spectra 1-13, with modelled DFT results overlaid.

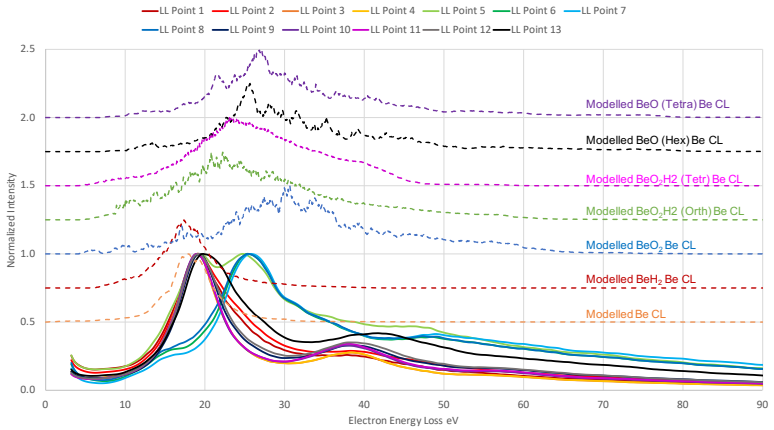


Figure 6.42: Low loss EELS spectra 1-13, with modelled DFT results overlaid.

It is clear from both regions in this second microstructure; Ni is playing a substantial role in the Be core loss fine structure, and phase compositions. Extreme heat loads and material mixing are clearly present in this second microstructure. Greater oxidation in region 2, at the local side of the surface globule, suggests even a modicum of plasma shadowing and a location closer to the substrate, lowers heat loads, whilst elongating cooling times and diffusion; resulting in grain coarsening and lower Ni levels. In line with literature, Ni is present up to ∼20at% in solution.

6.4.3 Integrated TDS data showing relative H isotopes present at dump plate in JET

These results were undertaken by CCFE's erosion & deposition group on the first ITER-like wall campaign. The castellation which underwent microstructure analysis, was unfortunately, too large to be accomodated into the TDS stage. The TDS results presented here are positioned one row above, in the poloidal direction, in figure 6.43(a).

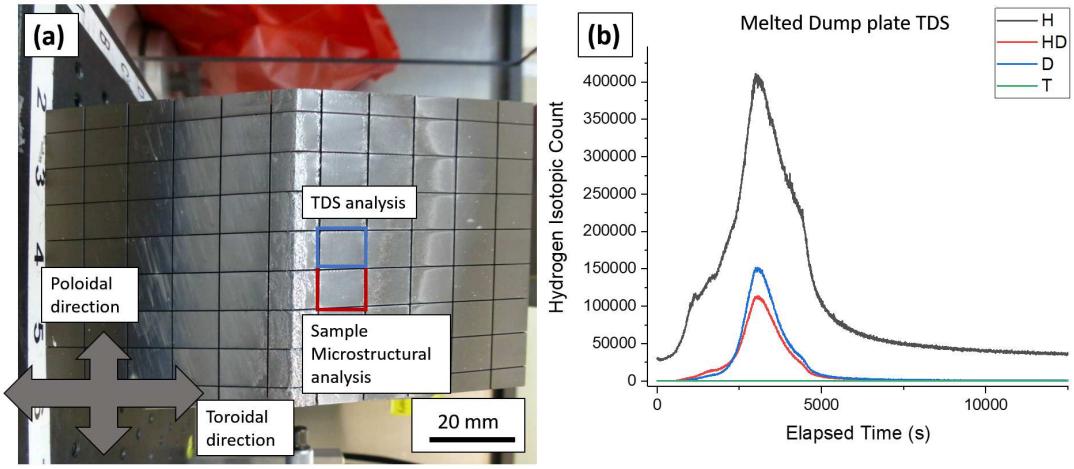


Figure 6.43: (a): Optical image of the JET dump plate tile. The sample marked in red, underwent microstructural analysis. The sample marked in blue underwent TDS analysis. (b): TDS desorption data from sample 92 (blue) against time (s)

Figure 6.43(b) shows almost coincident release of H, HD and D; unlike deposited and eroded regions where multiple primary H release peaks occurred prior to main D release. The dump plate desorption appears unique, and is perhaps linked to high Ni content. More homogeneous release, suggests greater trap homogeneity, and less low energy traps; potentially due to high implantation temperatures during operation.

Sample	TDS data				APT data		
	Total retained Hydrogen - all isotopic forms	% of Hydrogen isotopes			% of Hydrogen isotopes		
		H	D	T	H	D	T
Non-exposed sample	6.56E+17	99.92	0.08	0.0005	100.00	0.00	0.00
Inner wall eroded	7.86E+17	81.71	18.29	0.0000	99.13	0.87	0.00
Outer wall eroded	9.22E+17	83.59	16.41	0.0010	41.80	57.13	1.08
Inner wall deposit	1.93E+18	71.46	28.54	0.0000	16.20	13.20	70.60
Outer wall deposit	3.93E+18	44.41	55.59	0.0030	50.90	25.50	23.60
Melted dump plate	1.89E+18	88.81	11.19	0.0000			

Figure 6.44: A final comparison of hydrogenic retention in the JET samples found across the reactor to conclude the dump plate tile. Integrated area counts are calibrated via a calibrated leak of H_2, HD, and D_2. Calibration for DT and T_2, use the D_2 factors.

Figure 6.44 shows the final comparison between the integrated hydrogen isotopic desorption across $\sim$1cm^2 of area. Overall the melted dump plate retains an order of magnitude greater number of H atoms per unit area, whilst maintaining the lowest levels of deuterium retention below the inner wall eroded region.

All TDS data, underwent backgrounds prior to sample measurement. Measured backgrounds were negligible. The quoted TDS error is +/- 20%; making the inner wall eroded region and dump plate comparative results. Overall molten material whether alloyed or not appears to retain the least H isotopic content of all material microstructures analysed.

6.4.4 Summary and discussion of the results seen at the Dump plate castellation in JET

Molten dump plate materials were highly complex in both surface chemistry and macroscopic morphology. Complex melt processes produced two very distinct microstructures on the macroscopic scale.

Raman microscopy of the surface of the molten region displayed novel BeOD bonding and was published. Initially BeOD bonding was thought to account for very

little total JET retention. Originally it was assumed only present in melt pools, which represented 5-6% of the total surface area.

Further analysis of the remaining surface area with EELS showed; even within the second microstructure, amid significant material mixing, alloying, and oxidation between Be, O, and Ni; regions of solely BeO were present. Furthermore comparison to DFT modelled data, provided a high degree of correlation to tetragonal BeOD presence in the low loss region in particular. This bonding was found in regions where grain growth had occurred; and on a macroscopic length scale, where local plasma shaddowing and greater conductivity to the substrate volume, was present; resulting in prolonged diffusion times. Even, within a region, with extreme material mixing with Ni; BeOD bonding was possible.

Interestingly, unlike other JET samples where implication of BeH_2 and BeD_2 bonding was suggested, no such features were seen in these samples. These samples have formed under significantly higher temperatures. TDS results suggests these higher temperature loading conditions, have reduced overall retention, and perhaps led to isotopic exchange with H, post pulse duration, - a possible explanation for the massive increase in H vs D retention.

The implications for ITER are; molten material can be efficiently convected across castellated surfaces, changing surface levels by millimetres. Molten material provides opportunity for substantial material mixing, in the presence of a relevant binary alloying material. Even within regions where huge levels of surface erosion occurred, BeOD bonding was present under localised regions, which eased high heat loads, increasing diffusion times. Lower retention occurs in molten material. Some suggestion of isotopic exchange remains possible, which will need further investigation utilising tritiated samples.

Chapter 7

Conclusions

This thesis sought to understand how hydrogen, deuterium and tritium are retained in the JET ITER-like wall.

Very little microstructural analysis of both laboratory experiments trying to replicate relevant tokamak-like samples; nor tokamak in service beryllium materials had been undertaken to date. The current knowledge understood the impacts of fluence and implantation temperature to the greatest extents; matching thermal desorption spectroscopy peaks to temperatures and likely trapping types, both via IBA depth profiles and decomposition temperatures of, for instance, BeD_2 and BeOD. However, very little physical inspection of the implanted materials had occurred. From the literature, three micrographs in total were found applying either SEM or TEM. These micrographs provided evidence of bubble formation under very high ion implantation energies and fluence.

This thesis found at the eroded region in subsection 4.6, that EELS presented evidence of BeD_2 in the matrix, and orthorhombic and tetragonal BeOD at oxide precipitates; with a few sporadic hexagonal large oxide features as well. Atom Probe Tomography found that BeD and D clustered at the outer wall, whilst at the inner wall, no clustering was observed either within grain or at the grain boundaries, which were rich in Mg, Si and O. Furthermore, release from atom probe was found to occur first via D ions at the outer surfaces of the bubble, and subsequently by BeD molecular ion release. This release was thought to be real and not an effect of non-equilibrium release, simply because the opposite bond breaking would be expected when the internal bubble content reaches extremely high electrostatic fields. Many techniques were applied to these materials, which had not been applied to date in any study. An approach starting at the macroscopic and refining microstructural analysis to the nano-metric at the final stages, suggested that the resolution of the SEM-EDX system, could only perceive greater correlated oxidation and number densities at the

outer wall versus the inner wall. For the level of fluence and implantation in JET, additional higher resolution microscopic techniques are required to understand the effect of retention in the beryllium lattice in detail; and provided much greater information and understanding than IBA and TDS techniques, previously used to characterise these samples. This may not be the case for ITER. If significantly higher fluences and implantation conditions were to occur, perhaps bubble formation may present at the micron level and be counted by 3D milling techniques via a combination of FIB and SEM-EDX. Thermal Desorption Spectroscopy provided the final fuel retention data, distinguishing the outer wall from the inner wall. The outer wall retained far more hydrogen (in the form of deuterium) and was concluded to have reached saturation conditions. In comparison, the retention at the inner wall was much lower, correlating to the lack of clustering seen.

The co-deposited regions were presented in section 5.7. Low magnification techniques such as SEM and EDX showed incomplete co-deposit coverage at the inner wall surface area; with total coverage at the outer wall co-deposit. Sub-surface investigation, showed greater morphological changes at the outer wall in regards to the toroidal space. Evidence of bubble formation at the interface between the TVA Be marker layer at the inner wall co-deposited region was consistent across the co-deposited covered regions. The inner wall co-deposit occurred consistently with two microstructures. A type 2 Cu rich beryllium matrix and a slight thickness (less than 2μm) stratified co-deposited layer at the surface; suggesting a change in operational parameters towards the end of the campaign time. Indeed the Be Cu rich type-2 region, suggested from the literature that high temperature wall operation would be necessitated, close to the melt temperature of Be. This evidence alongside many reports of melting at the inner limiters; as well as similar microstructures here compared to the melted dump plate morphologies, suggested the inner wall eroded tile had received greater neutral beam and power loadings, and explains so far a lack of total hydrogen retained at the inner wall, even in the eroded regions. The outer wall again showed subsurface changes in the toroidal direction, with greater deposit thickness occurring at the right poloidal edge versus the left poloidal edge. The outer wall co-deposit was a full thickness stratified layer in all samples; however at the left poloidal edge void formation similar to the inner wall at the same TVA interface was observed. Towards the right poloidal edge, the outer wall co-deposit formed at greater thickness with reduced void presence; however here cracking between layers appeared to grow from grain structures beneath and was present consistently across the region. The centre of the castellation occurred as an intermediate between these

two microstructural extremes. A greater number of outer wall co-deposited samples were produced for TEM to survey changes in metallic impurities other than Be and O with EDX. Despite the apparent morphological changes in the deposit at the scale of the SEM, at higher resolution in the TEM, EDX was found to be relatively consistent, with very low levels of Ni, W and Cu impurities. Generally speaking the co-deposit was governed by light elements, with very localised inclusion of W and Ni particles on scales of a 100nm. EELS of the two regions, inner and outer wall co-deposits showed co-deposition at the inner wall to be governed by Be co-deposition in the presence of D; whilst at the outer wall co-deposition was governed by BeO in the presence of D. Oxidation at the outer wall, whilst apparent from EELS stoichiometric measurements and O core loss fine structure; only occurred to a maximum of 8 at%; substantially reduced from the common stoichiometric wurtzite structure, seen at both eroded regions. Comparison between EUROFusion HiPIM co-deposits and JET samples showed good reproducibility to the BeOD provided sample. However JET-DFT comparisons suggested samples more closely correlated to BeD_2. The conclusions here are limited. It is clear the co-deposit is far from stoichiometric conditions, and therefore perhaps limited in the application of DFT modelling of outer shell electrons; nevertheless the EUROFusion samples provide a relevant material for comparison and study, of tokamak in-service beryllium. However, greater production precision and cleanliness would be optimum in the EUROFusion samples. Thermal Desorption Spectroscopy of the co-deposited samples once again showed decreased retention at the inner wall, here the same conclusion was drawn as from the literature, that the increased retention was weighted to relative thickness between the positions and less likely the effect of chemistry. It is suggested therefore that the physical structure of a spongelike morphology is a much more efficient trapping mechanism of gaseous species than chemistry formed through bonding. Despite, the presence of layers under the SEM-EDX length scale, further inspection at the scale of the TEM, suggested these were semi-continuous; however, future work could prepare samples from rotating collectors of the samples' campaign, and analyse the patterns of materials deposited in these diagnostic material tests. Whilst, the rotating collectors exist in the divertor, their data would, if correlative, give further indication of a time parameter to the deposits seen in the limiters; and even further, may provide a direct link to plasma operations.

The final results presented, are those from the dump plate melted materials summarised in section 6.4.4. Two distinct morphologies were present at the surface. A melted mounded region ($\sim$4-5% of the castellations total surface area) substantially

raised from the relative surface height of the rest of tile (∼95-96%). Inspection of these surfaces suggested increased oxidation present in the mounded melt pool, and mixed material composition in the rough globules present at the surface of the second region. Raman spectroscopy was used to investigate bonding in the surface of the dump plate tile, which found BeOD in the melted mound, specific to orientations on the left poloidal side, equivalent to a localised shadowed region. It was suggested cautiously both that the BeOD formation was sensitive to power loadings and thermal environments, but also that the high roughness of the second microstructure at the surface was sufficient to cause loss of Raman collection due to scattering. Further investigation of the Raman spectral region linked to BeOD suggested a minimum of two BeOD stoichiometries present from Raman. EELS analysis of the surface region displayed 50:50; 60:40; and 80:20; between Be and O respectively. This correlates well to the Raman results of the same region. EDX of the region, displayed the beryllium oxide free of other metallic contaminants, aiding validity to both the Raman and EELS results. Interestingly the subsurface matrix beneath the melted oxide displayed similar properties to the inner wall type 2 deposit; which was suggested formed under or close to molten conditions.

EDX of the second microstructure present at the surface produced a material with a beryllium bulk subsurface at approximately 20μm depths, above which sat a minimum of three Be/Ni rich microstructures with transitioning features. The surface microstructure was indicative of quench formation due to its fine two phase structure, showing directionality perpendicular to the original surface axis. EELS of this region was expanded to include Ni and C in the O and Be spectral windows, respectively. The results showed at the very surface of the globule perpendicular to the plasma, Be and Ni were present in the matrix with the second phase precipitates incorporating oxygen up to 10 at%. A further region was inspected towards the base of the globule relative to the original surface and found a two phase system present of Be/Ni grains with solely BeO surrounding in the second phase. Both phases in this second region were coarsened, suggesting that diffusion had greater time to occur. Comparison of the BeO phase to previous results and DFT strongly reproduced BeOD bonding. This concluded that localised shadowing producing lower thermal loadings; enabled and facilitated BeOD formation. Thermal desorption of a castellation one poloidal position removed from the castellation investigated; with the same toroidal geometry; produced single homogeneous release peaks of H, D and HD. The hydrogen mass 2 signal of this sample was an outlier compared to all other samples. The TDS data of this sample was also an outlier, comparative to all other samples. Whilst the H peak

remained high, the overall, retention discarding the hydrogen peak was exceptionally low. It is difficult to assess how much of the H signal is due to outgassing and exchange with H from the air. The final conclusion is that both material mixing, and high operational temperatures has changed the retention dynamic substantially.

Whilst evidence of isotopic variation and segregation appears present between all sample locations, it would take an eroded sample loaded past saturation in a D, T campaign to be able to distinguish D from T clustering if present in the Atom Probe. This result would once and for all answer the question of whether hydrogen trapping is effected by isotopic concentrations. This is an area of future work. Currently the answer is incomplete, and all that can be assumed is that the trapped isotope is an opportunistic result of whatever is available in the local environment.

The final piece of future work concerns thermal desorption spectroscopy and modelling. Ideally, and perhaps with an over eagerness to answer many questions; a complete thermal release model and mechanism was another aim of this thesis. A significant amount of microstructural, chemical and spatial work has been done to these samples to analyse H isotopic retention. However, the literature method has always produced conclusions based on desorption times and temperatures seen via TDS measurement. For completeness the work done collating these prior suggestions from the literature, alongside JET desorption peak release temperatures has been tabulated and summarised in Appendix C. Early work, which started to produce a model utilising TMAP7 release parameters, was sufficient to understand and predict eroded release, but insufficient to calculate and predict co-deposit release. This work is also included in Appendix C. It remains to be said, that the outcome of correct predictions for eroded samples seems understandable. Largely speaking the system could be reduced to a beryllium matrix, a supersaturated Be/D surface, and a secondary region of trailing D ion implanted retention into depth. The chemistry considerations would largely involve BeD_2 and BeO_2D_2. Diffusion and surface limited release with varying rates through the release time may with iteration fully describe the system. However, the co-deposit 3D sponge-like morphology is much more complex. Here it is suggested that greater future work is necessitated building a 3D model utilising slice and view data that can be converted into a 3D net and input as a starting substrate. This area of research would be extremely useful to ITER to acknowledge the importance of co-deposit release, which after all governs total retention. Once release parameters were fully understood via a working thermal release model, operational parameters could be back calculated and their interaction and causation to deposit growth better understood. Fusion will be an extremely important energy source for

the future, and it is my belief that all aspects of an integrated machine: operation, material, and plasma understanding; need to play their part in order to achieve the long term goal of commercial viability.

Appendix A

Supplementary work on eroded regions: TEM brightfield, and EELS fitting examples,

A.1 Supplementary table of precipitate image analysis of eroded regions

Sample	Mean particle area (nm^2)	Standard error (nm^2)	Percentage standard error (%)	Total precipitate area (μm^2)	Total area per single slice (μm^2)	Total area of 12 slices (μm^2)	Precipitate Percentage area (%)	Precipitate Percentage error (%)
Inner wall eroded	270	12	4	0.6	101	1212	0.05	0.09
Outer wall eroded	630	19	3	11.7	227	2726	0.43	0.02
As received beryllium	760	54	7	1.1	329	3947	0.03	0.2

Figure A.1: Extracted statistics comparing thresholded precipitates of the inner wall and outer wall eroded regions, against the unexposed as received JET beryllium

A.2 Supplementary Brightfield TEM images of eroded regions

Standard TEM images of the eroded regions, included for the readers ease and indicative of the supersaturated beryllium lattice in the eroded inner wall, and bubble coarsening at the outer wall to perceive features seen in the atom probe results.

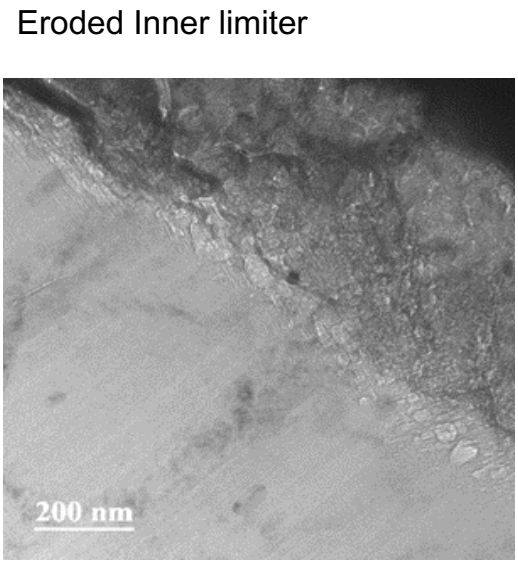


Figure A.2: Figure displaying the supersaturated region at the surface of the eroded inner wall, indicated from the TDS desorption spectra and EELS BeD_2 inference.

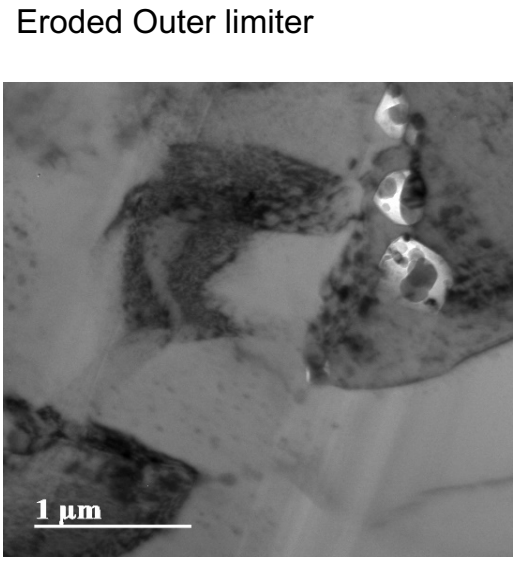


Figure A.3: Figure displaying the bubble coarsening at the surface of the eroded outer wall, indicated from the APT clustering data, TDS desorption spectra, and EELS BeD_2 inference.

A.3 Supplementary examples of EELS hyperspy curve fitting accuracy for integrated stoichiometric calculations

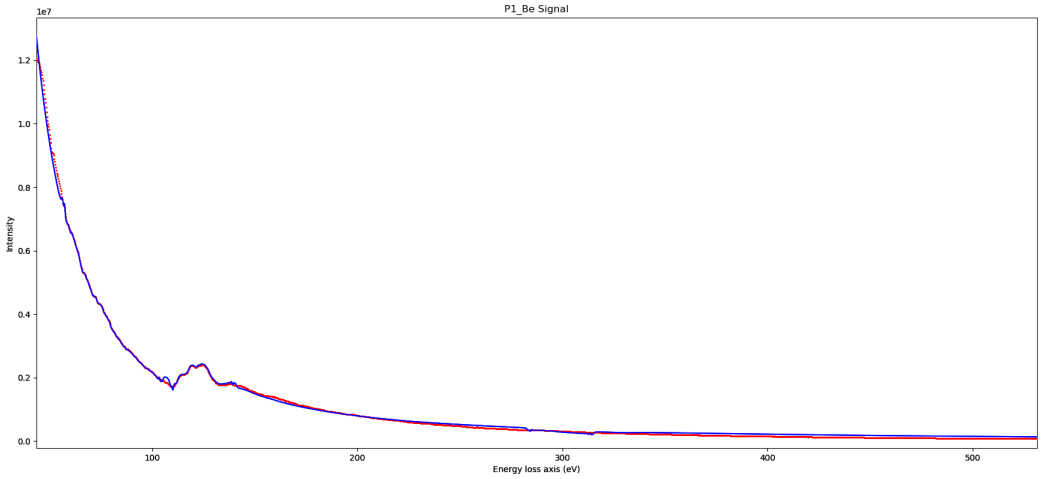


Figure A.4: Figure displaying an example of EELS Be spectral fitting for quantification in hyperspy. The data set is the second presented of a point in the second microsctructure seen in the dump plate found in figure 6.36.

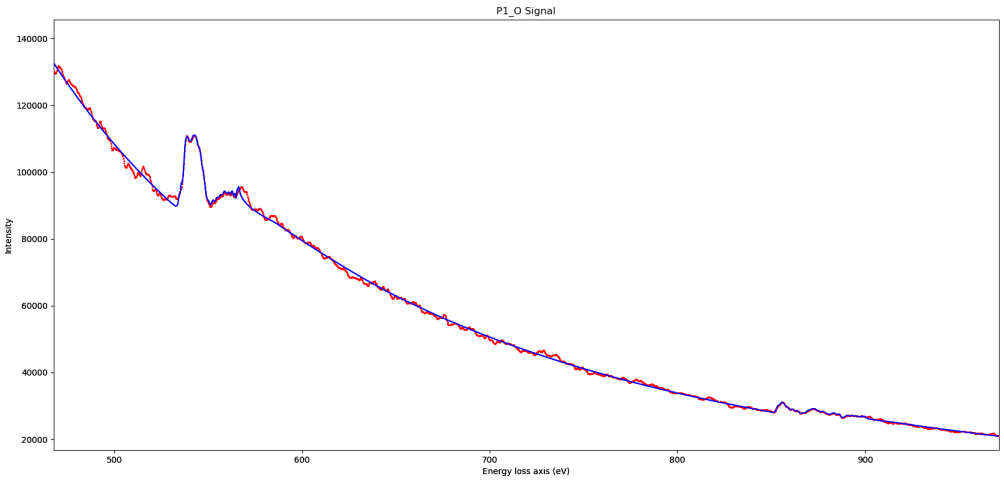


Figure A.5: Figure displaying an example of EELS O spectral fitting for quantification in hyperspy. The data set is the second presented of a point in the second microsctructure seen in the dump plate found in figure 6.36.

Appendix B

Further supplementary work on melted materials: Expanded Image analysis, further examples of STEM-EDX and STEM-EELS

B.1 Thresholding melted regions

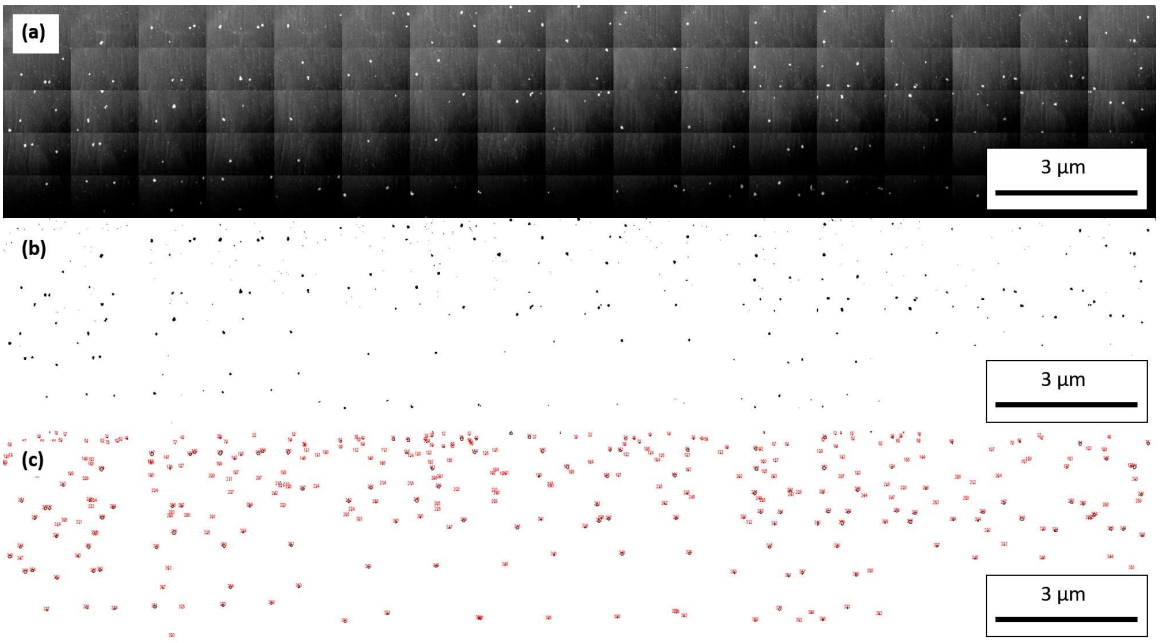


Figure B.1: Figure shows every tenth slice of the 3D milling study (1). Image (a) shows the extracted SEM SE images of each 10th slice iteration. Image (b) the result of thresholding the SE images. Image (c) shows the results of particle analysis, with the particles marked.

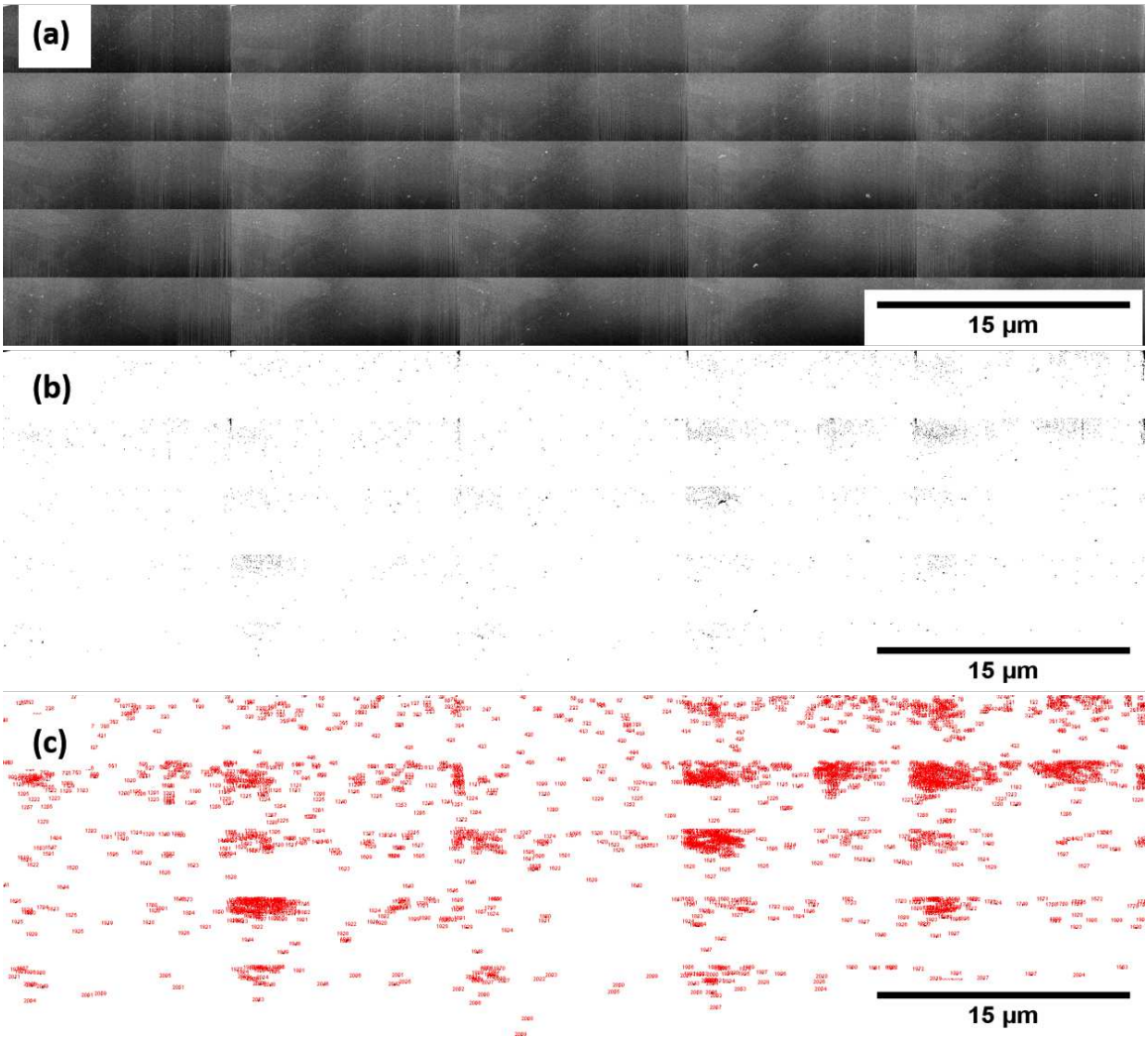
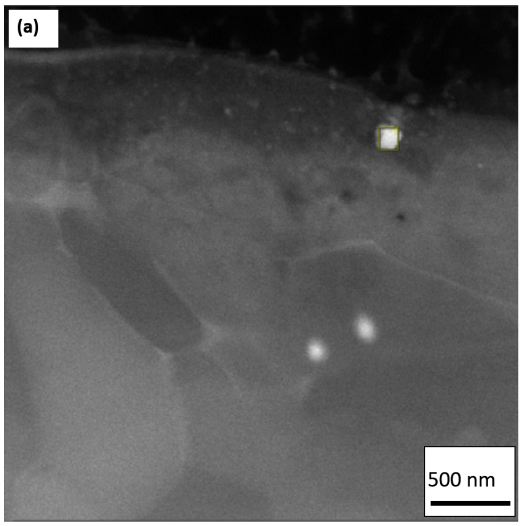


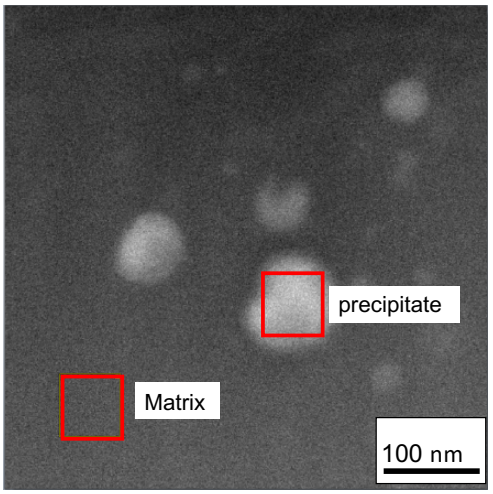
Figure B.2: Figure shows every tenth slice of the 3D milling study (2). Image (a) shows the extracted SEM SE images of each 10th slice iteration. Image (b) the result of thresholding the SE images. Image (c) shows the results of particle analysis, with the particles marked.

B.2 Further STEM-EDX examples



Average across map	Atom %	Atom % err
Be K	14.57	0.75
B K	0.00	0.00
C K	3.98	0.07
N K	2.35	0.12
O K	74.41	0.53
F K	3.66	0.25
Al K	0.04	0.00
Si K	0.03	0.00
S K	0.01	0.00
Ni K	0.03	0.00
Cu K	0.02	0.00
Ga L	0.82	0.01
Zr L	0.07	0.00
W L	0.00	0.00
W M	0.00	0.00

Figure B.3: a) A STEM HAADF image of the EELS area scan and b) the average EDS composition with errors of the total area shown.



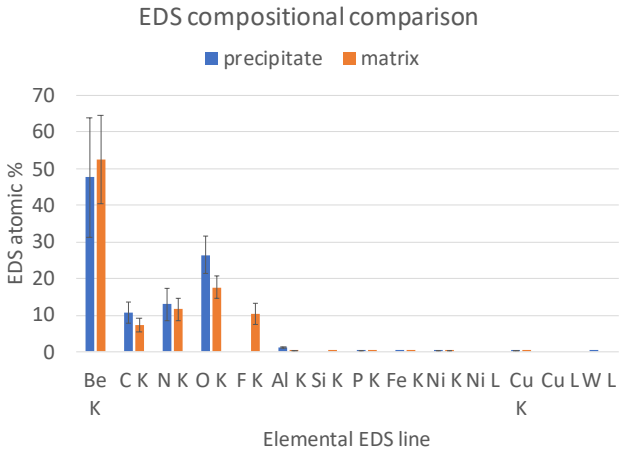


Figure B.4: a) A STEM HAADF image of the sub oxide matrix region, on and off precipitates showing their EDS composition with errors shown.

B.3 Further STEM-EELS examples

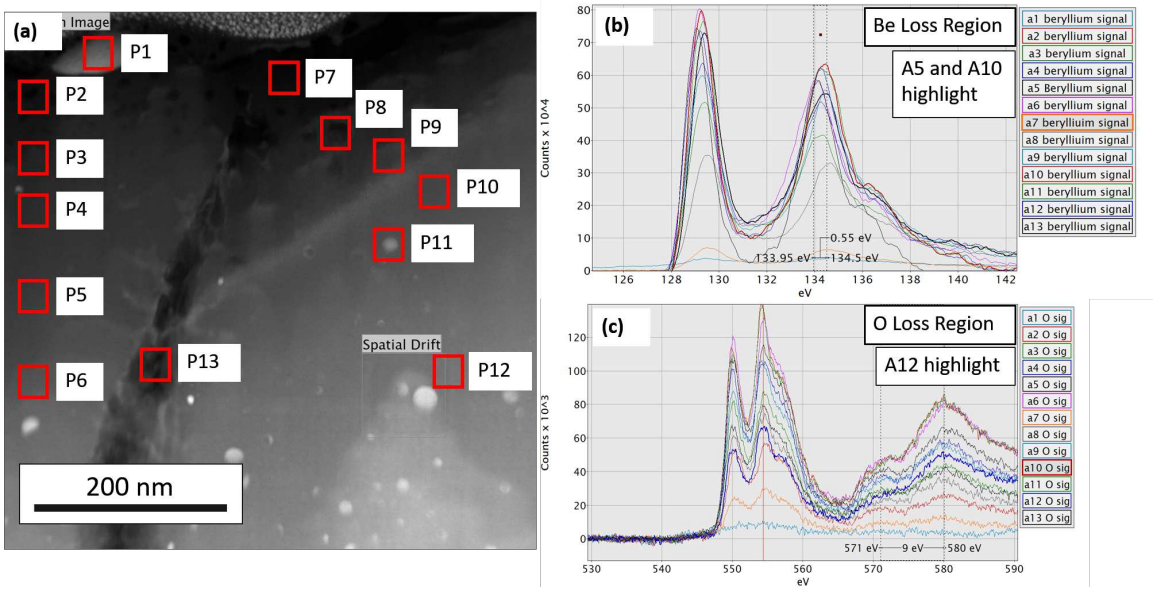


Figure B.5: A higher magnification STEM HAADF area of the surface oxide and their extracted spectra of the beryllium core loss (b) and the oxygen core loss (c).

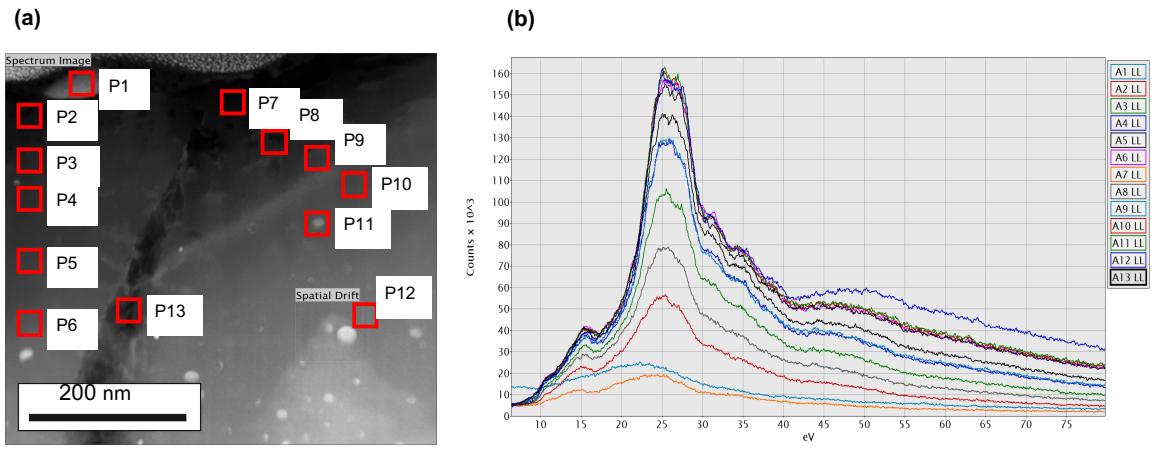


Figure B.6: A higher magnification STEM HAADF area of the surface oxide and extracted EELS low loss spectra.

Appendix C

Supplementary Wall temperature information, and Thermal Desorption Spectroscopy graphs and analysis for future work

C.1 Supplementary JET thermocouple data, showing the inaccuracies of wall measurement and high uncertainties

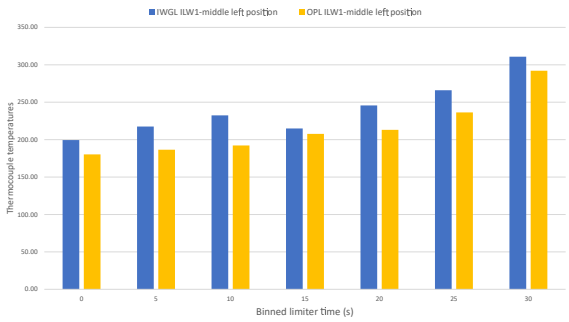


Figure C.1: A comparison of thermocouple temperature measurements between the outer and inner wall limiter with increasing integrated plasma time of the first ITER-like wall campaign

C.2 Supplementary Thermal Desorption Spectroscopy graphs: eroded materials

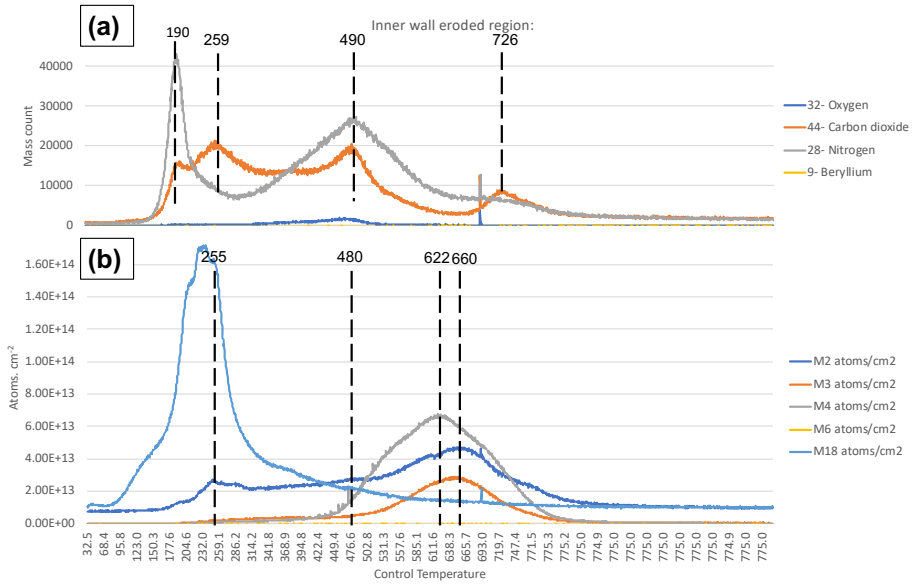


Figure C.2: Figure displaying the Inner wall Eroded TDS data: a) Nitrogen, Oxygen, CO_2 release; (b) Mass 2 -H_2 release, Mass 3-HD release, Mass 4 -D_2 release, Mass 5 -DT release, Mass 6 -T_2 release, and M18 -H_2O release.

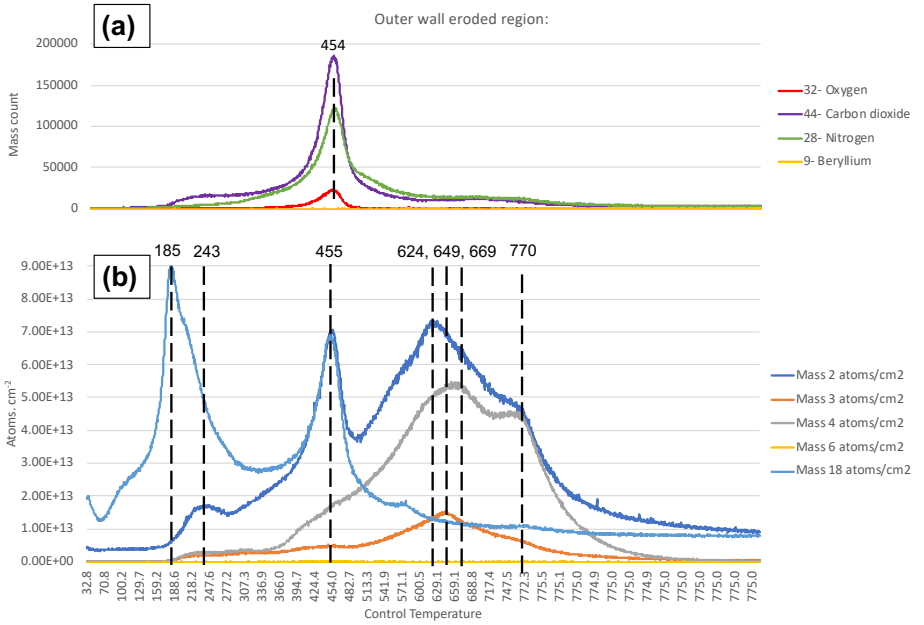


Figure C.3: Figure displaying the Outer wall Eroded TDS data: a) Nitrogen, Oxygen, CO_2 release; (b) Mass 2 -H_2 release, Mass 3-HD release, Mass 4 -D_2 release, Mass 5 -DT release, Mass 6 -T_2 release, and M18 -H_2O release.

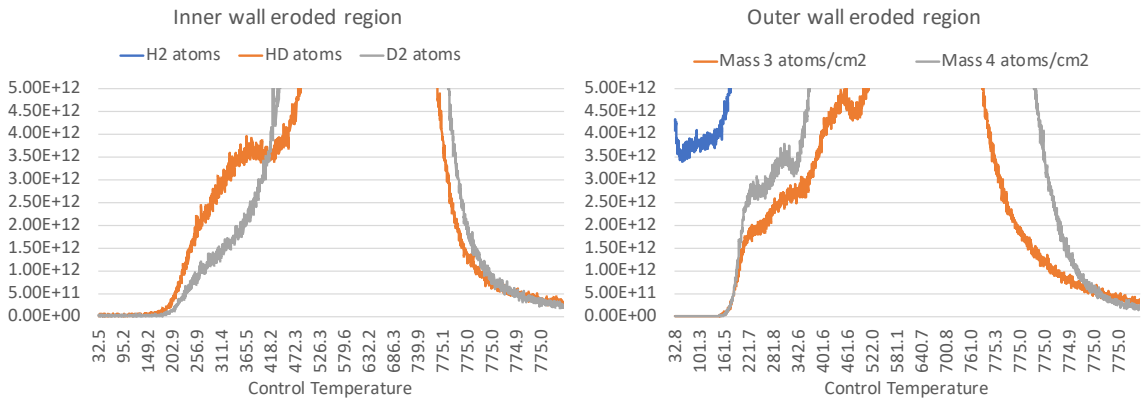


Figure C.4: Figure displaying the inner (left) and outer (right) TDS spectra of the mass 3 and 4 peaks corresponding to HD and D_2 peaks respectively. From the literature these peaks are thought the response of a supersaturation of the H isotope at the surface, which is greater in the D_2 for the outer wall.

Molecular release	Inner wall Eroded zone					Outer wall eroded zone				
	180-280 Surface limited release + impurity gases	280-350 BeHD	480 BeOH/(BeOD) [21]	600-700 Traps at the end of the ion stopping range [21, 75]	770 Not found in the literature	180-280 Greater surface retention	280-350 BeD_2	455 BeOH/BeOD [21] + impurity release (greater plasma /machine gasses)	550-670 Saturated ion induced traps and intrinsic point defects [21, 75]	770 Greater diffusion into the bulk - higher operational temperature
H2	✓ & M18 H_2O		✓	✓	✓	✓ & M18 H_2O		✓ & M18 H_2O	✓	✓
HD		✓		✓		✓	✓		✓	✓
D2			✓	✓		✓	✓	✓	✓	✓
N	✓		✓					✓		
O			✓					✓		
CO2	✓		✓		✓			✓		

Table C.1: Table displaying a summary of the eroded materials trapping release peaks and literature informed microstructural correlations.

C.3 Supplementary Thermal Desorption Spectroscopy graphs: deposited materials

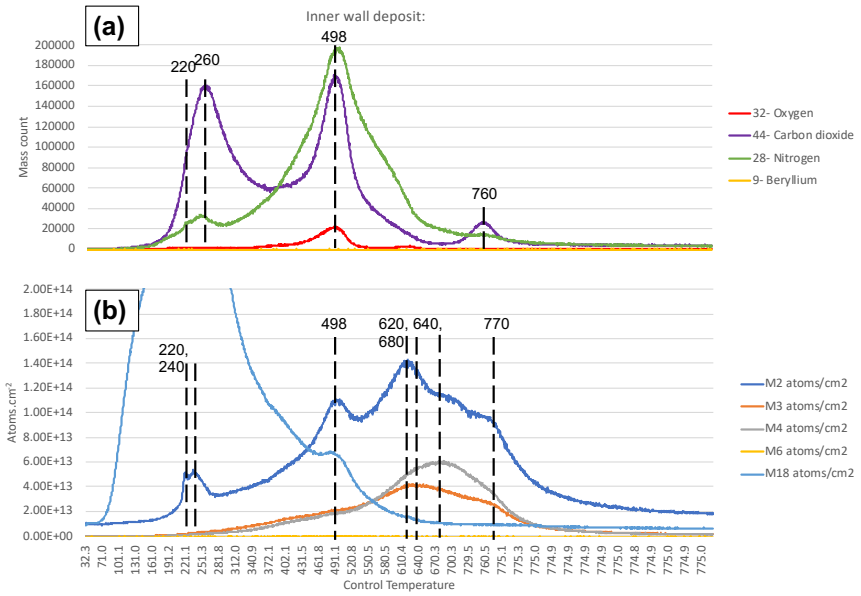


Figure C.5: Figure displaying the Inner wall deposited TDS data: a) Nitrogen, Oxygen, CO_2 release; (b) Mass 2 -H_2 release, Mass 3-HD release, Mass 4 -D_2 release, Mass 5 -DT release, Mass 6 -T_2 release, and M18 -H_2O release.

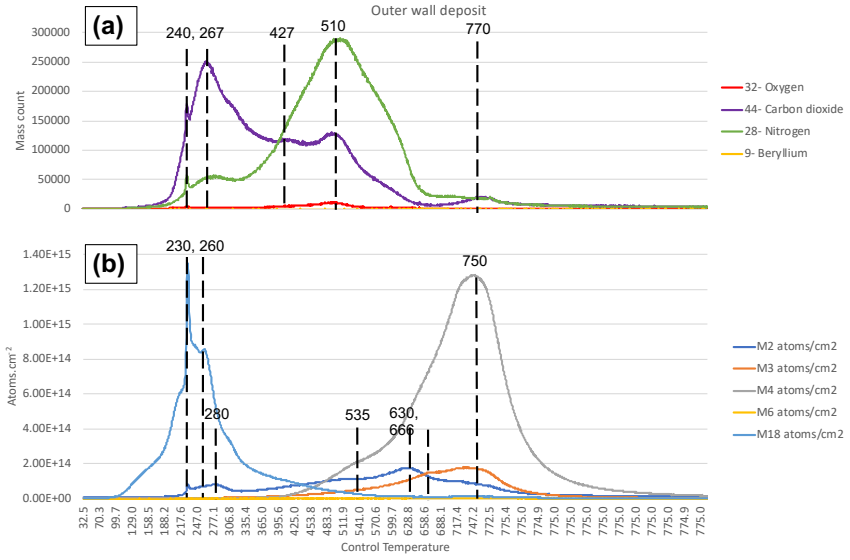


Figure C.6: Figure displaying the Outer wall deposited TDS data: a) Nitrogen, Oxygen, CO_2 release; (b) Mass 2 -H_2 release, Mass 3-HD release, Mass 4 -D_2 release, Mass 5 -DT release, Mass 6 -T_2 release, and M18 -H_2O release.

Molecular release	Inner wall codeposit					Outer wall codeposit				
	220, 260 Surface limited release + impurity gases	280-350 BeHD/ BeD_2 [18, 98]	498 BeOH/(BeOD) [21, 23, 26, 98] +implantation of co-deposits above 570K-300ºC [98] + O related peaks	600-700 Traps at the end of the ion stopping range [21, 75]	770 Not found in the literature	220, 240, 260, Greater surface retention	280-350 BeHD/BeD_2 [18, 98]	510-530 BeOH/BeOD [21, 23, 26] + impurity release (greater plasma /machine gasses) + O related peaks	600-670 Saturated ion induced traps and intrinsic point defects [21, 75]	750-770 Far larger feature at the outer wall, linked to deposit thickness? And physical surface areas?
$H2/H_2O$	✓ -two peaks & M18 H_2O		✓ & M18 H_2O	✓ M18 **H_2O only** 620, 680	✓ M18 **H_2O only**	✓ M2-H_2: 230 M18 H_2O: 220,230, 260	✓ M2-H_2: 280 M18 H_2O: 310	✓ M18 H_2O only 510	✓ M18 H_2O only 630	✓ M18 H_2O only 750
HD			✓	✓ 620-640	✓		✓ 310-350	✓ 510-530	✓ 600-680	✓ 750-smaller
D2			✓	✓ 680-broad	✓-largest			✓ 510-530	✓ 600-680	✓ 750-large
N	✓		✓	✓ 620	✓	✓ 240,265	✓ 290	✓ 510	✓ 630	✓ 750
O			✓	✓ 640		✓ 240		✓ 510		
CO2	✓		✓		✓	✓ 240,265	✓ 320	✓ 510		✓ 750

Table C.2: Table displaying a summary of the deposited materials trapping release peaks and literature informed microstructural correlations.

C.4 Supplementary Thermal Desorption Spectroscopy graphs: melted materials

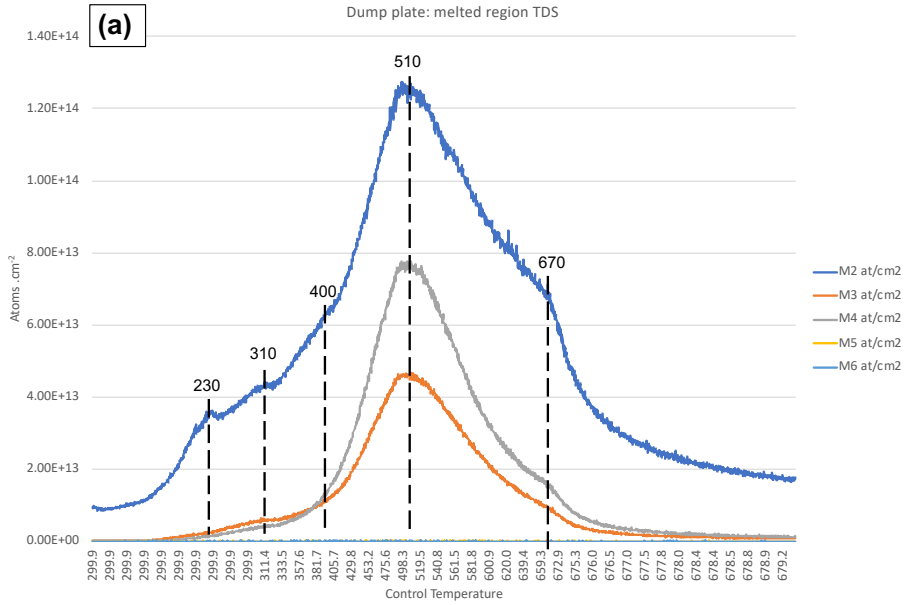


Figure C.7: Figure displaying the melted dump plate TDS data: Mass 2 -H_2 release, Mass 3-HD release, Mass 4 -D_2 release, Mass 5 -DT release, Mass 6 -T_2 release, and M18 -H_2O release.

C.5 Initial results in collaboration with modellers, using TMAP7 to model release from eroded and deposited materials

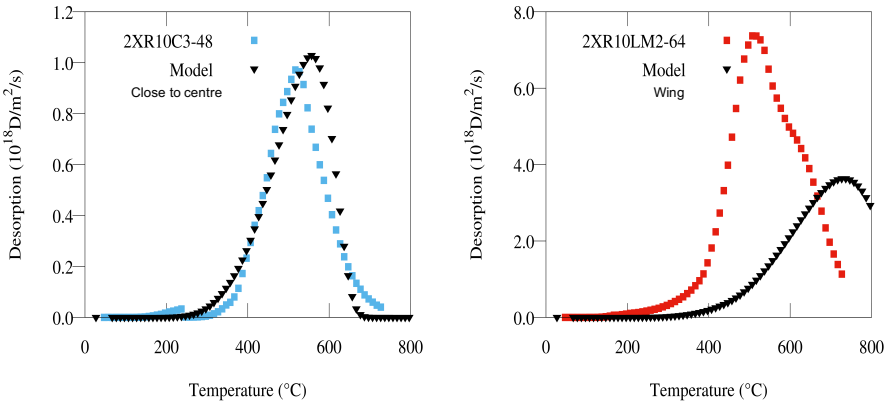


Figure C.8: Figure displaying the modelled release, utilising a recombination limited surface: left the eroded central limiter region and right the outer wing deposit.

Appendix D

Supplementary Raman results on beryllium lift-outs from the JET ILW1

Raman Data of lift-outs produced from the FIB, showing hydride formation linked to forward shifted Be Raman shifts.

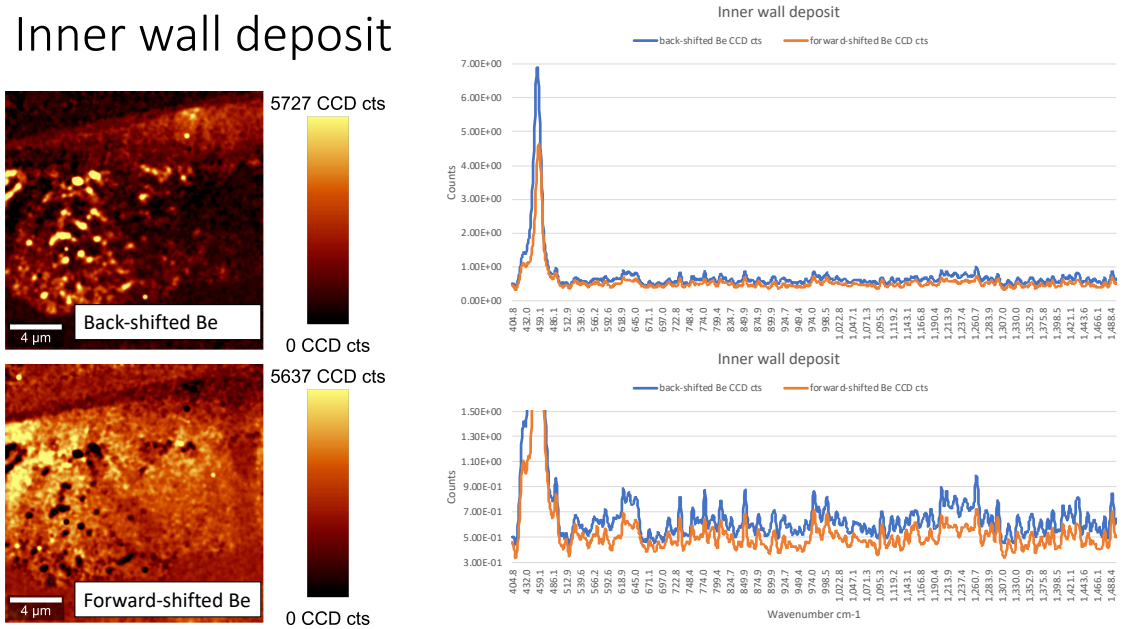


Figure D.1: Figure of the Inner Wall deposit, displaying: left: maps corresponding to the, right: spectra presented with increased resolution provided of the Raman spectra in the bottom graph, showing hydride formation.

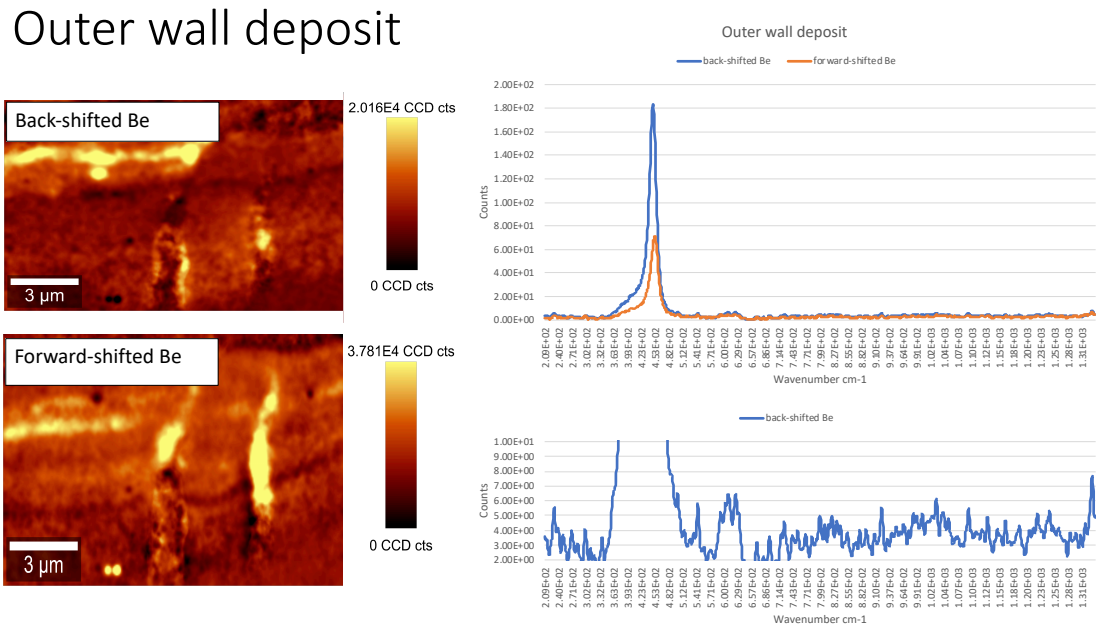


Figure D.2: Figure of the Outer Wall deposit, displaying: left: maps corresponding to the, right: spectra presented with increased resolution provided of the Raman spectra in the bottom graph, showing hydride formation.

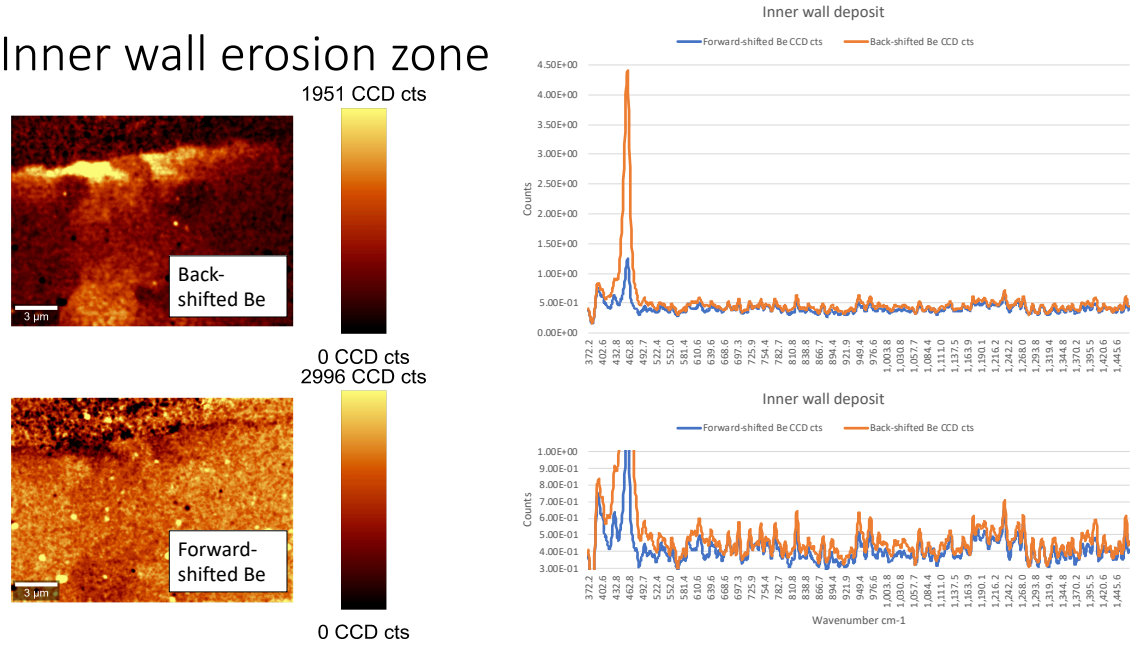


Figure D.3: Figure of the Inner Wall erosion zone, displaying: left: maps corresponding to the, right: spectra presented with increased resolution provided of the Raman spectra in the bottom graph, showing hydride formation.

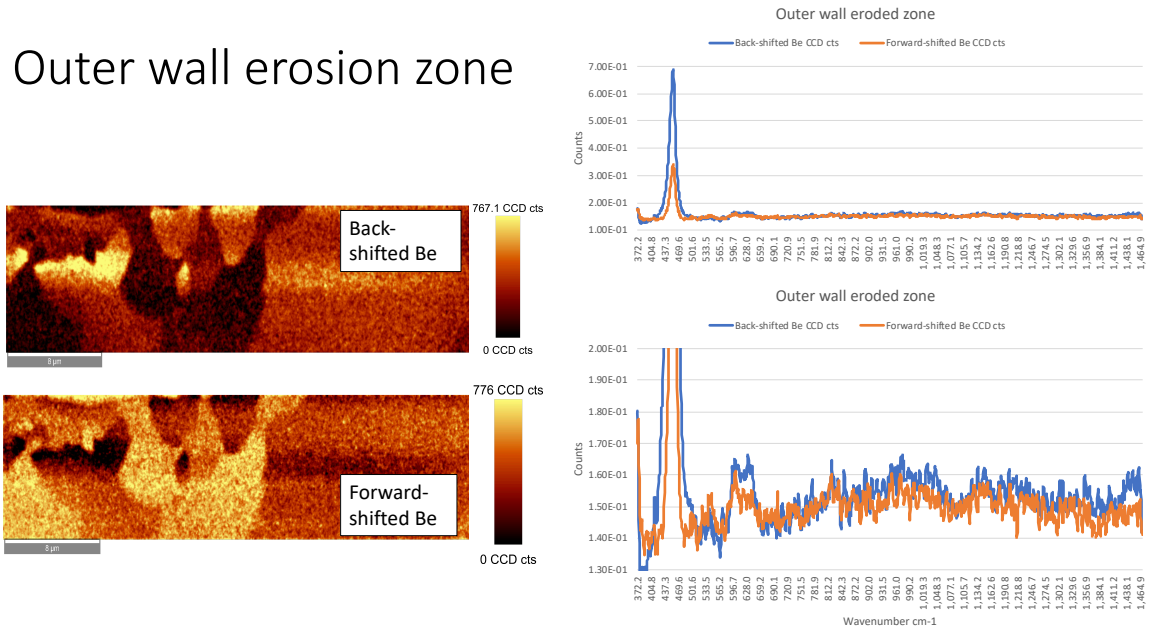


Figure D.4: Figure of the Outer Wall erosion zone, displaying: left: maps corresponding to the, right: spectra presented with increased resolution provided of the Raman spectra in the bottom graph, showing hydride formation.

Bibliography

[1] Jérôme Paméla, Guy F Matthews, Volker Philipps, Richard Kamendje, JET-EFDA Contributors, et al. An iter-like wall for jet. *Journal of nuclear materials*, 363:1–11, 2007.

[2] V Thompson, Y Krivchenkov, V Riccardo, and Z Vizvary. Analysis and design of the beryllium tiles for the jet iter-like wall project. *Fusion Engineering and Design*, 82(15-24):1706–1712, 2007.

[3] Marek J Rubel, V Bailescu, JP Coad, T Hirai, J Likonen, J Linke, CP Lungu, GF Matthews, L Pedrick, V Riccardo, et al. Beryllium plasma-facing components for the iter-like wall project at jet. In *Journal of Physics: Conference Series*, volume 100, page 062028. IOP Publishing, 2008.

[4] Lorne Horton. The jet iter-like wall experiment: First results and lessons for iter. *Fusion Engineering and Design*, 88(6):434 – 439, 2013. Proceedings of the 27th Symposium On Fusion Technology (SOFT-27); Liège, Belgium, September 24-28, 2012.

[5] Joachim Roth, Emmanuelle Tsitrone, Thierry Loarer, Volker Philipps, Sebastijan Brezinsek, Alberto Loarte, Glenn F Counsell, Russell P Doerner, Klaus Schmid, Olga V Ogorodnikova, et al. Tritium inventory in iter plasma-facing materials and tritium removal procedures. *Plasma Physics and Controlled Fusion*, 50(10):103001, 2008.

[6] A Widdowson, E Alves, C F Ayres, A Baron-Wiechec, S Brezinsek, N Catarino, J P Coad, K Heinola, J Likonen, G F Matthews, M Mayer, and M Rubel and. Material migration patterns and overview of first surface analysis of the JET ITER-like wall. *Physica Scripta*, T159:014010, apr 2014.

[7] K. Heinola, A. Widdowson, J. Likonen, E. Alves, A. Baron-Wiechec, N. Barradas, S. Brezinsek, N. Catarino, P. Coad, S. Koivuranta, G.F. Matthews,

M. Mayer, and P. Petersson. Fuel retention in jet iter-like wall from post-mortem analysis. *Journal of Nuclear Materials*, 463:961 – 965, 2015. PLASMA-SURFACE INTERACTIONS 21.

[8] A. Baron-Wiechec, K. Heinola, J. Likonen, E. Alves, N. Catarino, J.P. Coad, V. Corregidor, I. Jepu, G.F. Matthews, and A. Widdowson. Thermal desorption spectrometry of beryllium plasma facing tiles exposed in the jet tokamak. *Fusion Engineering and Design*, 133:135 – 141, 2018.

[9] E. Pajuste, G. Kizane, A. Vitins, I. Igaune, L. Avotina, and R. Zarins. Structure, tritium depth profile and desorption from 'plasma-facing' beryllium materials of iter-like-wall at jet. *Nuclear Materials and Energy*, 12:642 – 647, 2017. Proceedings of the 22nd International Conference on Plasma Surface Interactions 2016, 22nd PSI.

[10] A. Widdowson, J.P. Coad, E. Alves, A. Baron-Wiechec, N. Catarino, V. Corregidor, K. Heinola, S. Krat, C. Makepeace, G.F. Matthews, M. Mayer, K. Mizohata, and M. Sertoli. Deposition of impurity metals during campaigns with the jet iter-like wall. *Nuclear Materials and Energy*, 19:218 – 224, 2019.

[11] A. Widdowson, J.P. Coad, E. Alves, A. Baron-Wiechec, N.P. Barradas, S. Brezinsek, N. Catarino, V. Corregidor, K. Heinola, S. Koivuranta, S. Krat, A. Lahtinen, J. Likonen, G.F. Matthews, M. Mayer, P. Petersson, and M. Rubel and. Overview of fuel inventory in JET with the ITER-like wall. *Nuclear Fusion*, 57(8):086045, jul 2017.

[12] WR Wampler. Trapping of deuterium in beryllium. *Journal of nuclear materials*, 196:981–985, 1992.

[13] V Kh Alimov, VN Chernikov, and AP Zakharov. Depth distribution of deuterium atoms and molecules in beryllium implanted with d ions. *Journal of nuclear materials*, 241:1047–1051, 1997.

[14] VN Chernikov, V Kh Alimov, AV Markin, AE Gorodetsky, SL Kanashenko, AP Zakharov, and IB Kupriyanov. Gas-induced swelling of beryllium implanted with deuterium ions. *Journal of nuclear materials*, 233:860–864, 1996.

[15] R.P. Doerner, A. Grossman, S. Luckhardt, R. Seraydarian, F.C. Sze, D.G. Whyte, and R.W. Conn. Response of beryllium to deuterium plasma bombardment. *Journal of Nuclear Materials*, 257(1):51 – 58, 1998.

[16] M Reinelt, A Allouche, M Oberkofler, and Ch Linsmeier. Retention mechanisms and binding states of deuterium implanted into beryllium. *New Journal of Physics*, 11(4):043023, apr 2009.

[17] K. Sugiyama, C. Porosnicu, W. Jacob, I. Jepu, and C.P. Lungu. Investigation of deuterium retention in/desorption from beryllium-containing mixed layers. *Nuclear Materials and Energy*, 6:1 – 9, 2016.

[18] RA Anderl, RA Causey, JW Davis, RP Doerner, G Federici, AA Haasz, GR Longhurst, WR Wampler, and KL Wilson. Hydrogen isotope retention in beryllium for tokamak plasma-facing applications. *Journal of nuclear materials*, 273(1):1–26, 1999.

[19] Rion Causey, Ken Wilson, Tom Venhaus, and W R Wampler. Tritium retention in tungsten exposed to intense fluxes of 100 ev tritons. *Journal of Nuclear Materials*, 266:467–471, 1999.

[20] R.P Doerner, A.A Grossman, S Luckhardt, R Seraydarian, F.C Sze, and D.G Whyte. Mixed-material coating formation on plasma-facing components. *Journal of Nuclear Materials*, 266-269:392 – 398, 1999.

[21] K. Sugiyama, J. Roth, A. Anghel, C. Porosnicu, M. Baldwin, R. Doerner, K. Krieger, and C.P. Lungu. Consequences of deuterium retention and release from be-containing mixed materials for iter tritium inventory control. *Journal of Nuclear Materials*, 415(1, Supplement):S731 – S734, 2011. Proceedings of the 19th International Conference on Plasma-Surface Interactions in Controlled Fusion.

[22] E. Abramov, M.P. Riehm, D.A. Thompson, and W.W. Smeltzer. Deuterium permeation and diffusion in high-purity beryllium. *Journal of Nuclear Materials*, 175(1):90 – 95, 1990.

[23] M.J. Baldwin and R.P. Doerner. Thermal release of d2 from new be-d co-deposits on previously baked co-deposits. *Journal of Nuclear Materials*, 467:383 – 391, 2015.

[24] Larry Kaufman and L.E. Tanner. Coupled phase diagrams and thermochemical descriptions of the iron-beryllium, cobalt-beryllium, nickel-beryllium and copper-beryllium systems. *Calphad*, 8(2):121 – 133, 1984.

[25] M. Klimenkov, P. Vladimirov, J. Hoffmann, N. Zimber, A. Möslang, and V. Kuksenko. First simultaneous detection of helium and tritium inside bubbles in beryllium. *Micron*, 127:102754, 2019.

[26] V Kuksenko, K Ammigan, B Hartsell, C Densham, P Hurh, and S Roberts. Irradiation effects in beryllium exposed to high energy protons of the numi neutrino source. *Journal of Nuclear Materials*, 490:260–271, 2017.

[27] R. Mateus, C. Porosnicu, C.P. Lungu, C. Cruz, Z. Siketić, I. Bogdanović Radović, A. Hakola, and E. Alves. Analysis of retained deuterium on be-based films: Ion implantation vs. in-situ loading. *Nuclear Materials and Energy*, 17:242 – 247, 2018.

[28] C Pardanaud, M I Rusu, C Martin, G Giacometti, P Roubin, Y Ferro, A Allouche, M Oberkofler, M Köppen, T Dittmar, and Ch Linsmeier. Hydrogen retention in beryllium: concentration effect and nanocrystalline growth. *Journal of Physics: Condensed Matter*, 27(47):475401, nov 2015.

[29] MI Rusu, C Pardanaud, Y Ferro, G Giacometti, C Martin, Y Addab, P Roubin, M Minissale, L Ferri, F Virot, et al. Preparing the future post-mortem analysis of beryllium-based jet and iter samples by multi-wavelengths raman spectroscopy on implanted be, and co-deposited be. *Nuclear Fusion*, 57(7):076035, 2017.

[30] Craig A Thompson and Lester Andrews. Reactions of laser ablated be atoms with h2o: infrared spectra and density functional calculations of hobeoh, hbeoh, and hbeobeh. *The Journal of Physical Chemistry*, 100(30):12214–12221, 1996.

[31] B. K. Bose. Global warming: Energy, environmental pollution, and the impact of power electronics. *IEEE Industrial Electronics Magazine*, 4(1):6–17, March 2010.

[32] Sing Lee and Sor Heoh Saw. Nuclear fusion energy—mankind's giant step forward. *Journal of Fusion Energy*, 30(5):398–403, Oct 2011.

[33] M.F. Akorede, H. Hizam, M.Z.A. Ab Kadir, I. Aris, and S.D. Buba. Mitigating the anthropogenic global warming in the electric power industry. *Renewable and Sustainable Energy Reviews*, 16(5):2747 – 2761, 2012.

[34] K Tokimatsu, J Fujino, and Y Asaoka. Studies on nuclear fusion energy potential based on a long-term world energy and environment model. Technical report, 2001.

[35] Lutz Mez. Nuclear energy–any solution for sustainability and climate protection? *Energy Policy*, 48:56 – 63, 2012. Special Section: Frontiers of Sustainability.

[36] Yousry Gohar. Fusion solution to dispose of spent nuclear fuel, transuranic elements, and highly enriched uranium. *Fusion Engineering and Design*, 58-59:1097 – 1101, 2001.

[37] M Keilhacker, A Gibson, C Gormezano, P.J Lomas, P.R Thomas, M.L Watkins, P Andrew, B Balet, D Borba, C.D Challis, I Coffey, G.A Cottrell, H.P.L. De Esch, N Deliyanakis, A Fasoli, C.W Gowers, H.Y Guo, G.T.A Huysmans, T.T.C Jones, W Kerner, R.W.T König, M.J Loughlin, A Maas, F.B Marcus, M.F.F Nave, F.G Rimini, G.J Sadler, S.E Sharapov, G Sips, P Smeulders, F.X Söldner, A Taroni, B.J.D Tubbing, M.G. von Hellermann, D.J Ward, and JET Team. High fusion performance from deuterium-tritium plasmas in JET. *Nuclear Fusion*, 39(2):209–234, feb 1999.

[38] A.E. Costley. On the fusion triple product and fusion power gain of tokamak pilot plants and reactors. *Nuclear Fusion*, 56(6):066003, apr 2016.

[39] Mitsuru Kikuchi, Karl Lackner, and Minh Quang Tran. Fusion physics. 2012.

[40] GF Matthews, P Edwards, T Hirai, M Kear, A Lioure, P Lomas, A Loving, C Lungu, H Maier, Ph Mertens, et al. Overview of the iter-like wall project. *Physica Scripta*, 2007(T128):137, 2007.

[41] P Batistoni, Jari Likonen, N Bekris, S Brezinsek, P Coad, L Horton, G Matthews, Marek Rubel, G Sips, B Syme, et al. The jet technology program in support of iter. *Fusion engineering and design*, 89(7-8):896–900, 2014.

[42] Enzo Bertolini. Impact of jet experimental results and engineering development on the definition of the iter design concept. *Fusion Engineering and Design*, 27:27 – 38, 1995. Proceedings of the Third International Symposium on Fusion Nuclear Technology.

[43] V Riccardo, P Lomas, GF Matthews, I Nunes, V Thompson, E Villedieu, and JET EFDA Contributors. Design, manufacture and initial operation of the beryllium components of the jet iter-like wall. *Fusion Engineering and Design*, 88(6-8):585–589, 2013.

[44] C Thomser, V Bailescu, S Brezinsek, JW Coenen, H Greuner, T Hirai, J Linke, CP Lungu, H Maier, G Matthews, et al. Plasma facing materials for the jet iter-like wall. *Fusion science and technology*, 62(1):1–8, 2012.

[45] Joachim Roth, E. Tsitrone, A. Loarte, Th. Loarer, G. Counsell, R. Neu, V. Philipps, S. Brezinsek, M. Lehnen, P. Coad, Ch. Grisolia, K. Schmid, K. Krieger, A. Kallenbach, B. Lipschultz, R. Doerner, R. Causey, V. Alimov, W. Shu, O. Ogorodnikova, A. Kirschner, G. Federici, and A. Kukushkin. Recent analysis of key plasma wall interactions issues for iter. *Journal of Nuclear Materials*, 390-391:1 – 9, 2009. Proceedings of the 18th International Conference on Plasma-Surface Interactions in Controlled Fusion Device.

[46] S Brezinsek, T Loarer, V Philipps, HG Esser, S Grünhagen, R Smith, R Felton, J Banks, P Belo, A Boboc, et al. Fuel retention studies with the iter-like wall in jet. *Nuclear Fusion*, 53(8):083023, 2013.

[47] GF Matthews, JET EFDA Contributors, et al. Plasma operation with an all metal first-wall: comparison of an iter-like wall with a carbon wall in jet. *Journal of Nuclear Materials*, 438:S2–S10, 2013.

[48] M Firdaouss, R Mitteau, E Villedieu, V Riccardo, P Lomas, Z Vizvary, C Portafaix, L Ferrand, P Thomas, I Nunes, et al. Power deposition modelling of the iter-like wall beryllium tiles at jet. *Journal of Nuclear Materials*, 390:947–950, 2009.

[49] I. Nunes, P. de Vries, and P.J. Lomas. Optimization of the jet beryllium tile profile for power handling. *Fusion Engineering and Design*, 82(15):1846 – 1853, 2007. Proceedings of the 24th Symposium on Fusion Technology.

[50] R.D. Watson, D.L. Youchison, D.E. Dombrowski, R.N. Guiniatouline, and I.B. Kupriynov. Low cycle thermal fatigue testing of beryllium grades for iter plasma facing components. 2 1996.

[51] Sebastijan Brezinsek, JET-EFDA contributors, et al. Plasma-surface interaction in the be/w environment: conclusions drawn from the jet-ilw for iter. *Journal of nuclear materials*, 463:11–21, 2015.

[52] E.B Deksnis, A.T Peacock, H Altmann, C Ibbot, and H.D Falter. Beryllium plasma-facing components: Jet experience. *Fusion Engineering and Design*, 37(4):515 – 530, 1997.

[53] V Riccardo, M Firdaouss, E Joffrin, G Matthews, Ph Mertens, V Thompson, and E Villedieu. Operational limits for the iter-like wall in jet. *Physica Scripta*, 2009(T138):014033, 2009.

[54] V. Philipps, Ph. Mertens, G.F. Matthews, and H. Maier. Overview of the jet iter-like wall project. *Fusion Engineering and Design*, 85(7):1581 – 1586, 2010. Proceedings of the Ninth International Symposium on Fusion Nuclear Technology.

[55] V. Riccardo, P. Lomas, G.F. Matthews, I. Nunes, V. Thompson, and E. Villedieu. Design, manufacture and initial operation of the beryllium components of the jet iter-like wall. *Fusion Engineering and Design*, 88(6):585 – 589, 2013. Proceedings of the 27th Symposium On Fusion Technology (SOFT-27); Liège, Belgium, September 24-28, 2012.

[56] CP Lungu, I Mustata, V Zaroschi, AM Lungu, A Anghel, P Chiru, Marek Rubel, Paul Coad, and GF Matthews. Beryllium coatings on metals for marker tiles at jet: Development of process and characterization of layers. *Physica scripta*, 2007(T128):157, 2007.

[57] F Moons. European fusion programme. iter task t23: Beryllium characterisation. progress report. tensile tests on neutron irradiated and reference beryllium. Technical report, Centre de l'Etude de l'Energie Nucleaire, 1996.

[58] Materion Beryllium and Materion Brush Inc Composites. *Materion Specification Sheet: S-65-H Beryllium Grade*, 2018.

[59] David E Dombrowski. Manufacture of beryllium for fusion energy applications. *Fusion Engineering and Design*, 37(2):229 – 242, 1997.

[60] Kenneth A Walsh. *Beryllium chemistry and processing*. ASM international, 2009.

[61] A Widdowson, MJ Baldwin, JP Coad, RP Doerner, J Hanna, DE Hole, GF Matthews, M Rubel, R Seraydarian, H Xu, et al. Testing of beryllium marker coatings in pisces-b for the jet iter-like wall. *Journal of Nuclear Materials*, 390:988–991, 2009.

[62] G F Matthews, M Beurskens, S Brezinsek, M Groth, E Joffrin, A Loving, M Kear, M-L Mayoral, R Neu, P Prior, V Riccardo, F Rimini, M Rubel, G Sips, E Villedieu, P de Vries, and M L Watkins and. JET ITER-like wall—overview and experimental programme. *Physica Scripta*, T145:014001, dec 2011.

[63] G.F. Matthews. Plasma operation with an all metal first-wall: Comparison of an iter-like wall with a carbon wall in jet. *Journal of Nuclear Materials*, 438:S2 – S10, 2013. Proceedings of the 20th International Conference on Plasma-Surface Interactions in Controlled Fusion Devices.

[64] Peter Sigmund. Theory of sputtering. i. sputtering yield of amorphous and polycrystalline targets. *Phys. Rev.*, 184:383–416, Aug 1969.

[65] V. Philipps, T. Loarer, H.G. Esser, S. Vartanian, U. Kruezi, S. Brezinsek, and G. Matthews. Dynamic fuel retention and release under iter like wall conditions in jet. *Journal of Nuclear Materials*, 438:S1067 – S1071, 2013. Proceedings of the 20th International Conference on Plasma-Surface Interactions in Controlled Fusion Devices.

[66] A. Baron-Wiechec, A. Widdowson, E. Alves, C.F. Ayres, N.P. Barradas, S. Brezinsek, J.P. Coad, N. Catarino, K. Heinola, J. Likonen, G.F. Matthews, M. Mayer, P. Petersson, M. Rubel, W. van Renterghem, and I. Uytdenhouwen. Global erosion and deposition patterns in jet with the iter-like wall. *Journal of Nuclear Materials*, 463:157 – 161, 2015. PLASMA-SURFACE INTERACTIONS 21.

[67] A Widdowson, A Baron-Wiechec, P Batistoni, E Belonohy, J P Coad, P Dinca, D Flammini, F Fox, K Heinola, I Jepu, J Likonen, S Lilley, C P Lungu, G F Matthews, J Naish, O Pompilian, C Porosnicu, M Rubel, and R Villari and. Experience of handling beryllium, tritium and activated components from JET ITER like wall. *Physica Scripta*, T167:014057, jan 2016.

[68] K Heinola, C F Ayres, A Baron-Wiechec, J P Coad, J Likonen, G F Matthews, and A Widdowson and. Tile profiling analysis of samples from the JET ITER-like wall and carbon wall. *Physica Scripta*, T159:014013, apr 2014.

[69] K Heinola, A Widdowson, J Likonen, E Alves, A Baron-Wiechec, N Barradas, S Brezinsek, N Catarino, P Coad, S Koivuranta, S Krat, G F Matthews, M Mayer, P Petersson, and JET Contributors. Long-term fuel retention in JET ITER-like wall. *Physica Scripta*, T167:014075, feb 2016.

[70] J P Coad, E Alves, N P Barradas, A Baron-Wiechec, N Catarino, K Heinola, J Likonen, M Mayer, G F Matthews, P Petersson, and A Widdowson and. Surface analysis of tiles and samples exposed to the first JET campaigns with the ITER-like wall. *Physica Scripta*, T159:014012, apr 2014.

[71] Anže Založnik, Sabina Markelj, Iztok Čadež, Primož Pelicon, Primož Vavpetič, Corneliu Porosnicu, and Cristian P. Lungu. The influence of nitrogen co-deposition in mixed layers on deuterium retention and thermal desorption. *Journal of Nuclear Materials*, 467:472 – 479, 2015.

[72] R.A. Anderl, R.A. Causey, J.W. Davis, R.P. Doerner, G. Federici, A.A. Haasz, G.R. Longhurst, W.R. Wampler, and K.L. Wilson. Hydrogen isotope retention in beryllium for tokamak plasma-facing applications. *Journal of Nuclear Materials*, 273(1):1 – 26, 1999.

[73] M Reinelt and Ch Linsmeier. Temperature programmed desorption of 1 keV deuterium implanted into clean beryllium. *Physica Scripta*, T128:111–114, mar 2007.

[74] James F Ziegler, Matthias D Ziegler, and Jochen P Biersack. Srim–the stopping and range of ions in matter (2010). *Nuclear Instruments and Methods in Physics Research Section B: Beam Interactions with Materials and Atoms*, 268(11-12):1818–1823, 2010.

[75] D. Nishijima, R.P. Doerner, M.J. Baldwin, and G. De Temmerman. Erosion yields of deposited beryllium layers. *Journal of Nuclear Materials*, 390-391:132 – 135, 2009. Proceedings of the 18th International Conference on Plasma-Surface Interactions in Controlled Fusion Device.

[76] R.P Doerner, R.W Conn, S.C Luckhardt, F.C Sze, and J Won. Outgassing from and deuterium retention in beryllium and be/c mixed-material plasma-facing components. *Fusion Engineering and Design*, 49-50:183 – 188, 2000.

[77] William R. Wampler. Retention and thermal release of deuterium implanted in beryllium. *Journal of Nuclear Materials*, 123(1):1598 – 1602, 1984.

[78] Rion A. Causey and Kenneth L. Wilson. Tritium inventory and permeation in the iter beryllium. *Journal of Nuclear Materials*, 212-215:1436 – 1442, 1994. Fusion Reactor Materials.

[79] Andrey V. Markin, Vladimir N. Chernikov, Sergey Yu. Rybakov, and Andrey P. Zakharov. Thermal desorption of deuterium implanted into beryllium. *Journal of Nuclear Materials*, 233-237:865 – 869, 1996.

[80] R.P. Doerner, M.J. Baldwin, D. Buchenauer, G. De Temmerman, and D. Nishijima. The role of beryllium deuteride in plasma-beryllium interactions. *Journal of Nuclear Materials*, 390-391:681 – 684, 2009. Proceedings of the 18th International Conference on Plasma-Surface Interactions in Controlled Fusion Device.

[81] J Bohdansky and J Roth. Light ion sputtering of low z materials in the temperature range 20–1100 c. *Journal of Nuclear Materials*, 123(1-3):1417–1424, 1984.

[82] Robert W Conn, Russell P Doerner, and Jongik Won. Beryllium as the plasma-facing material in fusion energy systems—experiments, evaluation, and comparison with alternative materials. *Fusion Engineering and Design*, 37(4):481 – 513, 1997.

[83] RD Monk, A Loarte, A Chankin, S Clement, SJ Davies, JK Ehrenberg, HY Guo, J Lingertat, GF Matthews, MF Stamp, et al. Interpretation of ion flux and electron temperature profiles at the jet divertor target during high recycling and detached discharges. *Journal of nuclear materials*, 241:396–401, 1997.

[84] S Zalkind, M Polak, and N Shamir. Adsorption of hydrogen on clean and oxidized beryllium studied by direct recoil spectrometry. *Applied Surface Science*, 115(3):273 – 278, 1997.

[85] S. Zalkind, M. Polak, and N. Shamir. The adsorption of h2o vs o2 on beryllium. *Surface Science*, 385(2):318 – 327, 1997.

[86] S. Zalkind, M. Polak, and N. Shamir. Oxidation of ion-bombarded vs. annealed beryllium. *Surface Science*, 513(3):501 – 510, 2002.

[87] S Zalkind, M Polak, and N Shamir. Effects of preadsorbed hydrogen on the adsorption of o2, co and h2o on beryllium. *Surface science*, 539(1-3):81–90, 2003.

[88] S. Zalkind, M. Polak, and N. Shamir. Temperature dependent interactions of water vapor with a beryllium surface. *Surface Science*, 529(1):189 – 196, 2003.

[89] S. Zalkind, M. Polak, and N. Shamir. The initial interactions of beryllium with o2 and h2o vapor at elevated temperatures. *Surface Science*, 601(5):1326 – 1332, 2007.

[90] S. Zalkind, M. Polak, and N. Shamir. Electron-stimulated oxidation of beryllium by water vapor and by oxygen. *Phys. Rev. B*, 71:125413, Mar 2005.

[91] MG Ganchenkova, Vo A BOrodin, and Risto M Nieminen. Hydrogen in beryllium: Solubility, transport, and trapping. *Physical Review B*, 79(13):134101, 2009.

[92] Pengbo Zhang, Jijun Zhao, and Bin Wen. Vacancy trapping mechanism for multiple hydrogen and helium in beryllium: a first-principles study. *Journal of Physics: Condensed Matter*, 24(9):095004, jan 2012.

[93] L Ferry, F Virot, Y Ferro, D Matveev, Ch Linsmeier, and M Barrachin. Diffusivity of hydrogen and properties of point defects in beryllium investigated by dft. *Journal of Nuclear Materials*, 524:323–329, 2019.

[94] MG Ganchenkova and Vo A BOrodin. Ab initio study of small vacancy complexes in beryllium. *Physical Review B*, 75(5):054108, 2007.

[95] M. Mayer, R. Behrisch, H. Plank, J. Roth, G. Dollinger, and C.M. Frey. Codeposition of hydrogen with beryllium, carbon and tungsten. *Journal of Nuclear Materials*, 230(1):67 – 73, 1996.

[96] JD Fowler, Dipankar Chandra, TS Elleman, AW Payne, and Kuruvilla Verghese. Tritium diffusion in a12o3 and beo. *Journal of the American Ceramic Society*, 60(3-4):155–161, 1977.

[97] C.H. Wu, E. Hechtl, H.R. Yang, and W. Eckstein. Erosion of beryllium by oxygen. *Journal of Nuclear Materials*, 176-177:845 – 847, 1990.

[98] JT Hurd and RO Adams. Adsorption of nitrogen, hydrogen, oxygen, and carbon monoxide on a beryllium film. *Journal of Vacuum Science and Technology*, 6(1):229–233, 1969.

[99] M.J. Baldwin, R.P. Doerner, D. Nishijima, K. Schmid, D.G. Whyte, J.G. Kulpin, and G. Wright. Mixed-material layer formation on graphite exposed to deuterium plasmas containing beryllium. *Journal of Nuclear Materials*, 358(2):96 – 105, 2006.

[100] GR Longhurst. Tmap7: Tritium migration analysis program. *Idaho National Laboratory, ineel/ext-04-02352, rev*, 2, 2004.

[101] WA Swansiger. *Tritium solubility in high purity beryllium.* PhD thesis, AVS, 1986.

[102] M.J. Baldwin, T. Schwarz-Selinger, and R.P. Doerner. Experimental study and modelling of deuterium thermal release from be–d co-deposited layers. *Nuclear Fusion*, 54(7):073005, apr 2014.

[103] R.G. Macaulay-Newcombe and D.A. Thompson. The effects of surface contamination on absorption and desorption of deuterium in beryllium and beryllium oxide. *Journal of Nuclear Materials*, 212-215:942 – 947, 1994. Fusion Reactor Materials.

[104] G. De Temmerman, M.J. Baldwin, D. Anthoine, K. Heinola, A. Jan, I. Jepu, J. Likonen, C.P. Lungu, C. Porosnicu, and R.A. Pitts. Efficiency of thermal outgassing for tritium retention measurement and removal in iter. *Nuclear Materials and Energy*, 12:267 – 272, 2017. Proceedings of the 22nd International Conference on Plasma Surface Interactions 2016, 22nd PSI.

[105] D. Matveev, P. Hansen, T. Dittmar, H.R. Koslowski, and Ch. Linsmeier. Modeling of h/d isotope-exchange in crystalline beryllium. *Nuclear Materials and Energy*, 20:100682, 2019.

[106] VP Afanas'ev, AS Gryazev, PS Kaplya, M Köppen, O Yu Ridzel, N Yu Subbotin, and P Hansen. Investigation of deuterium implantation into beryllium sample by electron energy loss spectroscopy. In *IOP Conf. Series: Journal of Physics: Conf. Series*, volume 891, page 012303, 2017.

[107] M. Rubel, J.P. Coad, A. Widdowson, G.F. Matthews, H.G. Esser, T. Hirai, J. Likonen, J. Linke, C.P. Lungu, M. Mayer, L. Pedrick, and C. Ruset. Overview of erosion–deposition diagnostic tools for the iter-like wall in the jet tokamak. *Journal of Nuclear Materials*, 438:S1204 – S1207, 2013. Proceedings of the 20th

International Conference on Plasma-Surface Interactions in Controlled Fusion Devices.

[108] C P Lungu, I Mustata, V Zaroschi, A M Lungu, A Anghel, P Chiru, M Rubel, P Coad, and G F Matthews. Beryllium coatings on metals for marker tiles at JET: development of process and characterization of layers. *Physica Scripta*, T128:157–161, mar 2007.

[109] Hendrix Demers, Nicolas Poirier-Demers, Alexandre Réal Couture, Dany Joly, Marc Guilmain, Niels de Jonge, and Dominique Drouin. Three-dimensional electron microscopy simulation with the casino monte carlo software. *Scanning*, 33(3):135–146, 2011.

[110] Johannes Schindelin, Ignacio Arganda-Carreras, Erwin Frise, Verena Kaynig, Mark Longair, Tobias Pietzsch, Stephan Preibisch, Curtis Rueden, Stephan Saalfeld, Benjamin Schmid, et al. Fiji: an open-source platform for biological-image analysis. *Nature methods*, 9(7):676, 2012.

[111] M. Kumar, C. Makepeace, C. Pardanaud, Y. Ferro, E. Hodille, C. Martin, P. Roubin, A. Widdowson, T. Dittmar, C.h. Linsmeier, C.P. Lungu, C. Porosnicu, I. Jepu, P. Dinca, M. Lungu, O.G. Pompilian, and JET contributors. Identification of beo and beoxdy in melted zones of the jet be limiter tiles: Raman study using comparison with laboratory samples. *Nuclear Materials and Energy*, 17:295 – 301, 2018.

[112] C. Makepeace, C. Pardanaud, P. Roubin, I. Borodkina, C. Ayres, P. Coad, A. Baron-Wiechec, I. Jepu, K. Heinola, A. Widdowson, S. Lozano-Perez, and J.E.T. Contributors. The effect of beryllium oxide on retention in jet iter-like wall tiles. *Nuclear Materials and Energy*, 19:346 – 351, 2019.

[113] F. de la Peña, M.-H. Berger, J.-F. Hochepied, F. Dynys, O. Stephan, and M. Walls. Mapping titanium and tin oxide phases using eels: An application of independent component analysis. *Ultramicroscopy*, 111(2):169 – 176, 2011.

[114] Francisco de la Peña, Eric Prestat, Vidar Tonaas Fauske, Pierre Burdet, Petras Jokubauskas, Magnus Nord, Tomas Ostasevicius, Katherine E. MacArthur, Mike Sarahan, Duncan N. Johnstone, Joshua Taillon, Jonas Lähnemann, Vadim Migunov, Alberto Eljarrat, Jan Caron, Thomas Aarholt, Stefano Mazzucco, Michael Walls, Tom Slater, Florian Winkler, pquinn dls, Ben Martineau,

Gaël Donval, Robert McLeod, Eric R. Hoglund, Ivo Alxneit, Daniel Lundeby, Trond Henninen, Luiz Fernando Zagonel, and Andreas Garmannslund. hyperspy/hyperspy: Hyperspy v1.5, July 2019.

[115] Baptiste Gault, Michael P Moody, Julie M Cairney, and Simon P Ringer. *Atom probe microscopy*, volume 160. Springer Science & Business Media, 2012.

[116] A. Baron-Wiechec, K. Heinola, J. Likonen, E. Alves, N. Catarino, J.P. Coad, V. Corregidor, I. Jepu, G.F. Matthews, and A. Widdowson. Thermal desorption spectrometry of beryllium plasma facing tiles exposed in the JET tokamak. *Fusion Engineering and Design*, 133:135–141, August 2018.

[117] Dennis R Floyd and John N Lowe. *Beryllium science and technology*, volume 2. Springer, 2014.

[118] L. E. Tanner and H. Okamoto. The be−ni (beryllium-nickel) system. *Bulletin of Alloy Phase Diagrams*, 9(5):563–573, Oct 1988.

[119] D. J. Chakrabarti, D. E. Laughlin, and L. E. Tanner. The be−cu (beryllium-copper) system. *Bulletin of Alloy Phase Diagrams*, 8(3):269–282, Jun 1987.